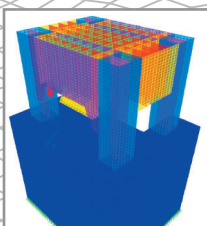
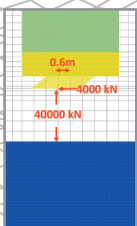
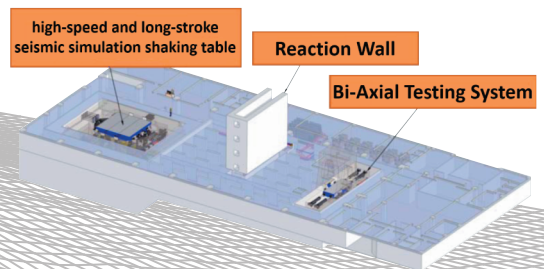
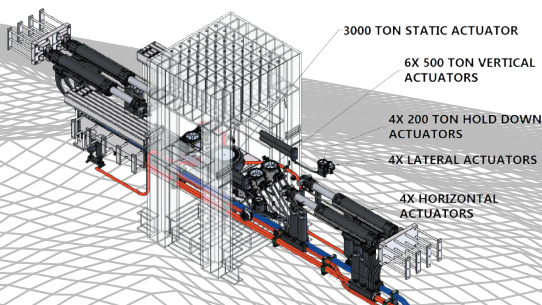


2017

NCREE Research Programs and Accomplishments



National Center for Research on
Earthquake Engineering

Contents

- 1 **Earthquake Occurrence Probability of Taiwan Faults Over the Next 50 Years**
Yu-Wen Chang, Chin-Hsiung Loh and Wen-Yu Chien
- 5 **Shallow Shear-wave Velocity Structures of TSMIP Stations in Taiwan**
Che-Min Lin, Chun-Hsiang Kuo, Jyun-Yan Huang, Ching-Chang Si and Kuo-Liang Wen
- 9 **Overview the Versions of Active Map for Seismic Source Characterization**
Kuan-Yu Chen, Yi-Ping Chen, Ying-Ping Kuo, Yan-Ru Chang, Chin-Tung Cheng, I Ting, Yi-Rui Lee, Yi-Rung Chuang, Kuo-Shih Shao, Bor-Shouh Huang, Tien-Shun Lin, Chin-Hsun Yeh and Kevin Clahan
- 13 **Soil Gas Radon Monitoring in Different Faults and Tatun Volcanic Areas of Northern Taiwan**
Vivek Walia, Arvind Kumar, Shih-Jung Lin, Ching-Chou Fu and Kuo-Liang Wen
- 17 **Development of Vertical-to-Horizontal Response Spectrum Ratio Model for Taiwan**
Shu-Hsien Chao, Po-Shen Lin, Che-Min Lin, Ching-Hsiao Kuo, Jyun-Yan Huang and Chiao-Chu Hsu
- 21 **A Simplified Procedure to Simulate the Interaction between a Low-rise Building and Liquefiable Soil**
Chih-Chieh Lu, Yu-Wei Hwang and Jin-Hung Hwang
- 25 **Higher-Mode Effects on Seismic Responses of Buildings**
Jui-Liang Lin
- 29 **Effects of M3 or PMM Nonlinear Hinges in Pushover Analysis of Reinforced Concrete Buildings**
Yeong-Kae Yeh and Te-Kuang Chow

- 33 **Damage Status and Seismic Assessment of Mid-to High-rise Buildings in the 2016 Meinong Earthquake in Taiwan**
Tirza Paramitha Pamelisa , Fu-Pei Hsiao and Yu-Chen Ou
- 37 **An Experimental Study of the In-Plane Cyclic Behavior of Steel-Plate Composite Walls with Boundary Elements**
Chang-Ching Chang, Yin-Nan Huang, Yu-Cheng Cheng and Chi-An Ho
- 41 **Seismic Health Monitoring of Space RC Frame Structure Using Piezoceramic-based Sensors**
Wen-I Liao, Juin-Fu Chai and Tsung-Jen Teng
- 45 **Structural Health Monitoring for Local Damages of RC Walls using Piezoceramic-Based Sensors under Seismic Loading**
Wen-I Liao, Juin-Fu Chai, Wen-Yu Jean and Tsung-Jen Teng
- 49 **Application of Metadata Technology for a Bridge Management System**
Chun-Chung Chen, Chia-Chuan Hsu, Kuang-Wu Chou, Hsiao-Hui Hung, Yu-Chi Sung and Kuo-Chun Chang,
- 53 **Design Concept and Verification of Temporary Rescue Bridge Using GFRP and Steel Hybrid Structures**
Fang-Yao Yeh, Kuo-Chun Chang and Yu-Chi Sung
- 57 **Seismic Risk Assessment and Screening of Large Water Pipes in Taiwan**
Gee-Yu Liu, Chin-Hsun Yeh, Lee-Hui Huang and Hsiang-Yuan Hung
- 61 **Evaluation of Failure Probability for Emergency Power Supply Systems in Hospitals**
Chi-Hao Lin and Cheng-Tao Yang

- 65 **Seismic Evaluation Methods for Fire-Protection Sprinkler Piping Systems in Buildings**
Fan-Ru Lin, Chang-Chen Yeh, Juin-Fu Chai and Kuo-Chun Chang
- 69 **Study on Behavior of Seismic Bracing Attachment for Fire Protection Sprinkler Piping System**
Wei-Hung Hsu, Juin-Fu Chai, Fan-Ru Lin, Zen-Yu Lin, Jian-Xiang Wang, Wen-I Liao and Shu-Yu Kao
- 73 **An Experimental Study of a Residual Heat Removal Piping System in an NPP**
Zih-Yu Lai, Juin-Fu Chai, Fan-Ru Lin, Wen-Fang Wu and Yin-Nan Huang
- 77 **Numerical Modelling and Experimental Validation of the Flange Joint of a Piping System in Numerical Power Plants**
Juin-Fu Chai, Fan-Ru Lin, Zih-Yu Lai and Wen-Fang Wu
- 81 **Experimental and Analytical Study on Multiaxial Hysteresis Behavior of Lead Rubber Bearings**
Wang-Chuen Lin, Shiang-Jung Wang, Jenn-Shin Hwang, Cho-Yen Yang and Chung-Han Yu
- 85 **The Bi-Axial Testing System in Tainan Laboratory of Taiwan's National Center for Research on Earthquake Engineering**
Te-Hung Lin, Ker-Chun Lin and Keh-Chyuan Tsai
- 89 **Online Model Updating with the Gradient-based Parameter Identification Method for Advanced Hybrid Simulations**
Ming-Chieh Chuang
- 93 **Cloudization of An In-house Discrete Element Simulation Platform**
Wei-Tze Chang

97 **Development of Adaptively Smoothed-Distributed
Seismicity Model**

Hsun-Jen Liu, Norman A. Abrahamson and Chin-Hsun Yeh

Earthquake Occurrence Probability of Taiwan Faults Over the Next 50 Years

Yu-Wen Chang¹, Chin-Hsiung Loh² and Wen-Yu Chien³

張毓文¹、羅俊雄²、簡文郁³

Abstract

Time-dependent probability model are considered because studies of paleoseismic records on well-studied faults in Taiwan have found them to be technically defensible characterizations of the timing of earthquakes. Although time-independent earthquake occurrence behavior characterization requires only an assessment of the mean recurrence interval (T_r) for a given magnitude, this study considers the elapsed time since the previous earthquake (T_e) in time-dependent probability model for the 25 major faults in Taiwan. For faults with a long paleoseismic record and a documented most recent event, time-dependence can be incorporated into probabilistic seismic hazard analysis using an alternative models to account for the active fault rupture cyclic characteristics from the present time up to a particular lifetime (such as for the Chelungpu fault). The conditional probability in the next subsequent time windows (T_p) corresponds to a renewal model with the coefficient of variation of the recurrence interval. The Taiwan earthquake probability map for the 25 major faults in the 50-year periods from 2017 to 2067 is developed in this study.

Keywords: Probabilistic Seismic Hazard Analysis, Time-dependent Model, Renewal, Poisson, Recurrence Interval

Introduction

According to the principles of probabilistic seismic hazard analysis (PSHA), technically defensible models of fault behavior must be included in the analysis. The model most commonly used in the PSHA for earthquake occurrence, the Poisson process, considers that earthquakes occur randomly in time when viewed over a long interval; it belongs to the memory-less assumptions in which time, size and location of preceding events are independent.

In reality, there is increasing evidence showing that the behavior of earthquake occurrence, which is related to the individual fault source, follows an inherent time model. Based on the observation that during repeated rupture episodes occurring on the individual fault (or fault system), some characteristics remain approximately constant over a large timescale; the rupture characterization of the earthquake occurrence behavior does not match the assumption

used in the Poisson process. It is important to properly consider the variability in recurrence rates caused by multiple-segment ruptures that change from event to event due to fault interaction.

The frequency of large earthquake occurrence forms the basis for seismic hazard assessments, while the concept of a stress-driven earthquake renewal inspires time-dependent earthquake probability calculations. In fact, in recent years, the time dependent occurrence model has been applied increasingly as part of PSHA (e.g., González et al., 2006; Chang et al., 2007; Akinci et al., 2010; Field et al., 2015). The time-dependent hazard analysis in the San Francisco Bay region using the probability models for the major Bay Area faults was considered by the U.S. Geological Survey's Working Group on the California Earthquake Probabilities study (WGCEP, 2003). It performed time-dependent probability calculations for the next 30 years using historic earthquake data from the segmentations of active

¹ Associate Researcher, National Center for Research on Earthquake Engineering

² Professor, National Taiwan University, Department of Civil Engineering

³ Research Fellow, National Center for Research on Earthquake Engineering

faults.

Paleoseismicity Data and Renewal Model

From the report on the paleoearthquake study on the Chelungpu fault, the intervals in the past 2 ka (kiloyears ago) range from about 700 years to 100 years and are related to coefficient of variation (COV) = 0.356. In addition, COV is a key parameter in time-varying probability estimates, particularly the standard deviation of recurrence intervals for a given fault system between large events. In the statistical analyses, the QQ plot displays a quantile-quantile plot of two observed data samples and model values. If the samples are obtained from the same distribution, the plot will be linear or close to 1:1. Based on these paleoearthquake data from the Chelungpu Fault, the QQ plots of the five distribution models show that the four renewal models have the best performance for describing the characteristic behavior compared to the exponential (Poisson) model, as illustrated in Fig. 1. In the plot, the sample data is displayed with the symbol “+” and the red line is a robust linear fit of the order statistic of the two samples. In the test, the exponential (Poisson) model result indicates that the rupture episode behaviour for specific faults cannot unilaterally be described by a constant occurrence rate. Therefore, the WGCEP (2003) has considered the weighting for the time-independent and time-dependent models to build the hazard map. The data show good agreement with the assumed probability distribution function, which indicates that the uncertainty of the time investigation for the paleoearthquake occurrence is consistent with a COV of 0.35 to 0.5.

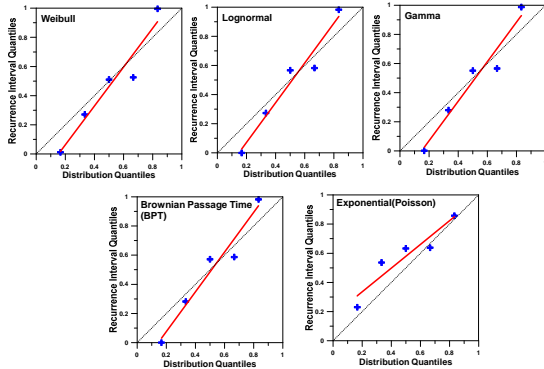


Fig. 1. The QQ-plots of the paleoearthquake data of the Chelungpu fault and the five distribution models. COV = 0.356 of the Chelungpu fault is assumed.

Earthquake Probability Model with Time

To represent the earthquake occurrence with respect to time, it is assumed that the occurrence of large earthquakes is periodic. This assumption is taken into consideration along with the energy accumulation of previous events through an earthquake renewal

model. Renewal models were applied to different distributions which allow the probability of fault occurrence to increase with respect to the elapsed time (T_e) since the occurrence of the last event with the subsequent time window (T_p) year. Several typical probability distributions for describing earthquake recurrence intervals include the exponential (Poisson), lognormal, Weibull, gamma, or Brownian Passage Time (BPT) (Matthews et al., 20020). The BPT distribution is based on a simple physical earthquake cycle model and has highly desirable statistical properties for describing earthquake recurrence statistics. This distribution has been widely used in California and Japan (ERC, 2005; Field et al., 2015), among other studies.

Conditional Probability in T_p -year

Let $f(\xi)$ denote a probability density function of the recurrence interval of the fault rupture that causes the earthquake. In the reliability, the probability of the event occurring at time t is based on a probability density distribution $f(t)$ and a cumulative distribution function $F(t)$ for the continuous random variable of T . The survivor function $R(t)$ simply indicates the probability that the event of interest characterized by cumulative distribution function (CDF) $F(t)$ has not occurred by duration t , as follows

$$R(t) = P\{T \geq t\} = 1 - F(t) \quad (1)$$

The conditional probability of a failure in the time interval from t to $t + \Delta t$ given that the fault has survived to the time is

$$P\{t \leq T \leq t + \Delta t | T \geq t\} = \frac{R(t) - R(t + \Delta t)}{R(t)} \quad (2)$$

If the elapsed time of a time-dependent active fault is given as T_e , the hazard analysis involves estimation of the occurrence probability of the fault during the subsequent T_p -year. For most structures, the earthquake design is estimated on the basis of the structural lifetime. In this case, T_p is set as the structural lifetime, and the seismic hazard due to the active fault can be estimated using engineering reliability theory. From Eq. (2), given a condition that the fault has survived during $[0, T_e]$, the probability of causing a fault rupture during $[T_e, T_e + T_p]$ is called the posterior failure probability (or recurrence probability):

$$P_{cod} = Q_c(T_e + T_p | T_e) = \frac{Q_c[T_e + T_p, T_e]}{Q_c[T_e]} = \frac{\int_{T_e}^{T_e + T_p} f(\xi) \cdot d\xi}{\int_{T_e}^{\infty} f(\xi) \cdot d\xi} \quad (3)$$

The probability $Q_c(T_e + T_p | T_e)$ represents the conditional probability (P_{cod}) in the consequent time period. Fig. 2 is the illustrating diagram for the calculation of conditional probability from a probability density function. The time interval of

interest (exposure time) is the gray area (A). The survivor function is equal to all the colored area (A+B). The conditional probability is the ratio of the two areas. Fig. 3 is the comparison of the five probability models used the estimate with Eq. (3), over the next 50-year conditional probabilities of earthquake occurrence as an example. The conditional probability of renewal model conforms to the Poisson model when COV is large.



Fig. 2. Diagram illustrating the calculation of conditional probability from a probability density function. The time interval of interest (exposure time) is the gray area (A). The survivor function is equal to the all colored area (A+B). The conditional probability is the ratio of the two areas.

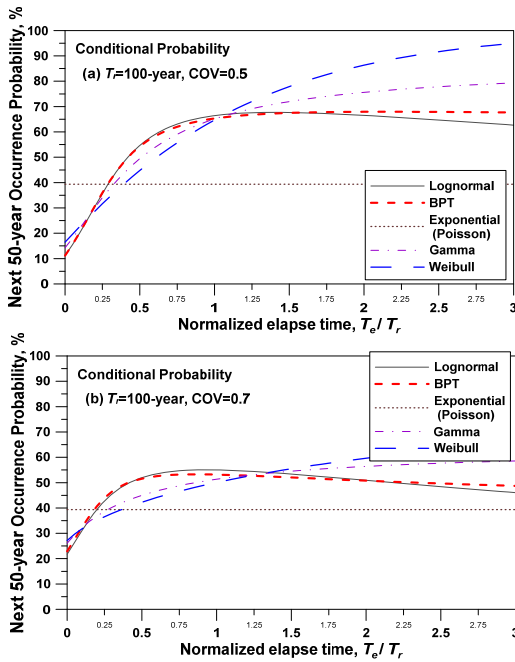


Fig. 3 Comparison of the five probability models used in estimating the next 50-year (T_p) conditional probabilities of earthquake occurrence as an example. All models have mean=100 year and COV = 0.5 and 0.7.

Earthquake Probability Map of Faults: 2017–2067

An active fault is defined as one that has moved repeatedly in recent geological time and has the

potential to cause earthquakes in the future. The Taiwan Central Geological Survey (CGS) has had a project for active fault research since 1997. Until 2010, thirty-three active fault locations in Taiwan were published by Lin et al. (2012). The study congregates relevant seismic, geological, and geophysical data of the faults to develop the database for the CGS version. On the other hand, thirty-eight on-land active seismogenic structures were identified by Shyu et al. (2016). The model combined information from pre-existing databases and a digitized three-dimensional seismogenic structure map for Taiwan. The fault parameters in both the databases include fault geometry, slip rate, the time of the most recent earthquake, etc. Specifically, some active faults consisting of the same geometry characteristic are combined in both the models.

In this study, the geometry and activity parameters of the twenty-five on-land active faults have been summarized from the CGS and Shyu et al. (2016) versions. Based on the information from the paleoseismological studies, three classifications of faults depending on these data were identified. The following is the classification due to the geometry and activity rate for each fault:

Category I: Sufficient information from geological, seismological, etc. to identify the activity rate. This only includes the Chelungpu fault. The COV is equal to 0.356.

Category II: Obvious information of geological features, but limited information of the paleoseismicity. Includes the Shihtan, Tuntzuchiao, Changhua, Meishan, Hsinhua, Milun, and Longitudinal Valley faults. The COV will be assumed as 0.5 because the last event time was known.

Category III: Limited geological and seismological information. Includes the Shanchiao, Hukou, Hsinchu, Hsincheng, Sanyi, Tamaopu – Shuangtung, Chiuchiungkeng, Chukou, Muchiliao – Liuchia, Houchiali, Tsochen, Hsiaokangshan, Chishan, Chaochou, Hengchun, Chimei, Central Range structure, and Luyeh faults. Although the time of the last event of the Shanchiao, Houchiali and Tamaopu – Shuangtung faults were known, the uncertainties are still larger. The T_e/T_r ratio and COV will be assumed as 0.5 and 0.7. The eighteen active faults was classed in this grouping.

The probable moment magnitude (M_w) of each fault rupture is estimated using the published regression results from Wells and Coppersmith (1994). The average recurrence interval for such earthquakes with fault ruptures were then calculated from the average slip (displacement) per event and the slip rates of the faults. The conditional probability over the next $T_p = 50$ years for these active faults are estimated using four renewal models (using equal weightings), and

have been mapped in Fig. 4. However, not all the paleoseismological studies can provide enough information to estimate the intervals and the last event times for some active faults. Both the recurrence interval between earthquakes and the size of earthquakes may lead to overestimation when the earthquakes are not characteristic ruptures of an entire fault. In this case, $COV=0.7$ and the T_e/T_r ratio $=0.5$ are used in the probability calculation. As a result of approximating using the constant rate Poisson process model, the calculation of the conditional probability for these faults containing the limited information is implemented.

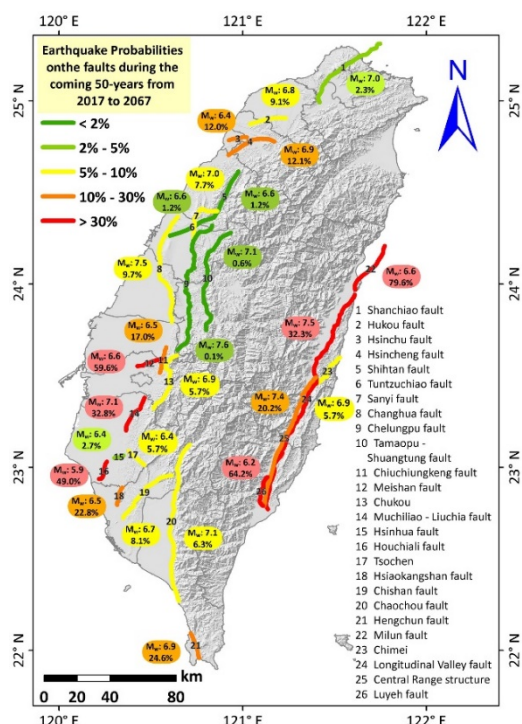


Fig. 4 The Taiwan earthquake probability map of the 25 major faults during the coming 50 years from 2017 to 2067. The probability earthquake magnitude of the fault is also shown.

Conclusions

Drawing on fault information and the methodologies for estimating earthquake probability, it is concluded that there is a high probability of a major, damaging earthquake striking western Taiwan over the next 50 years (2017–2067). Such earthquakes are most likely to occur on the Meishan, and Houchiali faults of the West of Taiwan identified in this study; but they may also occur on faults that were not characterized as part of the study (i.e., in the “background”). The earthquake probability map of faults in Taiwan of this study is appropriate for use in estimating seismic hazard in Taiwan, and estimating the intensity of the expected ground motion level for specified “scenario” earthquakes. In addition, it provides a basis for the seismic upgrade of structures and for developing building codes.

References

- Akinci, A., D. Perkins, A. M. Lombardi, and R. Basili (2010). Uncertainties in probability of occurrence of strong earthquakes for fault sources in the Central Apennines, Italy. *J. Seismol.* 14(1), 95-117.
- Chang, Y. W., W. Y. Jean, C. H. Loh, and K. L. Wen (2007). The Application of Time-Predictable Characteristic Earthquake Model for Evaluation of Design Earthquake in Taiwan, *Proceedings of 10th International Conference on Applications of Statistics and Probability in Civil Engineering (ICASP10)*, Japan, No.72.
- Earthquake Research Committee (ERC) (2005). National Seismic Hazard Maps for Japan, Headquarters for Earthquake Research Promotion. Available from World Wide Web. <http://www.jishin.go.jp/main/index-e.html>, 162 pp.
- Field, E. H., G. P. Biasi, P. Bird, T. E. Dawson, K. R. Felzer, D. D. Jackson, K. M. Johnson, T. H. Jordan, C. Madden, A. J. Michael, K. R. Milner, M. T. Page, T. Parsons, P. M. Powers, B. E. Shaw, W. R. Thatcher, R. J. Weldon, and Y. Zeng (2015). Long-Term Time-Dependent Probabilities for the Third Uniform California Earthquake Rupture Forecast (UCERF3), *Bull. Seismol. Soc. Am.* 105(2A).
- González, Á., J. B. Gómez, and A. F. Pacheco (2006). Updating seismic hazard at Parkfield, *J. Seismol.* 10(2), 131-135, doi:10.1007/s10950-005-9005-8.
- Lin, C. W., S. T. Lu, and W. S. Chen, (2012). Active Fault Map of Taiwan: An Explanatory Text (2012 Edition), Special Publication of the Central Geological Survey 26, 30pp. (in Chinese)
- Matthews, M. V., W. L. Ellsworth, and P. A. Reasenberg (2002). A Brownian model for recurrent earthquakes, *Bull. Seismol. Soc. Am.* 92.
- Shyu, J. B. H., Y. R. Chuang, Y. L. Chen, Y. R. Lee, and C. T. Cheng (2016). A new on-land seismogenic structure source database from the Taiwan Earthquake Model (TEM) project for seismic hazard analysis of Taiwan, *Terr. Atmos. Ocean. Sci.* 27(3), 311-323, doi:10.3319/TAO.2015.11.27.02(TEM).
- Working Group on California Earthquake Probabilities (WGCEP) (2003). Earthquake Probabilities in the San Francisco Bay Region: 2002-2031. U.S. Geological Survey, Open-File Report 03-214, 234 pp.
- Wells, D. L. and K. J. Coppersmith (1994). New empirical relationships among magnitude, rupture length, rupture width, rupture area, and surface displacement, *Bull. Seismol. Soc. Am.* 84, 974-1002.

Shallow Shear-wave Velocity Structures of TSMIP Stations in Taiwan

Che-Min Lin¹ Chun-Hsiang Kuo² Jyun-Yan Huang³ Ching-Chang Si⁴ and Kuo-Liang Wen⁵

林哲民¹、郭俊翔²、黃雋彥³、思靜章⁴、溫國樑⁵

Abstract

The high seismicity and major tectonic features of Taiwan result from active collisions. The wide range of alluvium basins amplify and extend incident seismic waves and can result in earthquakes because of the seismic site effect. In this study, the advantages of the evenly distributed strong motion stations and the numerous records in Taiwan were used to apply the Receiver Function (RF) technique to high-frequency acceleration seismograms recorded by Taiwan Strong Motion Instrumentation Program (TSMIP) stations to estimate the shallow shear wave velocity (V_s) structures. In the RF analyses, an average RF of each station was calculated to enhance the converted phases and reduce the inharmonic arrivals. Based on the geological data, the geophysical data, and the Engineering Geology Database for TSMIP (EGDT) drilling data, an initial layer model with variable V_s and thickness, in conjunction with a Genetic Algorithm (GA) search, was used to model RF and estimate the V_s profile of a station. Finally, the one-dimensional shallow V_s profiles of 763 stations were estimated by RF analysis and forward modeled with the GA search. All the results proved that this method is not only effective for teleseismic records but also strong motion records, and can reconstruct the shallow V_s structure of alluvium basins overlaying a hard bedrock. Based on the V_s structures estimated in this study, a shallow velocity model of Taiwan was preliminarily constructed for applications in seismology and earthquake engineering. In addition, the results were compared with the V_{s30} (average shear-wave velocity of the top thirty meters of ground) of the EGDT to verify the site conditions of TSMIP stations and to provide important site parameters such as engineering bedrock and $Z_{1.0}$ (depth of the velocity horizon where the shear-wave velocity reaches 1.0 km/sec).

Keywords: TSMIP, Strong-motion Station, Shear-wave Velocity, Receiver Function, Velocity Model

Introduction

Taiwan is located at the convergence boundary of the Philippine Sea plate and the Eurasian plate. The ongoing and active orogeny results in the high seismicity in Taiwan. It is essential to precisely predict the strong-motion intensities and the characteristics of an earthquake to improve hazard reduction plans. For earthquake engineering, the Ground Motion Prediction Equation (GMPE) is mostly applied to predict ground motion based on the empirical regression of historical records. Recently, for modern GMPEs, in addition to using V_{s30}

(average shear-wave velocity of the top thirty meters of ground), $Z_{1.0}$ (depth of the velocity horizon where the shear-wave velocity reaches 1.0 km/sec), and $Z_{2.5}$ (depth of the velocity horizon where the shear-wave velocity reaches 2.5 km/sec) have also been introduced as additional site factors to better estimate site amplification. For seismology, full-waveform numerical simulations based on 3D velocity models are developed and applied to estimate ground motions, including the source, path, and site effect. Nevertheless, many 3D velocity models have been constructed using seismic tomography inversions in

¹ Associate Researcher, National Center for Research on Earthquake Engineering

² Researcher, National Center for Research on Earthquake Engineering

³ Assistant Researcher, National Center for Research on Earthquake Engineering

⁴ Assistant Technologist, National Center for Research on Earthquake Engineering

⁵ Professor, Dep. of Earth Science, National Central University and Division Director, National Center for Research on Earthquake Engineering

Taiwan. The resolution of the shallow parts of these tomography models (within a depth of one or two kilometers) is not adequate to replicate the alluvium basins with low velocities because of insufficient and uneven seismic ray traces. Therefore, the lack of a detailed shallow velocity model in Taiwan is a serious challenge for the evaluation of seismic hazards.

The aim of this study is to apply the receiver function (RF) technique to seismograms recorded by Taiwan Strong Motion Instrumentation Program (TSMIP) stations, which are operated by the Central Weather Bureau (CWB), to estimate the shallow shear-wave velocity structures all over Taiwan. Finally, a shallow 3D velocity model is preliminarily constructed for Taiwan. The model will be constantly improved to include the detailed velocity distributions, the depths of engineering and seismic bedrock, and other important site parameters to provide fundamental data for seismology and earthquake engineering.

TSMIP Stations

The CWB started the Taiwan Strong Motion Instrumentation Program (TSMIP) in 1990 and distributed strong motion stations in metropolitan areas and near-fault regions to collect seismograms. The program is necessary for the planning of safe and economic building codes and to understand strong motion characteristics in different geologic conditions. The TSMIP network has proved that it can collect abundant and high-quality strong motion data, especially for the near-fault data from the 1999 Chi-Chi earthquake, which contributed significantly to seismology and engineering.

Figure 1 shows a topographic map of the distribution of TSMIP stations in Taiwan. There are over eight hundred stations. Most of them are spread over the plain regions. The average distance between stations is about five kilometers, but the distance is reduced to two kilometers in major metropolitan areas, such as the Taipei Basin, the Ilan plain, Taichung City, and Kaohsiung City. On the other hand, stations located in the mountainous regions are sparsely distributed. Some mountainous stations were only installed in the last decade by the Institute of Earth Sciences, Academia Sinica. The instruments installed at the TSMIP stations are all tri-axial accelerometers. They operate in trigger mode with a 200 Hz sampling rate and a GPS time system.

The data from TSMIP between 1992 and 2013 are analyzed in this study. The numbers of records for stations are different and can be between several records and hundreds of records because of their operating dates, positions, and data qualities. Finally, the RF analyses are completed for 763 stations to estimate their shallow velocity structure.

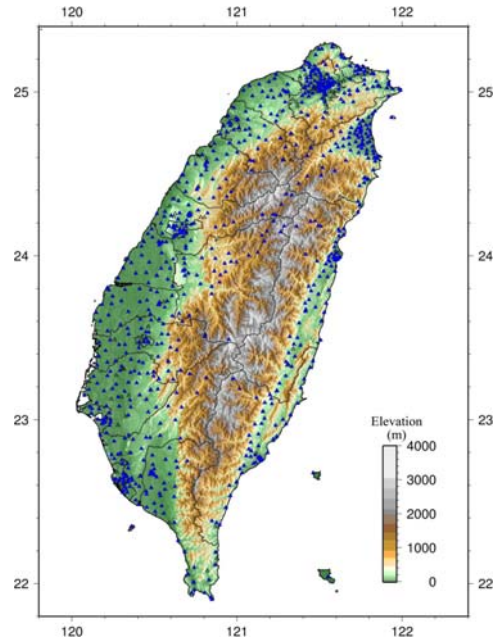


Fig. 1 Distribution map of the TSMIP stations

Receiver Function Analysis

The teleseismic RF method is used to provide local information on the S-wave velocity discontinuities of the crust or upper mantle beneath broadband stations (Langston, 1979; Ammon et al., 1990). This method is useful for showing the converted phases used to estimate the depth of the discontinuities, even if the seismograms are contaminated by noise and scattering waves. The RFs of stations distributed over a region can efficiently estimate the 3D structures of that region. Because the largest S-wave velocity discontinuity generally coincides with the Moho, the RF method is a popular way to study the structures from the lower crust to the upper mantle. In some recent studies, it was proven that the RF waveforms are also controlled by the sedimentary structures within the first few seconds of the direct P arrival. This method can be used in high-frequency strong motion records to construct a sediment velocity model by simulating an RF waveform (Ni and Somerville, 2013; Mostafanejad and Langston, 2017).

In the RF analysis of TSMIP stations, all horizontal waveforms were converted to radial components and divided by the vertical component in the frequency domain of the Fourier spectra with a Gaussian low-pass filter and a water level stabilization method. The spectral ratios are then converted back to time series to derive the RFs of events. The waveforms of RFs include converted phases generated from velocity interfaces beneath stations that represent the site information of sedimentary structures.

Figure 2 shows all receiver functions of station CHY001 arranged by back-azimuth as an example. Theoretically, all RFs generated from a station should be consistent if the structure is homogeneous in the horizontal direction. The systematic variation of

converted phase waveforms versus ray back-azimuths and the appearance of seismic energy on both the radial and transverse components reflect the existence of a dipping velocity discontinuity. Most RFs from CHY001 in Fig. 2 exhibit apparent converted phases at 0.2, 1.3, and 2.7 seconds. There are also some smaller phases that can be identified. They all represent velocity interfaces between strata at a depth of a few kilometers. The lower part of Fig. 2 is the average RF of all events for CHY001, which reduces the inharmonic arrivals and enhances the converted phases.

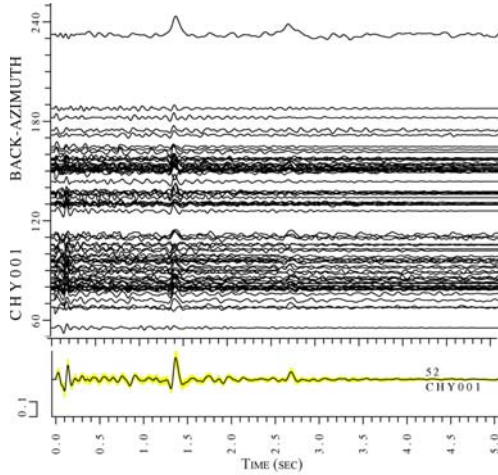


Fig. 2 RFs arranged by back-azimuths (upper part of figure) and average RF (lower part of figure) of CHY001

The average RFs of some TSMIP stations are shown in Fig. 3. They show obvious differences in the arrival times and amplitudes of converted phases because of the different geological backgrounds between stations. The stations located in the plain regions with thick sediments, such as stations CHY and TCU, show largely converted phases with later arrival times because their interfaces are deeper with higher velocity contrasts. The average RFs of the stations near or within the mountainous region, such as stations TTN and HWA, show earlier and more complex converted phases with high amplitudes. The near-surface velocity contrasts, which usually are the bedrocks, form waveforms oscillating between 0 and 0.5 seconds.

The genetic algorithm (GA) was applied to search for the shear-wave velocity model with the best fit between the observed and synthetic receiver functions. The GA search is a powerful global optimization method. The algorithm consists of selection, crossover, and mutation of individuals in a population and can search globally and locally for an optimal solution. Based on the geological, geophysical, and borehole data, we assumed a layer model covering a half space for the GA search. The shear-wave velocity and thickness of each layer are both variables in a set range. Figure 4 presents the results of the GA search for station CHY001 as an example. The results of the

GA search show the effective convergence of the wide searching ranges (blue dashed lines). The synthetic RF corresponding to the best model fits the observed one well.

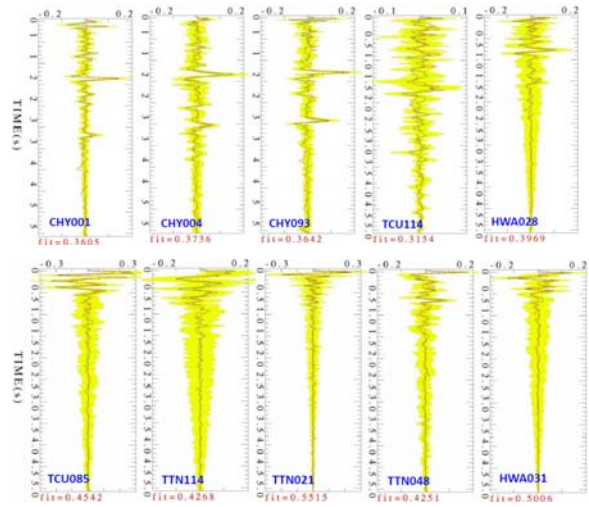


Fig. 3 Average RFs of some stations. The yellow areas are the ranges of standard deviation

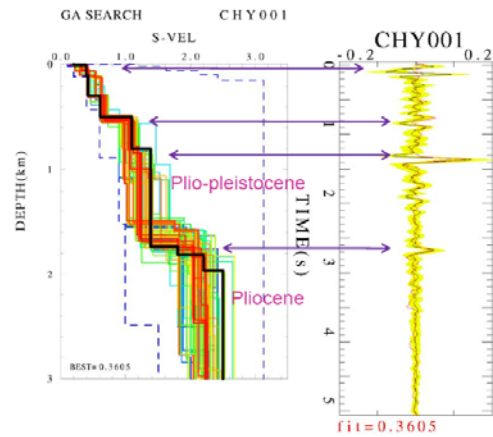


Fig. 4 Result of GA forward search for CHY001. The left figure shows 100 shear-wave velocity models with good RF fit using the GA search. The bolded black line is the best model. The right figure shows a comparison between the average observed RF (black line) and the best synthetic RF (red line).

Results and Discussion

The one-dimensional shallow shear-wave velocity (V_s) structures of 763 TSMIP stations were estimated using RF analysis and forward modeled with a GA search in this study. Geologic backgrounds vary considerably around Taiwan; therefore, the differences in the shallow velocity structures are distinct from region to region. The 763 results were integrated into a three-dimensional velocity model to give an overall description of the complex velocity structures of the sedimentary basins in Taiwan. The whole model can be discussed both in terms of the depths and the velocities. Figure 5 shows eight shear-wave velocity contour maps at depths from 50 to 1500 meters. The

station number used for each map is marked. The stations in the mountainous regions, especially in the Central Mountain Range, are fewer and have thin models, which are limited by their higher velocities and shallower bedrocks. Therefore, the deeper contour map includes fewer results from those stations. The non-uniform distribution of stations may induce some inaccuracies due to the interpolations of the model.

The contour map for the depth of 50 meters in Figure 5 shows that the major sedimentary basin, such as the Taipei Basin (TB), Ilan Plain (IP), Western Coastal Plain (WCP), etc., all exhibit V_s lower than 300 m/sec near the surface. The V_s values of other regions are mostly lower than 800 m/sec, though they are higher than 1000 m/sec for some mountainous regions. Although the V_s values smoothly increase at depths between 100 and 200 meters, the shapes of those sedimentary basins can still be identified clearly because of their lower V_s . Furthermore, there is a small low-velocity region that can be found in this depth range that corresponds to a small basin, named the Puli Basin, in central Taiwan. At depths between 400 and 600 meters, the low-velocity regions are still clear and gradually become smaller and smaller with increasing depths. The other regions show V_s values higher than 2000 m/sec. The fact that the low V_s of the TB disappear at a depth of 800 meters agrees with the structural shape of the TB, which has the deepest bedrock at a depth of about 700 meters to the northwest. However, the low-velocity zones along the coasts of the IP and the WCP extend to depths of more than 1000 meters. For depths beneath 600 meters, most of the regions in Taiwan show V_s values higher than 2000 m/sec, and some of the stations located in the mountainous regions exhibit V_s values higher than 3000 m/sec. Finally, the sedimentary basins with low V_s values have completely disappeared at a depth of 1500 meters all over Taiwan.

The results of this study provide not only the shallow three-dimensional velocity model of Taiwan, but also the essential site parameters of the TSMIP stations for earthquake engineering as a secondary product. Figure 6 presents the V_{s30} and $Z_{1.0}$ contour maps estimated from the V_s structures of the TSMIP stations. The variations of these two parameters exhibited on the two maps have a good correlation with the distribution of sedimentary basins, and appropriately represent the effect of site differences on the seismic ground motion. The reliability of the estimated V_{s30} has been proven by comparing it with the measured V_{s30} from the Engineering Geology Database for TSMIP (EGDT), based on the downhole P-S loggings. The $Z_{1.0}$ estimated by this study is the first dataset in Taiwan that can provide the site information of the bottoms of basins defined for GMPE studies. The linear relationship between the $Z_{1.0}$ and V_{s30} is clear because they are both dominated by the sedimentary basins. Furthermore, the different bedrocks defined by V_s can also be

evaluated based on the integrated three-dimensional velocity model. All the results will benefit ground motion predictions and numerical simulations in seismology and earthquake engineering.

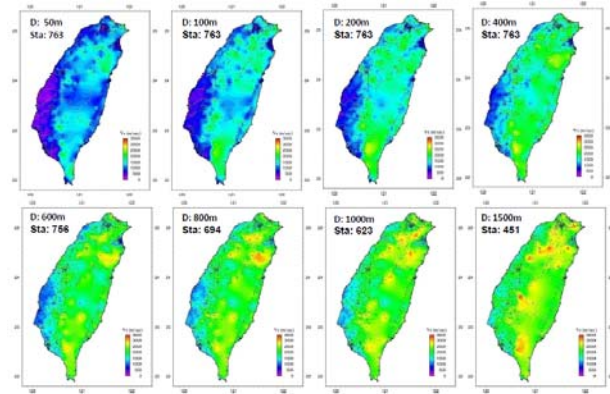


Fig. 5 Iso-depth contour maps of the shallow shear-wave velocity structures of TSMIP stations at eight depths

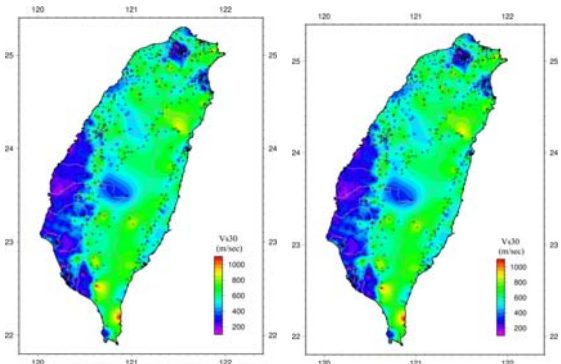


Fig. 6 V_{s30} (left) and $Z_{1.0}$ (right) contour maps of the TSMIP stations

References

- Ammon, C. J., Randall, G. E., and Zandt, G. (1990), "On the Non-uniqueness of Receiver Function Inversions," *J. Geophys. Res.*, 95, 15303–15318.
- Langston, C. A. (1979), "Structure under Mount Rainier, Washington, Inferred from Teleseismic Body Waves," *J. Geophys. Res.*, 84, 4749–4762.
- Mostafanejad, A., and Langston, C. A. (2017), "Velocity Structure of the Northern Mississippi Embayment Sediments, Part II: Inversion of Teleseismic P-Wave Transfer Functions," *Bull. Seism. Soc. Am.*, 107, 106–116.
- Ni, S., and Somerville, P. (2013), "Estimating site response by constraining shallow velocity structure with local P waves in the Central and Eastern United States," URS Group, Inc., final technical report, pp. 57.

Overview of the Versions of Active Maps for Seismic Source Characterization

Chen, Kuan Yu¹ Chen, Yi Ping¹ Kuo, Ying Ping¹ Chang, Yan Ru¹
Cheng, Chin Tung² Ting, I² Lee, Yi Rui² Chuang, Yi Rung² Shao, Kuo Shih²
Huang, Bor Shouh³ Lin, Tien Shun⁴ Yeh, Chin Hsun¹ Kevin Clahan⁵

Abstract

To consider and integrate comprehensive data of active faults in Taiwan and adjacent offshore faults, the SSHAC project has unified many seismic source versions of active faults, including the version from the Central Geological Survey (Lin et al., 2012) and the National Central University (Cheng, 2002). Professor J. Bruce H. Shyu from National Taiwan University was contacted to assess and provide an overview of former active fault versions and the Taiwan Earthquake model in Taiwan (Shyu et al., 2017). For other active fault sources, especially for offshore faults, the relevant data were compiled by a support team. Finally, 59 strips of active faults have been proposed in the seismic source characterization (SSC) model by the SSC TI team.

Keywords: Seismic source characterization, active faults

Introduction

After 1998, the seismic source versions of active faults can be differentiated into official and academic. Official versions are the active fault maps officially announced by the Central Geological Survey (CGS), which will only confirm an active fault if there is obvious geological evidence and the fault is definitely determined to be an active fault. Meanwhile, the academic version is formed by drawing on the research from the Graduate Institute of Applied Geology (GIAG) at the National Central University (NCU) and summarizing the results of previous surveys.

In this paper, the contents and evolutions of three fault versions will be described from the CGS, the NCU, and the Taiwan Earthquake model (TEM) established by J. Bruce H. Shyu.

Definition of active faults

In Taiwan, there are a total of 33 strips of active faults announced by the CGS. These faults are set on the basis of historical earthquake records and fault

study data. Their definitions are as follows:

- (1) Active faults: Faults that have been active in the past 100,000 years and will possibly have activity again in the future.
- (2) Type 1 active faults: Those that have been active in the past 10,000 years.
- (3) Type 2 active faults: Those that have been active between the past 100,000 to 10,000 years.
- (4) Suspected active faults: Those that have been active in the past 500,000 years, but for which it is uncertain whether the faults have been active in the past 100,000 years.

The tectonic structure and geological distribution of Taiwan are both different from those of other countries. Moreover, ever since the CGS announced the first version of active faults in 1998, all relevant literature of active faults in Taiwan has adopted this type of definition. The present project also relies on the active fault definition of the CGS.

¹ National Center for Research on Earthquake Engineering

² Sinotech Engineering Consultants, Inc.

³ Institute of Earth Sciences, Academia Sinica

⁴ Earth Science Department, Nation Central University

⁵ Lettis Consultants International. Inc. Earth Science Consultants

Central Geological Survey

The CGS has been carrying out general survey work on each active fault strip starting from 1997. The aim is to confirm the location and characteristics of the main active faults in Taiwan and to map out 1:25000 geological maps of the fault strip zone. Since 1998, it has begun to survey the ground surface line traces on active faults in Taiwan and has successively presented 1:25000 geological maps of the active fault strip zone. Using seismic and drilling data to review the studies of predecessors as well as LIDAR imaging and field geological surveys to further identify and confirm the accuracy of the ground surface location of faults, CGS published the active fault distribution map of Taiwan for 33 strips of active faults in 2012. These 33 active faults are divided into two categories: 20 strips of Type I active faults, which have been active in the past 10,000 years, and 13 strips of Type II active faults, which have been active for the past 100,000 years to 10,000 years (Fig. 1).

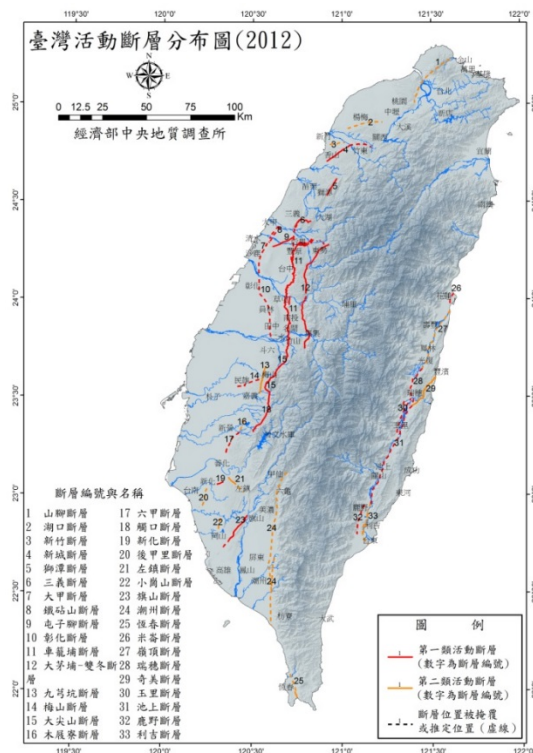


Figure 1. Active fault map published by the CGS with 33 onshore active faults in 2012 (Lin et al., 2012).

Graduate Institute of Applied Geology of National Central University

The scale bar in the “Active fault distribution map of Taiwan regions” created by Tsai Yi-Ben et al. (1998) is 1:500000; the map lists a total of 55 strips of active faults. The Engineering Geology and Hazard Mitigation Laboratory in the GIAG of the NCU used the research results of Lee (1999) and Tsai Yi-Ben et al. (1998) as the basis to compile new survey results

and have drawn the distribution map of active faults across the whole of Taiwan. Taking the aforementioned version as a basis, Cheng Chin-Tung (2002) compiled the studies of predecessors, historical earthquake records, and the sediments truncated by faults during the Holocene to late Pleistocene epochs with the intention of summarizing and merging faults with similar tectonic characteristics; the difference in the level of activities in each segment was also used to partition the faults. Furthermore, referring to the topographical characterization, the near-surface activity of buried faults was observed and additional active faults were drawn. In total, 50 strips of active faults were drawn (Fig. 2).

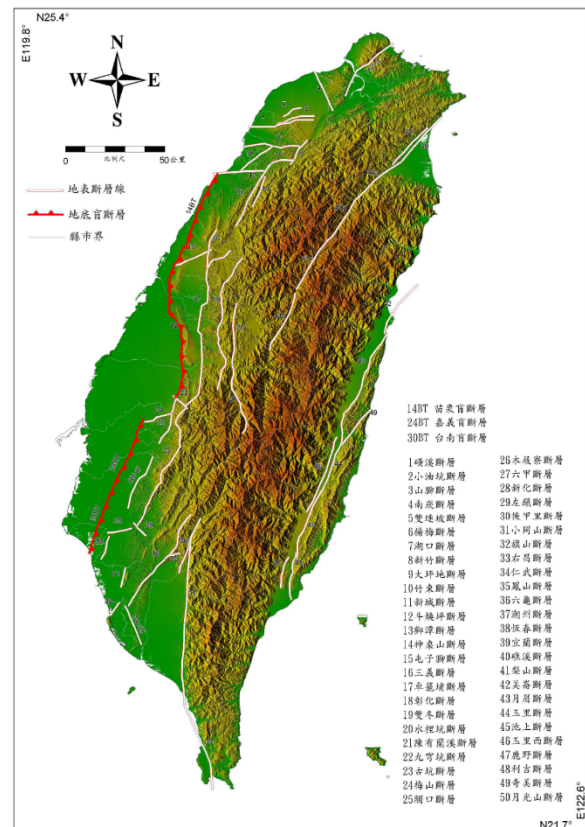


Figure 2. 50 active faults defined in active fault map by GIAG of NCU (Cheng, 2002).

Taiwan Earthquake Model

J. Bruce H. Shyu et al. (2017) integrated the existing presented seismogenic structure distributions in the Taiwan region and compiled two versions of onshore active faults: (1) the active fault distribution map of Taiwan presented by the CGS of the Ministry of Economic Affairs in 2012 and (2) the fault distribution map presented by the GIAG of NCU in 2002. Apart from integrating the active fault maps released by predecessors and using field surveys, satellite imaging, LIDAR imaging, terrain identification, and historical earthquakes, the front (blind) structures have been added. Even though these structures are not revealed on the ground surface, the

topographical characterization of ground surface deformations can still be interpreted as the presence of buried (blind) faults in this region. Referring to the latest research, the Persistent Scatterer Interferometry Synthetic Aperture Radar (PSInSAR) has been used to observe that some faults have obvious interseismic deformation behavior, such as the Lungchuan fault and the Youchang fault (Chun Chang-Lee, 2014; Hu Jyr-Ching et al., 2016). Taking these faults into consideration, in 2017, Shyu et al. proposed a map of 44 strips of active faults in the Taiwan area (Fig. 3).

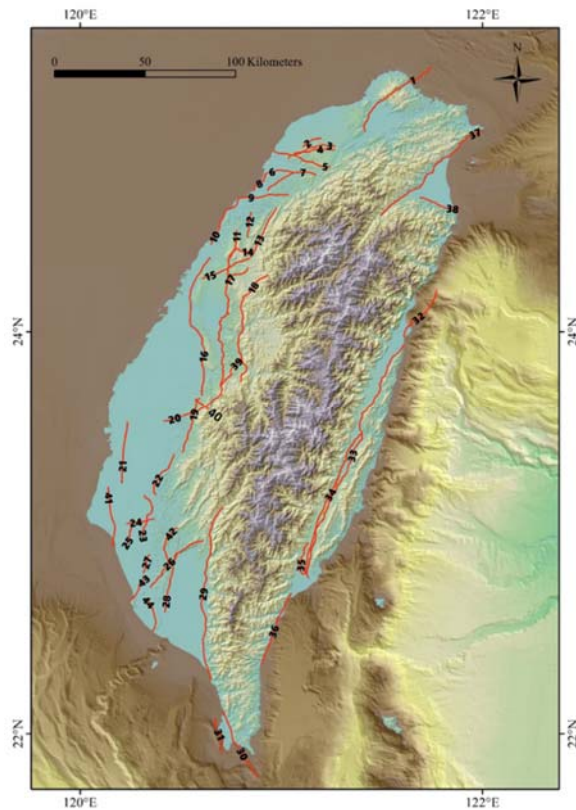


Figure 3. 44 active faults and suspect structures proposed by Shyu et al., 2017 in TEM.

Seismic source characterization model

The seismic source characterization (SSC) TI team comprehensively considered three versions of the active fault data: the versions from the CGS, the GIAG at the NCU, and the TEM. For other active fault sources in sea areas, the relevant data were compiled by a team of staff. Finally, 59 strips of active faults have been proposed in the SSC model by SSC TI team. Based on the magnitude of seismic hazard to nuclear power plants, these faults are classified as primary faults or other faults. The definitions are as follows:

Primary Fault Source: Among the fault sources considered in the project, these have significant contributions to the seismic hazard to nuclear power

plant sites in Taiwan; these refer to active fault sources located within a 20 km radius of a nuclear power plant.

Other Fault Source: These have a less significant contribution to the seismic hazard to nuclear power plant sites in Taiwan, but their fault structures and activities are well defined. These refer to active fault sources that are more than 20 km outside the radius of nuclear power plants.

Primary active faults can be divided into northern and southern primary faults. Northern primary faults include the Shanchiao fault system, the ST-II fault system, the S fault, the Aoti offshore faults, and the northern Ilan fault system. Meanwhile, the southern primary faults include the Hengchun fault system and the west Hengchun offshore structure. Other active fault sources are active fault sources that are more than 20 km outside the radius of nuclear power plants, including active faults onshore Taiwan and adjacent offshore (Fig. 4 and Table 1).

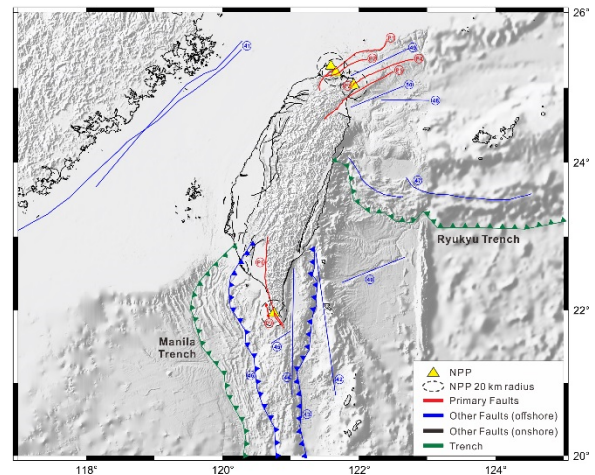


Figure 4. Active fault map of Taiwan seismic source characterization model. 7 primary fault sources, 2 subduction zone sources, 50 other fault sources, including 39 onshore and 11 offshore fault sources.

Table 1. List of active faults of the Taiwan SSC model.

Primary Fault Sources	
P1	Shanchiao Fault System
P2	ST-II Fault System
P3	Aoti Offshore Faults
P4	Northern Ilan Fault System
P5	S Fault
P6	Hengchun Fault System
P7	West Hengchun Offshore Structure
Subduction Zone Sources	
1	Ryukyu Subduction Zone Interface
2	Manila Subduction Zone Interface
Other fault Sources-Onshore	
1	Shuanglienpo Structure

2	Yangmei Structure
3	Hukou Fault
4	Fengshan River Strike-Slip Structure
5	Hsinchu Fault
6	Hsincheng Fault
7	Hsinchu Frontal Structure
8	Touhuanping Structure
9	Miaoli Frontal Structure
10	Tunglo Structure
11	East Miaoli Structure
12	Shihtan Fault
13	Sanyi Fault
14	Tuntzuchia Fault
15	Changhua Fault
16	Chelungpu Fault
17	Tamaopu - Shuangtung Fault
18	Chiuchungkeng Fault
19	Meishan Fault
20	Chiayi Frontal Structure
21	Muchilia - Liuchia Fault
22	Chungchou Structure
23	Hsinhua Fault
24	Houchiali Fault
25	Chishan Fault
26	Hsiaokangshan Fault
27	Kaoping River Structure
28	Milun Fault
29	Longitudinal Valley Fault
30	Central Range Structure
31	Luyeh Fault
32	Taimali Coastline Structure
33	Southern Ilan Structure
34	Chushiang Structure
35	Gukeng Structure
36	Tainan Frontal Structure
37	Longchuan Structure
38	Youchang Structure
39	Fengshan Hills Frontal Structure
Other fault Sources-Onshore	
40	Binhai Fault
41	Additional Fault E
42	Additional Fault I
43	Ryukyu Strike Slip Fault
44	Okinawa Trough Fault
45	Taitung Canyon Fault
46	Hengchun Ridge Offshore Fault
47	North Luzon Strike Slip Fault
48	North Luzon Backthrust Fault
49	East Hengchun Offshore Fault
50	Manila Splay Fault

Mater Thesis, Department of Geomatic, National Cheng Kung University, Tainan, Taiwan.110pp. (in Chinese)

Cheng, C.-T. (2002). Uncertainty Analysis and Deaggregation fo Seismic Hazard in Taiwan. Ph.D Thesis, Institute of Geophysics, National Central University, Chung-Li, Taiwan, 227pp. (in Chinese).

Hu, J.-C., Liu, C.-C., Yang, T.-Y., Ching, K.-E., Cheng, C.-T. (2016). Observation of Fault Activity (III): Integrated Monitoring of Active Faults and Earthquake Probabilities Analysis (4/4) ° Project report of Central Geological Survery, 369pp. (in Chinese)

Lee, C. T. (1999). Neotectonics and active faults in Taiwan, Proceedings of the 1999 Workshop on Disaster Prevention/Management and Green Techonolgy, Foster City, California, 61-74.

Lin, C.-W., Lu, S.-T., Chen, W.-S., Chang, Y.-J. (2012) Active Fault Map of Taiwan and description. Special publication of the Central Geological Survey, 26, 30pp.(in Chinese)

Shyu J. Bruce H., Chuang, Y.-R., Tsui, S.-K. (2017) Constructing fault model and parameters for Taiwan. NCREE 2017 report, 33pp. (in Chinese)

Tsai, Y.-B., Wang, C.-Y., Lee, C.-T., Sheu, M.-S., Liu, C.-S. (1998). Active fault survey and Earthquake Resistance Assessment for Schools in Taiwan. K-12 Education Administration, Ministry of Education report,278pp. (in Chinese)

References

Chang-Lee, C. (2014) Behavior analysis of the LCNF-CHNF fault system using geodetic measurements °

Soil Gas Radon Monitoring in Different Faults and Tatum Volcanic Areas of Northern Taiwan

Vivek Walia¹, Arvind Kumar², Shih-Jung Lin³, Ching-Chou Fu⁴ and Kuo-Liang Wen⁵

Abstract

In the present study, soil gas radon data retrieved from established continuous monitoring stations in different faults zones have been correlated with the seismic activity in the region under defined criteria. The Nuclear Track technique using the SSNTDs has also been used at some chosen sites in the Shanchiao fault with regard to seismotectonic activity to examine the affectability of the sites. From these sites, a site planning to be chosen for future long duration continuous observance on the premise of its affectability towards the seismotectonic activity inside the region. Integrated radon monitoring in Tatum volcano group (TVG) stations using solid state nuclear track detectors (SSNTD's) to test and verify the hypothesis proposed in our earlier study has been generated.

Keywords: Fault, Volcano, Soil-Gas, SSNTDs, Northern Taiwan

Introduction

The island of Taiwan is the exceptionally dynamic seismic locales of the earth which can be credited to its structural setting. It's situated at a focussed boundary between the Eurasian Plate and the Philippine Sea Plate. Eurasian Plate is subducting under the Philippine Sea Plate within the Southern part whereas in the Northern area the Philippine Sea Plate surrounded by the Ryukyu Trench, is subducting to a lower place the Eurasian Plate. Back of the Ryukyu Trench, the widening Okinawa Trough has matured. In step with historical records, the foremost damaging earthquakes in the island resulted in chiefly by inland active faults. For instance, the 1999 Chi-Chi earthquake also known as the 921 earthquake occurred in central Taiwan was ascribed to the Chelungpu fault. After 1998, Central Geological Survey (CGS) of Taiwan printed and published active fault maps of Taiwan. In 2012, 33 active faults have been acclaimed. A detailed study of these active faults will provide information about the activity of these faults and give basis which may significantly help to reduce the damage can cause by some unavoidable large earthquakes.

In the northern part of Taiwan Island, a group of volcanoes is distributed. These volcanoes are known

as the Tatum volcano group (TVG). TVG on the northern tip of the island of Taiwan covers an area of approximately 300 km². It is only about 10 km north of the capital city of Taipei. A look at historical volcanic eruptions has suggested that volcanism has been extinct since the last major activity that occurred from 0.8 to 0.2 Ma BP (e.g., Tsao 1994). However, recent studies offer suggestions that the potential for volcanic activity exists in the area: extensive hydrothermal activity is discharging a large amount of heat (e.g., Chen 1970); there are strongly acidic hot springs (pH approximately 1 to 3) (e.g., Ohsawa et al. 2013); magmatic contributions are found in fumarolic gases (e.g., Lee et al. 2005; Ohba et al. 2010); relatively young ejecta can be observed (< 20 ka, Chen and Lin 2002; 6 ka, Belousov et al. 2010), and the presence of clustered seismicity and shallow pressure sources suggest fluid flows (Lin et al. 2005; Konstantinou et al. 2007; Murase et al. 2013). Recent seismic (Lin et al. 2005; Konstantinou et al. 2007) and geochemical data (Ohba et al. 2010) infer that a magma chamber may exist under northern Taiwan.

The variations of soil gas radon concentration has been recognised as a useful tool for geodynamical monitoring in active fault zones (Walia et al. 2013) for surveillance in volcanic areas (Monnin and Seidel 1997; Segovia et al. 2003) and for tracing neotectonic

¹ Research Fellow, National Center for Research on Earthquake Engineering, walia@ncree.narl.org.tw

² Associate Researcher, National Center for Research on Earthquake Engineering, kumar@ncree.narl.org.tw

³ Assistant Researcher, National Center for Research on Earthquake Engineering, sjlin@ncree.narl.org.tw

⁴ Postdoctoral Fellow, Institute of Earth Sciences, Academia Sinica, ccfu@earth.sinica.edu.tw

⁵ Professor, National Center for Research on Earthquake Engineering, wenkl@ncree.narl.org.tw

faults (Burton et al. 2004). Presently, we are carrying temporal geochemical variations of soil-gas composition at established geochemical observatories (Fig. 1) along different faults in Hsinchu (HC) (i.e. along Hsincheng fault), Tainan (HH) (along Hsinhua Fault) and Ilan (at Jaosi (JS)) areas of Taiwan using active detectors and to find the correlation of enhanced concentrations of radon with the seismic activity in the region from data generated during the observation period and test the efficiency of the proposed tectonic setting based model (see previous reports). Also, the seismic sensitivity of sites selected from soil gas geochemical surveys in and around the Shanchiao fault (Fig. 1) has been examined by integrated radon monitoring using solid state nuclear track detectors (SSNTDs). In addition to that integrated radon monitoring using SSNTDs in Tatun Volcanic Areas (Fig. 1) of northern Taiwan has been carried out for volcanic and seismic study.

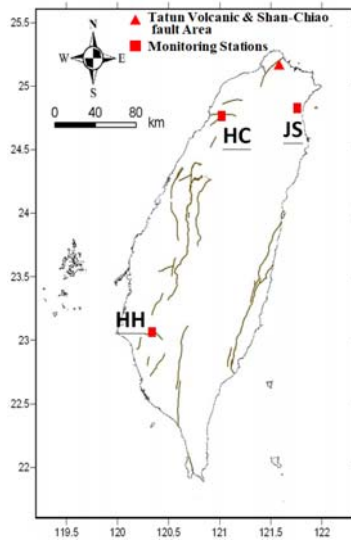


Fig. 1: Location of radon monitoring stations along different faults & Tatun Volcanic areas of northern Taiwan

Methodology

To carry out the continues monitoring, investigation at the established monitoring stations, soil-gases compositions variations were measured regularly using RTM2100 (SARAD) for radon and thoron measurement following the procedure as described in Walia et al, 2009b. Seismic parameters (viz. Earthquake parameters, the intensity at a monitoring station, etc.) and meteorological parameter data were obtained from Central Weather Bureau of Taiwan (www.cwb.gov.tw).

The Nuclear Track technique using the SSNTDs has been used at some chosen sites in the Shanchiao fault and Tatun volcanic areas on the premise of its sensitivity towards the tectonic activity inside the region. In this passive technique, LR-115 alpha detector films have been used. Before using these films in the field, the laboratory experiments have

been carried out in different modes of exposures of LR-115 for the calibration study (Kumar et al. 2013). LR-115 alpha detector films were placed in the augur hole of about 50 cm depths to study the variations in the radon concentrations using radon-thoron discriminator. Radon-thoron discriminator of 25 cm long, has up and down position to place the film detectors. It is based on the large ratio of their half-lives and consequent difference in their diffusion lengths. It can be computed that a length of about 25 cm of an air column is adequate to eliminate thoron almost completely while radon is not much affected. So the film detectors placed at up position records the tracks due to radon alone whereas, the film detectors placed at down position records tracks due to radon and thoron both. The discriminator has been kept in the augur hole of 50 cm depth for a time period of two weeks to one month. After removing the film detectors from the augur hole, it has been etched in 2.5 N NaOH solutions at a stable temperature of 60° C for 90 minutes using the etching machine. Semiautomatic methodology (Arias et al. 2005) has been used for counting the tracks formed in the film detectors. The computed tracks per cm² in the films were converted to kBq/m³ using the calibration factor calculated within the earlier study (Kumar et al. 2013a).

Results and Discussions

Data have been retrieved from established continuous monitoring stations and have been correlated with seismic activity in the region under defined criteria (Fig. 2,3 &4). During observation period (Jan. to Dec. 2017) 20 earthquakes with $M \geq 5$ were recorded from which only 7 qualified under defined criteria (presented by a star in fig. 5). Five earthquakes have shown precursory signals (presented by a green star in fig. 5) and two have not shown precursory signals (presented by a red star in fig. 5), due to many possible reasons (e.g. No data due to instrument problem or due to Typhoon /heavy rain etc.).

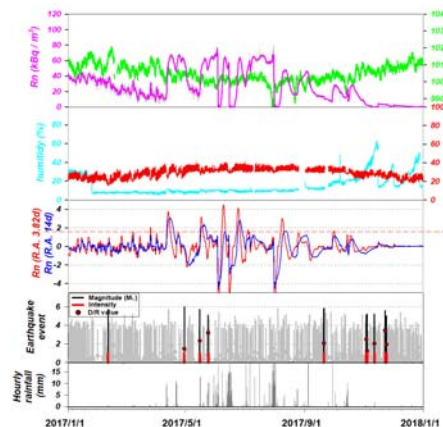


Fig. 2: Observed continuous soil gas radon monitoring data of HH station along with other parameters.

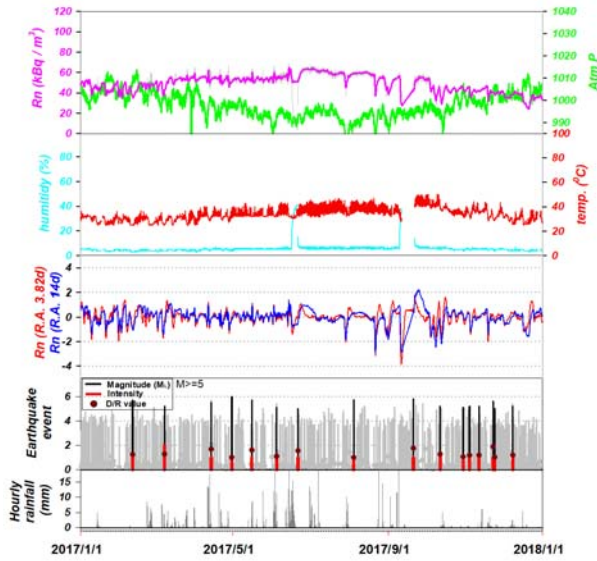


Fig. 3: Observed continuous soil gas radon monitoring data of HC station along with other parameters.

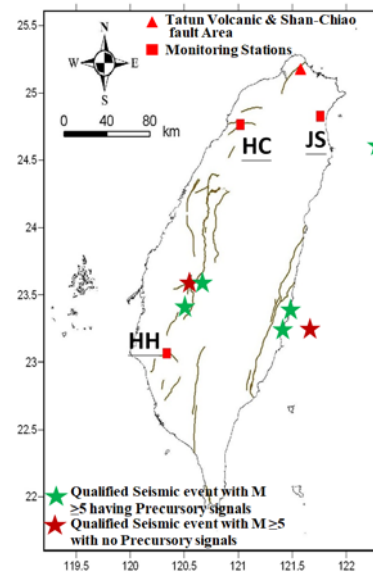


Fig. 5: Correlations of retrieved data from established continuous monitoring stations with seismic activity in region under defined criteria

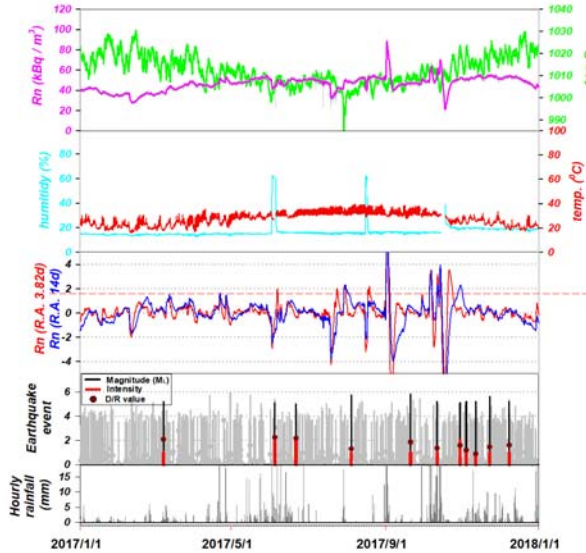


Fig. 4: Observed continuous soil gas radon monitoring data of JS station along with other parameters.

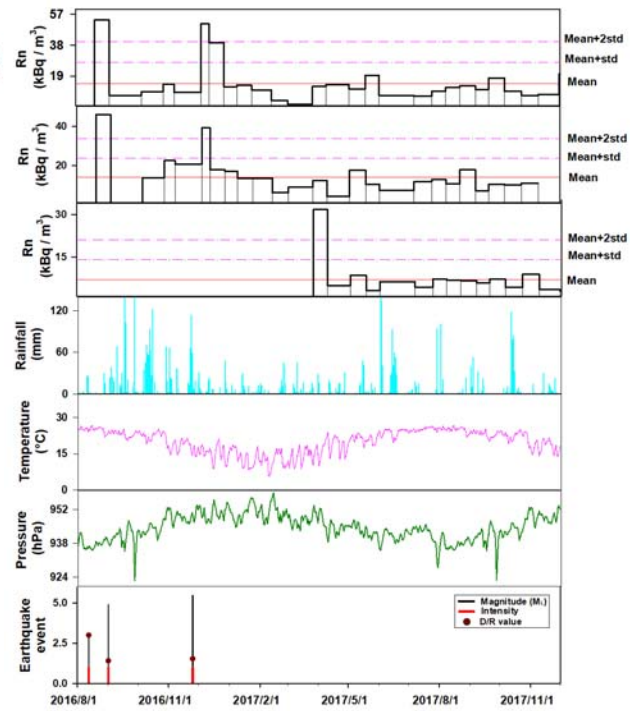


Fig. 6: Plots of observed integrated soil gas radon data using SSNTDs along with other parameters at SF-2, SF-3 and SF-4 sites in tectonically active zones of Shanchiao fault.

Figure 6 shows the observed radon data along with temperature, pressure, rainfall and seismic events recorded by central weather bureau at SF-2, SF-3 and SF-4 sites (selected from soil gas surveys results) in tectonically active zones of Shanchiao fault. Site SF-1 was not suitable for radon monitoring as at the site SF-1 water level was high and we were unable to put our films in the hole. From these three sites, a site will be chosen for future long-term continuous monitoring on the premise of its sensitivity towards the tectonic activity inside the region, which will be helpful for earthquake prediction study will be helpful for earthquake prediction study in Taiwan.

We are in the process to build a continuous radon monitoring station in tectonically active zones of Shanchiao fault. Figure 7 shows the observed radon data along with temperature, pressure, rainfall and seismic events recorded by central weather bureau at Gungtzeping (GTP), Hsiaoyoukeng (SYK), Dayoukeng (DYK) and Bayen (BY). The radon average value recorded for this time period at SYK and DYK are 12.4 kBq/m³ and 28.4 kBq/m³

respectively whereas radon average value recorded for this time period at BY and GTP are 21.2 kBq/m³ and 8.2 kBq/m³ respectively. This year only one earthquake of magnitude 4.0 which satisfy our criteria occurred on 2017/06/11. In our earlier study, it was concluded that our monitoring stations in TVG area are sensitive to the events within distance of 60 km (Kumar et al., 2013). Continues radon monitoring in these stations are needed to test and verify this hypothesis in future.

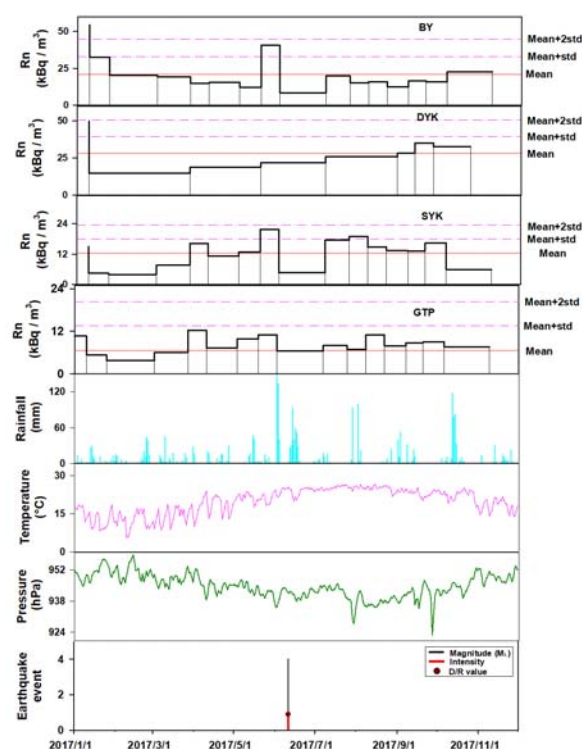


Fig. 7 : Plots of recorded integrated soil gas radon using SSNTDs along with other parameters at GTP, SYK, DYK and BY.

References

- Belousov, A. M., C.-H. Chen., G.F. Zellmer, 2010: Deposits, character and timing of recent eruptions and gravitational collapses in Tatun Volcanic Group, Northern Taiwan: Hazard-related issues. *J Volcanol Geotherm Res.*, **191**, 205–221.
- Burton M., M. Neri, and D. Condorelli, 2004: High spatial resolution radon measurements reveal hidden active faults on Mt. Etna. *Geophys. Res. Lett.*, **3**, L07618.
- Chen C.-H., 1970: Geology and geothermal power potential of the Tatun volcanic region. *Geothermics*, **2**, 1134–1143.
- Chen, C.-H., S.-B. Lin, 2002: Eruptions younger than 20 ka of the Tatun Volcano Group as viewed from the sediments of the Sungshan Formation in Taipei Basin. *West Pac Earth Sci.*, **2**, 191–204.
- Konstantinou, K. I., C. H. Lin, and W. T. Liang, 2007: Seismicity characteristics of a potentially active Quaternary volcano: The Tatun Volcano Group, northern Taiwan. *J. Volcanol. Geotherm. Res.*, **160**, 300–318.
- Kumar, A., V. Walia., T.F. Yang., C.H. Hsien., S.J. Lin., K.P. Eappen., B.R. Arora, 2013: Radon-thoron monitoring in Tatun volcanic areas of northern Taiwan using LR-115 alpha track detector technique: Pre Calibration and Installation. *Acta Geophysica.*, **61** (4), 958–976.
- Lee, H.-F., T.F. Yang., T.-F. Lan., S.-R. Song., S. Tsao, 2005: Fumarolic gas composition of the Tatun Volcano Group, northern Taiwan. *Terr Atmos Ocean Sci.*, **16**, 843–864.
- Monnin, M.M. and J. Seidel, 1997: Radon and Volcanic Surveillance, in Radon Measurements by Etched Track Detectors. Application in Radiation Protection, Earth Science and the Environment, edited by Durrani, S.A. and R. Ilic (World Scientific, Singapore), 301–318.
- Murase, M, C.-H. Lin., F. Kimata., H. Mori., A. Suzuki, 2013: Estimated pressure source and vertical deformation in Tatun volcano group, Taiwan, detected by precise leveling during 2006–2013. In: Abstracts of IAVCEI 2013 scientific assembly, Kagoshima prefectural citizens exchange center & Kagoshima citizens social support plaza, Kagoshima.
- Ohba, T., T. Sawa., N. Taira., T.F. Yang., H.-F. Lee., T.-F. Lan., M. Ohwada., N. Morikawa., K. Kazahaya, 2010: Magmatic fluids of Tatun volcanic group, Taiwan. *Appl Geochem.*, **25**, 513–523.
- Ohsawa, S., H.-F. Lee., B. Liang., S. Komori., C.-H. Chen., T. Kagiya., 2013: Geochemical characteristics and origins of acid hot spring waters in Tatun Volcanic Group, Taiwan. *J Hot Spring Sci.*, **62**, 282–293. (in Japanese with English abstract) (in Japanese with English abstract)
- Segovia N., M.A. Armienta., C. Valdes., M. Mena., J.L. Seidel., M. Monnin., P. Pena., M.B.E. Lopez, and A.V. Reyes, 2003: Volcanic monitoring for radon and chemical species in the soil and in spring water samples. *Rad. Meas.*, **36**, 379–383.
- Tsao, S., 1994: K-Ar age determination of volcanic rocks from the Tatun Volcano Group. *Bull Central Geological Surv.*, **9**, 137–154. (in Chinese).
- Walia, V., T.F. Yang., S.J. Lin., A. Kumar., C. Fu., J.M. Chiu., H.H. Chang., K.L. Wen., C.H. Cheng, 2013: Temporal variation of soil gas compositions for earthquake surveillance in Taiwan. *Radiat Meas* **50**, 154–159

Development of Vertical-to-Horizontal Response Spectrum Ratio Model for Taiwan

Shu-Hsien Chao¹ Po-Shen Lin² Che-Min Lin¹
Ching-Hsiao Kuo³ Jyun-Yan Huang⁴ Chiao-Chu Hsu⁵

趙書賢¹ 林柏伸² 林哲民¹ 郭俊翔³ 黃雋彥⁴ 許喬筑⁵

Abstract

According to the current building seismic design code, the design vertical ground motion response spectrum can be derived by multiplying the horizontal ground motion response spectrum with the design vertical-to-horizontal response spectrum ratio (V/H ratio). The design V/H ratio is a period-independent constant of 2/3 for target sites nearby the active fault and 1/2 for other target sites. However, recent studies have shown that the V/H ratio strongly depends on the earthquake magnitude, distance and site condition of the ground motion, and structural period. They also found that the V/H ratio of some periods may be larger than 1 for the near-fault soil site struck by an earthquake of large magnitude. In this study, the horizontal and vertical ground motion characteristics were investigated simultaneously, and a V/H ratio model applicable for Taiwan was developed. The results of this study can provide valuable information for the revision of the design V/H ratio in the current seismic design code.

Keywords: ground motion model, V/H ratio, site effect

Introduction

The horizontal ground motion characteristics have been investigated comprehensively and many horizontal ground motion models have been proposed by different researchers. However, only a few have studied the vertical ground motion characteristics as well as the vertical ground motion model. Recently, some studies have shown that the vertical ground motion may induce additional seismic demand for some specific structures, such as base-isolated structures. Some studies have also shown that the vertical ground motion characteristics are significantly different to the horizontal ground motion characteristics. Therefore, in recent years, researchers have focused on the vertical ground motion characteristics and vertical ground motion models, and vertical-to-horizontal response spectrum (V/H) ratio models have been developed (Pacific Earthquake Engineering Research Center (PEER), 2013). In this study, based on the experience of developing a horizontal ground motion model for Taiwan (Chao et.

al., 2017), the differences between horizontal and vertical ground motion characteristics are investigated by analyzing the horizontal and vertical ground motion records simultaneously, and a V/H ratio model that is applicable for Taiwan is proposed. The results of this study can provide valuable information for the revision of the design V/H ratio in the current seismic design code.

Selected Ground Motion Records

This study used the ground motion database involving horizontal and vertical ground motion components compiled by the Taiwan SSHAC Level 3 Project (National Center for Research on Earthquake Engineering (2018), 2018). A part of ground motion records in the ground motion database was selected and used in this study. The selection criteria for developing the horizontal ground motion model for Taiwan (Chao et. al., 2017) was used, with the exception that only the ground motion records within

¹ Associate Researcher, National Center for Research on Earthquake Engineering

² Research Fellow, Sinotech Engineering Consultants, INC.

³ Research Fellow, National Center for Research on Earthquake Engineering

⁴ Assistant Researcher, National Center for Research on Earthquake Engineering

⁵ Research Assistant, National Center for Research on Earthquake Engineering

the Rmax range were selected to simplify the regression analysis procedure.

V/H Ratio Model and Coefficients

In this study, the horizontal and vertical ground motion records were assumed to have the same event term and similar path term. The horizontal and vertical ground motion records were analyzed simultaneously to derive the same event term and path term for both. Consequently, the function form for the horizontal and vertical ground motion models proposed in this study is expressed as follows:

$$\begin{aligned} \begin{bmatrix} \ln S_{a,H} \\ \ln S_{a,V} \end{bmatrix} &= \begin{bmatrix} \ln S_{a,H}^{ref} \\ \ln S_{a,V}^{ref} \end{bmatrix} + S_{source} + S_{path} + \begin{bmatrix} S_{site,lin,H} \\ S_{site,lin,V} \end{bmatrix} \\ &+ \begin{bmatrix} S_{site,non,H} \\ S_{site,non,V} \end{bmatrix} + c_v R_{rup} F_V + \delta_e + \begin{bmatrix} \delta_{s,H} \\ \delta_{s,V} \end{bmatrix} + \begin{bmatrix} \delta_{r,H} \\ \delta_{r,V} \end{bmatrix} \end{aligned}$$

The function form of each scaling and residual term is identical to the horizontal ground motion model (Chao et. al., 2017). The reference spectrum, site scaling, and residual are separated into horizontal and vertical parts. The model coefficients of the horizontal and vertical components are derived simultaneously through the regression analysis. An additional term $c_v R_{rup} F_V$ is used to address the possible difference between the attenuation rates of horizontal and vertical components and F_V is a flag for the vertical component. By using this equation, the function form of the proposed V/H model can be expressed as follows:

$$\begin{aligned} S_{site,non,V} &= c_{4,V} u(V_{s30}^{ref} - V_{s30}) \left\{ -1.5 \ln \left(\frac{V_{s30}}{V_{s30}^{ref}} \right) \right. \\ &\quad \left. - \ln(\hat{S}_{a1100,V} + 2.4) \right. \\ &\quad \left. + \ln \left(\hat{S}_{a1100,V} + 2.4 \left(\frac{V_{s30}}{V_{s30}^{ref}} \right)^{1.5} \right) \right\} \\ S_{site,non,H} &= c_{4,H} u(V_{s30}^{ref} - V_{s30}) \left\{ -1.5 \ln \left(\frac{V_{s30}}{V_{s30}^{ref}} \right) \right. \\ &\quad \left. - \ln(\hat{S}_{a1100,H} + 2.4) \right. \\ &\quad \left. + \ln \left(\hat{S}_{a1100,H} + 2.4 \left(\frac{V_{s30}}{V_{s30}^{ref}} \right)^{1.5} \right) \right\} \end{aligned}$$

Here $\hat{S}_{a1100,H}$ and $\hat{S}_{a1100,V}$ are the horizontal and vertical spectral acceleration for site condition Vs30 1100 m/s. The V/H ratio majorly represents the differences between horizontal and vertical reference spectra and site scaling because the same event term and similar path term are used for both components. Model coefficient c_1 represents the V/H ratio for the reference site condition Vs30 760 m/s. Model coefficients c_2 and c_3 represent the differences in horizontal and vertical Vs30 scaling and Z1.0 scaling, respectively. Model coefficients control the degree of the nonlinear site effect for horizontal and vertical

ground motions. Model coefficient c_v represents the difference of the attenuation rate for the horizontal and vertical components.

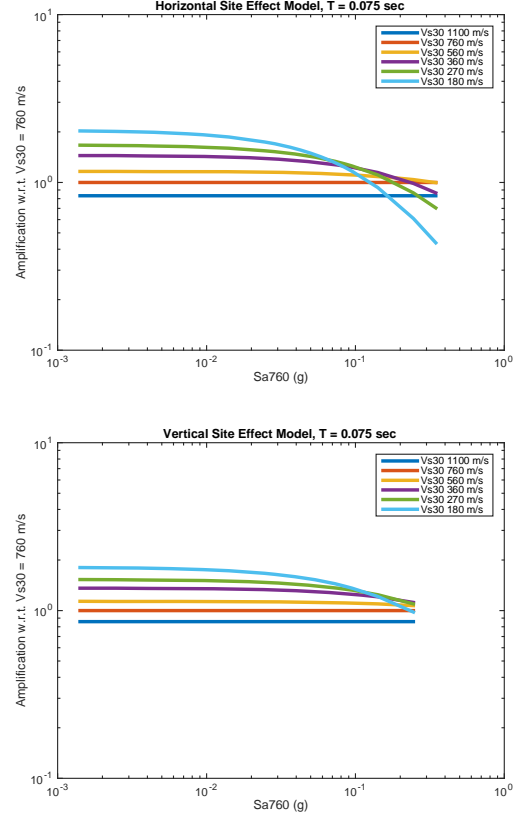


Fig. 1. Site amplification of the proposed model in this study for period 0.075 s.

The model coefficients derived through regression analysis are shown in Table 1. The c_1 range from -0.8 to -0.4 ; the corresponding V/H ratio for the reference site condition Vs30 760 m/s ranges from 0.45 to 0.6 . The range of c_2 is always positive from 0.1 to 0.5 , indicating that the Vs30 scaling of horizontal ground motion is stronger than that of vertical ground motion. The range of c_3 is from -0.07 to 0.03 , whose absolute value is smaller than c_2 , indicating that the Z1.0 scaling of V/H is not significant compared to the Vs30 scaling. The absolute value range is from $1E-4$ to $1E-3$, indicating that the attenuation rate difference between horizontal and vertical components is not significant.

Although the site effect of horizontal ground motion has been widely discussed, the site effect of vertical ground motion has not been discussed comprehensively in the past. Figure 1 shows the horizontal and vertical site amplifications for period 0.075 s predicted by the proposed model, and Figure 2 shows the comparison between the predicted site amplification and measurements from ground motion record for the horizontal and vertical components. The results indicate that the nonlinear site effect can also be found in the vertical ground motion components.

The horizontal nonlinear site de-amplification will always be stronger than the vertical one because the value of $\hat{S}_{a1100,H}$ will always be larger than $\hat{S}_{a1100,V}$. This is a main reason for why the V/H ratio increases when the soil site is struck by a near fault large-magnitude earthquake.

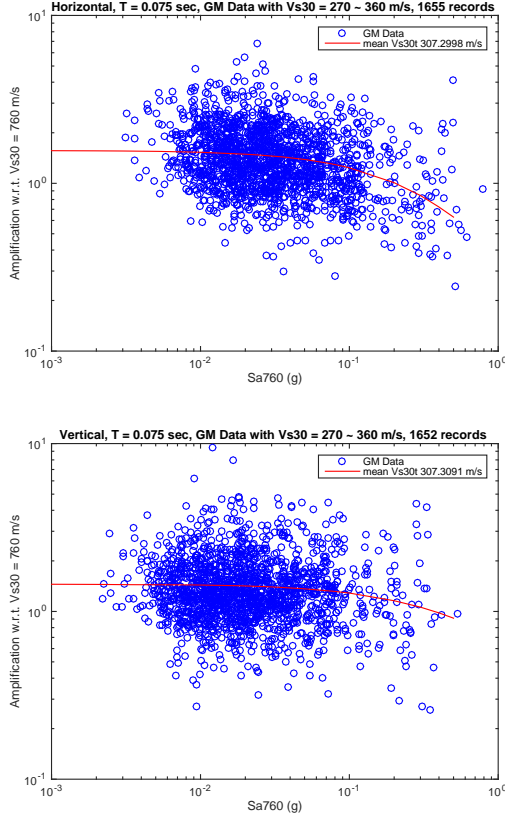


Fig. 2. Comparison between the predicted site amplification and measurements from ground motion records for horizontal and vertical components of period 0.075 s.

Prediction of Proposed V/H Model

The predicted V/H ratios for a crustal earthquake with a rupture plane up to the ground surface are presented. Figure 3 shows V/H spectrum ratios of distance 10 km and site condition Vs30 255 m/s for different earthquake magnitudes. The short-period V/H ratios increase as the earthquake magnitude increases. Figure 4 shows the V/H spectrum ratios of earthquake magnitude Mw 7.5 and site condition Vs30 255 m/s for different distances. The short-period V/H ratios increase as the distance decreases. Figure 5 shows V/H spectrum ratios of earthquake magnitude Mw 7.5 and distance 10 km for different site conditions. The V/H spectrum ratios for the soil site strongly depend on the structural period, but not for the rock site. The V/H spectrum ratios for the soil site for $T < 0.2$ s are lower than those for the rock site, but for $T > 0.2$ s, the V/H spectrum ratios for the soil site are higher than those for the rock site. The

dependences of the soil site V/H spectrum ratio on magnitude, distance, and structural period are all related to the difference of the nonlinear site effect for the horizontal and vertical components of the ground motion.

Figure 6 shows the spectral correlation coefficients between the horizontal component, vertical component, V/H ratio, and H/V ratio of the ground motion intensity. While the horizontal component of the ground motion intensity is higher than the median prediction, the vertical component of the ground motion intensity will also be potentially higher than the median prediction with about 0.75 correlation coefficient. The H/V ratio of the ground motion will also be potentially higher than the median prediction with about 0.4 correlation coefficient and the V/H ratio of the ground motion will be potentially lower than the median prediction with about -0.4 correlation coefficient. The proposed spectral correlation coefficients can be used to derive the conditional vertical component, V/H ratio, or H/V ratio of the ground motion intensity when the horizontal ground motion intensity is known.

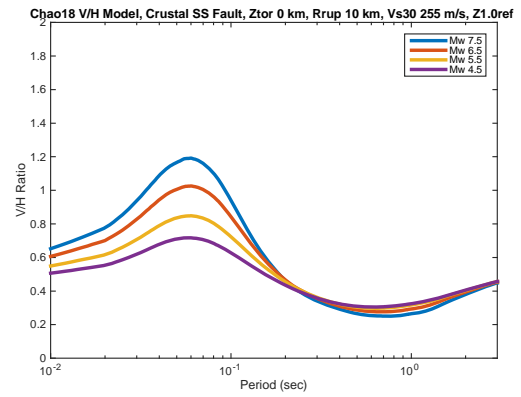


Fig. 3. V/H spectrum ratios of distance 10 km and site condition Vs30 255 m/s for different earthquake magnitudes.

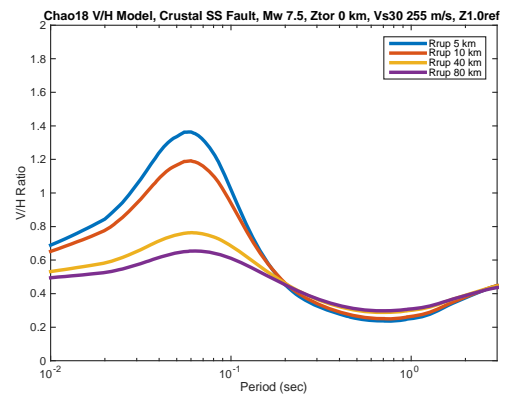


Fig. 4. V/H spectrum ratios of earthquake magnitude Mw 7.5 and site condition Vs30 255 m/s for different distances.

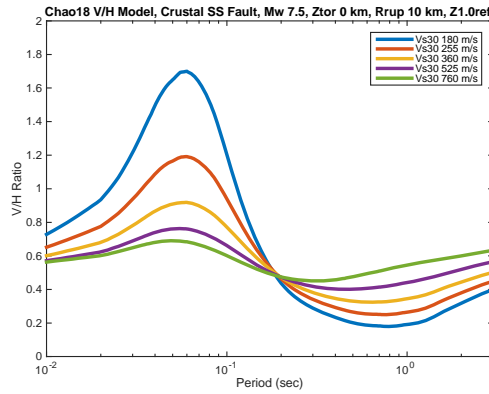


Fig. 5. V/H spectrum ratios of earthquake magnitude Mw 7.5 and distance 10 km for different site conditions.

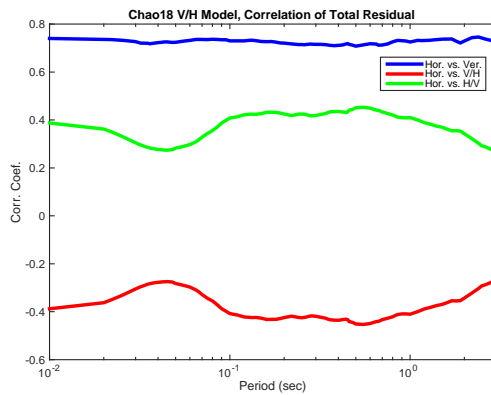


Fig. 6. Spectrum of correlation coefficient between the horizontal component, vertical component, V/H ratio, and H/V ratio of the ground motion intensity.

Conclusions

In this study, the differences between the ground motion characteristics of horizontal and vertical components were discussed, and a V/H ratio model which is applicable for Taiwan was developed. The proposed V/H spectrum ratio model is majorly influenced by the site condition and input rock motion. Soil site V/H spectrum ratio strongly depends on magnitude, distance, and structural period because of the difference in the nonlinear site effects for the horizontal and vertical components of the ground motion. In summary, the design constant V/H ratio in the current building seismic design code is applicable for the rock site. For the soil site, the applicability of the design constant V/H ratio should be further discussed, especially for the large-magnitude and short-distance ground motion scenarios.

References

Bommer, J. J., Akkar, S., and Kale, O., (2011). A model for vertical-to-horizontal response spectral

ratios for Europe and the Middle East, *Bulletin of the Seismological Society of America* 101, 1783–1806.

Chao, S.H., Y.H. Chen, C.C. Hsu, P.S. Lin (2017). Development of Horizontal Taiwan Ground Motion Model for Crustal Earthquake and Subduction Earthquake, Report No. NCREE-17-009, National Center for Research on Earthquake Engineering, Taipei, Taiwan.

National Center for Research on Earthquake Engineering (NCREE) (2018). GMC Technical Report of Taiwan SSHAC Level 3 Project, June 2018. (in preparation)

Pacific Earthquake Engineering Research Center (PEER) (2013). NGA-West2 Ground Motion Prediction Equations for Vertical Ground Motions. Report PEER 2013/03, University of California, Berkeley, CA.

Yousef Bozorgnia and Kenneth W. Campbell (2016) Ground Motion Model for the Vertical-to-Horizontal (V/H) Ratios of PGA, PGV, and Response Spectra. *Earthquake Spectra*: May 2016, Vol. 32, No. 2, pp. 951-978.

Zeynep Gülerce, Norman A. Abrahamson, (2011) Site-Specific Design Spectra for Vertical Ground Motion. *Earthquake Spectra*: November 2011, Vol. 27, No. 4, pp. 1023-1047.

A Simplified Procedure to Simulate the Interaction between a Low-rise Building and Liquefiable Soil

Chih-Chieh Lu¹, Yu-Wei Hwang², and Jin-Hung Hwang³

盧志杰¹、黃郁惟²、黃俊鴻³

Abstract

The purpose of this project was to establish a simplified procedure for a finite difference method (FDM) in order to model the interaction between liquefiable soil and a structure, as well as to propose a parameter reduction factor for FDM. The first working item is to collect the databases for liquefaction case histories for the 1999 Chi-Chi earthquake and the 2016 Meinong earthquake. Then, the standardized soil profiles for each studied area were built. The critical liquefiable layers of the standardized soil profiles were identified by the evaluation of simplified procedures, and the settlement of the structure due to the liquefaction of soil was then analyzed by FDM using the parameter reduction approach. The parameters of critical liquefiable soil were reduced until the calculation results were comparable to the observed settlement of the buildings. The results of all analyzed cases were integrated to summarize an approach for the setting of parameter reduction for liquefiable soil under different liquefaction conditions.

Keywords: low-rise building, liquefaction, simplified, parameter reduction, FDM

Introduction

Soil liquefaction is an earthquake-induced natural phenomenon and is one of the major causes of damage to buildings, lifeline systems, and harbor facilities. This is due to the liquefaction-induced weakening of the bearing capacity of the soil and ground deformation. It is a topic of high concern to the public because of the recent serious damage to surface buildings caused by soil liquefaction during the 2016 Meinong earthquake (Hwang et al., 2016). According to field investigations conducted by a survey team from the National Center for Earthquake Engineering (NCREE), serious soil liquefaction occurred on both Huian St. and Sanmin St. In addition to the recent Meinong earthquake, there have been many catastrophic earthquakes throughout history that have caused soil liquefaction, resulting in serious loss of life and property, such as the 1964 Niigata and the 1995 Kobe earthquakes in Japan, and the 1999 Chi-Chi earthquake in central Taiwan (Hwang et al., 2003). Soil liquefaction degrades the strength of the soil; hence, the structure situated above the liquefied soil tilts and settles because of the insufficient bearing capacity of the liquefied foundation soil. As the

demolition and reconstruction of existing old buildings in urban areas is difficult, the reinforcement and assessment of existing buildings in areas of potential soil liquefaction is an important issue in the field of engineering. The Ministry of the Interior of Taiwan has also been actively promoting various projects that serve to enhance the safety performance of old buildings located in potential soil liquefaction areas.

The interaction between liquefiable soil and a low-rise building is an important concern in seismic areas. However, simulation of the highly nonlinear interaction between the liquefied soil and the surface structure is difficult because the mechanical behavior of the liquefiable soil dramatically changes when excess pore water pressure is generated during seismic shaking. Early estimations for earthquake loss mainly emphasized the effect caused by the shaking of the ground alone (FEMA, 1994; Ye, 2002). As the techniques of computer and statistical analysis have been improved, the estimation of the soil-liquefaction-induced loss has been recently included (FEMA, 2003; Bird et al., 2006; Bird and Bommer, 2004). To closely simulate the dynamic interaction between liquefiable

¹ Associate Researcher, National Center for Research on Earthquake Engineering

² Assistant Researcher, National Center for Research on Earthquake Engineering

³ Division Director, National Center for Research on Earthquake Engineering

soil and surface structures with shallow foundations, Lu et al. (2011) even used a finite difference method (FDM)-based program to establish a dynamic analysis model. When the liquefiable soil liquefied and broke the equilibrium conditions of the system, however, the maximum unbalanced force of the numerical system became so large that it was difficult to reduce, and a satisfying steady-state solution could therefore never be achieved. Calculation by the numerical program was usually stopped because of the overly large deformation of the numerical mesh, and the dynamic time history analysis could never be completed.

In practice, the parameter reduction approach is preferred. By reducing the soil parameters to a certain level, the mechanical behavior of the liquefiable soil can be approximated. Hence, through this method, the modeling of the interaction between the liquefiable soil and the structure becomes easier and produces rational results. The key issue of this approach is choosing a suitable parameter of reduction for the liquefiable soil under different liquefaction conditions for the corresponding modeling tools, such as the spring model or the finite element method (FEM)/FDM. Some Japanese codes have provided recommendations for designers using the spring model to follow. For surface building with shallow foundations located on a liquefiable deposit, however, this study focused on FEM/FDM; this approach has a more powerful soil structure interaction (SSI) simulation ability, because defining a single spring that may reflect the behavior of the layered formations, especially when parts of them may liquefy, is difficult. The purpose of this project was to establish a practical procedure through which the FDM can model the interaction between the liquefiable soil and structure. The suggestion of the parameter reduction factor for the liquefied soil in the FDM was then calibrated by using the documented case histories from the 1999 Chi-Chi and the 2016 Meinong earthquakes.

Framework of this study

The framework of this study is shown in Figure 1. The aim of this study was to establish a practical procedure by considering the local characteristics of the earthquakes and geology of Taiwan. This was done to evaluate the performance of a low-rise building on a liquefiable deposit. The first working item was to collect the documented liquefaction case histories from databases of the 1999 Chi-Chi earthquake and the 2016 Meinong earthquake. Then the information concerning the liquefiable deposits and stories of low-rise buildings on corresponding settlements was summarized. The analyzed sites, Yuanlin, Wufeng, Nantou, Annan, and Sinshih, were located in central and southern Taiwan. Using the database, standardized soil profiles for each studied area were built according to boreholes near the locations of the settled buildings that expressed evidence of liquefaction. The critical

liquefiable layers of the standardized soil profiles were then identified by the simplified procedures, HBF (NCREE, 2017), Seed (Seed et al., 1985), NCEER (Youd and Idriss, 1997), AIJ (AIJ, 2001), and JRA (JRA, 1996), in order to identify the depths and thicknesses of the critical liquefied layers. The FDM numerical models of the corresponding standardized soil profiles for each site with low-rise structures of differing numbers of stories were then separately developed. During analyses of the FDM numerical models for each site, the settlement of the structure due to soil liquefaction was monitored, and the performance of the identified critical liquefiable soils was simulated by using the parameter reduction approach. The stiffness and strength of the critical liquefiable soils were then reduced until the calculation results were comparable to those for the observed building settlement. Figure 2 shows the settlement of a three-story building due to the liquefaction of the foundation soil. The results of all analyzed cases were then integrated to provide a suggestion for setting the parameter of reduction for liquefied soil, as shown in Figure 3.



Fig. 1. The locations of the analyzed sites.

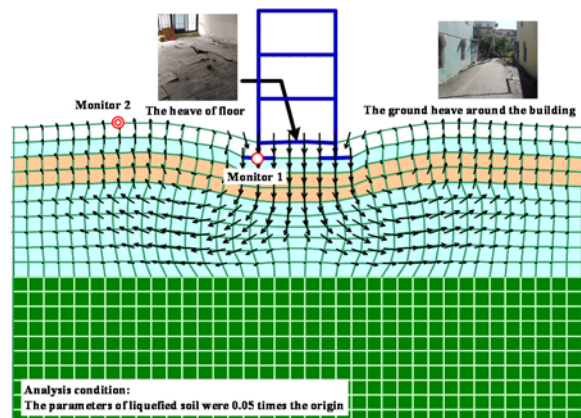


Fig. 2. The analyzed settlement due to the softening of the liquefied layer (Lu et al., 2016).

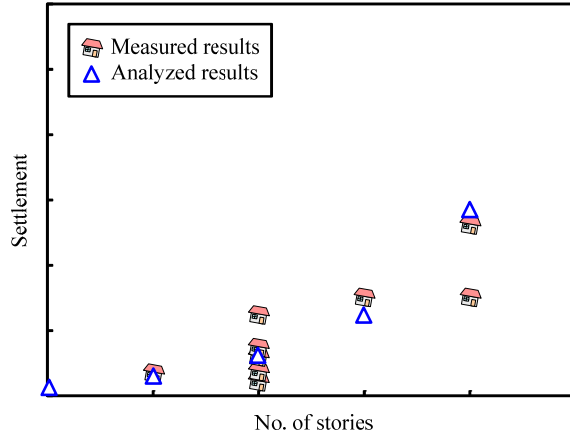


Fig. 3. An example of the comparison between the analyzed and measured settlements.

Analysis results

With the three-story building's shallow foundation as an example, the displacement of the liquefied sandy soil layer was not obvious until the liquefied sandy soil layer weakened to 0.3 times the original strength. However, the overall strength of the foundation soil was too small to support the weight of the upper structure and became unstable after the strength of the liquefied soil became less than 0.3 times its original value. As the surface structure began to sink, the foundation soil, squeezed by the settling building, was pushed out on both sides, resulting in further soil uplift around the building. During the subsidence of the structure, the soil underneath the first floor of the building provided a reaction force on the foundation slab, and the distribution of the load exerted on the slab by the first floor might have resulted in bending-moment damage of the slab. **Figure 4** shows the enlarged deformed mesh when the liquefied sand layer weakened to 0.15 times the original strength. In addition, the plastic zone and the shear strain distribution (**Figures 5 and 6**, respectively) of the formation show that the entirety of the soil exhibited total shear failure and that the lower boundary of the damaged area was located on the boundary of the liquefied and non-liquefied layers.

Figure 7 shows the relationship between the subsidence of the buildings with differing numbers of stories and their parameter reduction ratios. We can see that the amount of subsidence increased as the parameter reduction ratio of the liquefied soil decreased. As shown in the figure, the amount of building settlement was not obvious while the parameter reduction ratio of the liquefied soil was higher than a certain level, resulting in subsidence of the building mainly due to the reduction of the soil stiffness. However, when the parameter reduction ratio of the liquefied soil was below a certain level, the total settlement of the buildings began to increase substantially because of the total shear failure caused

by the inability of the foundation soil to bear the weight of the surface structure. The relationship between the building subsidence and the parameter reduction is related to the number of building floors (i.e., the building weight). As shown by the subsidence trend of the five-story building in **Figure 7**, there was an obvious turning point when the parameter reduction ratio reached to 0.3. The amount of settlement of the three-story building was smaller than that of the five-story building because of the lighter weight of three-story building. The turning point of the settlement trend for the three-story building model was also smaller. As shown in the figure, the settlement of the three-story building began to increase at a greater rate when the parameter reduction ratio was smaller than 0.15.

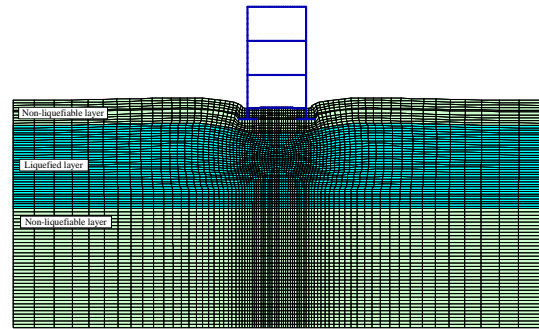


Fig. 4. The enlarged deformed mesh when the parameter reduction ratio was 0.15 (Yuanlin site).

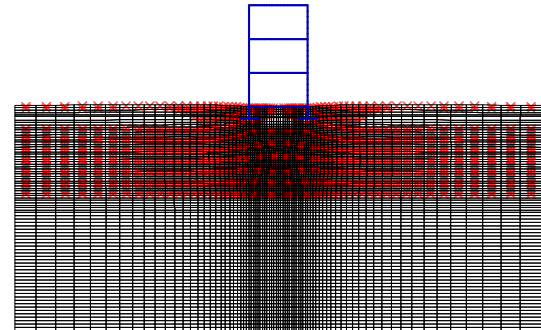


Fig. 5. The distribution of the plastic zones when the parameter reduction ratio was 0.15 (Yuanlin site).

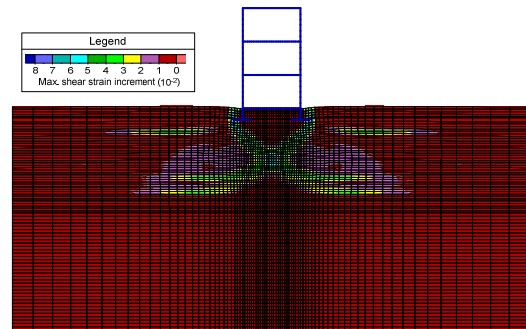


Fig. 6. Distribution of the maximum shear strain when the parameter reduction ratio was 0.15 (Yuanlin site).

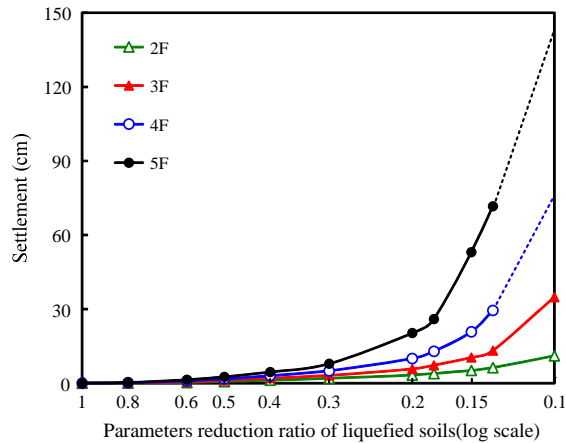


Fig. 7. Relationship between the settlement of the buildings and the parameter reduction ratio (Yuanlin site).

Conclusions

1. This study proposed a practical procedure for evaluating the potential settlements of low-rise buildings on a liquefiable deposit using an FDM program. In order to consider the local characteristics of earthquakes and the geology of Taiwan, we summarized documented liquefaction and geological investigation data, and the damage conditions of low-rise buildings, among others, from the 1999 Chi-Chi and the 2016 Meinong earthquakes.

2. The analysis results show that when the parameter reduction ratio of liquefied soil was higher than a certain value, the settlement of the building was not obvious, mainly because of the softening of the soil. When the parameter reduction ratio of the liquefied formations was lower than a certain value, however, the total settlement of the buildings began to increase considerably because of general shear failure of the foundation soil.

3. According to the comparison of the analyzed and measured results, these two systems were comparable when the liquefied soil parameters were reduced to 0.1 to 0.4 times their original values. However, we suggest a parameter reduction ratio of the liquefied soil by 0.05 to 0.3 times their original values in order to provide a more conservative estimate that takes into consideration the uncertainty of the yielded results.

4. The proposed practical procedure is easily followed. With the use of the suggested parameter reduction ratio, the performance of the low-rise building on a liquefiable deposit can be evaluated using a FDM program. We believe that the suggested procedure provides a good reference for practical engineering.

References

- Architectural Institute of Japan (AIJ), 2001, Design recommendation for Foundation of Buildings. (In Japanese)
- Bird, J. F., and Bommer, J. J., 2004, "Earthquake losses due to ground failure," *Eng Geol*, Vol. 75, No. 2, pp. 147-179.
- Bird, J. F., Bommer, J. J., Crowley, H., and Pinho, R., 2006, "Modelling liquefaction-induced building damage in earthquake loss estimation," *Soil Dyn Earthq Eng*, Vol. 26, pp. 15-31.
- Federal Emergency Management Agency (FEMA), 1994, Assessment for state-of-the-art earthquake loss estimation methodologies, FEMA-249, FEMA, Washington, DC.
- Federal Emergency Management Agency (FEMA), 2003, HAZUS-MH technical manual, FEMA, Washington, DC.
- Hwang, J. H., Chen, C. H., Tsai, C. C., Wang, K. L., Hsu, S. Y., Yang, H. C., Chang, W. K., and Chen C. H., 2016, Field Investigation of the Liquefaction and Geotechnical Damage of the Meinong Earthquake in Tainan, NCREE-16-004, NCREE, Taipei. (In Chinese)
- Hwang, J. H., Yang, C. W., and Chen, C. H., 2003, "Investigations on soil liquefaction during the Chi-Chi earthquake," *Soils Found*, pp. 107-123.
- Japan Road Association (JRA), 1996, Road bridge specifications: part V Series of earthquake-proof design. (In Japanese)
- Lu, C. C., Hwang, J. H., Huang, C. R., and Lu, Y. D., 2011, "Earthquake loss estimation of building with shallow foundation due to soil liquefaction," 5th Cross-strait Conference on Structural and Geotechnical Engineering (SGE-5), Hong Kong.
- Lu, C. C., Hsu, S. Y., Hwang, Y. W., and Hwang, J. H., 2016, "Field investigation and liquefaction evaluation after Meinong Earthquake," The Thirteenth National Conference on Structural Engineering/The Third National Conference on Earthquake Engineering, Taoyuan, Taiwan.
- National Center for Research on Earthquake Engineering (NCREE), 2017, Local SPT-based HBF simplified procedure, <https://www.ncree.org/HBF.aspx>. (In Chinese)
- Yeh, C. H., 2002, Integration Study on the Earthquake Disaster Scenario Simulation and its Application Software, NCREE-02-009, NCREE, Taipei. (In Chinese)
- Youd T. L. and Idriss I. M., 1997, Proceedings of the NCEER workshop on evaluation of liquefaction resistance of soils, Technical Report NCEER-97-0022.

Higher-Mode Effects on the Seismic Responses of Buildings

Jui-Liang Lin¹

林瑞良¹

Abstract

Quantifying the higher-mode effects on the seismic demands of buildings is beneficial not only for increasing awareness of the characteristics of seismic responses of buildings but also in the development of rapid/simplified seismic assessment methods. This study proposes an approach that is applicable to quantifying the aforementioned effects, covering the full range of building heights and deformation types. The vehicle used for this proposed approach is the generalized building model, which is modified from the conventional cantilever beam model. The higher-mode effects on floor displacements, inter-story drift ratios, floor accelerations, and base shears are investigated.

Keywords: higher-mode effects, seismic demands, response spectrum, pure shear building, pure flexural building.

Introduction

Seismic loss estimation for a densely populated region, which may have hundreds of thousands of buildings, is one of the key tasks of modern earthquake engineering. In it, the seismic demands of buildings are generally estimated by considering only the contribution of the first mode. However, the accuracy of seismic loss estimation may be effectively improved by appropriately quantifying the effects of higher modes on the seismic demands of buildings. The framework of this quantification should be general and simple so that it can be coordinated with the inventory data of a large building stock. The cantilever beam model (Fig. 1(a)), which uses few parameters to imitate the complicated deformations of wall-frame tall building systems (Rosman 1967, Miranda and Taghavi 2005), is clearly a suitable technique for simulating high-rise buildings. Nevertheless, the cantilever beam model, which has a uniformly distributed mass and consists of a pure flexural beam and a pure shear beam, appears less appropriate for low-rise and mid-rise buildings. This study first proposes the generalized building model (GBM), instead of the cantilever beam model, as a vehicle for quantifying higher-mode effects in buildings covering the full range of building heights.

Maniatakis *et al.* (2013) investigated the effects of higher modes on the seismic responses of one nine-story RC frame structure subjected to thirty-four

earthquake records. They concluded that the higher-mode effects on floor accelerations and shear forces are more significant than those on floor displacements and inter-story drifts. In addition, the contribution of the higher modes depends on the modal strength ratios varying with different ground motion records (Maniatakis *et al.* 2013).

The aim of this study is to quantify the effects of higher modes on seismic demands, which include floor displacements, inter-story drift ratios, floor accelerations, and base shears. In particular, this study attempts to encompass a wide range of buildings, which vary from pure flexural buildings to pure shear buildings and from low-rise buildings to high-rise buildings. In addition to taking the extent of plasticity of higher modes and the soil category of a building site into consideration, the quantification results are expected to be representative (*i.e.*, independent of the selection of ground motion records).

Generalized Building Model

Considering the cantilever beam model (Fig. 1(a)), the GBM employed to simulate an N -story building, in which the story heights are h and the story diaphragms are rigid, consists of two sticks (Fig. 1(b)). The deformations of the two sticks subjected to lateral loads are considered to be pure shear and pure flexure (Figs. 1(c) and (d), respectively). These two sticks are

¹ Research Fellow, National Center for Research on Earthquake Engineering, jllin@ncree.narl.org.tw.

laterally connected to each other by axially rigid bars at all levels of the lumped story masses. Once the story masses of the N -story building are given, the mass matrix of the GBM, which is an $N \times N$ diagonal matrix, is straightforwardly obtained. The displacement vector of the GBM is expressed as $u = [u_N, u_{N-1}, \dots, u_1]^T$, where the subscript of u indicates the story number. Assuming that the ratio of the lateral stiffness of the r -th story to that of the first story of the N -story building is κ_r , the lateral stiffness matrix of the pure shear stick is:

$$\mathbf{K}_s = k_s \mathbf{E}_s \quad (1)$$

where $k_s = EI_s/h^3$ and EI_s is the flexural rigidity of the bottom segment of the pure shear stick. Additionally, the matrix \mathbf{E}_s (Eq. 1) is a matrix with a diagonal band of non-zero elements. On the other hand, the lateral stiffness matrix of the pure flexural stick is:

$$\mathbf{K}_b = \mathbf{F}_b^{-1} \quad (2)$$

where \mathbf{F}_b represents the $N \times N$ flexibility matrix of the pure flexural stick. By using the unit-load method, the i -th row and j -th column element of \mathbf{F}_b , denoted as f_{ij} , is:

$$f_{ij} = \frac{e_{ij}}{k_b} \quad (3)$$

where $k_b = EI_b/h^3$ and EI_b is the flexural rigidity of the bottom segment of the pure flexural stick. Additionally, e_{ij} (Eq. 3) is:

$$e_{ij} = \begin{cases} \sum_{n=i}^N \frac{1}{\kappa_{N+1-n}} \left\{ \frac{1}{3} [(n-i+1)^3 - (n-i)^3] + \frac{1}{2} (i-j) [(n-i+1)^2 - (n-i)^2] \right\}, & i \geq j \\ e_{ji}, & i < j \end{cases} \quad (4)$$

Therefore, \mathbf{K}_b (Eq. 2) can be expressed as:

$$\mathbf{K}_b = k_b \mathbf{E}_b \quad (5)$$

where \mathbf{E}_b is the inverse of the matrix consisting of elements e_{ij} , in which i and j range from 1 to N . As a result, the total lateral stiffness matrix of the GBM, denoted as \mathbf{K} , is:

$$\mathbf{K} = \mathbf{K}_s + \mathbf{K}_b = k_s \mathbf{E}_s + k_b \mathbf{E}_b = k [\alpha \mathbf{E}_s + (1-\alpha) \mathbf{E}_b] \quad (6)$$

where:

$$k = k_s + k_b = \frac{EI_b + EI_s}{h^3} = \frac{EI}{h^3}, \quad \alpha = \frac{k_s}{k_s + k_b} \quad (7)$$

The value of α is clearly between 0 and 1 (Eq. 7). When the value of α equals 0, the lateral deformation of the GBM is pure flexure. When the value of α equals 1, the lateral deformation of the GBM is pure shear. To ensure that this study is as general as possible, an ideal case (*i.e.*, uniformly distributed

mass and uniformly distributed stiffness), rather than a specific case of distribution of mass and/or stiffness, are addressed hereafter, except where specifically noted.

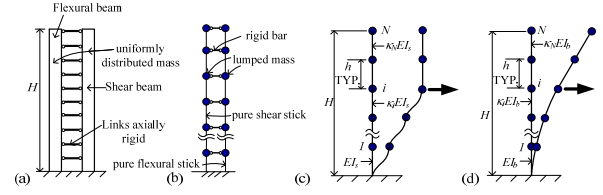


Fig 1. (a) The cantilever beam model. (b) A sketch of the GBM. (c) The lateral deformation of the pure shear stick and (d) the lateral deformation of the pure flexural stick subjected to a concentrated lateral load.

Higher-Mode Effects

Strictly speaking, modal analysis is valid only for linear responses and its extension to inelastic responses is merely an approximation whose accuracy decreases as the nonlinearity increases. As $T_1 > T_s$, $T_2 > T_s$, and $T_3 < T_s$, the higher-mode effects on the j -th floor displacement, the j -th inter-story drift ratio, the j -th floor acceleration, and the base shear, denoted as $H_{u,j}$, $H_{\theta,j}$, $H_{a,j}$, and H_V , respectively, are approximated as below:

$$H_{u,j} = \left[1 + \left(\frac{\Gamma_2 \phi_{2,j}}{\Gamma_1 \phi_{1,j}} \frac{S_{d2,in}}{S_{d1,in}} \right)^2 + \left(\frac{\Gamma_3 \phi_{3,j}}{\Gamma_1 \phi_{1,j}} \frac{S_{d3,in}}{S_{d1,in}} \right)^2 \right]^{1/2} = \left[1 + \left(\frac{\Gamma_2 \phi_{2,j}}{\Gamma_1 \phi_{1,j}} \frac{C_2 T_2}{C_1 T_1} \right)^2 + \left(\frac{\Gamma_3 \phi_{3,j}}{\Gamma_1 \phi_{1,j}} \frac{C_3 T_3}{C_1 T_1} \right)^2 \right]^{1/2} \quad (8a)$$

$$H_{\theta,j} = \left[1 + \left(\frac{\Gamma_2 (\phi_{2,j} - \phi_{2,j-1})}{\Gamma_1 (\phi_{1,j} - \phi_{1,j-1})} \frac{C_2 T_2}{C_1 T_1} \right)^2 + \left(\frac{\Gamma_3 (\phi_{3,j} - \phi_{3,j-1})}{\Gamma_1 (\phi_{1,j} - \phi_{1,j-1})} \frac{C_3 T_3}{C_1 T_1} \right)^2 \right]^{1/2} \quad (8b)$$

$$H_{a,j} = \left[1 + \left(\frac{\Gamma_2 \phi_{2,j}}{\Gamma_1 \phi_{1,j}} \frac{S_{a2,in}}{S_{a1,in}} \right)^2 + \left(\frac{\Gamma_3 \phi_{3,j}}{\Gamma_1 \phi_{1,j}} \frac{S_{a3,in}}{S_{a1,in}} \right)^2 \right]^{1/2} = \left[1 + \left(\frac{\Gamma_2 \phi_{2,j}}{\Gamma_1 \phi_{1,j}} \frac{T_1 R_1}{T_2 R_2} \right)^2 + \left(\frac{\Gamma_3 \phi_{3,j}}{\Gamma_1 \phi_{1,j}} \frac{T_1 R_1}{T_3 R_3} \right)^2 \right]^{1/2} \quad (8c)$$

$$H_V = \left[1 + \left(\frac{\Gamma_2^2 M_2}{\Gamma_1^2 M_1} \frac{S_{a2,in}}{S_{a1,in}} \right)^2 + \left(\frac{\Gamma_3^2 M_3}{\Gamma_1^2 M_1} \frac{S_{a3,in}}{S_{a1,in}} \right)^2 \right]^{1/2} = \left[1 + \left(\frac{\Gamma_2^2 M_2}{\Gamma_1^2 M_1} \frac{T_1 R_1}{T_2 R_2} \right)^2 + \left(\frac{\Gamma_3^2 M_3}{\Gamma_1^2 M_1} \frac{T_1 R_1}{T_3 R_3} \right)^2 \right]^{1/2} \quad (8d)$$

, in which T_n , Γ_n , M_n , and R_n , where $n = 1-3$, are the vibration period, modal participation factor, modal mass, and the strength ratio of the n -th vibration mode, respectively. In addition, $\phi_{n,j}$ and T_s are j -th component of the n -th mode shape and the corner period of the design response spectrum, respectively. Finally, $S_{dn,in}$ and $S_{an,in}$, where $n = 1-3$, are the maximum displacement and the maximum acceleration of the n -th single-degree-of-freedom (SDOF) modal system, respectively. FEMA-440 (2005) provides a simple expression of the coefficient that relates the maximum displacement of an inelastic SDOF system with elastic-perfect-plastic (EPP) hysteretic properties to the maximum displacement of the linear elastic response. This coefficient is expressed as:

$$C_n = 1 + \frac{R_n - 1}{\alpha T_n^2} \quad (9)$$

The constant a is equal to 130, 90, and 60 for site classes B, C, and D, respectively. In addition, for periods less than 0.2 s, the value of the coefficient C_n for 0.2 s may be used. For periods greater than 1.0 s, C_n may be assumed to be 1.0 (FEMA-440 2005). Equations 8(a) to (d) clearly indicate the trends in the effects of higher modes on the seismic demands accompanied by a change in the associated parameter values. For instance, as the value of T_1/T_i , where $i = 2$ and 3, increases, the higher-mode effects on floor displacements and inter-story drift ratios decrease (Eqs. 8(a) and (b)); however, the higher-mode effects on floor accelerations and base shears increase (Eqs. 8(c) and (d)). Note that the parameter C_n is essentially proportional to R_n (Eq. 9). Hence, when the value of R_1/R_i , where $i = 2$ and 3, increases, Eqs. 8(c) and (d) directly indicate that the higher-mode effects on floor accelerations and base shears increase, whereas Eqs. 8(a) and (b) indirectly indicate that the higher-mode effects on floor displacements and inter-story drift ratios decrease. In addition, as the value of $\Gamma_i^2 M_i / \Gamma_1^2 M_1$, where $i = 2$ and 3, increases, the higher-mode effect on base shear increases (Eq. 8(d)). When the value of $\Gamma_i \phi_{i,j} / \Gamma_1 \phi_{1,j}$, where $i = 2$ and 3, increases, the higher-mode effects on floor displacements and floor accelerations increase (Eqs. 8(a) and (c)). Finally, the higher-mode effect on inter-story drift ratios increases as the value of $\Gamma_i (\phi_{i,j} - \phi_{i,j-1}) / \Gamma_1 (\phi_{1,j} - \phi_{1,j-1})$, where $i = 2$ and 3, increases (Eq. 8(b)).

The proposed approach to approximate the quantification of higher-mode effects on the seismic demands of a wide range of buildings, from low-rise buildings to high-rise buildings and from pure-flexural to pure-shear types of deformations, is summarized as follows. First, the elastic modal properties of the various buildings are estimated using the GBM. Second, the peak modal responses, *i.e.*, $S_{dn,in}$ and $S_{an,in}$, of every building are computed, in which the values of T_n , C_n , R_n , and the elastic design response spectrum are required. Third, the elastic modal properties and the peak modal responses are then inserted into Eq. 8 for computing the higher-mode effects $H_{u,j}$, $H_{\theta,j}$, $H_{a,j}$, and H_v .

Figures 2 and 3 show the higher-mode effects $H_{u,j}$, $H_{\theta,j}$, and $H_{a,j}$ along the building height for pure-flexural buildings ($\alpha = 0$) and pure-shear buildings ($\alpha = 1$), respectively, as the number of stories, N , is varied from one to thirty. According to the definitions of higher-mode effects, it is natural for the values of $H_{u,j}$, $H_{\theta,j}$, and $H_{a,j}$ for single-story buildings ($N = 1$) to always equal 1. Additionally, a location along the building height with the value of $H_{u,j}$, $H_{\theta,j}$, or $H_{a,j}$ very close to 1 indicates that this location is almost free from the corresponding higher-mode effects. Figures 2(a) to (c) and 3(a) to (c) are the elastic cases (*i.e.*, $R_1 = 1$, $R_2 = 1$, and $R_3 = 1$) for buildings located on site class B. Regardless of the

number of stories, Figs. 2(a), 2(c), 3(a), and 3(c) indicate that the higher-mode effects $H_{u,j}$ and $H_{a,j}$ on the top story appear to be negligible in comparison with those on the lower stories. The locations with values of $H_{u,j}$ approaching 1 in pure-flexural and pure-shear buildings are approximately 0.8 (Fig. 2(a)) and 0.7 (Fig. 3(a)) of the building height, respectively. This indicates that the locations where the floor displacements are almost free from the higher-mode effects are exactly at or very close to the locations of the nodes (*i.e.*, stationary points) of the corresponding second mode shape.

Conclusions

A general-purpose-oriented building model, designated as a generalized building model (GBM), was developed in this study. The GBM retains the advantage of the conventional cantilever beam model (*i.e.*, the simplicity in modeling the complicated seismic responses of wall-frame tall buildings). Furthermore, the GBM is suitable for simulating buildings without a lower bound on the number of stories. By exploiting the GBM along with the design response spectrum rather than some particular ground motion records, the higher-mode effects on the seismic demands of a wide range of ideal buildings (*i.e.*, uniform distribution of mass and stiffness along the buildings' heights) were explored. Therefore, the higher-mode effects explored in this study are very general, which might be valuable for a rapid seismic evaluation of a large building stock. The results of the approximate quantification of higher-mode effects on seismic demands from the standpoint of the design response spectrum are briefly summarized as follows.

The investigated higher-mode effects increased as the building height increased. For elastic buildings sitting on site class B, the higher-mode effects on the top-floor displacements and the top-floor accelerations appear to be negligible. The estimated maximum inter-story drift ratios of pure-flexural and pure-shear high-rise elastic buildings obtained by considering only the contribution of the first mode should be corrected by multiplying by approximately 1.02 and 1.067, respectively, to account for the higher-mode effects. The higher-mode effects on the base shears of pure-flexural and pure-shear high-rise elastic buildings are approximately 1.69 and 1.07, respectively. The higher-mode effects on the seismic demands of inelastic buildings are generally greater than those of their elastic counterparts. In addition, the increments of $H_{a,j}$ and H_v are much more obvious than those of $H_{u,j}$ and $H_{\theta,j}$. For buildings with the same strength ratio of the first mode, the lower the strength ratios of the higher modes are, the larger the values of $H_{a,j}$ and H_v become, but the smaller the values of $H_{u,j}$ and $H_{\theta,j}$ become. In addition, the higher-mode effects decrease for a building sitting on a softer site.

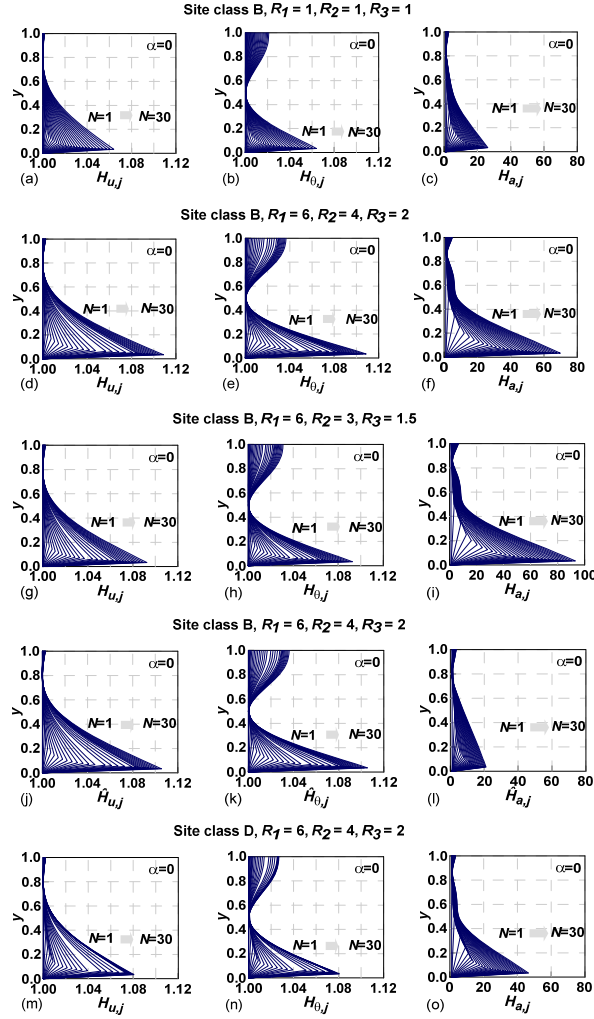


Fig 2. Higher-mode effects in pure flexural buildings: (a, b, c) for $R_1 = 1, R_2 = 1, R_3 = 1$, and site class B; (d, e, f) for $R_1 = 6, R_2 = 4, R_3 = 2$, and site class B; (g, h, i) for $R_1 = 6, R_2 = 3, R_3 = 1.5$, and site class B; (j, k, l) for $R_1 = 6, R_2 = 4, R_3 = 2$, and site class B but without considering the third mode; and (m, n, o) for $R_1 = 6, R_2 = 4, R_3 = 2$, and site class D.

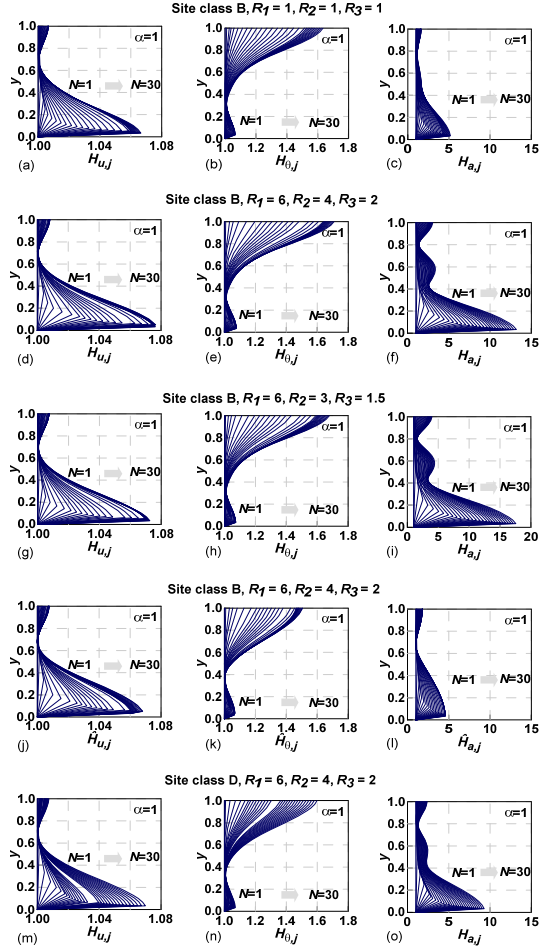


Fig 3. Higher-mode effects in pure shear buildings: (a, b, c) for $R_1 = 1, R_2 = 1, R_3 = 1$, and site class B; (d, e, f) for $R_1 = 6, R_2 = 4, R_3 = 2$, and site class B; (g, h, i) for $R_1 = 6, R_2 = 3, R_3 = 1.5$, and site class B; (j, k, l) for $R_1 = 6, R_2 = 4, R_3 = 2$, and site class B but without considering the third mode; and (m, n, o) for $R_1 = 6, R_2 = 4, R_3 = 2$, and site class D.

References

- Rosman, R. (1967), "Laterally loaded systems consisting of walls and frames", *Tall Buildings*, Pergamon Press, Ltd., London, England, 273-289.
- Miranda, E. and Taghavi, S. (2005), "Approximate floor acceleration demands in multistory buildings I: formulation", *Journal of Structural Engineering*, ASCE, 131(2), 203-211.
- Maniatakis, C.A., Psycharis, I.N. and Spyrakos, C.C. (2013), "Effect of higher modes on the seismic response and design of moment-resisting RC frame structures", *Engineering Structures*, 56, 417-430.
- FEMA-440 (2005), "State Improvement of nonlinear static seismic analysis procedures", prepared by Applied Technology Council for the Federal Emergency Management Agency, Washington.

Effects of M3 or PMM Nonlinear Hinges in Pushover Analysis of Reinforced Concrete Buildings

Yeong-Kae Yeh ¹ and Te-Kuang Chow ²

葉勇凱 ¹、周德光 ²

Abstract

In Taiwan, the detailed seismic evaluation procedures used by engineers are nonlinear static analyses, known as pushover analyses, which are based on the Capacity Spectrum Method, where the nonlinear behavior of the building is concentrated by the nonlinear hinge of the components. The seismic evaluation program TEASPA developed by the NCREC uses M3 nonlinear hinges for X-direction pushover analysis (where the Y-direction is M2). M3 nonlinear hinges do not consider axial force–moment interaction and their strength is determined by the column axial force at the static load stage. On the other hand, the moment nonlinear hinge PMM can consider axial force–moment interaction and its strength is determined by the column axial force of the pushover process. In this paper, three sample structures are used to discuss the influence of the nonlinear hinge setting of M3 or PMM on the pushover analysis of reinforced concrete structures. The three sample structures are a three-story traditional school building structure, a ten-story moment-resisting frame structure, and a ten-story moment-resisting frame with shear wall structure. The results show that the PMM nonlinear hinge can reveal the influence of the change of axial force on the bending moment strength and can also reflect the reduction of bending moment strength by the biaxial bending moment. The difference in performance target ground acceleration estimated by the pushover analysis using M3 or PMM hinges does not exceed 10%.

Keywords: detailed seismic evaluation, nonlinear pushover analysis, PMM nonlinear hinges, performance target ground acceleration

Introduction

In Taiwan, school buildings have widely used TEASPA (Yeh et al., 2009; NCREC, 2013) to evaluate their seismic capacities. “Taiwan Earthquake Assessment for structures by Pushover Analysis” (TEASPA) was developed by the NCREC. TEASPA is a type of capacity spectrum method of ATC-40 (ATC, 1996), which uses a software package to perform nonlinear pushover analysis.

This paper employs the software ETABS, which is commonly used by engineers. The axes of the structural coordinate system of ETABS are denoted as X, Y, and Z, and the axes of each local coordinate system are denoted as 1, 2, and 3. In general, the +2 direction is parallel to the +X direction, and the +3 direction is parallel to the +Y direction. Thus, the X-direction pushover analysis will form a 3-axis bending moment in the columns, that is, M3, and the Y-

direction pushover analysis will form a 2-axis bending moment in the column, that is, M2. In nonlinear pushover analysis, TEASPA (NCREC, 2013) assumes that the nonlinear behavior of the structure is concentrated by the bending moment hinges at both ends of the beam and column members. The relationship between the bending moment and rotation angle of the nonlinear hinge is based on the results of a series of cyclic lateral load tests of fixed axial-force double-curvature non-ductile reinforced-concrete columns. The bending moment strength is determined by the configuration of the column section and the column axial force, so TEASPA uses M3 nonlinear hinges with fixed axial force to determine the moment strength and the relationship between bending moment and rotation angle. In the application to the Construction and Planning Agency for approval of seismic evaluation method certification for TEASPA, the review committee considered that the column axial force is not a fixed value during the pushover process,

¹ Research Fellow, National Center for Research on Earthquake Engineering, ykyeh@ncree.narl.org.tw

² Associate Technician, National Center for Research on Earthquake Engineering, tkchow@ncree.narl.org.tw

and that M3 nonlinear hinges may have large errors in the analysis of mid-to-high-rise buildings. Therefore, it is determined that TEASPA can only be applied to the seismic evaluation of low-rise buildings having story numbers less than or equal to six.

This paper discusses the influence of the axial column force on the results of pushover analysis. The bending moment strength of the PMM nonlinear hinge of ETABS (CSI, 2005) depends on the axial force–moment interaction of the column section. During the pushover process, the axial force of the column directly affects the moment strength of the nonlinear hinge. This paper uses three example structures with different numbers of floors and different structural systems to carry out pushover analyses with TEASPA M3 nonlinear hinges and PMM nonlinear hinges to discuss their effects on the results of pushover analysis.

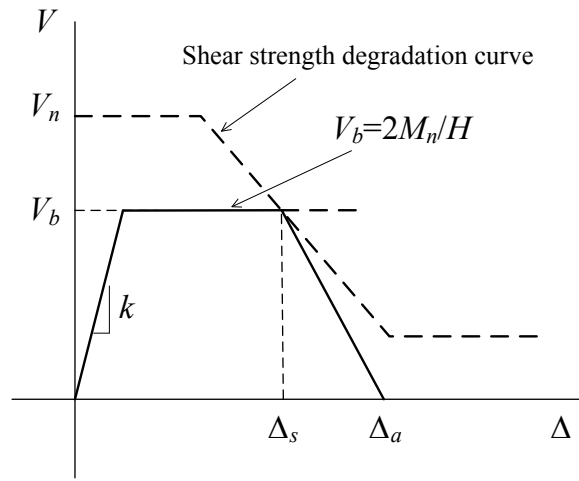


Fig. 1. Lateral force–displacement curve of a flexural-shear failure column

M3 and PMM Nonlinear Hinges

Before performing the pushover analysis, the nonlinear hinges of the structural elements need to be established. The most direct way to establish the nonlinear hinge properties is by regression analysis of the test data. The long columns of existing old building structures do not have sufficient amounts of stirrups, so the failure mode is mostly considered to be flexural-shear failure. The lateral force–displacement curve of a double curvature column is used to illustrate the flexural-shear failure. As shown in Figure 1, the column is deformed by a lateral force with stiffness k , and as the lateral force reaches V_b , the main ribs yield. For the sake of conservation and simplicity, it is assumed that the main ribs are not subject to strain hardening and the lateral force strength remains constant. When the lateral displacement Δ reaches Δ_s , the nonlinear hinge zone at the end of the column will produce significant shear cracks, and this state is called ductile shear failure or flexure-shear failure. After this state, the lateral strength decreases. When

the lateral displacement Δ reaches Δ_a , the lateral force strength approaches 0, and the column loses its axial load carrying capacity, which is called the axial failure state.

Elwood and Moehle (2005a) tested fifty reinforced-concrete column specimens of different sizes and different stirrup ratios. With double-curvature deformation test data, the drift ratio at the flexural-shear failure state can be calculated using the following formula:

$$\frac{\Delta_s}{H} = \frac{3}{100} + 4\rho'' - \frac{1}{133} \frac{v_m}{\sqrt{f'_c}} - \frac{1}{40} \frac{P}{A_g f'_c} \geq \frac{1}{100} \quad (1)$$

where H is the clear length of the column, $\rho'' = \frac{A_{st}}{b \times s}$ is the transverse reinforcement ratio, and $v_m = V_b/bd$ is the maximum shear stress.

Elwood and Moehle (2005b) also obtained the drift ratio when axial failure occurs using the following formula:

$$\frac{\Delta_a}{H} = \frac{4}{100} \frac{1 + (\tan \theta)^2}{\tan \theta + P \frac{s}{\kappa' A_{st} f_{yt} d_c \tan \theta}} \quad (2)$$

where d_c is the depth of the concrete core of the column section, θ is the crack angle measured from the horizontal line, and k' is a value between 1 and 0.7 according to the ductility ratio $\mu = \Delta_s/\Delta_y$.

Table 1 The parameters of the M3 bending moment nonlinear hinge

Points	Moment/SF	Rotation/SF
A	0	0
B	$\min(M_y/M_n, 0.95)$	0
C	1	a
D	1	b
E	0	c

In performing nonlinear pushover analysis, bending-moment nonlinear hinges are installed at both ends of the column to represent the flexural-shear or flexure failure modes, and the nonlinear hinge properties are defined by the double-curvature column test data. According to the previously discussed lateral-load displacement curve of a flexural-shear failure column, the moment nonlinear hinge parameters reflecting the flexural or flexural-shear failure modes can be defined conservatively. However, in order to avoid underestimating the initial stiffness

of the components, the yield bending moment M_y is added before the M_n point on the bending moment–rotation angle curve, and its value must not be greater than $0.95M_n$. Then the flexural rigidity of the column cracking section is adjusted to $0.7E_cI_g$. According to this method, the parameters of the M3 bending-moment nonlinear hinge can be defined as shown in Table 1. In Table 1, the moment scale factor (SF) is defined as M_n , the rotation scale factor (SF) is set to 1, and the other parameters are defined as follows:

$$a = \frac{\Delta_n}{H} - \frac{\Delta_y}{H} \quad (3)$$

$$b = \frac{\Delta_s}{H} - \frac{\Delta_y}{H} \quad (4)$$

$$c = \max\left(\frac{\Delta_a}{H}, \frac{\Delta_s}{H}\right) \quad (5)$$

$$\Delta_y = \frac{V_b}{k} = \frac{V_b H^3}{12(EI)_c} = \frac{V_b H^3}{12(0.7E_c I_g)} \quad (6)$$

According to the parameters of the bending moment nonlinear hinge, the five points A–E of the M3 or M2 nonlinear hinges for the X-direction or the Y-direction pushover analyses are modified, respectively.

ETABS has two types of bending-moment nonlinear hinges, M3 (or M2) and PMM. Their difference is that the M3 nonlinear hinge must specify the bending moment strength, while the PMM nonlinear hinge uses the P-M2-M3 interaction surface of the axial force P, the 2-axis moment M2, and the 3-axis moment M3 to determine the yield moment strength with the axial load of the columns during the pushover process.

Table 2 The parameters of the PMM bending-moment nonlinear hinge

Points	Moment/SF	Rotation/SF
A	0	0
B	1	0
C	1	a
D	1	b
E	0	c

The parameters of the PMM nonlinear hinge are shown in Table 2. The rotation SF is fixed to 1 and the moment SF is the yield moment strength determined by the axial force and the P-M2-M3 interaction surface. Point B is the yield state of the PMM nonlinear hinge. Since the purpose of this paper is to compare the change of the M3 nonlinear hinge of the original TEASPA when the PMM is considered, the B-point

bending moment is adjusted from M_y of the M3 hinges to M_n of the PMM hinges in order to avoid amplifying the bending moment strength of the PMM.

Comparison of M3 and PMM Models with Sample Structures

This section discusses the influence of the nonlinear hinge setting of M3 or PMM on the pushover analysis of reinforced-concrete buildings using three sample structures. These are a three-story traditional school building structure, a ten-story moment-resisting frame structure, and a ten-story moment-resisting frame with shear wall structure.

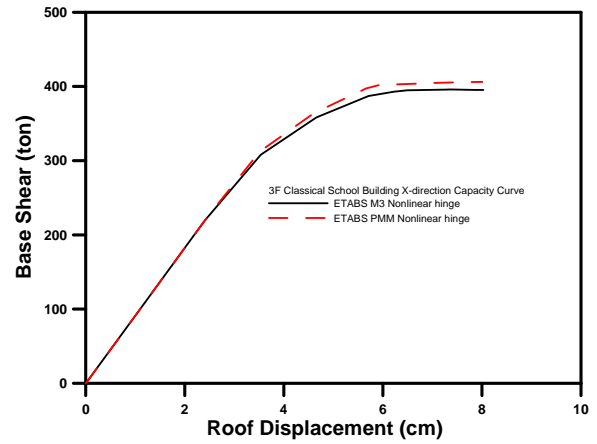


Fig. 2. The capacity curves of a three-story traditional school building with M3 and PMM hinges

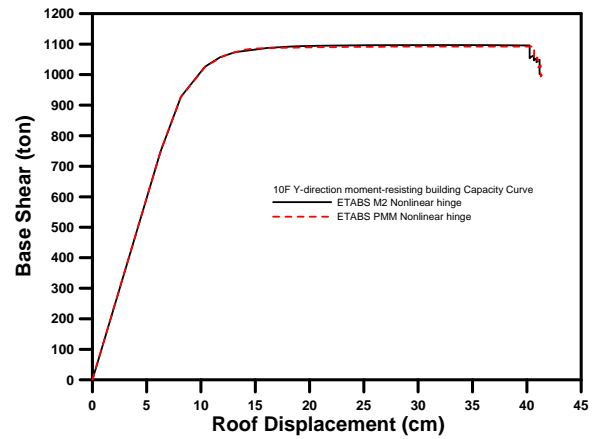


Fig. 3. The capacity curves of a ten-story moment-resisting frame structure with M2 and PMM hinges

The capacity curves of the pushover analysis of the two models of the M3 nonlinear hinge and the PMM nonlinear hinge of the typical three-story school building are shown in Fig. 2, and the two curves are quite similar. The capacity curve of the PMM model is slightly higher than that of the M3 model. If the last point of the capacity curve is the performance target, the performance target ground acceleration A_p of the M3 model is 0.208 g, the performance target ground surface acceleration A_p of the PMM model is 0.210 g,

and the error is less than 10%.

The capacity curves of the pushover analysis of the two models of the M2 nonlinear hinge and the PMM nonlinear hinge of the ten-story moment-resisting frame structure are shown in Fig. 3. If the strength degradation point of the capacity curve is the performance target, the performance target ground acceleration A_p of the M2 model is 0.566 g, the performance target ground surface acceleration A_p of the PMM model is 0.568 g, and the error is less than 10%.

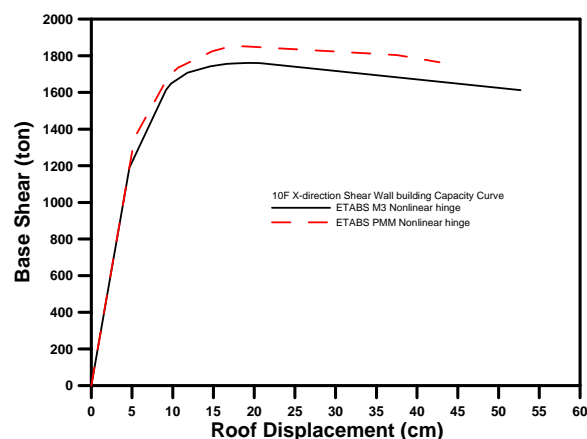


Fig. 4. The capacity curves of a ten-story moment-resisting frame with shear wall structure with M3 and PMM hinges

The capacity curves of the pushover analysis of the two models of the M3 nonlinear hinge and the PMM nonlinear hinge of the ten-story moment-resisting frame with shear wall structure are shown in Fig. 4. If the strength degradation point of the capacity curve is the performance target, the performance target ground acceleration A_p of the M3 model is 0.847 g, the performance target ground surface acceleration A_p of the PMM model is 0.789 g, and the error is less than 10%.

Conclusions

In this paper, a three-story traditional school building and two ten-story reinforced-concrete buildings were analyzed to determine the differences in seismic evaluation between the original TEASPA M3 model and the PMM nonlinear hinge model. The analysis results yielded the following conclusions:

1. Although the moment strengths of the moment hinges of the PMM model are different from those of the M3 model, the difference is minor because the column axial force is not changed significantly for a typical low-rise three-story school building. Thus, the performance target ground acceleration of the detailed seismic evaluation results has very little difference and the error is less than 10%. Therefore, for the low-rise school building, the

original M3 nonlinear hinge setting of TEASPA, which is used in detailed seismic evaluation, can still be used with considerable accuracy.

2. In the ten-story structure, the axial force of the column shows a significant change during the pushover process. However, due to the increase of the bending moment strength of the compression side and the decrease of the bending moment strength of the tension side of the PMM model, the resulting difference in capacity curves between the PMM model and the M3 model is slight. The performance target ground acceleration of the detailed seismic evaluation results shows very little difference and the error is less than 10%. Therefore, for the mid-rise ten-story building, the original M3 nonlinear hinge setting of TEASPA, which is used in detailed seismic evaluation, can still be used with considerable accuracy. It is still recommended to use PMM nonlinear hinges instead of M3 nonlinear hinges to consider the larger change in column axial force in the pushover process.

References

- Applied Technology Council (ATC) (1996), "ATC-40 Seismic Evaluation and Retrofit of Concrete Buildings", prepared by the Applied Technology Council, Redwood City, Calif.
- CSI (2005), ETABS, Integrated Building Design Software, Version 9, Computers and Structures, Inc., Berkeley, California.
- Elwood, K. J., and Moehle, J. P., (2005a), "Drift capacity of reinforced concrete columns with light transverse reinforcement," *Earthquake Spectra*, Vol. 21, No. 1, 71-89.
- Elwood, K. J., and Moehle, J. P., (2005b), "Axial capacity model for shear damaged columns," *ACI Structural Journal*, Vol. 102, No. 4, 578-587.
- NCREE (2013), Technology Handbook for Seismic Evaluation and Retrofit of School Buildings Third Edition, NCREE report NCREE-13-023, Taipei.
- Yeh, Y.-K., Hsiao, F.-P., Shen, W.-C., Yang, Y.-S., and Hwang, S.-J., (2009), Seismic evaluation of reinforced concrete structure with pushover analysis, NCREE report, NCREE-09-015.

Damage Status and Seismic Assessment of Mid- to High-rise Buildings in the 2016 Meinong Earthquake in Taiwan

Tirza Paramitha Pamelisa¹, Fu-Pei Hsiao² and Yu-Chen Ou³

Abstract

The most recent devastating earthquake to strike Taiwan was the Meinong earthquake in 2016, which led to the collapse of eight 2–16-story buildings. The reconnaissance results of two representative mid- to high-rise buildings, Xingfu and Weiguan, which collapsed during the 2016 Meinong earthquake, are introduced in this study. This study uses a seismic assessment method with pushover analysis and nonlinear response history analysis to understand the seismic capacity of the collapsed buildings in the earthquake. The effects of masonry brick walls on the response of mid-to high-rise buildings are also examined. The results indicate that the presence of brick walls adds a considerable amount of stiffness to the system structure and reduces the fundamental natural period. The collapse of a building can be defined using the parameters of axial load, drift ratio, and ductility ratio. The results of this research are expected to contribute to the prevention of collapse of mid- to high-rise buildings in future earthquakes.

Keywords: damage investigation, Meinong earthquake, mid- to high-rise buildings, nonlinear response history analysis, pushover analysis

Introduction

The Meinong earthquake in 2016, is the most recent devastating earthquake to strike Taiwan, leading to the collapse of eight 2–16-story buildings. A seismic evaluation study of mid- to high-rise buildings has thus become essential to prevent such failures from occurring in new buildings in the future. The seismic behavior of a building is usually investigated by nonlinear static analysis (pushover analysis). However, this method is not suitable for the analysis of mid- to high-rise buildings because only the first-mode failure mechanism can be identified. An alternative method is nonlinear response history analysis (NRHA), which analyzes the real behavior of buildings by inputting real ground motion data obtained from earthquake excitations to the model.

In structural analysis, a masonry brick wall is normally considered an architectural element and often neglected because of the complexity of its interaction with the structural frame. However, brick walls tend to interact with the structural frame when the structure is subjected to a lateral load, resulting in an increase in the

lateral load capacity of the structure (Wakchaure, 2012). In contrast, if the brick walls have irregular configurations, they can induce significant local damage to the structural element (Lee & Woo, 2002). Many mid- and high-rise buildings in Taiwan have a soft-story configuration to meet the building's purpose. Lower stories are usually used for commercial purposes and have a minimum number of brick walls, whereas upper stories are used for residential purposes and have many separation walls. Therefore, the effects of masonry brick walls on the response of mid- to high-rise buildings will be examined in this study.

Analysis Methodology

In this study, the NRHA method is used with the ground motion as the input to the model. Taiwan Earthquake Assessment for Structures by Pushover Analysis (TEASPA), a seismic assessment method introduced by the National Center for Research on Earthquake Engineering (NCREE), is used to determine the stiffness reduction factor in inelastic hinge properties. The plastic hinges assigned by TEASPA can capture the capacity of the reinforced concrete (RC) members,

¹ Research Assistant, National Center for Research on Earthquake Engineering

² Research Fellow, National Center for Research on Earthquake Engineering; Associate Professor (joint appointment), National Cheng Kung University

³ Professor, National Taiwan University

including brick walls, beams, columns, and RC walls (Luu, 2011).

The initial stiffness for all the columns is set to $0.7 E_c I_g$. At the yield moment point, the stiffness degrades to $0.35 E_c I_g$ until the nominal moment point. The yield deformation Δ_y is calculated using the following equation proposed by Elwood and Moehle (2005) and is required to be less than $0.04H$:

$$\Delta_y = \frac{V_b}{k} = \frac{V_b H^3}{12 \alpha E I_g} \quad (1)$$

As the lateral displacement reaches the drift value Δ_s , shear failure is initiated in the column. The drift value Δ_s can be calculated using the following equation proposed by Elwood and Moehle (2005) on the basis of the observation of fifty shear-critical column databases:

$$\frac{\Delta_s}{H} = \frac{3}{100} + 4 \rho^n - \frac{1}{133} \frac{v_m}{\sqrt{f'_c}} - \frac{1}{40} \frac{P}{A_g f'_c} \geq \frac{1}{100} \quad (2)$$

The stiffness reduction factor input in Midas Gen is divided into two parts, P1 and P2. P1 is defined as the stiffness reduction after the yielding point, which is set according to the TEASPA value. P2 is defined as the stiffness reduction factor after the nominal moment has been reached and the displacement reaches the yielding point; it is set to 0. As Midas Gen cannot detect the failure of the element in the nonlinear response history analysis, the drift limit on the element is set manually by inputting the deformation index D/D1 based on the ratio Δ_y/Δ_s from TEASPA. The nonlinear dynamic backbone curve is illustrated in Figure 1.

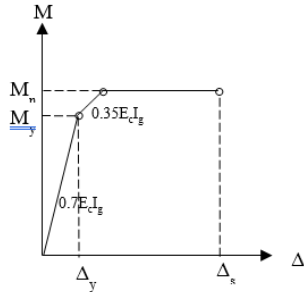


Figure 1 Backbone curve

Case Study

Two cases of building collapse during the Meinong earthquake were analyzed in this study. The first one is the Xingfu building, which was a seven-story RC building constructed in around 2000 in Guiren District. The first and second floors of the Xingfu building were used for office purposes and the upper stories were used for residential purposes. According to the building's function, this is a soft-story building because there were fewer walls in the lower stories, which were used for commercial purposes.

Three cases were simulated in the program: the frame only (Case A), the frame with a brick wall (Case B), and the frame with a brick wall for the third floor until the roof (Case C). In Case C, the existence of the brick wall was neglected for the first and second floors, corresponding to the real situation of the building after the Meinong earthquake, where the brick walls in these two floors were totally crushed. The 3D model obtained by Midas Gen is shown in Figure 2.

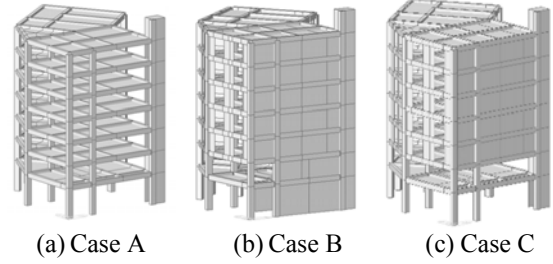


Figure 2 3D model of the Xingfu building

Two sets of seismic data from stations CHY 063 (0.425 g) and CHY 085 (0.24 g) were considered to be the most suitable ground motion data.

The second study case is the Weiguan building, which was constructed in 1994 in Yongkang District, Tainan City. The preliminary study of the building's floor plan drawing revealed that the lower floors had fewer walls as they were used for commercial purposes. Two cases were simulated in the program: the frame only (Case A) and the frame with a brick wall (Case B). The brick wall modeling for the Weiguan building considers only the separation walls inside the building as there were many windows and holes on the outer wall of the building. The 3D model obtained using Midas Gen is shown in Figure 3.

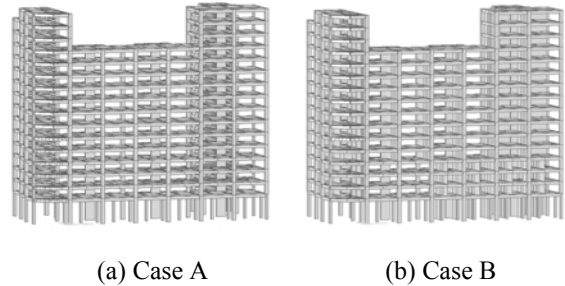


Figure 3 3D model of the Weiguan building

Two sets of seismic data from stations CHY 063 (0.425 g) and CHY 064 (0.14 g) were considered to be the most suitable ground motion data.

Analytical Result

Xingfu Building

Under the CHY 063 ground motion, the axial forces resisted by the column are generally high. In Cases A and C, all columns could be classified as high axial columns (with axial ratios more than $0.3A_{g'c}$). The axial forces of the building under the CHY 085 ground motion were relatively smaller than those under the CHY 063 ground motion. Maximum and average values of the axial column force ratio ($P/A_{g'c}$) for each case and ground motion are shown in Table 1.

Table 1 Axial column forces for the Xingfu building

$P/A_{g'c}$	CHY 063 (0.425 g)			CHY 085 (0.24 g)		
	Case A	Case B	Case C	Case A	Case B	Case C
Max	1.89	0.71	0.82	1.10	0.49	0.52
Ave	0.67	0.44	0.44	0.51	0.35	0.37

Under the CHY 063 ground motion, the story drifts in Cases A and C were maximum on the first floor. In Case B, maximum story drift ratios occurred on the second floor, which is attributed to the fewer brick walls in the second floor compared with those in the first and third floors.

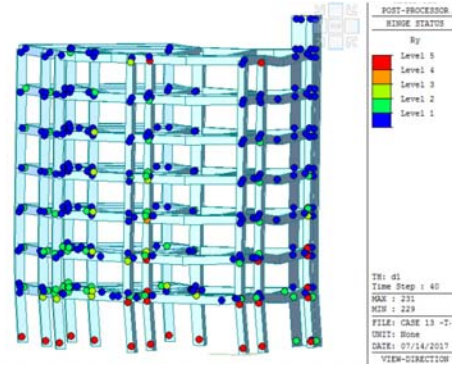
The deformation limit was determined in the nonlinear dynamic analysis to define the failure of the system structure. The maximum deformation capacity provided in the TEASPA method (Δ_s/H) was chosen in this study. After the nonlinear dynamic analysis was performed, the column with the maximum drift ratio was selected to represent the critical column. The results are shown in Table 2. It can be stated that Cases A and C failed under the CHY 063 ground motion as the maximum story drift ratios exceeded the deformation limit Δ_s/H . On the other hand, all cases could be presumed to be safe during an earthquake with similar characteristics as CHY 085. The Δ_s/Δ_y value was also calculated using TEASPA to determine the ductility ratios of the elements.

Table 2 Maximum story drift and drift limit for the Xingfu building

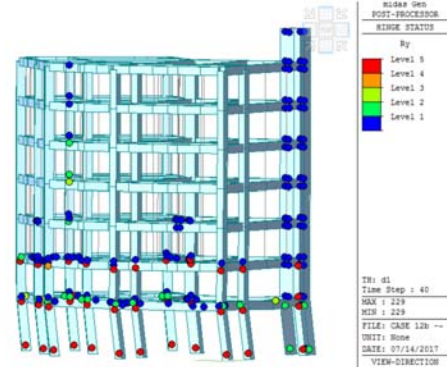
Case	Ground Motion	Max drift (%)	Δ_s/H (%)	Δ_s/Δ_y
A	CHY 063	3.533	2.078	3.281
	CHY 085	0.899	2.516	3.972
B	CHY 063	0.521	2.299	3.706
	CHY 085	0.360	2.737	4.411
C	CHY 063	3.606	2.532	4.081
	CHY 085	1.144	2.695	4.344

The D/D1 output from Midas Gen was compared with the Δ_s/Δ_y values. The column with D/D1 exceeding Δ_s/Δ_y was determined to have failed. Under the CHY 063 ground motion, all columns in Cases A and C failed

under this type of earthquake. Under the CHY 085 ground motion, several columns failed in Case C. This result shows that the soft-story configuration of the building has an adverse effect as the ductility ratio increases. The locations of failure in both building cases under the CHY 063 and CHY 085 ground motions are shown in Figures 4 and 5, respectively.



(a) Case A



(b) Case B

Figure 4 Xingfu column failure (CHY 063)

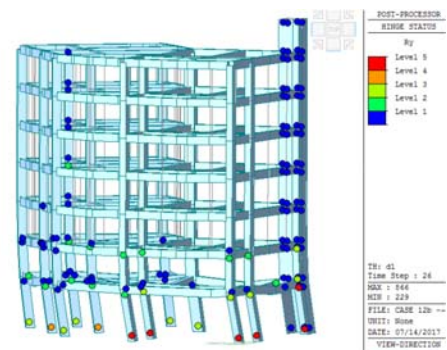


Figure 5 Xingfu column failure (CHY 085)

Weiguan Building

The axial ratios in the Weiguan building were extremely high in Case B. In the east side columns, all

columns achieved more than $0.3A_gf'_c$, even exceeding $A_gf'_c$ for Case B. The results are shown in Table 3.

Table 3 Axial column forces for the Weiguan building

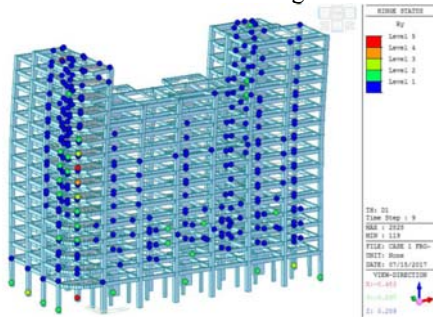
$P/A_gf'_c$	CHY 063 (0.425 g)		CHY 064 (0.14 g)	
	Case A	Case B	Case A	Case B
Max	0.66	2.61	0.63	1.15
Ave	0.33	0.98	0.30	0.50

The maximum drift ratios were compared with the story drift limits given in Table 4. In Case B, the maximum story drift ratios occurred on the first floor because of fewer brick walls compared with those in the upper stories. On the contrary, for Case A, maximum story drift ratios occurred on the upper stories.

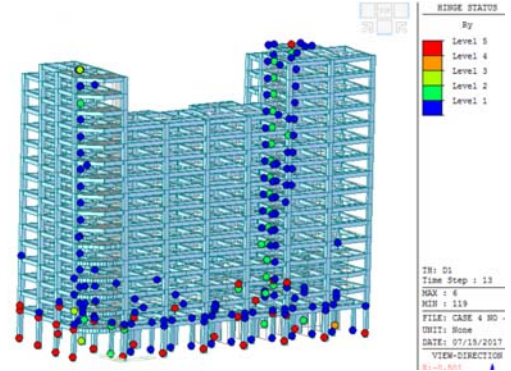
Table 4 Maximum story drift and drift limit for the Xingfu building

Case	Ground Motion	Max drift (%)	$\Delta S/H$ (%)	Δ_g/Δ_y
A	CHY 063	2.093	3.092	1.989
	CHY 064	1.083	3.129	2.013
B	CHY 063	3.271	3.101	1.995
	CHY 064	1.322	2.145	4.617

The ductility ratios were also checked by inputting the D/D1 limit into Midas Gen. In all cases, under the CHY 064 ground motion, the maximum drift ratios did not exceed the story drift limit; therefore, the rotation that occurred in all columns was still under the safe limit. In Case A, under CHY 063, even though the values did not exceed the story drift limit, one column failed due to a high rotation value. By contrast, in Case B under CHY 063, the rotation values of seventeen columns were beyond the acceptable limit. The locations of failure in both building cases under CHY 063 ground motion are shown in Figure 6.



(a) Case A



(a) Case B

Figure 6 Weiguan column failure (CHY 063)

Conclusion

Based on the analysis performed in this study, the main conclusions are summarized as follows:

1. Including brick walls in the analysis resulted in different behaviors for the buildings. The presence of brick walls added a considerable amount of stiffness to the system structure and reduced the fundamental natural period.
2. Since no earthquake station was located close to the Xingfu building, the behavior of the Xingfu building could be assumed to be somewhere between the two ground motions chosen in this study (between 0.24 g and 0.425 g). On the other hand, the CHY 064 station (PGA 0.14 g) was located relatively close to the site of the Weiguan building but oriented behind the building. Therefore, the real seismic behavior of the Weiguan building could be assumed to be slightly larger than 0.14 g.
3. A collapse can be defined using the parameters axial load, drift ratio, and ductility ratio.
4. Based on the analysis of the Xingfu building, Case C under PGA 0.24 g could be defined as collapsed since the maximum ductility ratio exceeded the limit. Case A and Case C under 0.425 g could also be defined as collapsed since the deformation and ductility ratio exceeded the limit.
5. Based on the analysis of the Weiguan building, Case B under PGA 0.14 g could be defined as collapsed since eleven of its columns suffered axial loads more than their capacity. Case B under 0.425 g could be defined as collapsed since the axial load, ductility ratio, and deformation exceeded the limits.

An Experimental Study of the In-Plane Cyclic Behavior of Steel-Plate Composite Walls with Boundary Elements

Chang-Ching Chang¹, Yin-Nan Huang², Yu-Cheng Cheng³ and Chi-An Ho³

張長菁¹、黃尹男²、鄭與錚³、何其安³

Abstract

This paper summarizes the results of in-plane cyclic tests of three steel-plate composite (SC) walls with boundary elements. The tests were executed in a laboratory at the National Center for Research on Earthquake Engineering (NCREE) in Taiwan. Thick steel plates were used as boundary elements of five specimens. To study two kinds of failure modes, we included in the test 1) four shear-critical walls with aspect ratios of 0.75 and 1.04 and a thicknesses of 3 cm and 5 cm for boundary elements; and 2) one flexure-critical wall with an aspect ratio of 1.22 and a thickness of 2 cm for boundary elements. The failure mode and cyclic behavior of each specimen are reported. The test results are compared with the recommendations of AISC N690s1 and predictions of selected literature data. The impact of wall aspect ratio on in-plane shear strength of SC walls with boundary elements is discussed.

Keywords: steel-plate composite wall; boundary element; cyclic loading test; aspect ratio

Introduction

Steel-plate composite (SC) walls are being constructed in nuclear power plants (NPPs) in the United States and China. These walls are composed of steel faceplates, infill concrete, welded connectors that tie the plates together and provide out-of-plane shear reinforcement, and shear studs that enable composite action of the faceplate and the infill concrete and delay buckling of the faceplate. The use of SC walls in safety-related nuclear facilities in Korea, Japan, and the United States has been studied (e.g., Ozaki et al. 2004, Epackachi et al. 2014, Varma et al. 2014) for the past 20 years. Previously, most numerical studies and experimental investigating SC walls have focused on the elastic range of response, because NPPs remain elastic under shaking up to their design limit. Over the last decade, the nonlinear behavior of SC walls has drawn more and more attention.

A SC wall is very often connected perpendicularly to SC walls at the ends. The perpendicular walls become the boundary elements of the longitudinal wall. Ozaki et al. (2004) and Varma et al. (2014) developed an approach to predict the yield point of an SC wall subjected to an in-plane lateral force using composite shell theory. The approach was

simplified and codified in AISC N690-12s1 (AISC 2015) for the purpose of design. Booth et al. (2015) further proposed that the in-plane shear strength of a SC wall with boundary elements should include two parts: the shear force required to yield the steel plates and an incremental shear resisted by the concrete in diagonal compression up to the failure of the wall. The study on the nonlinear flexural-critical behavior of SC walls with boundary elements is relatively rare.

This paper addresses the inelastic response of three SC walls with boundary elements subjected to reversed, in-plane cyclic loading. In this study, thick steel plates, termed endplates, attached at the ends of a SC-wall specimen are used to represent the boundary elements of the specimen. To study two kinds of failure modes, we included in the test 1) two shear-critical walls with an aspect ratio of 0.75 and a thickness of 3 cm for boundary elements; and 2) one flexure-critical wall with an aspect ratio of 1.22 and a thickness of 2 cm for boundary elements. The following sections of the paper describe the testing program, present key experimental results, and the predictions of the strength of SC walls with boundary elements.

¹ Associate Research Fellow, National Center for Research on Earthquake Engineering

² Associate Professor, National Taiwan University

³ Graduate Student, National Taiwan University

Experimental Program

Five SC walls with boundary elements (SCB1 through SCB5) were constructed and tested under displacement-controlled, reversed cyclic loading. The tests were performed at the National Center for Research on Earthquake Engineering (NCREE) in Taiwan. The design variables considered in the testing program were aspect ratio and concrete strength. The aspect ratios (height-to-length, H/L) are 0.75 (for SCB1 and SCB2) and 1.04 (for SCB3 and SCB4) for the shear-critical walls, and 1.22 for the flexural-critical wall SCB5. To study the impact of concrete strength on the lateral strength of SC walls with boundary elements, we used concretes with significantly different strengths for SCB1 and SCB2 (237 and 431 kgf/cm², respectively). The strength of concrete for SCB5 is similar to that for SC1. Table 1 presents the key parameters for the three specimens.

In Table 1, T is the overall thickness of the wall, t_p is the thickness of each faceplate, $2t_p/T$ is the reinforcement ratio, S/t_p is the slenderness ratio of the faceplate, and tie rods serve as connectors for all three specimens, spaced at distance S . The tie rods had a diameter of 13 mm and a length of 8 cm for all walls, and were fabricated using ASTM A490 carbon steel. The steel faceplates had a thickness of 4.5 mm and were fabricated using JIS G3131 SPHC steel. The thickness of the endplates for SCB1 through SCB3 was 3 cm, SCB4 was 5 cm and SCB5 was 2 cm. All endplates were fabricated using SN490B steel.

Table 1. Test specimen details.

Specimen	Wall dimension ($H \times L \times T$) (cm × cm × cm)	Concrete strength (kgf/cm ²)	Tie rod spacing (cm)	Reinforcement Ratio (%)	End-plate thickness (cm)
SCB1	90×120×25.9	210	11	3.47	3
SCB2	90×120×25.9	350	11	3.47	3
SCB3	104×100×22.5	210	10	4	3
SCB4	104×100×22.5	210	10	4	5
SCB5	146×120×25.9	210	11	3.47	2

Panel (a) of Figure 1 presents an elevation view of SCB1 and SCB2 and panel (b) presents that of SCB5. The base of each wall included a 50-mm thick A572 Gr.50 steel baseplate. Endplates and faceplates of specimens were welded to the baseplate. Two rows of 19-mm diameter headed studs were welded to the baseplate to improve the transfer of shearing and tensile forces. Transverse reinforcement (tie rods) was passed through holes in the embedded sections of the faceplates to further anchor the faceplates.

An optical measurement system, strain gauges, linear variable displacement transducers, and dial gauges were used to monitor the response of the wall piers. Linear variable displacement transducers were attached to the ends of the walls to measure in-plane displacement. The movements of 1) the foundation block relative to the strong floor and 2) the loading

block relative to the specimen were monitored using dial gauges. The trackers of the optical measurement system were attached to one steel faceplate to measure in-plane and out-of-plane deformations. Strain gauges were installed on the other faceplate and both endplates to directly measure strains.

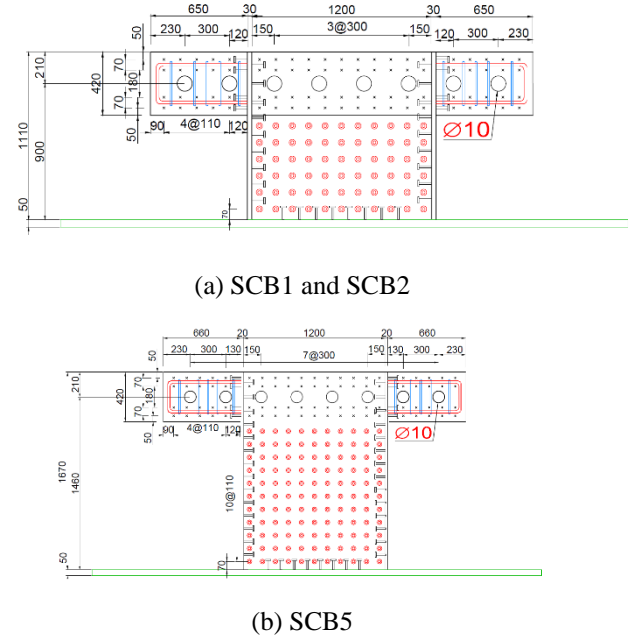


Figure 1. Dimensions of the specimens of this study



Figure 2. SC wall test setup

Experimental Results

Key test results are presented in Table 2. The initial stiffness of the SC wall piers, calculated at drift angles of less than +0.1%, are presented in the column 2 of Table 2(a). The values of the lateral force and drift angle corresponding to the onset of endplate (faceplate) yielding are listed in columns 3 and 4 (columns 5 and 6) of Table 2(a). First yielding of the faceplates was identified using strain gage data. Columns 2 and 3 of Table 2(b) present the lateral force and drift angle corresponding to the onset of faceplate buckling. Columns 4 and 5 of Table 2(b) present the peak loads and the corresponding drift angles in the positive and negative directions. Both the initial stiffness and peak load for SCB2 are greater than those for SCB1 because although the two specimens have the same dimension,

the strength of concrete for SCB2 is greater than that for SCB1. For the four shear-critical walls (SCB1 through SCB4), the yielding of endplates and faceplates occurred at the same time and earlier than the onset of faceplate buckling. For the flexural-critical wall (SCB5), the yielding of faceplates occurred much later than the yielding of endplates since the flexural behavior dominated the demand of the wall.

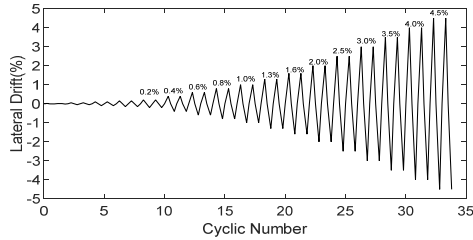


Figure 3. Loading history

Table 2(a). Summary of test results

Specimen	Initial stiffness (ton/cm)	Onset of endplate yielding		Onset of faceplate yielding	
		Load (ton)	Drift ratio (%)	Load (ton)	Drift ratio (%)
SCB1	1333.4	-311.3	0.4	-311.3	0.4
SCB2	1543.7	-338.2	0.4	-338.2	0.4
SCB3	704.3	-289.5	1.0	232.6	0.6
SCB4	735.9	246.6	0.8	230.4	0.4
SCB5	537.8	200.1	0.4	-254.0	1.0

Table 2(b). Summary of test results

Specimen	Onset of faceplate buckling		Peak load	
	Load (ton)	Drift ratio (%)	Load (ton)(+/-)	Drift ratio (%) (+/-)
SCB1	-428.4	1.6	461.5/-449.8	2.0/-2.0
SCB2	497.7	2.0	541.2/-537.2	1.3/-1.6
SCB3	317.1	2.5	324.1/-315.7	2.0/-1.3
SCB4	326.5	2.5	332.3/-330.0	2.0/-2.0
SCB5	-289.0	1.0	336.3/-327.3	2.0/-1.6

Figure 4 illustrates the sequence of damage to the faceplates and endplates of SCB1, including (1) the yielding of the endplates and faceplates, (2) welding rupture between the faceplate and endplate, (3) buckling of the faceplates, and (4) rupture of the faceplates. Figure 5 illustrates the sequence of damage to the faceplates and endplates of SCB5, which is different from that for SCB1 through SCB4, including (1) the yielding of the endplates (first) and faceplates (later), (2) welding rupture between the faceplate and endplate, (3) buckling of the faceplates near the toes of the specimen, and (4) rupture of welding between the endplate and baseplate. The lateral-load capacity of SCB5 dropped significantly after the brittle failure of the welding between the endplate and baseplate, which terminated the test.

A steel faceplate was removed from each of the three specimens for the purpose of documenting damage to the infill concrete. The shear-critical and

flexural-critical walls show entirely different damage mechanism. Panels (a) through (d) of Figure 6 presents the result for SCB1 through SCB4. Infill concrete was severely damaged along the diagonal lines of the specimens. Panel (e) of Figure 6 presents the result for SCB5. Although some diagonal cracks in the lower half of the wall and crushing of concrete near the toes of the wall were observed, most of the infill concrete stayed undamaged.



Figure 4. Sequence of damage of SCB1



Figure 5. Sequence of damage of SCB5

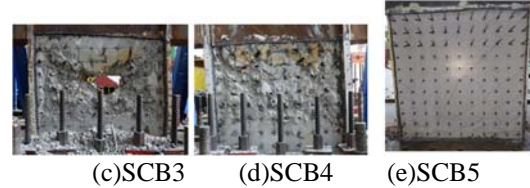
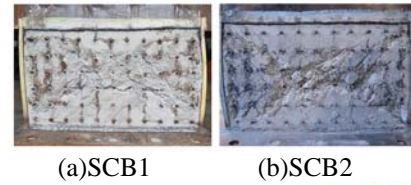


Figure 6. Damage to in-fill concrete after testing

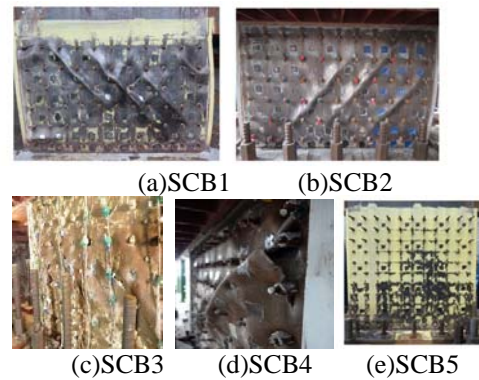


Figure 7. Damage to faceplates after testing

Panels (a) through (d) of Figure 7 present the pictures of faceplates of SCB1 through SCB4 after testing. The faceplates were buckled and ruptured severely. Panel (e) of Figure 7 presents the result for SCB5. Outward buckling of the steel faceplates close to the base of the specimen was observed. The brittle rupture of the welding at the base of the endplates took away the ability of the wall to further dissipate energy.

Figure 8 shows the hysteresis loops for SCB1 through SCB5. SCB1 has the best ductility among the three. The strength of SC1 did not show degradation and the pinching of the loop was not obvious before a draft ratio of 2.5%. Above a draft ratio of 2.5%, the faceplates buckled significantly and could not provide enough confinement to the infill concrete. The strength of SCB1 began to degrade and the pinching in the loop became more obvious. However, the specimen still maintained 80% of its peak lateral-load capacity until a draft ratio of 3.5%. The strength of SCB2 began to degrade immediately after the specimen reached its peak capacity. A possible reason is that the specimen was subjected to higher shear and moment demands than SCB1 and the increasing moment in the specimen reduced its shear capacity. SCB2 maintained 80% of its peak strength until a draft ratio of 3%.

Figure 8 presents the backbone curves of the hysteresis loops. SCB5 has the worst ductility among the five due to the failure mode for the specimen being brittle failure of the welding at the bottom of the endplates.

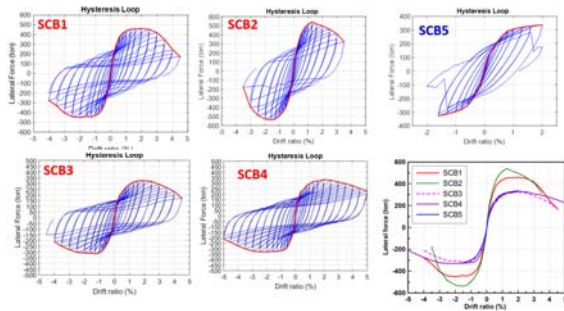


Figure 8. Lateral loading-displacement behavior of the three SC wall specimens from this study

Prediction of the Strength of SC Walls with Boundary Elements

(1) Shear-Critical SC Walls

As described earlier, Booth et al. (2015) proposed that the in-plane shear strength of a SC wall with boundary elements should include two parts: the shear force required to yield the steel plates (V_y) and an incremental shear resisted by the concrete in diagonal compression up to the failure of the wall (ΔV). The authors of this paper evaluated the effectiveness of the model using experimental data from the literature and found that the model can be further improved by taking into account the impact of the aspect ratio of a wall. The results (termed V_{ub}'') are presented in Table 3.

(2) Flexural-Critical SC Walls

Table 4 presents the peak strength of SCB5 from the test (V_{exp}) and the prediction of simple section analysis using XTRACT software (V_{XTRACT}). The value of V_{XTRACT} was computed using the moment capacity of the section of SC3 divided by the height of the specimen. The ratio of V_{exp} to V_{XTRACT} for SCB5 is 1.02. The strength of flexural-critical SC walls can be predicted using section analysis.

Table 3. Test results and model predictions on the strength of SCB1 through SCB4.

Specimen	H/L	f'_c (kgf/cm ²)	V_{exp} (ton)	V_{ub} (ton)	V_{exp}/V_{ub}	V_{ub}' (ton)	V_{exp}/V_{ub}'
SCB1	0.75	237	461	397	1.16	449	1.03
SCB2	0.75	431	541	490	1.11	554	0.98
SCB3	1.04	271	324	323	1.00	318	1.02
SCB4	1.04	289	332	331	1.00	325	1.02

Table 4. Experimental and results calculated using XTRACT on the strength of SCB5.

Specimen	V_{exp} (ton)	XTRACT	
		V_{XTRACT} (ton)	$\frac{V_{exp}}{V_{XTRACT}}$
SCB5	336	330	1.02

Conclusions

1. The shear-critical specimens of this study demonstrated very ductile behavior. Both specimens retained 80% of their peak capacity up to a drift ratio of 3%.
2. The model of Booth et al. (2015) for predicting the shear strength of a shear-critical SC wall with boundary elements can be improved by taking into account the aspect ratio of the wall.
3. The lateral-load strength of a flexural-critical SC wall can be accurately predicted using section analysis.

References

- AISC (2015). "Specification for safety-related steel structures for nuclear facilities, Supplement No. 1." N690s1, American Institute of Steel Construction, Chicago, IL.
- Ozaki, M., Akita, S., Osuga, H., Nakayama, T., Adachi, N. (2004). "Study on steel plate reinforced concrete panels subjected to cyclic in-plane shear." *Nuclear Engineering and Design*, 228, 225–244.
- Varma, A. H., Malushte, S., Sener, K., Lai, Z., (2014). "Steel-plate composite (SC) walls for safety-related nuclear facilities: design for in-plane force and out-of-plane moments." *Nuclear Engineering and Design*, 269, 240–249.
- Booth P., Varma, A.H., and Seo, J., (2015). "Lateral load capacity of steel plate composite wall structures." *SMIRT23*, Manchester, United Kingdom.

Seismic Health Monitoring of Space RC Frame Structure Using Piezoceramic-based Sensors

Wen-I Liao¹, Juin-Fu Chai² and Tsung-Jen Teng²

廖文義¹、柴駿甫²、鄧崇任²

Abstract

In this study, a piezoceramic-based active sensing system was used for the health monitoring of a two story on bay space reinforced concrete (RC) frame structure under earthquake excitations. The RC moment frame instrumented with piezoceramic-based sensors was tested by using shake table with different ground excitation intensities. The distributed sensors embedded in the RC structures were used to monitor the health status of the structures during the tests. The sensitiveness and effectiveness of the proposed piezoceramic-based approach were investigated and evaluated by analyzing the measured piezoelectric signals.

Keywords: health monitoring, piezoceramic, reinforced concrete, shake table, sensor

Introduction

Structural health monitoring of RC structures under seismic loads or impacts has attracted attention in the earthquake engineering research community. Throughout the life cycle of a concrete structure, many important issues should be addressed to ensure the safe operation of these structures. During the service life of a structure, it is important to perform structural health monitoring to detect the damage status or health status after an earthquake event. Currently, the state of structural safety of the majority of civil structures is assessed by means of visual inspections and nondestructive evaluations (NDE) for local monitoring, performed by engineers. The main limitation of visual inspection and some of the traditional approaches is that they require access to the potentially damaged regions of the structure, which may be dangerous or not possible to access. In recent years, piezoelectric materials have been successfully applied to the health monitoring of concrete structures due to their advantages of active sensing, low cost, quick response, availability in different shapes, and simplicity for implementation.

There have two major categories of piezoelectric-based health monitoring. The first one is the impedance-based approach, in which the impedance of piezoelectric transducers is applied to the health

monitoring of structures. One of the successful applications of the impedance-based health monitoring was firstly reported by Sun *et al.* (1995) who have conducted an automated real-time health monitoring on an assembled truss structure. Although the impedance-based approach is difficult to identify the distribution and severity of a large damage region, the advantage of the impedance based approach is that the knowledge of the modal parameters or other failure information of the structure is not required. Besides, other successful implements of the impedance-based method to the health monitoring of concrete structures were performed by Ayres *et al.* 1998, Soh *et al.* 2000, and Tseng and Wang 2004. The second approach of piezoelectric-based health monitoring is the wave-based health monitoring approach (Saafi and Sayyah 2001), in which the wave-propagation properties are studied to detect and evaluate the cracks and damages inside the concrete structures. Wang *et al.* (2001) studied the debonding behavior between steel rebar and concrete using the PZT (lead zirconate titanate) patches fixed on the rebar. Sun *et al.* (2008) used the PZT patch transducer to initiate and receive the elastic waves in the concrete, and obtained the modulus of elasticity utilizing the wave propagation characteristics. Gu *et al.* (2006) and Song *et al.* (2007) developed smart aggregate (SA), an innovative multifunctional piezoceramic based device, to perform structural health monitoring for concrete structures.

¹ Professor, National Taipei University of Technology, and Research Fellow, National Center for Research on Earthquake Engineering

² Research Fellow, National Center for Research on Earthquake Engineering

The smart aggregates have also been utilized in the structural health monitoring of a two-story concrete frame structure (Gu *et al.*, 2007) under monotonic pushover test. Using the piezoceramic-based sensors, Liao *et al.* (2008) conducted the dynamic stress measurement and health monitoring of single concrete column subjected to shake table excitation with gradually increased ground acceleration. Using the post-embedded piezoceramic-based sensors, Liao *et al.* (2011) also conducted the on-situ health monitoring of large-scale RC piers of an existing bridge in Taiwan under cyclic loading reversals.

From the aforementioned successful applications of health monitoring using piezoelectric based sensors, it is found that most of the applications were conducted for the single element specimens under quasi-static loading condition. The study on the health monitoring of concrete frame structures subjected to shake table excitation is relatively few. In this paper, piezoelectric based-smart aggregates are adopted to form a distributed intelligent sensor network to perform structural health monitoring for concrete frame structures after earthquake excitation. A RC frame was tested using a shake table with different excitation intensities. Through a series of shaking table tests, the local damage status was identified from the response measurements. The intensity-scaled ground motion TCU078 recorded during the 1999 Taiwan Chi-Chi earthquake was used as the excitation. The experimental results demonstrate the sensitiveness and the effectiveness of the proposed piezoceramic-based approach in the structural health monitoring of the RC structures under the shake table excitation.

Experimental Setup

A two stories one bay reinforced concrete frame was designed with reinforcement details satisfying the seismic ductile requirements of Taiwan Building Code. The dimension of the RC frame structure is shown in Fig. 1, and the test setup is illustrated in Fig. 2. The span lengths in longitudinal and transverse directions are 182 cm and 114 cm, respectively, and the story height is 98 cm. Seismic reactive mass is simulated by lead blocks with a weight of 2.0 metric tons (19.6 kN) added to the each floor of the specimen. The cross sections of the column and beam are 18x18cm and 16x18cm, respectively. The input ground acceleration history for all tests is the E-W component of TCU078 station recorded during the 1999 Taiwan Chi-Chi earthquake. The frame is tested with different ground excitation intensities as given in Table 1. White noise excitation is used to investigate the frequency change of each test before and after the earthquake excitation. The first modal frequency in shake direction of the test frame before the tests was 12 Hz, after the final run of the shake table test, the modal frequency of the specimen was 4.8 Hz.

In this experimental study, PZT type piezoceramic patches are embedded in a half-inch cube of cement mortar and are referred to as smart aggregate. Piezoceramic patches are very fragile and can be easily damaged by the vibrator during the casting of concrete structures. In order to protect the fragile piezoelectric transducer, the piezoceramic patch is coated with bitumen to prevent water and/or moisture damage, and then embedded into a small concrete block to form a smart aggregate as shown in Fig. 3. Fig. 4 shows the embedded locations of smart aggregates in the test frame specimen. A total number of 10 smart aggregates are fixed with the rebar cage at predetermined locations before casting of the concrete structure. The smart aggregates numbered with “S” are used as sensors, and smart aggregates numbered with “A” are employed as actuators. From the arrangement of sensors (S1-S6) and actuators (A1-A4) shown in Figure 4, the monitoring by sensors located in the beams and columns can be used to justify the health status of the entire frame structure.

The piezoelectric strain constant (coefficient for direct piezoelectric effect in the normal direction of PZT patch) and the piezoelectric voltage constants of the PZT patches used as sensors and actuators obtained from the catalogue are shown in Table 2. A NI (National Instrument, Inc.) system is used to generate the excitation source signal for the actuator and to record signals from the sensors. The single frequency sinusoidal signals all with duration of 10 seconds and frequencies of respectively 100 Hz, 1 kHz and 5 kHz are used as the excitation sources for the smart aggregate actuator. The adopted smart aggregate sensing unit has the advantage of low cost and active sensing. Active sensing will allow one smart aggregate to be actively excited by a desired wave form so that other distributed smart aggregates are able to detect the responses. By analyzing the sensor signals, many important properties of the structures such as the severity of cracking and damage status can then be monitored and evaluated.

Table 1. Input PGA and identified frequencies

Run No.	Input PGA(g)	Identified Frequency after test run (Hz)	Maximum roof displacement (cm)
0	0.22	12.0	0.16
1	0.44	10.5	0.34
2	1.06	8.0	1.73
3	1.41	7.5	2.16
4	1.79	4.8	3.53

Table 2. The piezoelectric constants

function	PZT strain constant d_{33}	PZT voltage constants g_{33}
Sensors	430×10^{-12} m/V	25×10^{-3} V-m/N
Actuator	650×10^{-12} m/V	14×10^{-3} V-m/N

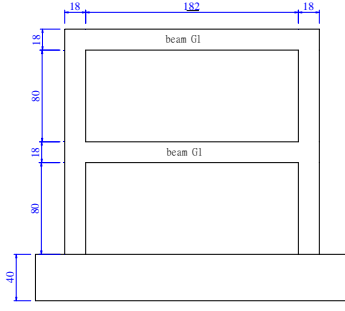


Fig. 1. Dimensions of the specimen (unit: cm)



Fig. 2. Test set-up of the experiment.

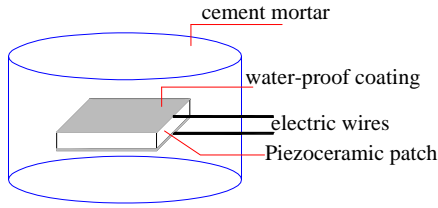


Fig. 3. Illustration of the smart aggregates

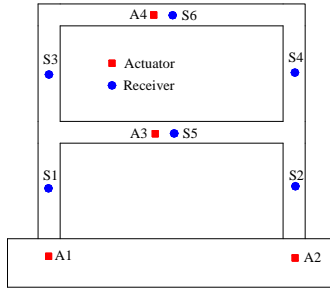


Fig. 4. Locations of actuators and sensors.

Health Monitoring and Test Results

The operating principle of the smart sensing system is that one smart aggregate is used as an actuator to generate excitation waves; other distributed smart aggregates are used as sensors to detect the response. Cracks or damages in the concrete structure acted as stress relief in the wave propagation path, and the energy of the propagation waves will be attenuated due to the existence of cracks. The drop value of the transmission energy will be correlated with the severe degree of damages inside. The transmission energy of smart aggregate sensor is calculated as

$$E = \int_{t_0}^{t_f} u^2 dt \quad (1)$$

where t_0 , t_f are respectively the starting time and end time of recording, and u is the sensor voltage. Using Eq. (1), the energy E_h is calculated when the structure is undamaged or healthy, and the energy for the damage status of specimen i is denoted as E_i . The damage index for specimen i is defined as

$$I = \frac{|E_h - E_i|}{E_h} \quad (2)$$

The proposed damage index simply represents the transmission energy loss caused by structural damage. When the damage index is close to 0, the structure is considered to be in a healthy condition. When the damage index is very close to 1, it means the concrete structure is near complete failure.

The input ground acceleration history for all tests is the E-W component of TCU078 station recorded during the 1999 Taiwan Chi-Chi earthquake. A sequence of dynamic tests up to a total of five test runs was applied to the specimen with gradually increased excitation intensities. The RC frame is tested with different ground excitation intensities as given in Table 1. Some cosmetic cracking was observed in the frame during the second test run. The concrete cracks continued to develop during the third test run. Concrete spalling and large shear cracks occur at the fourth test run. Fig. 5 shows the photo of the damage status of the specimen after fourth test run in which the concrete spalled at the beam column joint and steel bars buckled slightly.

After each test run of the shake table tests, the smart aggregates were utilized for the structural health monitoring of the concrete frame. The PZT A1-A4 shown in Fig. 4 behaving as actuators are used to send the stress waves of frequencies 100Hz, 1 kHz and 5 kHz, respectively, and PZT sensors (S1-S6) located in the columns and beams are employed to receive the stress waves. The proposed damage index is utilized in the structural health monitoring of tested RC frame panel. Due to the health monitoring results by excitation frequencies 100 Hz and 5 kHz are similar to the results of 1 kHz, only the results from excitation frequency 1 kHz are presented in this paper. The damage index of sensors is shown in Fig. 6 in which, the sensors PZT-S1 to S6 are numbered from 1 to 6. From the figure, the damage indices of each PZT sensor have an increased trend that reveals the increased severity of damage of the RC frames. The results have validated the effectiveness of the proposed damage index matrix for evaluating the severity of the damage of the frame structure. In additional, from Table 1 knowing that the natural frequency of the frame structure has a little bit decrease after the first test run. The change of natural frequency means the structure have some very slightly cracks generated in the structure during the test run.

But from the inspection after first test run there was no cracks can be observed. This demonstrates that the very slight cracks can be detected by piezoelectric sensor due to the high frequency response properties.



Fig. 5. Failure mode of the frame specimen.

Conclusions

To study the health monitoring of concrete structures under seismic excitations, a RC frame was fabricated and tested by a recorded earthquake ground motion. The multi-functional transducer device, the smart aggregate, is used in the structural health monitoring test. From the experimental results, the smart aggregate-based sensors demonstrated their capability in monitoring and predicting the health status of the tested frames through the proposed damage index matrix. Therefore, the smart aggregate-based sensor has a high potential for practical implementation to concrete frame structures for health monitoring. The advantages of piezoelectric sensors compare with conventional system are active sensing, low cost, availability in different shapes of structures, and simplicity for implementation. In additional, the very slight cracks can be detected by piezoelectric sensor due to the high frequency response properties.

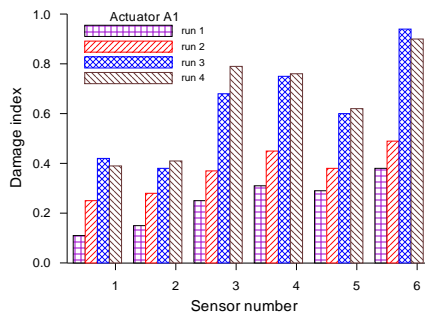


Fig. 6(a). Damage index of sensors excited by actuator A1 with frequency 1 kHz.

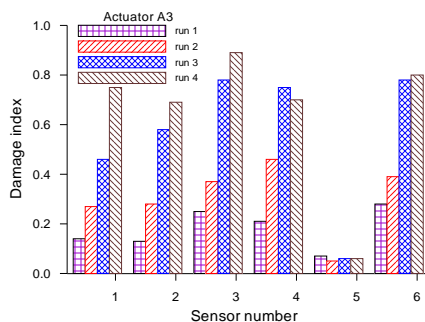


Fig. 6(b). Damage index of sensors excited by actuator A3 with frequency 1 kHz.

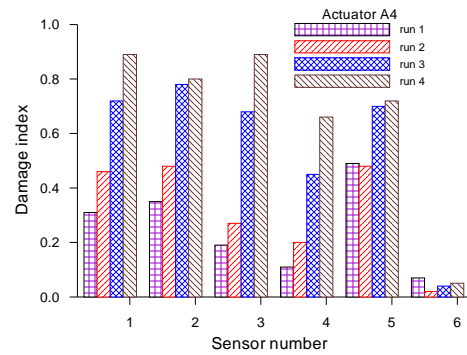


Fig. 6(c). Damage index of sensors excited by actuator A4 with frequency 1 kHz.

References

- Ayres J.W., Lalande F., Chaudhry Z. and Rogers C., (1998), "Qualitative impedance-based health monitoring of civil infrastructures", *Smart Materials and Structures*, vol.7, no. 5 , 1998, pp. 599-605
- Gu, H., Song, G., Dhonde, H., Mo, Y.L. and Yan, S., (2006), "Concrete early-age strength monitoring using embedded piezoelectric transducers", *Smart materials and structures*, 15, 1837–1845.
- Gu H, Olmi C, Araghdeep L and Mo YL., (2007) Structural health monitoring of a reinforced concrete frame using piezoceramic based smart aggregates SMSST007: World Forum on Smart Materials and Smart Structures Technology (Chongqing).
- Liao W.I., Gu H, Olmi C, Song G, and Mo Y.L., (2008), "Structural Health Monitoring of a Concrete Column Subjected to Shake Table Excitations Using Smart Aggregates", 2008 ASCE Earth & Space Conference, March 3-5, 2008, Long Beach, CA, USA.
- Liao W.I., Wang J.X., Song G, Gu H., Olmi C, Mo Y.L., Chang K.C., and Loh C.H. (2011), "Structural Health Monitoring of Concrete Columns Subjected to Seismic Excitations Using Piezoceramic-based Sensors", *Smart Materials and Structures*, Vol. 20, 125015.
- Saafi M. and Sayyah T., (2001), "Health monitoring of concrete structures strengthened with advanced composite materials using piezoelectric transducers", *Composites Part B: Engineering*, vol. 32, no.4, pp. 333-342
- Soh C. H., Tseng K.K., Bhalla S. and Gupta A., (2000), "Performance of smart piezoceramic patches in health monitoring of a RC bridge", *Smart materials and Structures*, vol. 9, no. 4, pp.533-542.
- Song G., Gu H., Mo Y. L., Hsu T., and Dhonde H., (2007) "Concrete structural health monitoring using embedded piezoceramic transducers", *Smart Materials and Structures*, vol. 16, pp. 959-968.

Structural Health Monitoring for Local Damages of RC Walls using Piezoceramic-Based Sensors under Seismic Loading

Wen-I Liao¹, Juin-Fu Chai², Wen-Yu Jean² and Tsung-Jen Teng²

廖文義¹、柴駿甫²、簡文郁²、鄧崇任²

Abstract

Structural health monitoring of reinforced concrete (RC) structures under seismic loads have recently attracted dramatic attention in the earthquake engineering research community. In this study, reversed cyclic loading test of structural health monitoring of RC shear walls using piezoceramic(PZT)-based sensors are presented. The piezoceramic-based sensors called “smart aggregate(SA)”, was pre-embedded before casting of concrete and adopted for the structural health monitoring of the RC shear wall under seismic loading. Two RC walls were adopted in this test, one is the wall having damages in the boundary columns and foundation of the specimen, and the other is the wall having damages in the upper part of the wall panel. During the test, SAs embedded in the foundation were used as actuators to generate propagating waves, and the other selected SAs were used to detect the waves. By analyzing the wave response, the existence and locations of cracks and damages can be detected and the severity can be estimated. The experimental results demonstrate the sensitiveness and the effectiveness of the piezoceramic-based approach in the structural health monitoring and the identification of damage locations of shear governed concrete structures under seismic loading.

Keywords: health monitoring, piezoceramic, sensor, reinforced concrete wall, seismic loading

Introduction

During the service life of a structure, it is important to perform structural health monitoring to detect the damage status or health status after an earthquake event. In recent years, piezoelectric materials have been successfully applied to the health monitoring of concrete structures due to their advantages of active sensing, low cost, quick response, availability in different shapes, and simplicity for implementation.

Song *et al.* (2007) developed smart aggregate (SA), an innovative multifunctional piezoceramic based device, to perform structural health monitoring for concrete structures. The smart aggregates have also been utilized in the structural health monitoring of a two-story concrete frame structure (Gu *et al.*, 2007) under monotonic pushover test. Using the piezoceramic-based sensors, Liao *et al.* (2008) conducted the dynamic stress measurement and health monitoring of single concrete column subjected to

shake table excitation with gradually increased ground acceleration. Using the post-embedded piezoceramic-based sensors, Liao *et al.* (2011) also conducted the on-situ health monitoring of large-scale RC piers of an existing bridge in Taiwan under cyclic loading reversals.

From the aforementioned successful applications of health monitoring using piezoelectric based sensors, it is found that most of the applications were conducted for the single column or frame specimens under seismic loading. The study on the health monitoring of concrete shear wall structures subjected to seismic loading is relatively few. In this paper, piezoelectric based smart aggregates (SAs) are adopted to form a distributed intelligent sensor network to perform structural health monitoring and local damage detecting for concrete wall structures after seismic loading. Two reinforced concrete walls were tested under reversed cyclic loading, one is the wall specimen having damages in the boundary columns and foundation of the specimen and the other

¹ Professor, National Taipei University of Technology, and Research Fellow, National Center for Research on Earthquake Engineering

² Research Fellow, National Center for Research on Earthquake Engineering

is the wall specimen having damages in the upper part of the wall panel. During the test, SAs embedded in the foundation were used as actuators to generate propagating waves, and the other selected SAs were used to detect the waves. By analyzing the wave response, the existence and locations of cracks and damages can be detected and the severity can be estimated.

Experimental Setup

Two low-rise shear wall specimens, SW1 and SW2, were tested under the reversed cyclic loading. The specimen SW1 has the dimensions of 300 cm in height, 420 cm in length, and 20 cm in thickness. The reinforcement is provided by D13 steel bars in the wall panel with a spacing of 20 cm. The specimen SW2 has the dimensions of 300 cm in height, 300 cm in length, and 18 cm in thickness, and the reinforcements in the wall panel of SW2 is same as SW1. The wall specimens SW1 and SW2 were designed with a 30 by 50 cm boundary column. The dimensions of the wall panel and steel arrangements of the boundary columns and beams are shown in Fig. 1 and Fig. 2, respectively. The average concrete compressive strengths of the wall panel, boundary column and foundation are shown in Table 1. Due to the low concrete strength of the foundation and boundary column of the specimen SW1, this specimen was damaged in the foundation and in the bottom parts of the boundary columns during the test. For the specimen SW2, it was firstly damaged in the upper part of the panel due to the shear friction failure between the top beam and the panel, and finally caused the crush of concrete in the boundary columns.

Table 1. Compressive strength of concrete (Mpa)

specimen	foundation	Column	Wall panel
SW1	116	137	259
SW2	243	196	218

Piezoceramic patches are very fragile and can be easily damaged by the vibrator during the casting of concrete structures. In order to protect the fragile piezoelectric transducer, the piezoceramic patch is coated with insulation (bitumen) to prevent water and/or moisture damage, and then embedded into a small concrete block to form a smart aggregate as shown in Fig. 3. The smart aggregates are embedded at the predetermined distributed locations before casting. Fig. 4 shows the embedded locations of smart aggregates in the test wall specimens. A total number of 9 smart aggregates for each wall specimen are fixed with the rebar cage at predetermined locations before casting of the concrete structure. The smart aggregates in the top beam and in the middle height position of the wall are used as sensors, and smart aggregates in the foundation are employed as actuators. From the arrangement of sensors (S1-S6) and actuators (A1-A3) shown in Fig. 4, the monitoring

by sensors located in the top beam and in the wall panel can be used to justify the health status and the damage places of the entire wall structure.

A NI (National Instrument, Inc.) system is used to generate the excitation source signal for the actuator and to record signals from the sensors. The single frequency sinusoidal signals all with duration of 10 seconds and frequencies of 100 Hz, 1 kHz and 5 kHz, respectively, and 10V amplitude are used as the excitation sources for the smart aggregate actuators. The selected excitation frequency range might cover the low to high frequency responses and could detect the possible damages. The adopted smart aggregate sensing unit has the advantage of low cost and active sensing. Active sensing will allow one smart aggregate to be actively excited by a desired wave form so that other distributed smart aggregates are able to detect the responses. By analyzing the sensor signals, many important properties of the structures such as the severity of cracking and damage status can then be monitored and evaluated.

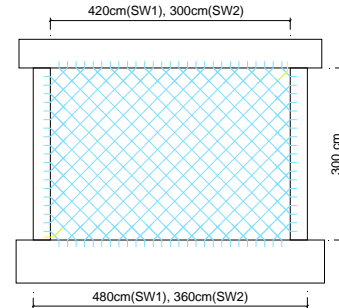


Fig. 1. Dimensions of the specimen (unit: cm)

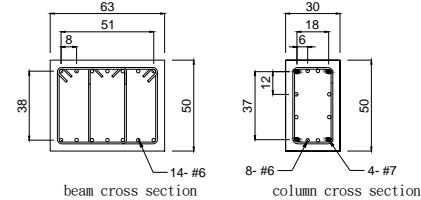


Fig. 2. Reinforcements of column and beam (cm)

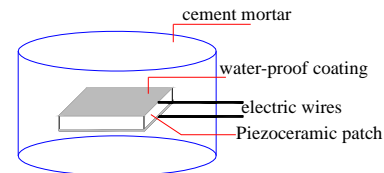


Fig. 3. Illustration of the smart aggregates

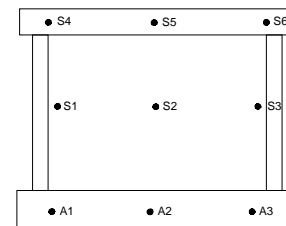


Fig. 4. Locations of actuators and sensors.

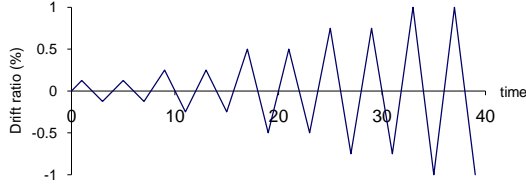


Fig. 5. Loading history of the test.

Health Monitoring and Test Results

Cracks or damages in the concrete structure acted as stress relief in the wave propagation path, and the energy of the propagation waves will be attenuated due to the existence of cracks. The drop value of the transmission energy will be correlated with the severe degree of damages inside. The transmission energy of smart aggregate sensor is calculated as

$$E = \int_{t_0}^{t_f} u^2 dt \quad (1)$$

where t_0 , t_f are respectively the starting time and end time of recording, and u is the sensor voltage. Using Eq. (1), the energy E_h is calculated when the structure is undamaged or healthy, and the energy for the damage status of specimen i is denoted as E_i . The damage index for specimen i is defined as

$$I = \frac{|E_h - E_i|}{E_h} \quad (2)$$

The proposed damage index simply represents the transmission energy loss caused by structural damage. When the damage index is close to 0, the structure is considered to be in a healthy condition. When the damage index is very close to 1, it means the concrete structure is near complete failure.

The specimens were tested under displacement control according to a predetermined displacement history. The displacement control scheme in terms of drift ratio of the reversed cyclic tests is shown in Fig. 5. The drift ratio is defined as the value of drift displacement expressed as a percentage of the height of the wall. Two reversed cycles of each of the predetermined displacement amplitudes were applied. For the specimen SW1, slight cracks have been observed at a drift ratio of 0.25% (drift=7.5mm). Cracks developed horizontally at the bottom parts of boundaries due to bending, and the cracks were distributed uniformly in the region of wall panel at an inclination angle close to 45 degrees approximately. A similar pattern of cracking occurred in the specimen when the drift ratio of the specimen was 0.5%. The number of cracks on the wall panel remained almost the same as previously drift ratio. But due to the concrete strengths of foundation and boundary column are relatively lower than the concrete strength of wall panel, there was slight spalling of the concrete cover at the bottom boundary column and foundation. The

failure of the specimen took place when the drift ratio was increased to 1.0% as shown in Fig. 6. Concrete at the bottom of boundary column and foundation crushed in the second cycle of 1.0% drift ratio.



Fig. 6. Failure mode of the specimen SW1.



Fig. 7. Failure mode of the specimen SW2

After reaching each test drift ratio of the reversed cyclic loadings, the smart aggregates were utilized for the structural health monitoring of the concrete frame. Firstly, the SA sensor A1 shown in Fig. 4 behaving as actuators are used to send the stress waves with frequencies $f = 100\text{Hz}$, 1 kHz and 5 kHz , respectively, and SA sensors S1 and S4 located in the wall panels and beams are employed to receive the stress waves. The proposed damage index is utilized in the structural health monitoring to identify the damage status in the propagation path from A1 to S4. Secondly, A2 used as actuator, and S2 and S5 used as sensors to identify the damages in the path from A2 to S5. Finally, A3 used as actuator to identify the damages in the path from A3 to S6. Due to the health monitoring results by excitation frequency 5 kHz is similar to the results by 1 kHz , only the results from excitation frequency 100Hz and 1 kHz are presented in this paper.

The damage indices of sensors of SW1 at different drift ratios are shown in Fig. 8(a) and 8(b) for excitation frequency $f = 100\text{ Hz}$ and 1 kHz , respectively, in which, the SA sensors S1 to S6 are numbered from 1 to 6. From these figures, the damage indices of each SA sensor in different excitation frequency all have an increased trend as the drift is increased, that reveals the increased severity of damage of this RC wall specimen. In Fig. 8(b), the damage indices of sensors SA1, SA4, SA3 and SA6 at drift ratio 1.0% are relatively higher than those indices of SA2 and SA5, this means the damage status in the two sides of the wall are more serious than the center part, and this result truly reflects the final failure pattern of the specimen, crush of concrete at bottom boundary columns. Although the damage indices excited by frequency 100 Hz (Fig. 8a) cannot identify the places which having seriously damage as Fig. 8(b), the results also reveals the increased severity of damage of the entire wall specimen. In conclusion, the experimental results have validated the effectiveness of the proposed damage index matrix for evaluating the severity of the damage of the wall structure, and having the ability to identify the seriously damaged places by high frequency excitation waves.

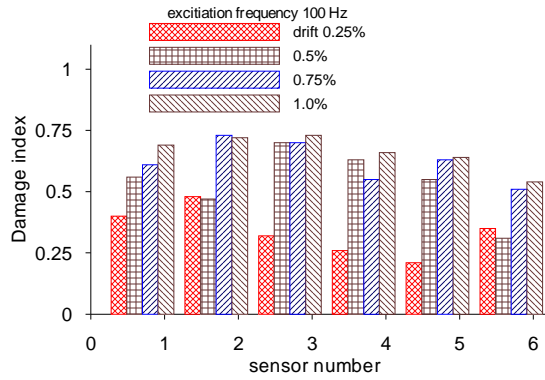


Fig. 8(a). Damage indices of sensors of specimen SW1 for excitation frequency 100 Hz.

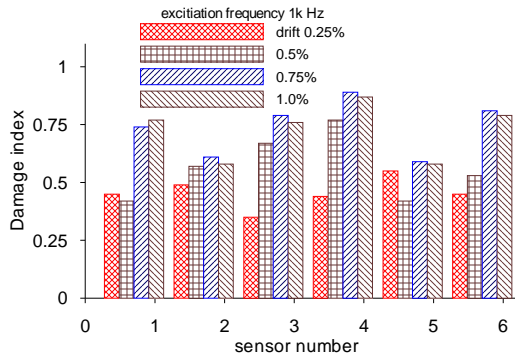


Fig. 8(b). Damage indices of sensors of specimen SW1 for excitation frequency 1 kHz.

The test results of specimen SW2 at different drift ratios are shown in Fig. 9(a) and 9(b) for excitation frequency $f = 100$ Hz and 1k Hz, respectively. Similar to Fig. 8, in these figures, the damage indices of each SA sensor also have an increased trend as the drift ratio is increased. In Fig. 9(b), the damage indices of sensors SA4 to SA6 at the final drift ratio 1.0% are relatively higher than those indices of SA1 to SA3, this means the damage status in the top part of the wall are serious than the bottom part, this result reflects the final failure pattern of the specimen, spalling of concrete on wall panel top and crush of concrete at top boundary columns.

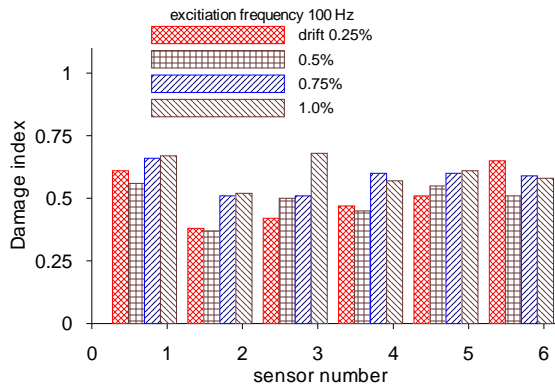


Fig. 9(a). Damage indices of sensors of specimen SW2 for excitation frequency 100 Hz.

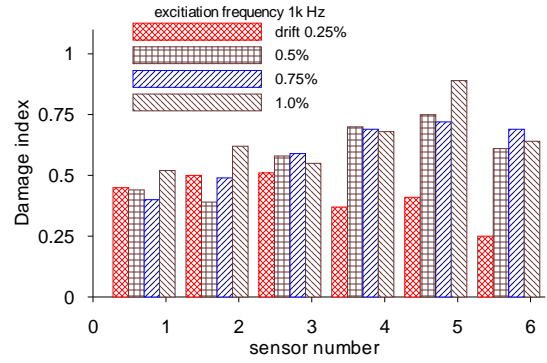


Fig. 9(b). Damage indices of sensors of specimen SW2 for excitation frequency 1 kHz.

Conclusions

Two reinforced concrete walls were fabricated and tested under reversed cyclic loading conditions. The multi-functional transducer device, the smart aggregate, is used in the structural health monitoring and local damages detection test. From the experimental results, the smart aggregate-based sensors demonstrated their capability in monitoring and predicting the health status of the tested specimens through the proposed damage index matrix. Therefore, the smart aggregate-based sensor has a high potential for practical implementation to concrete wall structures for health monitoring. The advantages of piezoelectric sensors compare with conventional system are active sensing, low cost, availability in different shapes of structures, and simplicity for implementation.

References

- Gu H, Olmi C, Araghdeep L and Mo YL., (2007) Structural health monitoring of a reinforced concrete frame using piezoceramic based smart aggregates SMSST007: World Forum on Smart Materials and Smart Structures Technology (Chongqing).
- Liao W.I., Gu H, Olmi C, Song G, and Mo Y.L., (2008), "Structural Health Monitoring of a Concrete Column Subjected to Shake Table Excitations Using Smart Aggregates", 2008 ASCE Earth & Space Conference, March 3-5, 2008, Long Beach, CA, USA.
- Liao W.I., Wang J.X., Song G, Gu H., Olmi C, Mo Y.L., Chang K.C., and Loh C.H. (2011), "Structural Health Monitoring of Concrete Columns Subjected to Seismic Excitations Using Piezoceramic-based Sensors", Smart Materials and Structures, Vol. 20, 125015.
- Song G., Gu H., Mo Y. L., Hsu T., and Dhonde H., (2007) "Concrete structural health monitoring using embedded piezoceramic transducers", Smart Materials and Structures, vol. 16, pp. 959-968.

Application of Metadata Technology for a Bridge Management System

Chun-Chung Chen¹, Chia-Chuan Hsu¹, Kuang-Wu Chou¹, Hsiao-Hui Hung²,
Yu-Chi Sung³ and Kuo-Chun Chang⁴

陳俊仲、許家銓、周光武、洪曉慧、宋裕祺、張國鎮

Abstract

In the past few decades, increasing attention has been paid to achieving longevity of infrastructure. The long-term environmental factors such as chloride invasion and carbonation penetration that are detrimental to concrete cause reinforcement corrosion and shorten the service time of bridge structures, resulting in a gradual deterioration of their structural performance. Our previous study showed the relationship between structural performance and service time and provided a prediction of the time point for the maintenance or retrofit of structures that perform below the threshold values. In this study, we present a novel lifecycle-based bridge management system (BMS) with an extendable structure which uses a novel technology known as “metadata”. Metadata enables the integration of all bridge inspection records and evaluation results in photos captured onsite. In other words, by superimposing data layers, a single photo capable of storing complete information related to bridge status could be created. Therefore, different photos taken at different time points constitute a resume of the bridge status. Accordingly, we can record and qualitatively and quantitatively evaluate the time history of the bridge status by considering material deterioration. Hence, the lifecycle-based BMS can effectively facilitate the data mining of inspection and evaluation and help in simplifying the decision making for maintenance efforts, to address the long-term problem of the deterioration of bridges. The proposed system is expected to be helpful for earthquake mitigation strategies in the future.

Keywords: bridge management system, metadata

Introduction

With the increasing number of natural disasters reported worldwide, the structural safety of infrastructure has been gaining increasing attention from both the government and the public. Bridges are the most crucial transportation infrastructure required for catering to the rapidly developing economy of Taiwan. Therefore, ensuring the structural safety of bridges is one of the primary public concerns in Taiwan. The subtropical, warm, and wet climate of Taiwan easily cause material deterioration, significantly reducing the service time of bridges. Also, Taiwan suffers from frequent earthquakes as it is situated in a

collision zone between the Philippine Sea and the Eurasian tectonic plates. Frequent earthquakes have inevitably caused significant damage to existing bridges, leading to considerable loss of human lives as well as a hindrance to rescue efforts, thereby incurring large-scale economic and social losses.

An efficient bridge management system (BMS) is crucial to increase the resilience of bridges after a disaster. This study introduces a new life-cycle-based BMS in Taiwan that can effectively manage problems such as material deterioration and damage caused by earthquakes and floods. The system is expected to benefit authorities in the decision-making process

¹ Associate Researcher Fellow, National Center for Research on Earthquake Engineering

² Research Fellow, National Center for Research on Earthquake Engineering

³ Division Director, National Center for Research on Earthquake Engineering, Professor, Department of Civil Engineering, National Taipei University of Technology

⁴ Professor, Department of Civil Engineering, National Taiwan University

regarding bridge maintenance.

Previous studies (Sung et al. 2010, 2011) have demonstrated methods to obtain the relationship between structural performance and service time and predict the time point for maintenance or retrofit when structural performance is below the threshold values. Based on those methods, the qualitative and quantitative evaluation of the time history of the bridge status, while considering material deterioration, can be performed. Consequently, the lifecycle-based BMS is developed. Accurate records of bridge inspection work would help engineers update the condition of the bridge structure, which will further benefit effective structural safety evaluation. In the proposed system, “metadata” is adopted to integrate all the available bridge inspection records as well as the evaluation results in photos captured onsite. Complete information of the bridge status for different periods of its lifecycle can be preserved; in other words, the whole resume of the bridge status can be established, thus enabling lifecycle-based bridge maintenance. The developed system can improve the efficiency and quality of bridge inspection work, facilitating an easier and more accurate evaluation of bridge safety.

Framework of the System

In general, a bridge’s lifecycle can be divided into four stages: planning, design, construction, and maintenance. Activities performed on the bridge during the maintenance stage, the longest in the total structural service time, play a significant role to ensure that the bridge functions with the qualified structural safety performance and satisfactory service quality. The framework of the developed BMS focuses on the maintenance stage and includes three main technical parts with cooperative functionalities (Thompson, P. D. & Kerr, B. 1998). The first part is the modularization function that involves the network, project, and element levels of data according to the different methods of management and applications.

The second functional part is the information database that stores bridge inspection data. The design principle of this part is customization functions and its system design frame focuses on Model, View, and Controller; thus, it is abbreviated as MVC. The MVC design frame, based on Microsoft ASP.NET, reduces the component coupling between each part of the components in the system, thereby raising the system’s capability to be extended flexibly. The tools used for data processing are MySQL Database and CouchDB, which can flexibly substantiate the table–column object in the database.

The third functional part of BMS is the module that applies expert system algorithms to evaluate and rate the structural conditions. In this module, a visual interface for interacting with specialist knowledge, an integration engine for expert algorithms, the analysis core of the neural-aided expert system, a graphical user interface for expert system operation, and database

management for bridge inspection data are designed and implemented. Because the structural evaluation of bridge deterioration needs a professional judgment, an expert algorithm is developed in the system. In general, the algorithms embedded in the BMS have to be reviewed and modified according to the back-fed information from field observations and from senior engineers’ determinations. In addition, the BMS focuses on integrating extendable and modifiable modules and make them available for practical use. Figure 1 shows the framework of the developed system; its input layer includes the inspection record, the bridge inventory, and descriptions of related regulations.

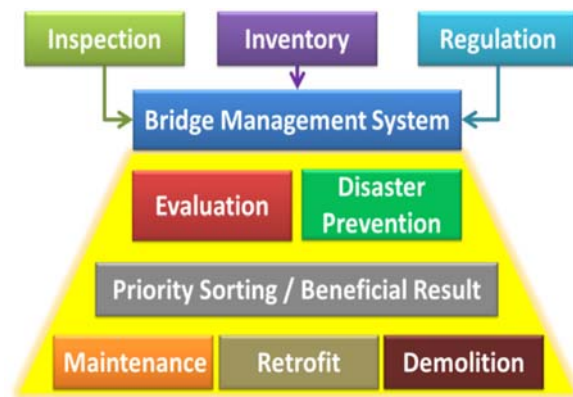


Figure 1. Framework of the developed BMS

In the proposed framework, the evaluation and disaster prevention modules are also included. The output layer provides information on the bridge condition, priority sorting, and beneficial suggestions to authorities to help them make optimal decisions. Figure 2 indicates a flexible service bus of the system that connects the functional modules of other applications.

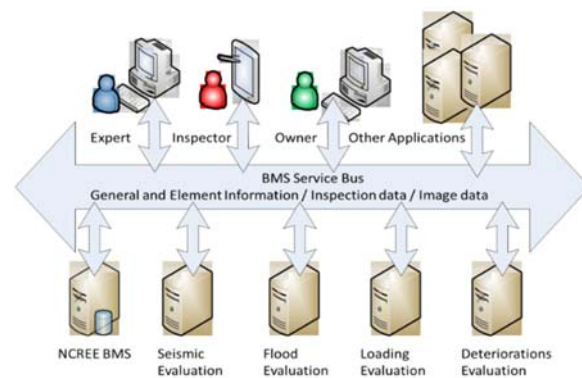


Figure 2. Service bus of the system

Metadata Technology Application

“Metadata”, used in the proposed system, is a novel information technology that is applied and integrated with bridge inspection record photos captured onsite. “Metadata” is defined as data or information that provides information about other data; using such data, the external field work and internal office work of

bridge inspection projects can be easily integrated and the division of labor can be done efficiently.

Recently, metadata has been extensively used to describe various data. For example, to describe a digital photo with metadata, the brand of the camera used to capture the image, exposure information (e.g., shutter speed), and descriptive keywords suitable for searching the photo on the internet need to be included.

Metadata can be written outside or into a digital photo file. In this study, we write the required metadata into photos to facilitate the management of a large number of inspection photos. Therefore, by simply managing photos that contain all available inspection results, we can handle the required inspection data easily.

This method of writing metadata into photos has the following advantages for bridge inspection. Users can classify, organize, or evaluate the metadata-embedded photos according to the preliminary inspection results contained in their metadata. In particular, the metadata embedded into a photo can be used to describe different deterioration patterns of the bridge part where the photo is taken. As a photo has embedded descriptive data, it provides all inspection results without any omission. In the case of photos that capture the cracks in the bridge part, the metadata can describe cracks using geometric objects such as points or polylines to obtain the crack distribution; such crack data may be depicted as a Geographic Information System (GIS) layer, which can then be overlaid on or removed from the photo taken on the bridge part where those cracks exist (see Figure 3).

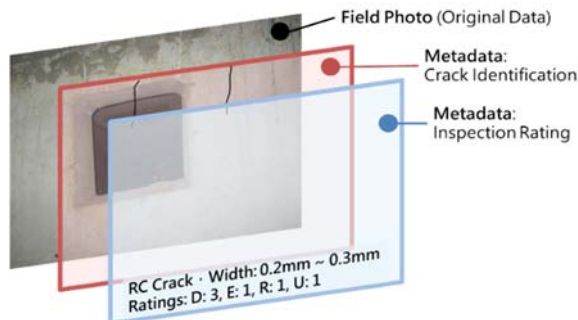


Figure 3. Depiction of metadata as GIS layers and overlaying them on a photo

Operation Tool (OT), External Operation Tool (EOT), and Internal Operation Tool (IOT). The developed BMS offers a Cloud Operation Tool (COT), a web application that helps the user upload inspection photos and then edit the metadata of those photos through its web interface. On the other hand, EOT is a mobile application that helps users write metadata onto inspection photos onsite. Then, users may upload these photos from their mobile devices to the developed BMS, or move these photos to their computers, and further process these photos using IOT, as shown in Figure 4.

IOT is a Windows application that extends the functionalities of Windows Explorer. This application

identifies the inspection photos containing metadata, interprets and shows their metadata, and offers user interfaces for users to edit the metadata of a photo, upload photos, and even create reports that incorporate inspection photos.

As shown in Figure 5, in addition to reading the metadata of photos, IOT offers users a grouping option to classify the photos in Windows Explorer. Three groups, namely, RP7, RP8, and RP12, exist in IOT. In addition, Windows Explorer identifies each photo containing the required metadata by displaying a graphical tag (an arrow inside a cloud) on the lower-left corner of the photo.

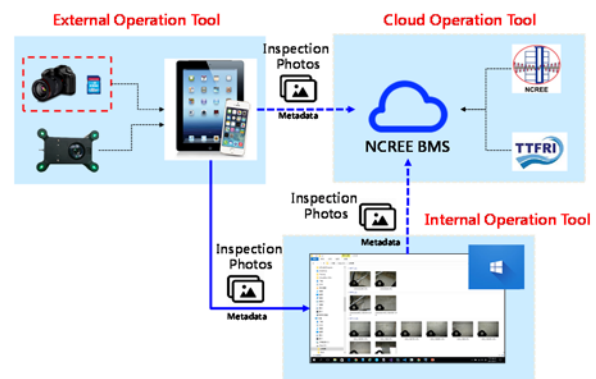


Figure 4. External, internal, and cloud operation tools to write metadata into inspection photos

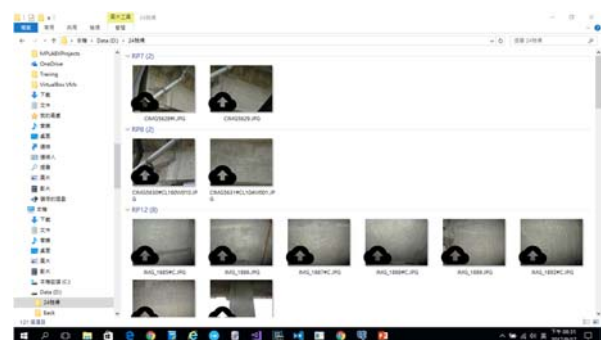


Figure 5. Photos are classified in Windows Explorer according to their metadata

In Figure 6, Windows Explorer shows the inspection results of photos including values of Ds, Es, Rs, and Us as well as the bridge names and element IDs for each of those photos. As shown in Figure 7, IOT enables users to preview and edit a photo containing the required metadata through a dialog that this tool offers in Windows Explorer. As shown in Figure 8, the users can select multiple photos that contain the required inspection metadata and upload them simultaneously. Note that except for the uploading operation, all IOT operations may be carried out off-line. Because the user interface of a desktop application is often considered easier to use and more efficient than that of a web application, the fact that users can perform most of their inspection activities off-line makes IOT more effective than COT.

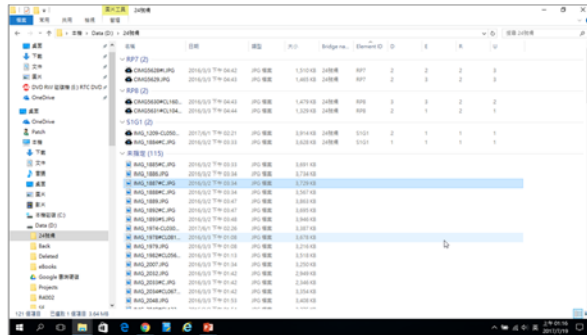


Figure 6. Inspection results are shown in Windows Explorer

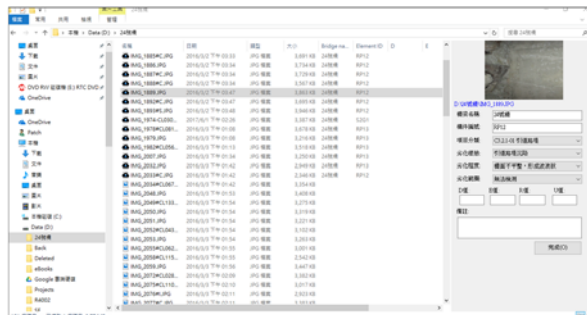


Figure 7. Deterioration pattern of a photo can be further detailed by previewing the photo in Windows Explorer

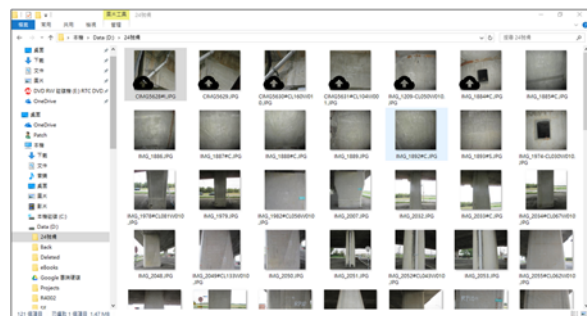


Figure 8. Photos may be uploaded simultaneously in Windows Explorer

Conclusion

In this study, the framework for a new lifecycle-based bridge management system for bridge inspection was introduced and the system performance was evaluated. Metadata is useful for data mining during the inspection and evaluation processes and can improve decision making on necessary maintenance efforts for seismic loss estimation and to resolve the long-term problem of the deterioration of bridges. The achievements in this study are expected to be helpful for disaster mitigation strategies in the future.

References

Sung, Y.C., Liao, W.I., Yen, W. Phillip, "Performance-Based Concept on Seismic Evaluation of The Existing Bridges," *Earthquake Engineering and*

Engineering Vibration, Vol. 8, No. 1, 2009, 127-135

Sung, Y.C., Huang, C.H., Liu, K.Y., Wang, C.H., Su, C.K., and Chang, K.C., "Life-Cycle Evaluation on Deteriorated Structural Performance of Neutralized Reinforced Concrete Bridges," *Structure and Infrastructure Engineering*, Vol. 6, No. 6, 2010, 741-751

Sung, Y.C. & Su, C.K. 2011. Time-dependent seismic fragility curves on optimal retrofitting of neutralised reinforced concrete bridges. *Structure and Infrastructure Engineering*, Vol. 7, No. 10, October 2011, 797–805.

Sung, Y.C., Hsu, C.C., Hung, H.H. & Chung, Y.J. 2011. Seismic risk assessment system of existing bridges in Taiwan. *Structure and Infrastructure Engineering*, Vol. 9, No. 9, 2013, 903-917

Thompson, P. D. & Kerr, B. 1998. A New Bridge Management System for Ontario, *ITX Stanley Ltd.*, Canada.

Design Concept and Verification of a Temporary Rescue Bridge Using GFRP and Steel Hybrid Structures

Fang-Yao Yeh¹, Kuo-Chun Chang² and Yu-Chi Sung³

葉芳耀¹、張國鎮²、宋裕祺³

Abstract

Typhoons and earthquakes, which occur frequently in Taiwan, often lead to the washout or collapse of river bridges, thereby interrupting traffic. A project was proposed at the National Center for Research on Earthquake Engineering (NCREE) to restore traffic as soon as possible and to provide necessary emergency rescue services in the aftermath of these events. The proposed solution is to develop a type of temporary rescue bridge that is portable, reusable, and easily assembled by unskilled residents. The objective of this paper is to present the emerging design concept and verification of this temporary rescue bridge. An asymmetric, self-anchored, cable-stayed bridge with heavyweight segments used as a counter-weight at the rescue end and river-spanning segments constructed of lightweight materials is proposed. In the design verification stage, a series of cross-river tests are performed to assess its adherence to design requirements, followed by in situ, full-scale, flexural and dynamic tests to examine its performance and feasibility. The experimental assembly and results demonstrate the feasibility of the proposed design concept and show the strong potential of using an asymmetric self-anchored cable-stayed bridge for temporary rescue operations.

Keywords: temporary rescue bridge; emergency disaster relief; asymmetrical cable-stayed bridge; glass-fiber-reinforced polymer and steel hybrid structures.

Introduction

As a result of recent climate change, typhoons, floods, and earthquakes have become the most common and problematic types of natural disaster in Taiwan. For example, Typhoon Morakot in 2009 caused 88 floods, in which more than 200 bridges were damaged and over 100 more were washed away (Fig. 1(a)). The Chi-Chi Earthquake in 1999 also caused more than 150 bridges to be damaged (Fig. 1(b)), isolating mountain communities and interfering with the delivery of emergency relief supplies.

The use of advanced composite materials in the aerospace, marine, and automobile industries has expanded during the past few years, thanks to the good engineering properties of these materials, such as high specific strength and stiffness, low density, high fatigue endurance, and high damping. The advantages of fiber-reinforced polymer (FRP) composites make them attractive for use in

replacement decks or new bridge systems. Examples of their use include the following: (1) bridge decks, including FRP-rebar-reinforced concrete deck systems, FRP-grid-and-grating-reinforced concrete deck systems, deck systems made completely out of FRP composite, and hybrid FRP-plate-reinforced concrete deck systems; (2) FRP composite bridge girders and beams, including glass-fiber-reinforced polymer (GFRP) composite girders, carbon-fiber-reinforced polymer composite girders, and hybrid girders; and (3) slab-on-girder bridge systems [1].



Fig. 1 Damage to bridges and disaster rescue operations following (a) Typhoon Morakot and (b) the Chi-Chi Earthquake.

¹ Research Fellow, National Center for Research on Earthquake Engineering, fyyeh@ncree.narl.org.tw

² Professor, Department of Civil Engineering, National Taiwan University, ciekuo@ntu.edu.tw

³ Division Director, National Center for Research on Earthquake Engineering, sung.yuchi@gmail.com
Professor, Department of Civil Engineering, National Taipei University of Technology, sungyc@ntut.edu.tw

Nowadays, FRP composites are used mostly in deck systems, footbridges, and vehicle bridges. This paper focuses on the advantages of FRP composites for use in typhoon, flood, and earthquake disaster rescue operations in Taiwan. The objectives of this paper are to present: (1) a novel lightweight bridge that is easily portable and reusable; (2) adjustable structural joints that combine bolts, welding, and adhesive methods for easy manufacture and rapid assembly; and (3) effective structural design techniques for increasing the bonding strength of joints and decreasing the deflection-to-span ratio.

Design Concept of a Temporary Rescue Bridge

Natural disasters often lead to the washout or collapse of bridges, thereby interrupting traffic. In order to restore traffic and to provide necessary emergency rescue services, the most commonly used temporary rescue bridges in Taiwan are temporary roadways made from concrete pipes, which often take three days to one week to construct (Fig. 2(a)) and temporary steel bridges, which take 1–3 weeks to install (Fig. 2(b)), but these assembly times are often too slow to provide urgently required aid.

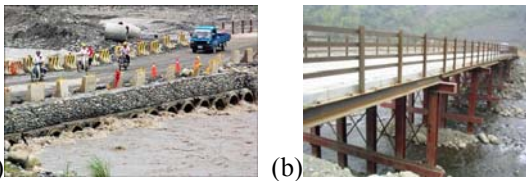


Fig. 2 The most commonly used temporary rescue bridges in Taiwan: (a) temporary roadways made from concrete pipes and (b) temporary steel bridges.

This paper proposes an emerging design concept developed using a logical procedure (Fig. 3) intended to help bridge designers with a problem-solving strategy for temporary rescue bridge design. Furthermore, the procedure considers the design review stage and design verification stage of the temporary rescue bridges to ensure that the design output meets the requirements of the design input, a crucial step in the design process.

Figure 3 shows the proposed design concept and procedure for a temporary rescue bridge. There are five design stages in the design concept and procedure, including (1) design input, (2) design process, (3) design output, (4) design review, and (5) design verification. (a) In the design input stage, functional requirements for temporary rescue bridges may include parameters such as: 1) the bridge should be constructed from the rescue end and 2) the bridge should be portable, reusable, and easily assembled, *etc.* (b) The design process stage begins with conceptual design, and includes the following: 1) bridge type selection to meet the requirements of temporary rescue bridges and 2)

construction sequences, where construction methodologies are considered in order to meet the requirements of temporary rescue bridges. Detailed design is then carried out. Different design codes should be considered in this process, corresponding to construction materials required, *etc.*

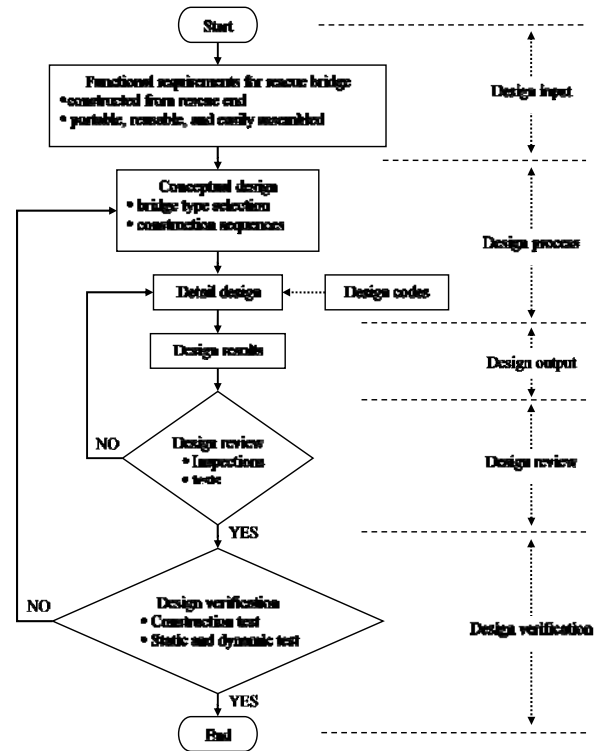


Fig. 3 Proposed design concept and procedure for temporary rescue bridges.

Design Case Study

Scenario and Design Thinking

The design case study looked at communities that were isolated by Typhoon Morakot in 2009. A river bridge with a 20-m span length was washed away by the floods, interrupting traffic travelling to and from surrounding areas. A temporary rescue bridge needed to be completed within 8 hours, so that small trucks of 5.0 tons could access and transport relief materials into the isolated area.

Conceptual Design

This study develops the bridge system by using a self-balancing approach and a cantilever incremental launching method. An asymmetric self-anchored cable-stayed bridge is proposed. The structural segments are constructed from heavyweight materials (*e.g.*, steel and concrete) that function as counterweights at the rescue end, and the spanning segments are constructed from lightweight materials (*e.g.*, composite materials). This allows the span to be increased so that it can easily reach the isolated island end without any further supports or foundations (Fig. 4).

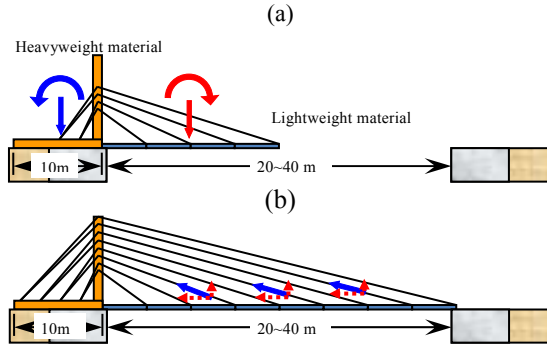


Fig. 4 Concept of a temporary composite bridge for emergency disaster relief: (a) the construction stage and (b) the commissioning and completion stage.

Detailed Design

The temporary rescue bridge was composed of structural steel and GFRP composite materials. In this paper, the steel structural design followed the Taiwanese local code for steel highway bridges [2], and the composite structure used the design code proposed by the U.S. Department of Agriculture (USDA) Forest Service [3] and the American Association of State Highway and Transportation Officials (AASHTO) [4].

Parallel FRP girder bridge systems were studied to assess the structural requirements necessary to meet the following design requirements: a 20-m span; a 3-m width; a 5-ton live load capability (for transportation of rescue goods in a truck weighing 3.5 tons); and a deflection-to-span ratio of $L/400$, which was recommended by the USDA [3]. The bridge system used $410 \times 20 \times 200 \times 18$ -mm H-shaped composite girders. The material properties of the GFRP were as follows: Young's modulus 20.03 GPa, density 1.72 g/cm^3 , and allowable stress 207 MPa. We designed a steel-and-composite cable-stayed bridge that met all the functional requirements for the assembly and river-crossing objectives. Figure 5 shows the design results of the asymmetric self-anchored cable-stayed bridge.

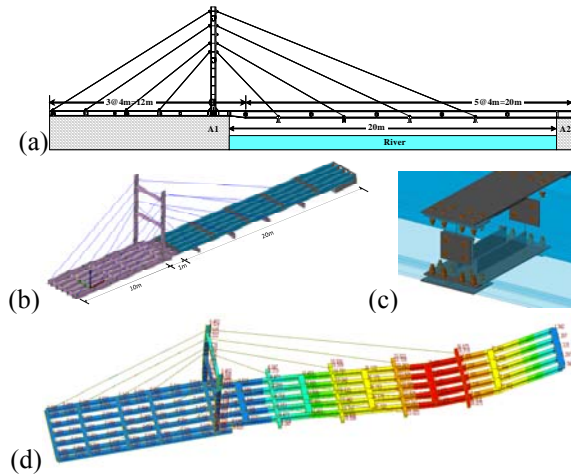


Fig. 5 Design results for the 20-m-span temporary composite bridge: (a) front view, (b) 3D view, (c) 3D view

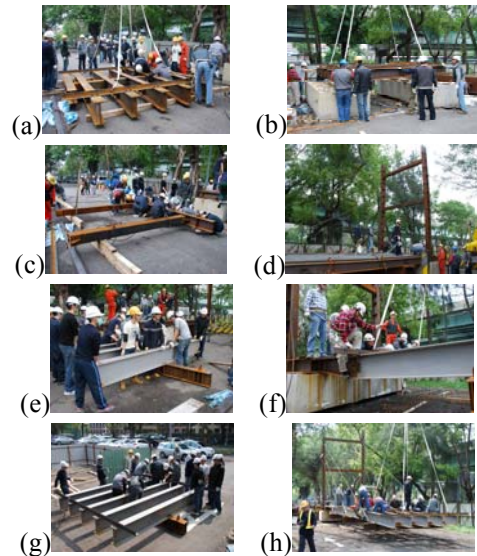
the bolted connection using bolts and a steel connection plate, and (d) the deformation shape.

In Situ Experiments and Design Verification

Construction Sequences and River-crossing Test

The construction sequence is shown in Fig. 6 and is as follows. Step 1: assembly of seven parallel steel girders with $294 \text{ mm} \times 200 \text{ mm} \times 8 \text{ mm} \times 12 \text{ mm}$ cross sections and a total length of 12 m ($3 \times 4 \text{ m}$), with box-girder cross beams ($200 \text{ mm} \times 200 \text{ mm} \times 6 \text{ mm}$) connecting them via bolts at the webs of the H-shaped girders (Figs. 6(a) and (b)). Step 2: assembly of H-shaped pillars with eighteen connection devices for the steel cable, $294 \text{ mm} \times 200 \text{ mm} \times 8 \text{ mm} \times 12 \text{ mm}$ cross sections, and a total height of 6.5 m (Fig. 6(c)), and a bolted connection with the top flange of the outer of the seven parallel steel girders in the third segment (Fig. 6(d)). Step 3: assembly of the first segment of five parallel GFRP girders (Fig. 6(e)) and connection to the third segment of the weight-balance structural module (Fig. 6(f)). Step 4: assembly of the second segment of five parallel GFRP girders using the same sequence as in the previous step (Fig. 6(g)) and connection to the first segment of the crossing structural module (Fig. 6(h)). Step 5: assembly of the third to final segments of five parallel GFRP girders using the same procedure as in the previous step (Fig. 6(i)) and completion of the construction sequence to cross the river (Fig. 6(j)).

This 20-m-span temporary composite bridge was constructed by thirty workers within six hours using manpower, simple tools, and a small truck with a crane, thereby meeting the requirements for emergency disaster relief.



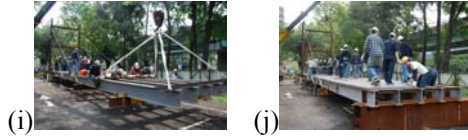


Fig. 6 Construction sequence of the 20-m-span temporary composite bridge: (a) assembly of seven parallel steel girders; (b) connection of the weight-balance structural module; (c) assembly of the double-H-shaped pillar; (d) connection of the bridge-tower structural module; (e) assembly of the first segment of GFRP girders; (f) connection of the crossing structural module; (g) assembly of the second segment of GFRP girders; (h) and (i) connection of the crossing structural module; and (j) completion of the bridge construction.

In Situ Full-Scale Flexural and Dynamic Tests

The experimental setup of the proposed temporary composite bridge with a span of 20 m is shown in Fig. 7(a), and the loading position of a small truck weighing 3.5 t (total weight 5 t) is shown in Fig. 7(b). The test program included a flexural test, an off-axis flexural test, and a dynamic test. The results of the flexural and dynamic tests are shown in Fig. 8. The shape deformation is shown in Figs. 8(a) and (b). The maximum displacements were 53.41 mm (flexural test) and 56.23 mm (off-axis flexural test); these occurred at connection G4. The maximum longitudinal strains were 5.05×10^{-4} (flexural test) and -5.53×10^{-4} (off-axis flexural test); these occurred in girder B3, on the left side of connection G4 (Fig. 8(c)). Deflection over time at connection G4 is shown in Figure 8(d). The flexural and dynamic test results indicate that the deflection-to-span ratio is around $L/356$, which is very close to the design requirement of $L/400$, for a live load of 5 t.

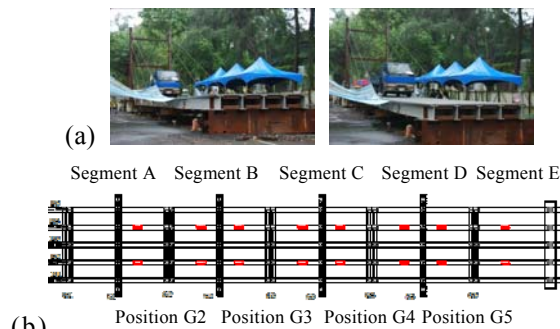


Fig. 7 The experimental setup of the 20-m-span temporary composite bridge: (a) test setup, and (b) wheel position for a small truck.

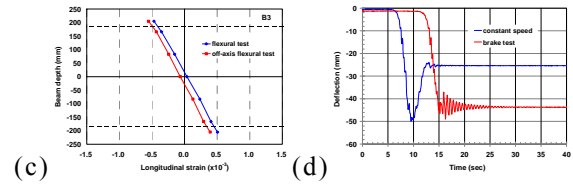
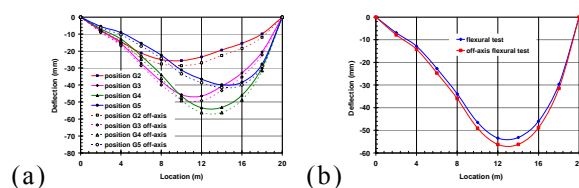


Fig. 8 Flexural and dynamic test results for the 20-m-span temporary composite bridge: (a) shape deformation (various loading positions), (b) shape deformation (loading at position G4), (c) longitudinal strain along the depth of the B3 girder, and (d) deflection over time at connection G4.

Conclusions

This paper presented a lightweight, portable, and reusable temporary composite bridge for emergency disaster relief. This bridge is an asymmetric self-anchored cable-stayed bridge designed using steel and FRP composite materials to improve the stiffness of the composite frame, reduce the deflection of the bridge, and allow easy travel across a river without any other supports or foundations. The bridge therefore achieved the goal of disaster relief, through its use of the concept of a weight balance and the incremental launching method. The results are summarized as follows: (1) the proposed design concept and procedure for designing a temporary rescue bridge is helpful for bridge designers in terms of problem-solving strategy for temporary rescue bridge design; (2) the bridge was constructed by thirty workers within six hours through the use of manpower, simple tools, and a small truck with a crane, which meets the requirements of emergency disaster relief; and (3) the flexural and dynamic test results indicate that the deflection-to-span ratio is around $L/356$, which is very close to the design requirement of $L/400$, for a live load of 5 t.

References

- L. Cheng, V.M. Karbhari, New bridge systems using FRP composites and concrete: a state-of-the-art review, readers write, *Progress in Structural Engineering Materials*, 8(4):143-154, 2006.
- MOTC, Design specification for highway bridges, Taiwan Area National Expressway Engineering Bureau, Ministry of Transport and Communications, 2009. (In Chinese)
- USDA Forest Service, A guide to fiber-reinforced polymer trail bridges, United States Department of Agriculture, second edition, 2011.
- AASHTO, Guide specifications for design of FRP pedestrian bridges, American Association of State Highway and Transportation Officials, first edition, 2008.

Seismic Risk Assessment and Screening of Large Water Pipes in Taiwan

Gee-Yu Liu¹, Chin-Hsun Yeh², Lee-Hui Huang³ and Hsiang-Yuan Hung⁴

劉季宇¹ 葉錦勳² 黃李暉³ 洪祥瑗⁴

Abstract

The seismic hazard mitigation of water supply systems is a crucial issue in Taiwan. In order to protect water pipes more effectively, the screening of large pipes is essential. A study was conducted to investigate the effects of seismic hazards like ground shaking, soil liquefaction, active faults, and landslides on buried pipes. The inventory of pipes of Taiwan Water Corporation (TWC) having a diameter of 800 mm or greater was collected and calibrated. This consisted of 2,229 km of pipes of various sizes and pipe types (joints). The seismic risk to each pipe, as a combination of hazard severity and pipe vulnerability, was quantified and ranked. The importance of each pipe was also classified according to its water conveyance capability and the existence or non-existence of redundancy. Finally, pipes of high importance that were at high seismic risk were screened out. They were grouped into three priorities for TWC to implement their seismic improvement program.

Keywords: water pipes, seismic risk, hazard mitigation

Introduction

Taiwan is located on the circum-Pacific seismic belt, one of the world's most earthquake-prone areas. The 1999 Chi-Chi earthquake (Mw 7.6), the most devastating event in decades, caused widespread damage to water supply systems. 4,411 incidents of damage to water pipes were recorded. Among these, 28 occurred in pipes of diameter 500 mm or larger. The most severe damage occurred in Fengyuan, where a 2000 mm diameter steel pipe, which was the only common outlet of both the Fengyuan First and Second Water Treatment Plants, and which provided the Taichung metropolitan area with 70% of its water, was bent 90 degrees and buckled by the offset of the Chelungpu fault (TWC, 2000). The 2016 Meinong earthquake (Mw 6.6) caused substantial damage to water pipes in Tainan. The 2000 mm diameter pipe conveying water from the Nanhua Water Treatment Plant to downtown Tainan was damaged at three locations. This caused widespread water outage lasting for a long time (Liu et al., 2016).

Evidence indicates that many large water pipes in Taiwan do not have enough strength to withstand

medium to large seismic events. In order to lower the risk more effectively, seismic risk assessment and the screening of large water pipes was performed in this study.

Goal and Methodology

This study focused on the water pipes of TWC (Taiwan Water Corporation) having a diameter of 800 mm or greater (up to 3,200 mm). The goal is to: (1) sort the target pipes according to their importance to the water supply systems, (2) rank the target pipes according to the seismic risk they are exposed to, and (3) screen out pipes of high importance and at high risk for the seismic improvement program of TWC.

The way to define the seismic risk to pipes depends on the resolution of the field data as well as how the risk information is used. For the sake of simplicity, the vulnerability of a "pipe evaluation unit" is assumed independent of the seismic hazards. The hazards of ground shaking, soil liquefaction, active fault ruptures, and landslides, which are inevitably the major causes of pipe damage, have been investigated. These hazards were assumed to be quantifiable and

¹ Research Fellow, National Center for Research on Earthquake Engineering, karl@ncree.narl.org.tw

² Research Fellow and Division Head, National Center for Research on Earthquake Engineering, chye@ncree.narl.org.tw

³ Assistant Researcher, National Center for Research on Earthquake Engineering, lhhuang@ncree.narl.org.tw

⁴ Assistant Researcher, National Center for Research on Earthquake Engineering, hyhung@ncree.narl.org.tw

addable. Similarly, the vulnerability of a pipe was quantified by its material (joint type) and size. The normalized hazard and vulnerability of each unit were obtained to decide its risk.

According to the value of risk, all pipe evaluation units could be ranked from high to low, and evenly divided into risk groups R1, R2, etc. Together with sorting pipes according to their importance, a risk-importance matrix can be achieved, from which pipes of high importance and those at high seismic risk can be easily identified.

Pipe Inventory and Importance

The inventory of the target pipes was first collected and calibrated. The total length of the pipes is 2,229 km. The digitized geographic information system (GIS) data consists of more than 6,500 polylines, varying greatly in length. They were re-organized into 1,687 units of similar length for the purpose of equal representation. This was achieved by either grouping together neighboring pipes or the division of long pipes. These units were termed “pipe evaluation units”, and were employed as the base units for analysis.

The importance of a pipe stems from two factors. The first is its role, which relates to the daily volume of water transported. The other is its criticality, i.e., the existence or non-existence of any redundant pipes as backup. Subsequently, all pipe evaluation units are sorted into one of the following four classes: very high, high, normal, and low.

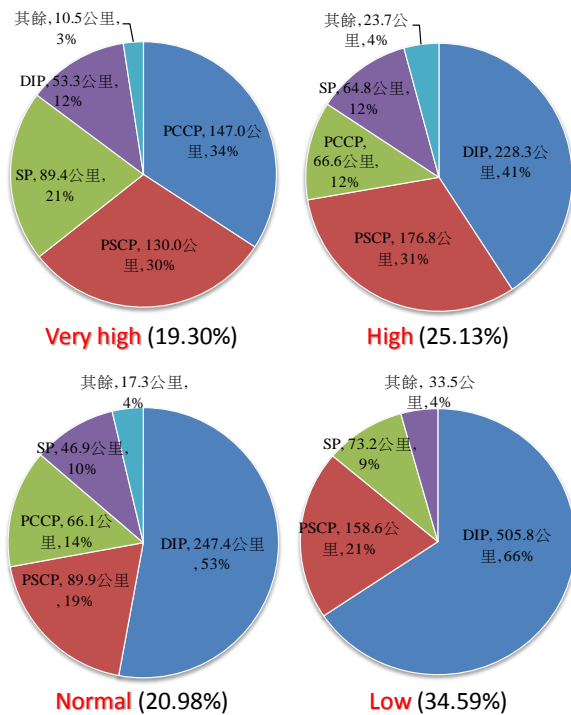


Figure 1 The composition of pipe types of each class of pipe importance.

Figure 1 summarizes the composition of pipe types of each class of importance. It can be seen that for pipes of very high importance, the majority are PCCP (pre-stressed concrete cylinder pipes, 34%) and PSCP (pre-stressed concrete pipes, 30%). Such pipes are brittle and seismically very vulnerable.

Seismic Hazards

Ground shaking is the most common cause of pipe damage. Theoretically, peak ground velocity (PGV) is proportional to the ground strain, the real mechanism of seismic action upon a pipe during ground shaking. It is widely used as the key factor in estimating the damage rate of pipes (number of repairs per unit pipe length). Therefore, the value of PGV at a return period of 10% in 50 years (design earthquake) is used to specify the hazard potential of ground shaking.

Soil liquefaction is another cause of pipe damage. Conventionally, the liquefaction potential index P_L proposed by Iwasaki et al. (1982) is used to indicate the susceptibility of a site to liquefaction. Similar to the liquefaction susceptibility categories in HAZUS (RMS, 1997), a map of the soil liquefaction susceptibility categories of Taiwan has been proposed by Yeh et al. (2015). It is based on the borehole database from the Central Geological Survey, MOEA, together with a geological map, a digital terrain model, and a map of drainage. A site can be classified as belonging to one of nine categories, Cat. 1 to 9, depending on how easily liquefaction will occur given the same condition of excitation, while Cat. 0 suggests that liquefaction will never occur. In addition, a set of empirical formulas have also been proposed by Yeh et al. (2015) to assess the P_L value of each category. The peak ground acceleration (PGA), earthquake magnitude (M), and ground-water depth (D) are the three parameters required in the formulas. With the code-specified PGA and M at a return period of 10% in 50 years (design earthquake), a hazard map of liquefaction in terms of the P_L value can be achieved.

According to the active fault map of Taiwan created by the Central Geological Survey (CGS), MOEA, there are 33 active faults on the island, 20 Category I and the rest Category II. The former refers to faults that have been active in the past 10,000 years and are considered more active, while the latter are those that have been active in the past 100,000 years and are less active (CGS website). In order to account for the damaging potential of fault ruptures to water pipes once they occur, two buffers have been created for each fault trace. The first is a 15 m radius buffer denoted as the fault crossing area, while the second is a 150 m radius buffer denoted as the fault vicinity area. For a normal or reverse fault, the two buffers are shifted to the hang-wall side by 5 m and 50 m, respectively, to account for the hang-wall effect. The

effective length of a pipe either crossing or close to an active fault can be decided by using GIS spatial analysis.

The CGS recently released a map of the landslide potential of Taiwan. It classified the landslide risk into four categories: none, low, medium, and high. In this study, a landslide score of 3, 1, 0, and 0 is specified to these categories, respectively. It is also assumed that the occurrence of earthquake-induced landslides is proportional to the score of the site.

Given the four seismic hazard potentials discussed above, the quantified hazard to a pipe evaluation unit can be defined and then computed. Furthermore, the four quantified hazards to a pipe evaluation unit have completely different physical meanings and numeric ranges. They have been transformed and normalized for addability. As a result, the transformed and normalized hazards of ground shaking \bar{H}_{GS} , liquefaction \bar{H}_{LQF} , fault rupture \bar{H}_F , and landslide \bar{H}_{LS} to each pipe evaluation unit can be obtained. Details can be found in Liu et al. (2017).

Finally, the combined seismic hazard \bar{H} to a pipe evaluation unit is defined as:

$$\bar{H} = 0.45 \cdot \bar{H}_{GS} + 0.45 \cdot \bar{H}_{LQF} + 0.08 \cdot \bar{H}_F + 0.02 \cdot \bar{H}_{LS},$$

which has a numeric range of [0,1]. The weightings 0.45, 0.45, 0.08, and 0.02 were carefully chosen so as to balance the contribution from each type of hazard.

Seismic Vulnerability of Pipes

The damage rate of water pipes under seismic loading has been investigated by Miyajima (2013). The research found that the damage rate is statistically proportional to

$$C_p \cdot C_d \cdot C_g \cdot (PGV - 15)^{1.14},$$

where C_p , C_d , and C_g are factors accommodating the effects from pipe type (joint), pipe diameter, and micro-topography, respectively.

In general, the stronger the pipe (type-joint), the lower the C_p value and damage rate; the larger the pipe diameter, the lower the C_d value and damage rate. In this study, the vulnerability V of a pipe given its type (joint) and diameter ϕ (measured in mm) was assumed to be quantifiable as

$$V = \log_{10} \left(10 \cdot C_p \right) \times \left(\frac{800}{\phi} \right)^{0.125}.$$

This functional form of V was carefully specified such that, given the wide ranges of C_p and ϕ , the range of V is small but sufficient to distinguish

fragile pipes from others. Whenever a pipe evaluation unit consists of more than one pipe, its V value should be the summation of vulnerability of all its member pipes weighted by the length ratio. Finally, the normalized vulnerability \bar{V} of each pipe evaluation unit may be expressed as

$$\bar{V} = \frac{V - V_{\min}}{V_{\max} - V_{\min}},$$

which has a numeric range of [0,1] as well.

Seismic Risk and Enhancement Priorities of Pipes

Given the hazard \bar{H} and vulnerability \bar{V} , the seismic risk of a pipe evaluation unit can be defined as

$$R = (1 + \bar{H}) \cdot (1 + \bar{V}),$$

which has a numeric range of [0,4]. The higher the seismic risk, the higher the hazard potential a pipe evaluation unit is exposed to, or the more vulnerable it is seismically. According to the value of seismic risk, all pipe evaluation units can be ranked from high to low, and evenly divided into ten “risk groups” from R1 to R10. Each risk group can be spread out with respect to the pipes’ importance classified earlier. Consequently, a risk-importance matrix of the target pipes can be obtained as summarized in **Table 1**.

In order to assure effective and financially feasible seismic enhancement of large water pipes, a prioritized implementation is preferred. According to the risk-importance matrix, three priorities were suggested, as specified in **Table 2**. Each priority consists of two elements from the matrix. For example, the first priority consists of 82 units, of which 29 are from the combination of (Very high, R1), while the other 53 are from (Very high, R2). A total of 232 pipe evaluation units were suggested to TWC for seismic enhancement in the future.

In practice, the suggested 232 pipe evaluation units are not evenly distributed. The units located in Taichung (74 in total) and Kaohsiung (65) outnumber those in other areas. In particular, the Taichung area, shown in **Figure 2**, is prone to ground shaking and fault rupture hazards due to the existence of many active faults in the neighborhood. Its large water pipes are mostly PCCP and PSCP.

Table 1 The risk-importance matrix of numbers of pipe evaluation units after assessment.

Risk group	Very high	High	Normal	Low	Sum
R1	29	51	38	51	169
R2	53	33	40	43	169
R3	46	38	34	51	169

Evaluation of Failure Probability for Emergency Power Supply Systems in Hospitals

Chi-Hao Lin¹ and Cheng-Tao Yang²

林祺皓¹、楊承道²

Abstract

The unpredictability of earthquakes is one of the major reasons for the occurrence of building damage and casualties during earthquake events. In addition to earthquake-induced structural damage to buildings, ground shaking can also cause critical effects on nonstructural components and systems in buildings. This study aimed to develop a probability-based approach for evaluating seismic damage to emergency power supply systems (EPSSs) in Taiwanese hospitals. Four case hospitals that were damaged during the Chi-Chi earthquake (September 21, 1999) were investigated. A component scoring system developed by the Multidisciplinary Center for Earthquake Engineering Research in the United States was referenced as the basis for developing seismic fragility curves for the components in the EPSSs of the case hospitals. Additionally, the logic tree method was employed to evaluate the failure probability of the EPSSs. The results exhibited acceptable consistency with the recorded damage status of the investigated systems, thereby verifying the feasibility of the proposed approach.

Keywords: seismic fragility, emergency power system, logic tree, failure probability

Introduction

First-aid hospitals are critical facilities that play an important role in receiving injured patients and performing emergency operations during severe earthquake events. Therefore, hospitals must maintain not only the safety of their building structures but also ensure the functionality of their nonstructural components and systems. These include emergency power supply systems (EPSSs), water supply systems, communication systems, and a range of medical equipment for patient care. Records of past earthquake disasters such as the 1971 San Fernando earthquake, 1994 Northridge earthquake, 1995 Hanshin earthquake, and 1999 Chi-Chi earthquake indicate that many hospitals could not provide medical services because of severe nonstructural damage. In particular, the EPSS is the most important system, because it provides electric power for other equipment and systems.

In this study, we focused on the failure probability analysis of EPSSs. There are several approaches to assessing failure probability. Our methodology involved applying a system logic tree,

analyzing component fragility data, and assessing site hazards. After the Chi-Chi Earthquake in Taiwan, Chuang et al. [1] investigated four severely damaged hospitals. They constructed logic trees for the EPSSs of these hospitals. Five types of emergency power supply components (EPSC) are involved in an EPSS, namely a control panel (CP), a generator (G), a battery rack (BR), a diesel tank (DT), and a cooling tower (CT). The seismic fragility function of these components was studied based on the component seismic scoring system developed by the Multidisciplinary Center for Earthquake Engineering Research (MCEER) [2-3]. We utilized logic trees to estimate the failure probabilities of the EPSSs on the basis of the peak ground acceleration (PGA) at the hospital sites, and then verified the suitability of the methodology.

Fragility Data of Emergency Power Supply Components

In earthquake engineering, fragility is usually used to quantify the failure probability of structures and nonstructures. In this study, we applied the PGA

¹ Assistant Researcher, National Center for Research on Earthquake Engineering

² Associate Researcher, National Center for Research on Earthquake Engineering

as the ground-motion parameter because it can be easily and accurately measured. The component fragility was assumed to be a two-parameter lognormal distribution function with median x_m and log-standard deviation β , as shown in Eqn. (1):

$$P(\alpha) = \Phi \left[\frac{\ln(\alpha/x_m)}{\beta} \right] \quad (1)$$

where P denotes the failure probability, $\Phi[\cdot]$ is the standardized normal distribution, and α is the ground-motion parameter, i.e., PGA.

In our previous study based on MCEER, we proposed fragility data for EPSCs [3]. These fragility data are considered to provide not only high standards for installation but also to function as performance modification factors (PMFs). PMFs describe a variety of poor installation cases for nonstructural components. Table 1 shows the fragility data for generators. The PMF descriptions reference the seismic score sheets developed by MCEER. The x_m and β were originally proposed by MCEER for the high-standard installation of each component [2]. In our study, the fragility data for each PMF were identified to accurately estimate the damage probabilities of EPSCs. x_m has a markedly higher value under the high-standard installation. This indicates that the component has a high seismic capacity. If the component has an installation deficiency, x_m is significantly reduced.

Table 1. Seismic fragility data for generators

Generator		x_m	β
high-standard installation		2.0	0.4
PMF1	No anchorage	0.78	0.5
PMF2	Poor anchorage	0.91	0.5
PMF3	Vibration isolator concerns	0.91	0.5
PMF4	Rigid attachment concerns	0.58	0.5
PMF5	Driver/generator different displacement	0.58	0.5
PMF6	Interaction concerns	0.91	0.5

Failure Probability of Emergency Power Supply Systems

On September 21, 1999 at 1:47 AM local time, an earthquake measuring 7.3 on the Richter scale occurred in central Taiwan. Its epicenter was at 23.87°N and 120.75°E in the Chi-Chi Township of Nantou County and was located at a depth of only 7.0 km. The earthquake originated along the Chelungpu fault line in western Taiwan and caused substantial damage. This incident was subsequently named “the Chi-Chi earthquake.”

Chuang et al. [1] investigated the four first-aid

hospitals (A–D) that were damaged in Nantou County. Fig. 1 shows the seismic intensity map of the Chi-Chi earthquake and the location of the four hospitals. The maximum PGA was approximately 1 g. Table 2 shows the PGA at the four hospitals. The Chelungpu fault is a reverse fault. Hospital D was located on the hanging wall, near the fault, and only a short distance from the epicenter. Thus, it experienced considerable ground motion. Although Hospital C was also near the fault, it was located on the foot wall. Thus, the ground motion it experienced was not substantial. Hospitals A and B were adjacent and experienced the same ground-motion intensity.

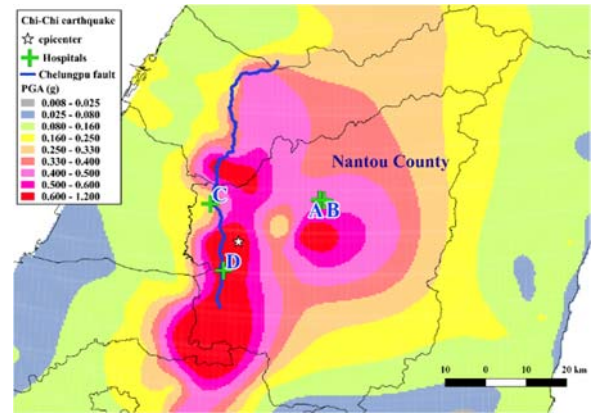


Fig. 1. Seismic intensity map of the Chi-Chi earthquake and the location of the four hospitals.

Table 2. PGA values of the four hospitals in the Chi-Chi earthquake.

	A	B	C	D
PGA (g)	0.45	0.45	0.28	0.67

System logic tree

Logic trees are graphical descriptions of the logical dependencies between systems and their subcomponents [4-5]. Mathematically, upper events are connected to lower events through an “and” gate (symbol: \square) or an “or” gate (symbol: \diamond). Eqn. (2) provides the probability for the upper event through an “and” gate. For an “or” gate, the probability of the upper event can be derived using Eqn. (3).

$$P[u] = 1 - \prod_{i=1}^n (1 - P[l_i]) \quad (2)$$

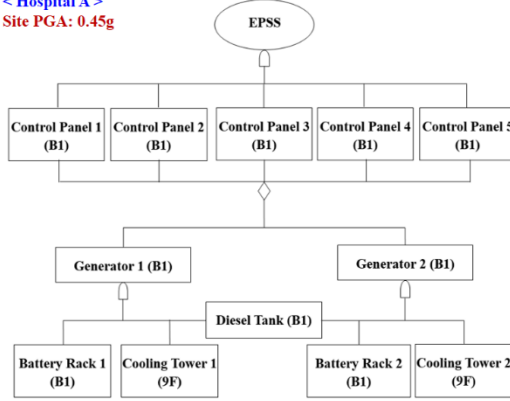
$$P[u] = \prod_{i=1}^n P[l_i] \quad (3)$$

where P denotes the failure probability, u represents the upper event, l_i are the lower events for the component, and \prod denotes the product.

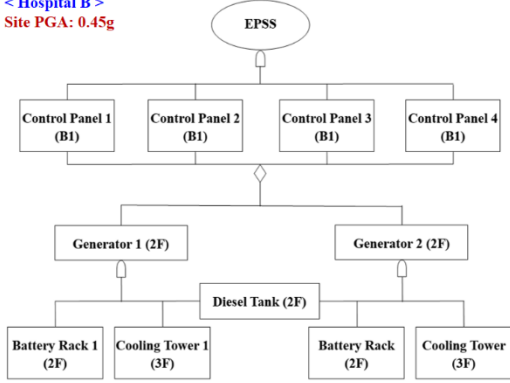
Fig. 2 shows a logic tree diagram of the EPSSs in the four hospitals. The EPSS in Hospital C had no cooling tower, whereas the other hospitals had all five major components. The floor where the component was located is indicated in parentheses in the figure. B1 refers to the basement first floor. RF denotes the

roof floor. The EPSSs in Hospitals A and B differ from Hospitals C and D in that their two generators used the same diesel tank. The failure path must be considered in the calculation of the probability. We took Hospital A as the example case. The detailed process of our computation is shown in the following section.

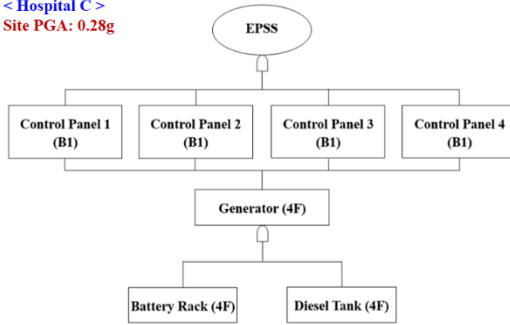
< Hospital A >
Site PGA: 0.45g



< Hospital B >
Site PGA: 0.45g



< Hospital C >
Site PGA: 0.28g



< Hospital D >
Site PGA: 0.67g

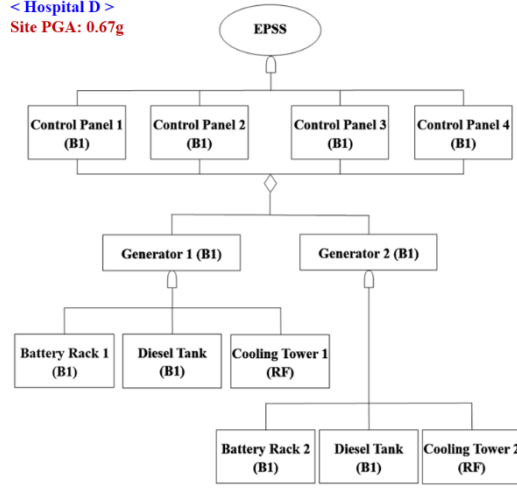


Fig. 2. Logic tree diagrams of the EPSSs in Hospitals A-D

Example case: Hospital A

The EPSS in Hospital A had two generators that shared the same diesel tank. Therefore, the generator subsystems did not operate independently. This problem cannot be solved entirely by Eqns. (2) and (3). The failure path must be considered for both subsystems. Furthermore, the peak floor acceleration (PFA) must include the acceleration amplification effect. In our study, the building floors were divided into three parts: the amplification factor of the bottom part was set at 1.0, the top part was set at 2.0, and the middle part was set at 1.5.

Hospital A was a 9-story building with one basement. The cooling tower was located on the top floor (9F). In the calculation of its failure probability, the acceleration at the top floor was considered to be 2.0 times the PGA. The other components were placed in the basement. The PFA was identical to the PGA at this site. In addition, according to Chuang et al.'s report [1], each component may have experienced many seismic losses (PMFs). In our study, we selected the appropriate fragility median in accordance with the post-earthquake investigation. Table 3 shows the x_m , β , floor, and PFA for each component in Hospital A.

Fig. 3 shows the detailed derivation for the failure probability of the EPSS (P_{EPSS}). In general, the failure probability of the upper event by using Eqn. (2) or Eqn. (3) can be obtained according to the “and” or “or” gate. At Step 1, the battery rack and the cooling tower were taken as the lower events. The failure probability of Upper Event 1 (P_1) was calculated using Eqn. (2). At Step 2, the diesel tank was not included. The failure probability of a generator subsystem (P_2) was derived through an “and” gate that was composed of P_1 and P_G . At Step 3, the failure probability of Upper Event 3 (P_3), which consisted of five control panels, was calculated. Because the two generators shared the same tank, we proposed the failure path shown in Step

4 for calculating the probability (P_4). Finally, we obtained P_{EPSS} by using P_3 and P_4 , which formed an “and” gate.

Tab. 3. x_m , β , floor, and PFA for each EPSC in Hospital A.

Component	x_m	β	Floor	PFA (g)
Generator	0.78	0.5	B1	0.45
Control Panel	1.22	0.5	B1	0.45
Battery Rack	0.58	0.5	B1	0.45
Diesel tank	0.56	0.5	B1	0.45
Cooling Tower	0.91	0.5	9F	0.90

identified in our study are appropriate for estimating the damage probability for each component impacted by the Chi-Chi earthquake. (2) Logic trees can fully represent the composition of each component. (3) Bottom-up probability analysis combined with failure paths can represent the seismic risk for EPSSs.

Table 4. P_{EPSS} compared with the disaster survey for Hospitals A–D

Hospital	A	B	C	D
Disaster survey	fail	fail	normal	fail
P_{EPSS}	69.2%	83.8%	34.3%	97.5%

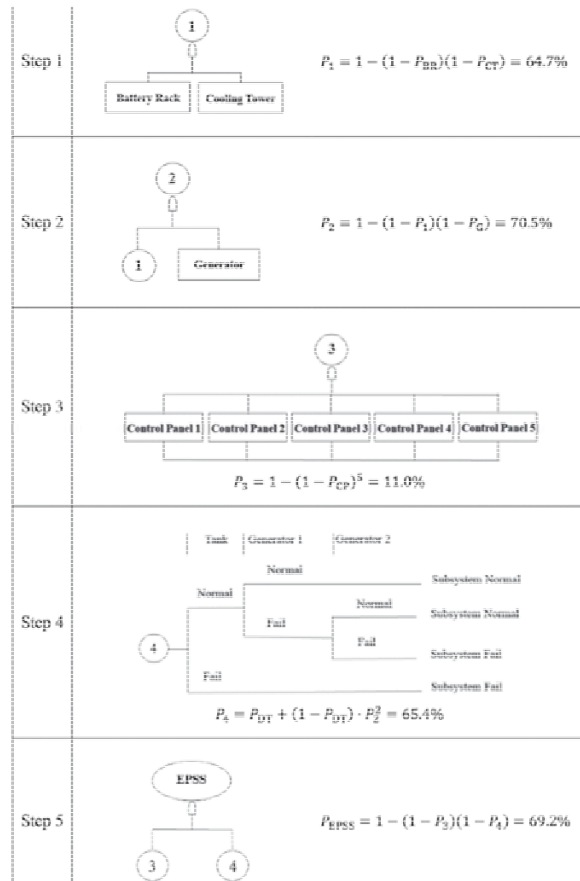


Fig. 3. Derivation process of P_{EPSS} for Hospital A.

Conclusions

Based on the above methodology, the P_{EPSS} for Hospitals A–D were obtained as listed in Table 4 and they were then compared with the disaster survey. The results exhibit acceptable consistency with the recorded damage status. This can be explained by the following three reasons: (1) The fragility data

References

- Chuang, C.C. & Yao, G.C., *Evaluation of Seismic Capacity of Designated Hospitals' Curative Equipment in Tainan Region*, Department of Emergency Medicine, National Cheng Kung University Hospital, College of Medicine, National Cheng Kung University, Taiwan, 2001.
- MCEER (Multidisciplinary Center for Earthquake Engineering Research), *Seismic Reliability Assessment of Critical Facilities: A Handbook, Supporting Documentation, and Model Code Provisions*, Technical Report MCEER-99-0008, 1999.
- Lin, C.H., Liu, X.Q., Kao, L.H., Tsai, C.Y. & Yang, C.T., Seismic Fragility Analysis for Hospital's Emergency Power Supply Equipment. *The Thirteenth National Conference on Structural Engineering & The Third National Conference on Earthquake Engineering*, Taiwan, Paper No. 1116, 2016.
- Porter, K. & Ramer, K., Estimating earthquake-induced failure probability and downtime of critical facilities. *Journal of Business Continuity & Emergency Planning*, **5**(4), pp. 352–364, 2012.
- Masri, S., Caffrey, J., Myrtle, R., Nigbor, R., Agbabian, M., Johnson, E., Petak, W., Shinozuka, M., Tasbihgoo, F., Tranquada, R. & Wellford, L., The FEMA-USC Hospital Project: Nonstructural Mitigation in Hospitals. *The Thirteenth World Conference on Earthquake Engineering*, Canada, Paper No. 2480, 2004.

Seismic Evaluation Methods for Fire-Protection Sprinkler Piping Systems in Buildings

Fan-Ru Lin¹, Chang-Chen Yeh², Juin-Fu Chai³, Kuo-Chun Chang⁴

林凡茹¹ 葉昶辰² 柴駿甫³ 張國鎮⁴

Abstract

Fire-protection sprinkler piping systems are likely to be harmed during earthquakes due to their vulnerability and mechanical properties. Even worse, leakage and falling objects caused by damaged piping and adjacent ceiling systems significantly affect the normal operation of critical buildings such as hospitals. This research aims to quantify the seismic capacity of sprinkler piping in hospitals by means of fragility curves, to enable a seismic evaluation or a performance design. A typical sprinkler piping system in a medium-scale hospital in Southern Taiwan, which was damaged due to the 2010 Chia-Shen earthquake, was taken as an example. Experimental results of in-situ ambient vibration tests and shaking table tests of the piping sub-system were used to verify the accuracy of the numerical model, including hangers, screwed fittings of small-bore pipes, adjacent partition walls, and ceiling boards. Fragility curves of the sprinkler piping system were then established according to a number of numerical analysis results, and a simplified seismic evaluation method was suggested as well.

Keywords: seismic assessment procedure for nonstructural systems, sprinkler piping systems, ceiling systems, screwed fittings, fragility analysis, simplified seismic evaluation method

Introduction

Based on experience with recent earthquakes in Taiwan, losses tend to result from damages of non-structural components instead of building structures. For instance, the leakage of fire protection sprinkler systems in hospitals during small earthquakes could result in a deficiency in medical function and fire protection, and additionally can cause malfunctions in medical equipment leading to required repair. The damage to sprinkler systems caused by strong earthquakes could even be life threatening. Taking a medium-scale hospital as an example (Fig. 1), this research proposes seismic evaluation methods for sprinkler piping in hospitals through fragility analysis according to the FEMA P-58 (ATC 2012) framework, and to conduct a simplified seismic evaluation method to improve the seismic performance of the fire protection sprinkler system in critical buildings.

Assessment Procedure for Seismic Performance of Nonstructural Systems

Based on the FEMA P-58 performance evaluation framework, in order to decrease the uncertainty of the assessment results of the seismic behaviors of nonstructural systems in buildings during extremely strong earthquake motions, we propose a modified assessment procedure for the calculation of seismic performance and the fragility analysis of nonstructural systems. As shown in Fig. 2, the proposed assessment procedure includes:

1. Select ground motions with more than 11 records in accordance with FEMA P695 (FEMA 2009).
2. Arrange the distribution of the scaling strength levels of earthquakes according to the risk of the failure modes of the evaluated nonstructural system.

¹ Assistant Researcher, National Center for Research on Earthquake Engineering.

² Graduate Student, Department of Civil Engineering, National Taiwan University.

³ Research Fellow, National Center for Research on Earthquake Engineering.

⁴ Professor, Department of Civil Engineering, National Taiwan University.

3. Design floor response from the time-history analysis of building structures under recorded or spectrum-compatible ground motions or design the artificial spectrum-compatible floor response in accordance with the AC-156 code (ICC-ES 2010).
4. In order to prevent the seismic performance of the building structure from affecting the accuracy of the fragility analysis of the attached nonstructural systems, determine the upper limit of the scaling strength level of ground motions for the analysis of the nonstructural system, according to the repair fragility of the building structure.
5. Evaluate the fragility of the nonstructural system according to a credible numerical analysis under the arranged distribution of the strength levels and the upper limit of the ground motions.
6. Implement a performance calculation in the framework of FEMA P-58 according to the evaluated fragility curves of the failure modes of the nonstructural system.

Numerical Analysis of the Sample Sprinkler Piping System

As shown in Fig. 3, a simplified numerical model of the fire protection sprinkler system in the sample hospital was established for fragility analysis with the SAP2000 v.15 software. Ambient vibration tests in the sample hospital were conducted with velocimeters to clarify the structural characteristics of the building structure and the sprinkler piping system. Appropriate parameters to simulate the threaded joint of piping and the gap between adjacent partition walls or ceiling systems were proposed and verified by the results of component tests and shaking table tests.

In order to establish more accurate nonlinear floor responses of the hospital building under the influence of strong earthquakes, the numerical analysis of the structure was executed using MIDAS software to consider the nonlinear behavior of the RC walls and columns (Fig. 4a). The input ground motions included the original or design-spectrum-compatible values. Fig. 4b depicts the median spectra of the floor responses obtained from the numerical model and the median spectra of the artificial floor acceleration compatible with the AC156 required response spectrum. The three types of floor responses were used to examine the effect in the fragility analysis of the sprinkler piping system. Referring to the first period of the piping system (identified by the magenta line), the spectral acceleration of the AC156-compatible floor motion is much smaller than the two others.

Fragility Analysis of the Piping System

As shown in Fig. 5, seismic fragility curves of the

fire-protection sprinkler system in the sample hospital were conducted by incremental dynamical analysis (Method A), which is the traditional method for fragility analysis. Numbers of detailed analysis were executed for eight strength levels with three types of floor accelerations. Three discussed damage states of the sprinkler piping and adjacent ceiling systems included the collapse of regional piping segments, the leakage of 1-inch threaded joints, and damage to ceiling boards according to the displacement of sprinkler heads. The accuracy of the numerical analysis was verified by the real damage caused by the Chia-Shen earthquake. The effects of parameters on the fragility results were examined. The engineering demand parameter (i.e., the horizontal axis of Fig. 5) for the fragility curves is the spectral acceleration at the first period of the piping system, to more accurately represent the failure probability of damage states. However, it can be seen that the fragility curves of the piping were still dependent on the type of floor acceleration. The possible cause is that the mass participation ratio of the first mode of the piping system is only 0.75, so the spectral acceleration at the fundamental period cannot reflect the effect of high modes on the fragility curves.

Simplified Seismic Evaluation Methods

Simplified fragility analysis procedures (Method B and Method C) for sprinkler piping systems in buildings are suggested for engineers as well. As shown in Fig. 6, Method B adopts numerical analyses of the main piping with specific assumptions to represent the behavior of the typical piping system. However, for Method C, the seismic behavior of typical sprinkler piping systems in hospitals can be estimated from the information obtained from an in-situ survey using evaluation sheets with Microsoft Excel 2013 software, which were established according to the tests and detailed analysis results. As shown in Fig. 7, the conservative level and accuracy of the evaluation results obtained from Method C are verified with detailed analysis results (i.e., from Method A).

References

- Applied Technology Council (2012), Seismic Performance Assessment of Buildings, FEMA P-58, Federal Emergency Management Agency.
- FEMA(2009). Quantification of Building Seismic Performance Factor, FEMA P-695 report.
- ICC Evaluation Service inc.(2010), Acceptance Criteria for Seismic Qualification by Shake-table Testing of Nonstructural Components and Systems, AC156, ICC-ES.

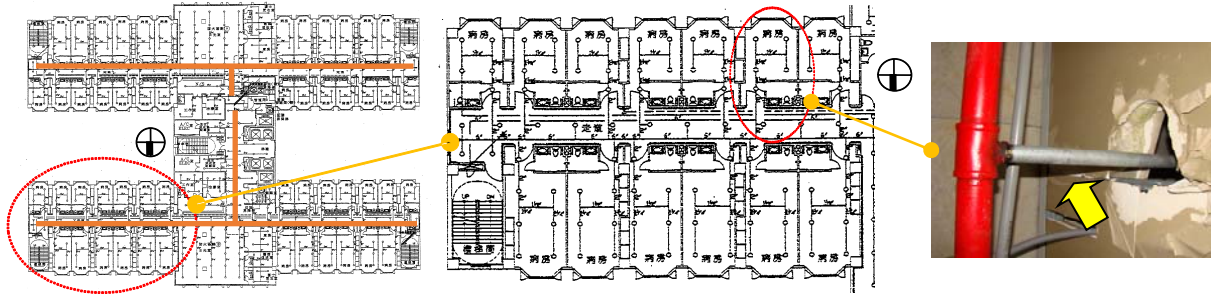


Fig. 1. Leakage of sprinkler piping in a hospital due to the 2010 Chia-Shen earthquake.

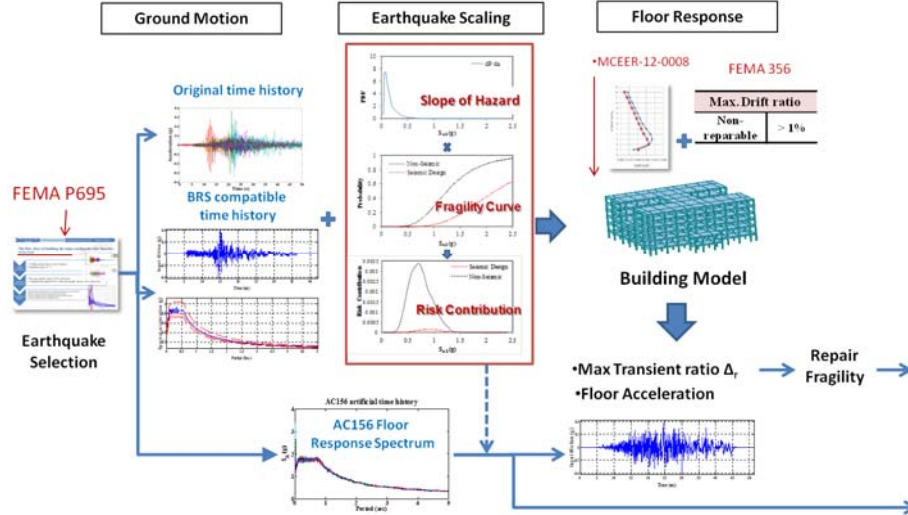


Fig. 2. Proposed evaluation procedure for the fragility of nonstructural systems in buildings.

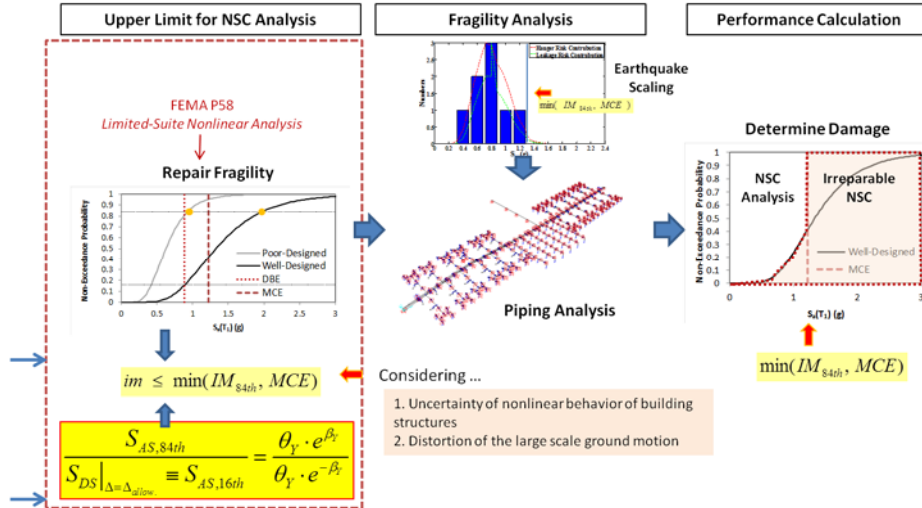


Fig. 2 (continued). Proposed evaluation procedure for the fragility of nonstructural systems in buildings.

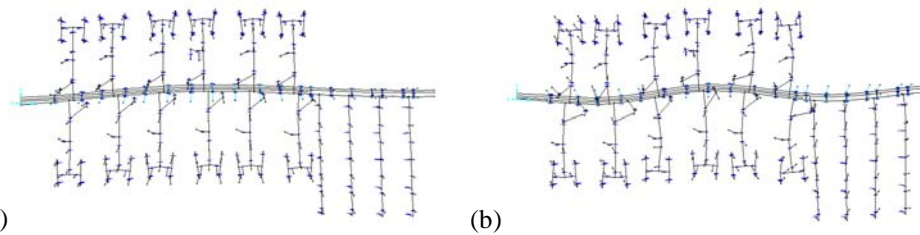


Fig. 3. Modal shapes of the sprinkler piping in the transverse direction: (a) 1st mode (1.62 Hz, mass participation ratio = 0.75); (b) 7th mode (2.62 Hz, mass participation ratio = 0.13).

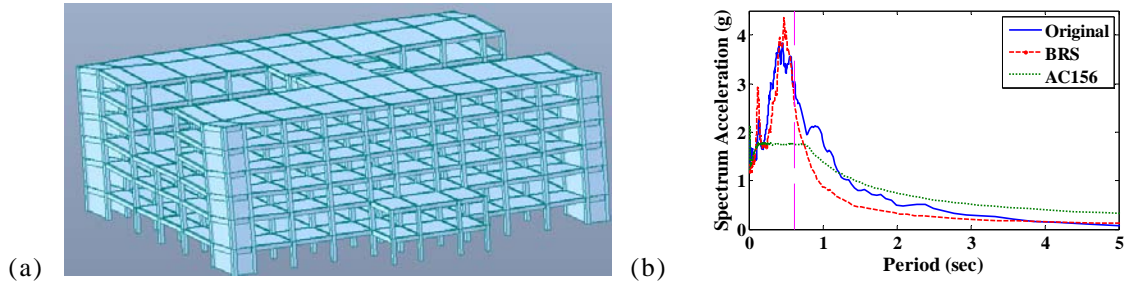


Fig. 4. (a) Modal shape of the building structure in the transverse direction (2.73Hz, mass participation ratio = 0.74); (b) Median acceleration spectra of three types of floor response at the top floor ($S_a(T_1) = 1g$).

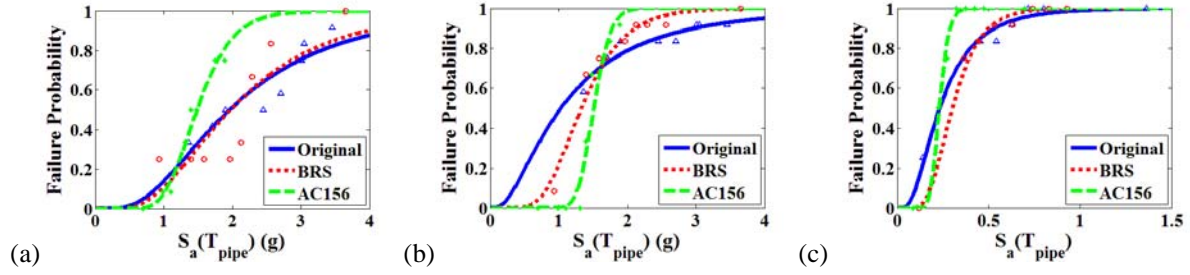


Fig. 5. Fragility curves of sprinkler piping under three types of floor acceleration: (a) Piping collapse; (b) leakage; (c) damage to ceiling boards.

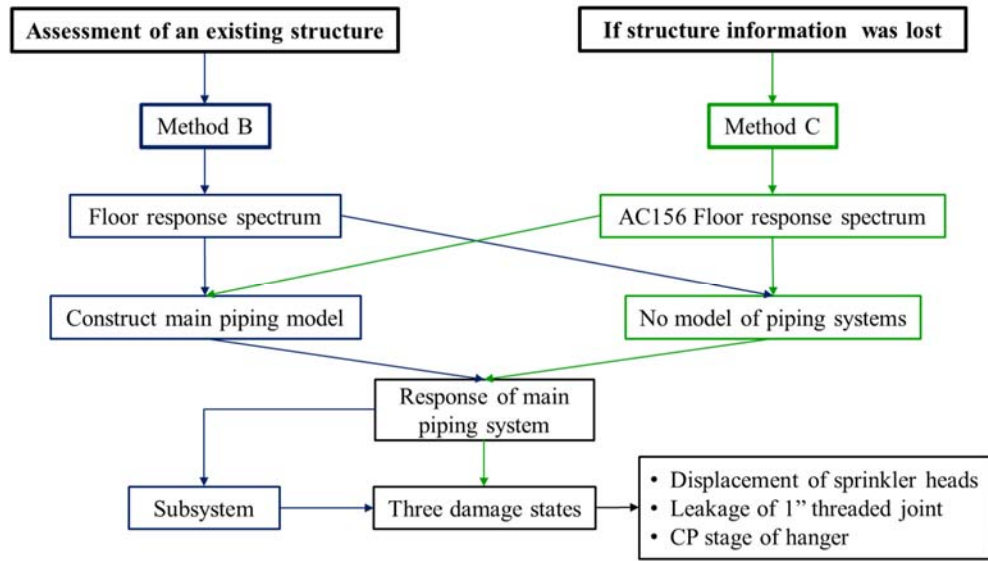


Fig. 6. Proposed evaluation procedures for the fragility of nonstructural systems in buildings.

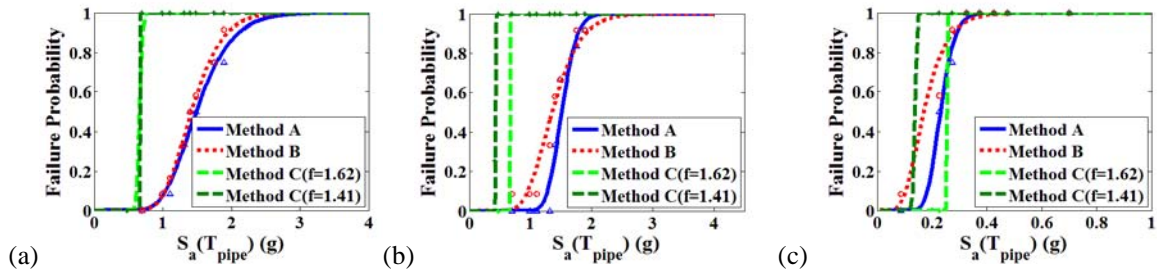


Fig. 7. Fragility curves of sprinkler piping obtained from different evaluation methods: (a) Collapse of piping; (b) leakage; (c) damage to ceiling boards.

Study of the Behavior of a Seismic Bracing Attachment for Fire Protection Sprinkler Piping System

Wei-Hung Hsu¹ Juin-Fu Chai¹ Fan-Ru Lin¹ Zen-Yu Lin¹ Jian-Xiang Wang¹ Wen-I Liao¹
Shu-Yu Kao¹

徐瑋鴻¹、柴駿甫²、林凡茹³、林震宇⁴、王鑑翔⁵、廖文義⁶、高樹禹⁷

Abstract

Taiwan is located in the Circum-Pacific Seismic Zone. The seismic capacity of buildings is relevant for protecting life and property. It is also an important topic for earthquake engineering research. In addition to the seismic capacity of building structures, earthquakes have an impact on nonstructural components, which will affect the operation of safety systems in buildings. For example, fire protection sprinkler piping systems in hospitals are very important and can reduce the incidence of fire after occurrence of an earthquake if their integrity is maintained. The standard NFPA13 developed seismic specifications for fire protection sprinkler piping systems. Among the specifications, the design of the seismic bracing was described in detail, but there were no detailed provisions for attachments between the seismic bracing and pipeline or building. Thus, the National Center for Research on Earthquake Engineering implemented research on the system in accordance with NFPA13. The study showed the weak point occurred in the attachment rather than the seismic bracing, and it reduced the seismic capacity. In this study, the deformation and the failure modes of a commercially available attachment were examined using tests and numerical analyses.

Keywords: seismic bracing, attachment, earthquake resistant design, ABAQUS analysis

Introduction

Taiwan is located in the Circum-Pacific Seismic Zone and it is frequently impacted by earthquakes. Therefore, the seismic capacity of buildings will be challenged by earthquakes. When earthquake demand exceeds the seismic capacity of buildings, it is possible to cause damage or even collapse buildings. People may get hurt or die in these circumstances. Additionally, earthquakes are often accompanied by other disasters such as tsunamis, landslides, floods, and fires, which can also cause serious damages. For example, if the fire protection system of a building functions correctly, building damages can be reduced and rescue operations can take place in the event of a fire occurring due to gas line or electric wire damage. The integrity of fire protection systems is very

important for patients if a fire occurs in a hospital.

General speaking, fire protection systems are nonstructural components. Typically, during structural design, the seismic capacity of the nonstructural components are not taken into consideration. Therefore, the influence of the seismic capacity of the nonstructural components on the buildings will be ignored. The standard NFPA13 (2013) is the earliest seismic design specification for nonstructural equipment. It provided provisions for the design of the seismic bracing of the fire protection sprinkler piping system. It also stated that some proper components can be used to reduce relative displacement between a pipeline and floor slab to avoid damage due to large displacement. These components include (1) Flexible Coupling, (2) Seismic Separation Assembly, (3)

¹ Assistant Researcher, National Center for Research on Earthquake Engineering

² Research Fellow, National Center for Research on Earthquake Engineering

³ Assistant Researcher, National Center for Research on Earthquake Engineering

⁴ Research Assistant, National Center for Research on Earthquake Engineering

⁵ Research Assistant, National Center for Research on Earthquake Engineering

⁶ Professor, Department of Civil Engineering, National Taipei University of Technology

⁷ Graduate Student, Department of Civil Engineering, National Taipei University of Technology

Clearance, (4) Piping Support, and (5) Sway Bracing. In the NFPA13 standard, the design of the seismic bracing was described in detail, but there were no detailed provisions for attachment between the seismic bracing and pipeline or building. Thus, the National Center for Research on Earthquake Engineering implemented research on systems following NFPA13 (2014). The study showed that the weak point occurred in the attachment rather than the seismic bracing, and it reduced the seismic capacity. In this study, the deformation and the failure modes of commercially available attachment will be determined with tests and numerical analyses.

Uniaxial Tensile Tests

This study aims to test and analyze the commercially available attachment constructed of ASTM A36 steel as shown in Fig. 1 It includes a main body, bolt and sleeve tube. The main body is fixed on structures and the sleeve tube is connected to seismic bracing. In uniaxial experiments, the attachment was installed in a universal testing machine by different fixtures for tensile and shear tests. The purpose of the uniaxial test is to obtain response and failure modes of the attachment under an applied force with various directions. Also, the weak point of the attachment was observed.

Fig. 2 shows tensile test results of three testing samples. It can be seen that tensile behaviors before ultimate load are similar, and the average ultimate load is about 33400 N. From the tests, the failure mode of the attachment can be seen in Fig. 3. It shows that a tearing break occurred in the region between the bottom and lateral sides of the attachment. Fig. 4 shows shear test results of two samples. It can be seen that the external load remains constant until the displacement is about 65 mm. Also, the shear behaviors before ultimate load are similar, and the average ultimate load is about 30850 N. From the test, the failure mode of the attachment can be seen in Fig. 5. It also shows a tearing break occurred in the region between the bottom and lateral sides of the attachment. By comparing Fig. 2 with Fig. 4, it was determined that the ultimate load and the break locations for the two cases are similar, but the displacement of the attachment during the shear test is larger.

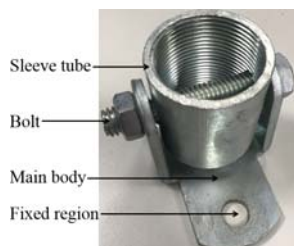


Fig. 1. Attachment picture.

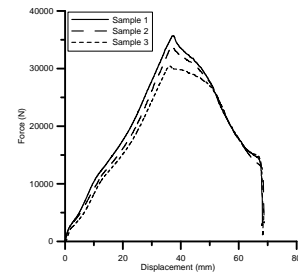


Fig. 2. The force-displacement relationship of 3 samples during tensile tests.



Fig. 3. Failure mode for the tensile test.

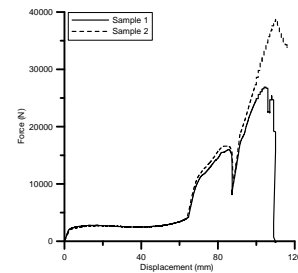


Fig. 4. The force-displacement relationship of 2 samples during shear tests.



Fig. 5. Failure mode for the shear test.

Finite Element Analysis

This study uses the commercial finite element analysis software ABAQUS to analyze all cases. The tensile cases are simulated and then compared with test results. After comparison, the case for a force at a 45 degrees angle is predicted with the simulation. Fig. 6 gives a schematic diagram for force directions.

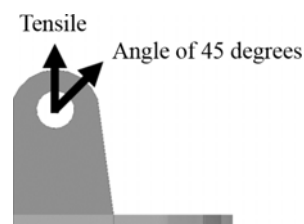


Fig. 6. Schematic diagram for force directions.

Tensile analysis of the attachment

Fig. 7 shows the numerical model for the base tensile case. This model only includes a main body, a bolt and a washer; other parts have relatively high stiffness and are modelled as linear spring elements. Additionally, one unknown part stiffness is added to the model to adjust the initial stiffness of the system. Table 1 gives spring constants of the parts used in the model. The spring constants were obtained by ABAQUS simulation. The attachment material is ASTM A36, and the bolt material is ASTM A325. It is assumed that the washer is made of steel with a 350 MPa yielding strength. The attachment is commercially available so the correct material properties are unknown. The procedure used in this study is to obtain material properties by comparing the results of tensile analysis with that of tensile tests. Once the material properties are obtained, all analysis cases are implemented. In this study, only the elastic-plastic behavior of the attachment is considered.

Fig. 8 shows the results of the tensile tests and tensile analysis. It gives the relationship between force and displacement. From the figure, it can be observed that the experimental and simulated results are very closed. The effective stress and principal strain contours for the analysis are shown in Fig. 9. The higher stress and strain occurs in the junction of the bottom side and lateral sides of the attachment. There is a stress concentration here because the region is a geometrically discontinuous area. This is very similar to the tearing break location of the tested samples. As the elongation of ASTM A36 is 20%, it can be assumed that the attachment failure occurs when the maximum principal strain approaches the elongation. At this point, the ultimate force, which is the capacity of the attachment to resist external force, is defined. The ultimate force can be used as a basis for judging the performance of the attachment. Fig. 10 shows the relationship between external force and principal strain at point A in the tensile analysis. From the figure, the external force will be 19000 N when the principal strain is 20%.

Table 1. Spring constants of the parts used in the model.

Spring Constants of Parts	
Parts	Spring constants (N/mm)
T type fixture (K_F)	127951
Bolt between main body and sleeve tube (K_{LB})	246697
Sleeve tube (K_S)	657560
Unknown part (K_{Att})	2475

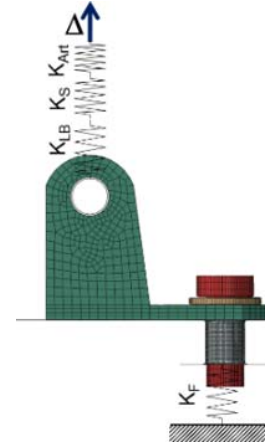


Fig. 7. Numerical model for the tensile analysis.

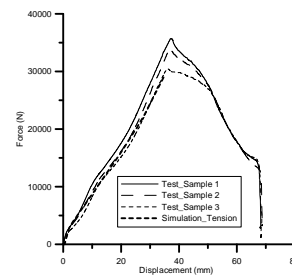
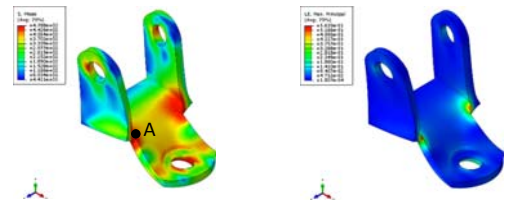


Fig. 8. The force-displacement relationship between tensile tests and tensile analysis.



(a) Effective stress (b) Principal strain

Fig. 9. The effective stress and principal strain contours for tensile analysis.

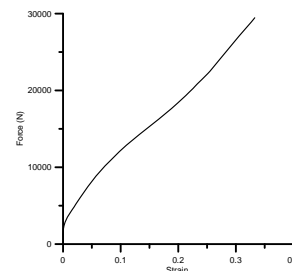


Fig. 10. The force-principal strain at point A for tensile analysis.

45° angle tensile analysis of the attachment

When seismic bracing is installed in a building, it is usually at a specific angle to a beam or column in the buildings. The angle will be positive or negative 45°, as shown in Fig. 11, due to construction considerations.

Fig. 12 shows the relationship between force and displacement of the 45° angle tensile analysis. From the results, it can be observed that the seismic bracing with an angle of negative 45° has a larger resisting force and higher stiffness. The effective stress and principal strain contours for angles of positive 45° and negative 45° are shown in Fig. 13 and Fig. 14, respectively. In addition to the junction of the bottom and lateral sides of the attachment, the region closed to the bolt also has a larger stress and strain. From the analysis, the predicted break location will be similar to the tensile analysis. Fig. 15 shows the relationship between external force and principal strain at point A in this 45° angle tensile analysis. From the result, the external force will be 14500 N and 20000 N for the positive and negative angle when the principal strain is 20%. This proves that the negative angle case can resist a larger external force than the positive angle case.

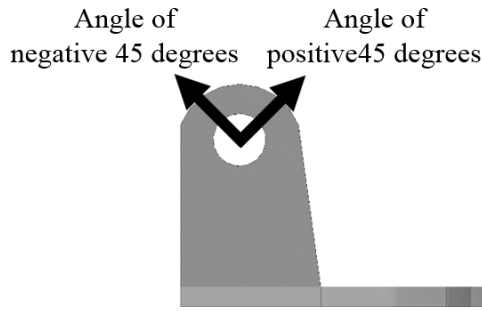


Fig. 11. Schematic diagram for force directions.

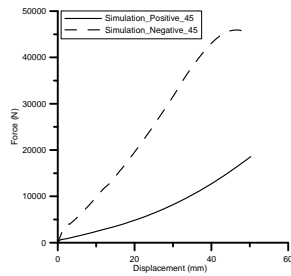
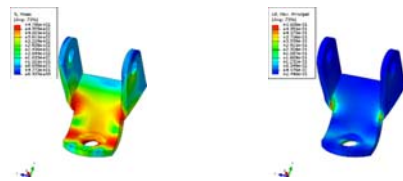
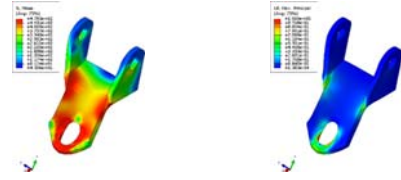


Fig. 12. The force-displacement results of the 45° angle tensile analysis.



(a) Effective stress (b) Principal strain

Fig. 13. The effective stress and principal strain contours for positive 45° angle tensile analysis.



(a) Effective stress (b) Principal strain

Fig. 14. The effective stress and principal strain contours for negative 45° angle tensile analysis.

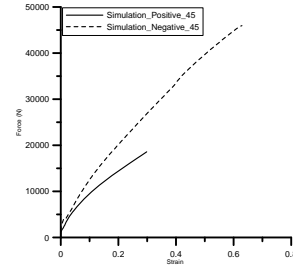


Fig. 15. The force-principal strain at point A for 45° angle tensile analysis.

Conclusions

To understand the behavior of a seismic bracing attachment for fire protection sprinkler piping system, a commercially available attachment was studied by uniaxial tests and numerical analyses. From the tests, the failure mode of the attachment was observed. The elastic-plastic behaviors of the attachment were examined by comparing the results of testing and numerical analyses. Finally, the results showed that the break location occurred at the junction of the bottom and lateral sides of the attachment or in the region close to the bolt. It also showed that the directions of external forces would affect the deformation and the capacity of the attachment. To obtain higher capacity to resist external forces, an angle of negative 45° is recommended.

References

- NFPA 13, (2013). "Standard for the Installation of Sprinkler Systems", National Fire Protection Association, Quincy, Massachusetts.
- Lin, F.R., Chai, J.F., Lin, Z.Y., Wang, J.X., Chang, K.C. and Liao, W.I., (2014). "Shaking Table Tests for Seismic Improvement of A Typical Sprinkler Piping System in Hospitals", 5th Asia Conference on Earthquake Engineering, Taipei, Taiwan.

An Experimental Study of a Residual Heat Removal Piping System in an NPP

Zih-Yu Lai¹, Juin-Fu Chai², Fan-Ru Lin¹, Wen-Fang Wu³ and Yin-Nan Huang⁴

賴姿妤¹、柴駿甫²、林凡茹¹、吳文方³、黃尹男⁴

Abstract

In order to highlight the vulnerability of Residual Heat Removal (RHR) piping systems for fragility analysis, a segment of the RHR piping that includes a heavy motor operated valve (MOV), a flanged joint, and reducer was numerically modelled to simulate the dynamic behavior during strong earthquakes. Three kinds of tests were completed in this study to verify the accuracy of the numerical model. First, pure bending tests with four-point cyclic loading were adopted for the flanged joint to investigate the nonlinear behaviors and establish reliable component models using finite element analysis software. Second, quasi-static tests for the chosen segments of piping were executed to carefully observe the response of the piping under cyclic loading. Finally, shaking table tests were completed to investigate its dynamic characteristics and to verify the results of the numerical analysis. According to the test results, the seismic performance of the RHR piping system in the sample NPP is better than the assessment results in the FSAR. However, it's noted that an unexpected failure mode of the flanged joint occurred during the pure bending test and caused the leakage of the tested specimen.

Keywords: Piping system, Flanged joint, Quasi-static tests, Shaking table tests

Introduction

The design of RHR piping system should meet the requirements of the ASME Boiler and Pressure Vessel Code, Section III, Division 1, Subsection NB. RHR piping systems consist of pipes, supports, piping components, etc. The latter are important for the integrity of the pipeline which including elbows, flanged joints, reducers, tees, and in-line equipment. According to EPRI-1019199, the heavy in-line components of risers should have a vertical support located close to the lateral support and the spans should be less than 7 times of the suggested vertical support. From the drawings and the in-situ investigation at the NPP, it was found that the in-line MOV, which is near the RCCV, causes serious damage to adjacent RHR piping during strong earthquakes. The MOV, weighing up to 1,624 kg, is mainly supported by the RCCV at one elbow. The lateral one is a pipe saddle with strap at the floor penetration across two elbows, a reducer, and a flanged joint.

In order to investigate the contribution of the RHR piping system to a nuclear melt-down, this study aims to establish creditable numerical models for the fragility analysis of the RHR piping system. Ideally, the scope of testing and analysis should run from structural anchor to structural anchor, but this is difficult to achieve in real applications. In general, instead of a real anchorage point, the boundary of an established model has to include at least three changes of direction and two seismic supports in each of three orthogonal directions, as shown in Fig.1. For the purpose of investigation, the seismic effects of the MOV on the adjacent RHR piping segments and components, nodes 1 and 13 are defined as the fixed ends of the model. This is done in order to represent the critical part of the RHR piping system according to the analysis results in Shen [1]. As shown in Fig.2, the sample RHR piping system is defined from the support of the floor-penetration guard at the floor EL12.3 m to the welded connection to the RCCV-penetration guard at EL14.6 m.

¹ Assistant Researcher, National Center for Research on Earthquake Engineering

² Research Fellow, National Center for Research on Earthquake Engineering

³ Professor, Dep. Mechanical Engineering National Taiwan University

⁴ Associate Professor, Dep. Civil Engineering National Taiwan University

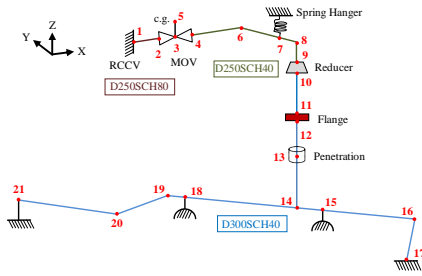


Fig. 1. Section diagram of the sample piping system

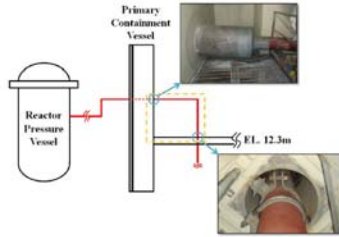


Fig. 2. The range of the piping specimen

As shown in Fig. 1 and Table 1, three types of sections are used in the sample piping system. Piping segments are made of seamless steel (ASME SA333 Gr.6) and welded together. For other components, the MOV, which comprises the bulk of the weight of the sample pipe system, consists of an electric motor and a valve. The material of the reducer and the flanged joint are SA420 WPL6 and SA350L2, respectively. The spring hanger consists of a pre-set helical coil spring and is used to compensate for the slight vertical displacements of the piping.

Table 1 Section and material properties of pipes

Section Name	Outer Diameter (mm)	Thickness (mm)	Yield Stress, F_y (MPa)	Ultimate Stress, F_u (MPa)	Young's modulus (MPa)
250 SCH40	273.05	9.27	327.5	451.5	2.03×10^5
250 SCH80	273.05	15.06			2.05×10^5
300 SCH40	323.85	10.31			2.11×10^5

In this study, three testing stages were arranged. They include component tests for the reducer and the flanged joint, and quasi-static tests and shaking-table tests for the research scope of the RHR piping system (Fig. 3). The purposes of these tests is to obtain mechanical properties of the joint components and to verify the accurate of the FEMs. This paper aims to discuss the results of the tests and analysis at the system level. More details about the component tests for the flanged joint are introduced in Chai [2].

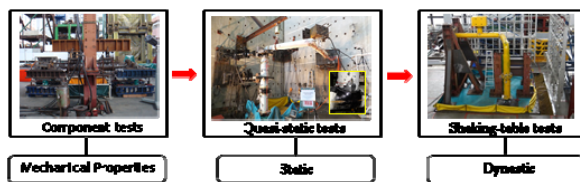


Fig. 3. Research process

Quasi-Static Test of the RHR Piping System

In order to estimate the quasi-static load pattern, a 3D FEM of the sample piping system was developed with SAP2000 to simplify the dynamic seismic force to the centralized static force. As shown in Fig. 3, the flanged joint was simulated by a linear link with a transfer stiffness of 30 kN/m and a rotation stiffness of 1000 kN-m/degree according to the results of the component test for the flanged joint. The MOV was simulated by a rigid link element to connect both sides of the pipe. The boundaries of the model were fixed to simulate the supports from the RCCV and the floor. Fig. 4 depicts the FEM of the sample piping system which is developed on the basis of the aforementioned detail and the original drawing.

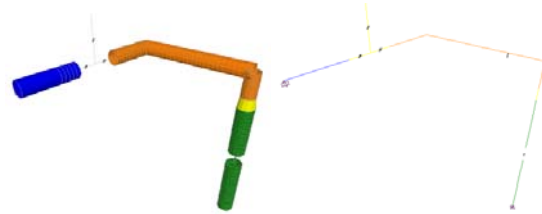


Fig. 4. Numerical model of the RHR piping system

The input motions for nonlinear response history analysis were derived for the node located on the floor of Reaction Building (RB) using a lumped mass model of the sample NPP subjected to SSE. The damping ratio was defined by 5% according to EPRI-6041. Based on the results of inertial force and the responses at critical locations of the piping system under SSE, four equivalent concentrated static loads were determined (Fig. 5).

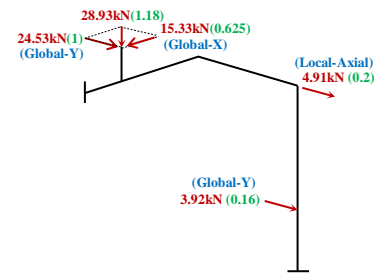


Fig. 5. The load pattern for quasi-static tests

As shown in Fig.6, the cyclic loading test of the RHR piping system was set up according to the numerical model. Two adapters with four load cells between them were placed on the tip of the specimen. They were attached to the reaction wall to simulate the RCCV, while the specimen was being welded on the other side of the adapters. On the other hand, the bottom of the specimen was connected to the strong floor with one load cell in between. The pipelines, flanges, reducer, and spring hanger in the full-scale test were duplicated from the one in the NPP with the same material and geometry. However, the MOV and its support were replaced by a block supported by a

concrete-filled steel pipeline with the same weight, stiffness and center of gravity as the actual ones in the NPP.

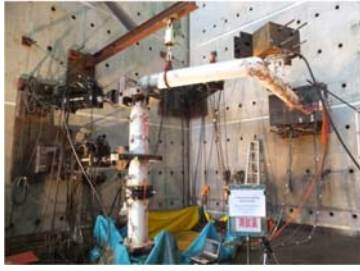


Fig. 6. The load pattern for quasi-static tests

For the cyclic loading test, the test protocol was defined by two types of input motions with different intensity levels. The one with the smaller intensity keeps the responses of the specimen within the elastic range, and the one with larger intensity is adopted for fragility testing.

The maximum strain and the associated stress occurred at the boundary connecting the RCCV (S11) and the T-joint supporting the MOV (S9). As shown in Fig.7, the maximum stress (119.4 MPa) is less than the yielding stress (331MPa), and consequently, the pipeline stays in the elastic range as expected.

From Fig.8, it can be seen that the stress at S9 increases significantly as the displacement of the MOV increases to the range of 20 to 30 mm. This is caused by the loss of enhancement from the infilled concrete due to its rupture and dropping-off in the T-shaped MOV support under these deformation conditions.

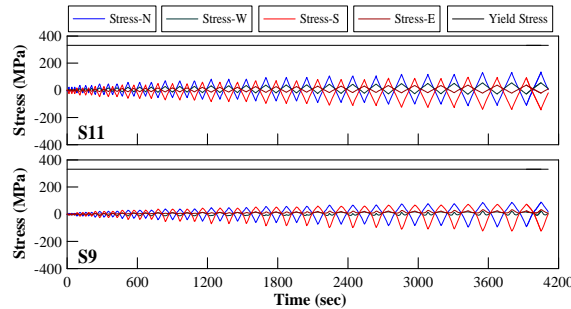


Fig. 7. Comparison of the induced stress and yielding stress for elastic testing

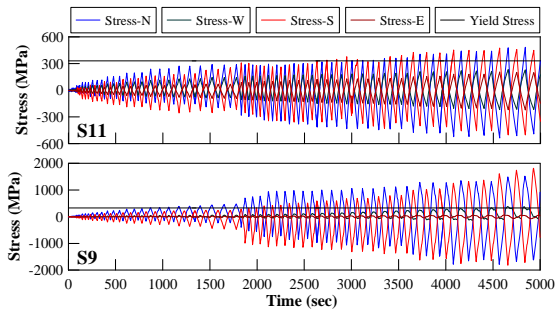
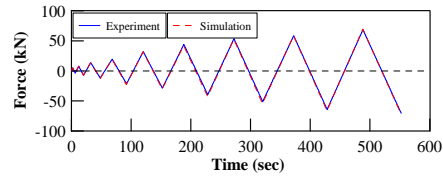


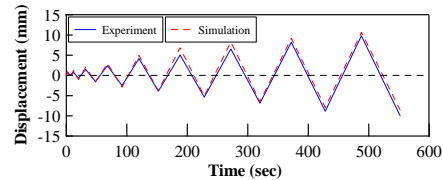
Fig. 8. Comparison of the induced stress and yielding stress for fragility testing

Because of the deformation of load cells arranged in the quasi-static tests, the fixed boundary condition assumed in the numerical analysis should be modified. The “link element” was adopted to model the load cells, and the axial and shear stiffness were taken to be 600 kN/mm and 45 kN/mm from the tension and shear tests of the load cells, respectively. The rotation stiffness of the load cell was 1.2×10^6 kN-mm/rad.

The reaction forces on the RCCV boundary, determined numerically and measured from the tests, are compared in Fig. 9a. Fig. 9b shows the comparison of the displacement responses at the spring hanger (D8X). The good agreement between the numerical and experimental results verifies the correctness of the proposed numerical model.



(a) Reaction Force_X (#1~#4)



(b) Displacement (D8X)

Fig. 9. Comparison of the numerical and experimental results

Shaking Table Test of the RHR Piping System

The specimen of the RHR piping system is almost the same as the one used in the quasi-static test. However, the stiffness of the MOV support was strengthened by increasing the thickness of the steel tube (SCH100) but not the infilled concrete. In addition, the spring hanger was removed.

The infilled water exerts a pressure of 7 kgf/cm². The load cells are arranged between the top end of the specimen and the rigid frame, and between the bottom end and the shaking table, to measure the reaction forces and moments. An accelerometer measures the three components of the acceleration response (Fig. 10).

Similar to the input motions for the nonlinear response-history analysis, the input motion is the floor response at the location supporting the sample RHR piping system under 2×SSE. The seed ground motion are EQ-342 and EQ-1059 from the PEER database and the ground motions recorded at ILA-057 and TAP-070 in the Taiwan Chi-Chi earthquake. The time histories of the input motion are shown in Fig. 11.

Based on the white-noise test, the essential frequencies of the piping system and reaction frame are listed in Table 2. Table 3 shows the maximum acceleration at the vertical and horizontal pipeline, the elbows in the vertical and horizontal places, and the MOV under the excitation of ILA-057 with an intensity of 2×SSE. The bending moment at critical locations with larger values are listed in Table 4.

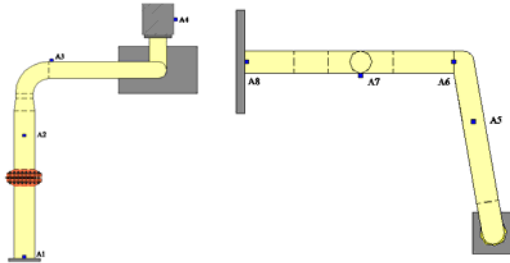


Fig.10 Arrangement of accelerometers

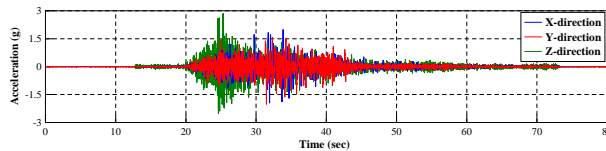


Fig.11 Time histories of the input motion corresponding to 200% SSE (ILA-057)

Table 2 Natural frequencies of the piping system and reaction frame

Unit : Hz	Reaction Frame	Piping system (w/o water)	Piping system (w/ water)
X-dir.	25.6	13.7	11.9
Y-dir.	41.2	8.0	7.4

Table 3 The maximum acceleration response under 2×SSE (ILA-057)

Unit : g	Vertical pipeline (A2)		Horizontal pipeline (A5)		Vertical elbow (A3)	
	w/o water	w/ water	w/o water	w/ water	w/o water	w/ water
X	7.6	7.0	4.3	4.1	9.5	7.7
Y	4.5	5.0	5.0	5.4	5.9	6.3
Unit : g	Horizontal elbow (A6)		MOV (A4)			
	w/o water	w/ water	w/o water	w/ water		
X	2.8	2.6	5.8	4.3		
Y	4.6	4.5	3.3	3.7		

Table 4 The maximum moment response under 2×SSE (ILA-057)

Unit : kN-m	RCCV boundary		Bottom of MOV support		Top of Flange	
	w/o water	w/ water	w/o water	w/ water	w/o water	w/ water
X	-- ⁽¹⁾	124	45.6	58.9	10.7	19.9
Y	59.7	-- ⁽¹⁾	28.2	36.8	4.6	14.5
Unit :	Horizontal elbow		Vertical elbow			

kN-m	w/o water	w/ water	w/o water	w/ water		
X	-- ⁽¹⁾	7.4	13.4	14.7		
Y	20.1	29.8	3.9	10.2		

Note (1) : No moment determined due to the damage of strain gauges

As shown in Fig. 12, the steel frame should be modelled together with the piping system in the numerical analysis. The time histories of acceleration response by the model for the case of no infill of water are also shown, and the results are in agreement with measurements taken during the shaking table test. However, for the case with infilled water, the numerical and experimental results do not agree very well. This is so because the numerical model cannot accurately reflect the behavior of infilled water under dynamic excitation.

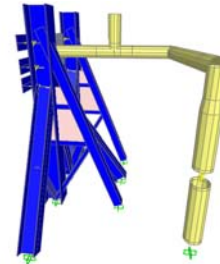


Fig.11 Combined numerical model for the shaking table test

Conclusions

In order to verify the accuracy of the numerical model for fragility analysis, a sequence of three types of experiments were carried out. However, it is noted that an unexpected failure mode of the flange joint occurred during the pure bending test and caused leakage of the tested specimen.

In this study, the numerical analysis of the sample RHR piping system was established by the SAP2000 software package. By comparison numerical and experimental results, it is seen that the proposed numerical model can predict the static response of the RHR piping system well. For dynamic analysis, the accuracy of the proposed model is acceptable for the case of no infilled water. However, the results are not good for the case with infilled water. This may be due to the limitation of SAP2000 when simulating the mechanical properties of hydraulic devices and the dynamic behavior of infilled water. Other software packages (e.g. PIPESTRESS) will be used for future studies of the dynamic behavior of piping systems.

References

- M.-Y.Shen, J.-F. Chai, F.-R. Lin, Z.-Y. Lai, Y.-N. Huang and C.-C. Yu (2014). "Numerical Analysis of a RHR Piping System Subjected to Seismic Loading," PVP 2014.
- J.-F. Chai, F.-R. Lin, Y.-S. Lyu, Z.-Y. Lai and W.-F. Wu (2017). "Numerical Modelling and Experimental Validation of the Flange Joint of a Piping System in Nuclear Power Plants," SMIRT 24.

Numerical Modelling and Experimental Validation of the Flange Joint of a Piping System in Nuclear Power Plants

Juin-Fu Chai¹, Fan-Ru Lin², Zih-Yu Lai² and Wen-Fang Wu³

柴駿甫¹、林凡茹²、賴姿妤²、吳文方³

Abstract

In a previous experimental study for the flanged joint of a RHR piping system in a NPP, leakage occurred at the tested flanged joint, due to its loosened bolts while the joint was subjected to pure-bending loading. To clarify the cause of this phenomenon, this study aims to investigate the effect of the deformation of the flange gasket on the decrease in the pre-stress of the bolts. In the first part of this study, a series of compression loading tests for components of the flange gasket is executed in order to understand in detail the behavior of the flange gasket with pre-stressed bolts. Next, according to the deformation behavior of the gasket obtained from tests, the flanged joint is modelled using the ABAQUS commercial code. Finally, shaking table tests for a part of the RHR piping system with the flanged joint are executed to verify the accuracy of the corresponding numerical model under dynamic loading. The applicability of ASME's Boiler and Pressure Vessel Code to evaluating of this type of flanged joints is discussed as well.

Keywords: Piping system, Flange gasket, Shaking table test, Numerical model,

Introduction

This paper aims to investigate the seismic performances of the flanged joint in order to ensure that the sealing ability of piping is maintained at this discontinuous segment during an earthquake. The tests conducted included component testing of the material of the flanged gasket under pure-bending loads. Further numerical analyses are also proposed to effectively estimate the capacity with relation to failure mode causing leakage. The accuracy of the numerical models is verified through component testing of flanged joints and through shaking table tests for the selected range of the RHR piping system.

According to the diagrammatic piping and in-situ investigation in the NPP, the flanged joint belonging to the RHR piping system is reproduced for further studies. As shown in Fig.1, the components of the flanged joint include a spiral-wound gasket, sixteen bolts and nuts. The flanged joint was mainly made of A350 carbon steel, and the material of pipes was SA333Gr6 carbon steel with yield and ultimate tensile strengths of 324 and 449 MPa, respectively.

A flanged joint belonging to the class 1 components of the nuclear facility, which are

subjected to the combinations of moment and pressure, must meet the requirements of the ASME B&PV Code [2] and design specification [3]. In order to compare the test results with the design requirements as specified for ASME Service Levels B and D, it is necessary to understand the plant events associated with earthquakes as well as the related service loading combinations, the expected performance levels, and the associated limitations of dynamic moments. There is little discussion on flanged joints in NUREG 1367 [4] since the loss of functional capability of a flanged joint was deemed to be implausible.

The moment demands for Levels B and D were calculated according to the equations given in paragraph NB-3658 "Analysis of Flange Joints" in the ASME Division 1-Subsection NB to prevent excessive leakage at the joints. In the ASME Code, the pressure shall not exceed 1.1 times the rated pressure for Level B given by :

$$M_{fd} \leq 43.4A_b \times C(S_y/250) \quad (1)$$

In addition, the acceptance criteria of Level D is given by:

$$M_{fd} \leq [78.1A_b - (\pi/16)D_f^2 P_{fd}] \times C(S_y/250) \quad (2)$$

¹ Research Fellow, National Center for Research on Earthquake Engineering

² Assistant Researcher, National Center for Research on Earthquake Engineering

³ Professor, Dep. Mechanical Engineering, National Taiwan University

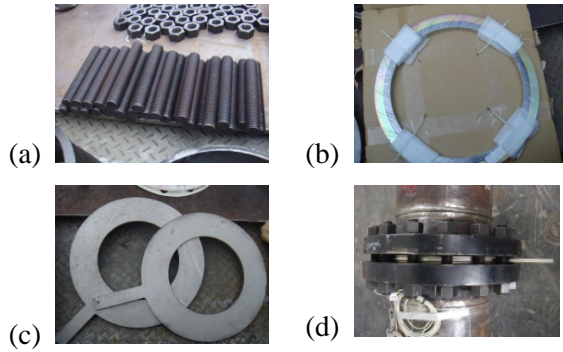


Fig.1 Components of the tested flanged joint: (a) stud bolts and nuts, (b) gasket, (c) pressure breakdown orifices, and (d) flanged joint.

Tests of the Flanged Joint and Gasket

Pure-bending Test of a Flanged Joint

The test setup was arranged in a four-point bending configuration. As shown in Fig. 2, the cyclic loading was applied by the actuator through the adapter composed of a beam and rotary fixtures allocated to both side of the piping joint to impose pure-bending loading on the segment between the rotary fixtures. The loading protocol was designed according to the cyclic displacement schedules proposed by ISO-16670. In this study, the ultimate displacement (v_u) was chosen to be 50 mm according to the numerical analysis results. Fig.3 depicts the amplitude of each cycle as a percentage of v_u .

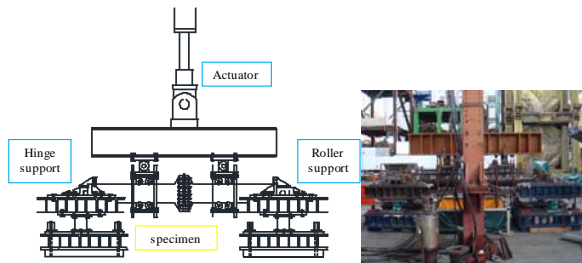


Fig.2 The configuration and image of the pure-bending test.

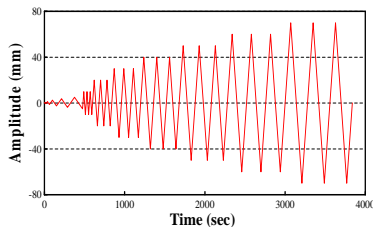
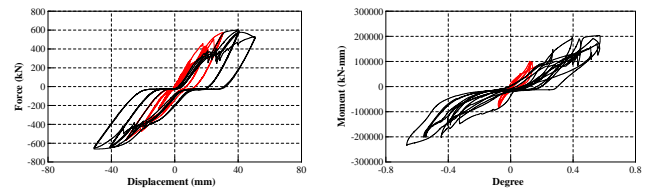


Fig.3 Displacement time-history input

In the pure-bending test for the flanged joint, the leakage condition occurred as a result of loosening of bolts without breakage. The force-displacement hysteretic loops of the flange specimen were established using the specified displacement and associated force of actuator (Fig.4(a)). The initial stiffness of vertical displacement in the elastic stage (red line) is approximately 30 kN/m, while the applied

force of the actuator was approximately 600 kN. The stress concentration at the area of the loading point caused local plastic deformation of the piping segment and also resulted in gaps between fixtures and specimen. The moment-rotation hysteretic loops are presented in Fig.4(b). The rotation stiffness in the elastic stage (red line) is approximately 1000 kN-m/degree and decreases to 250 kN-m/degree in the plastic stage (black line), due to several bolts at the top and bottom of the flange. Leakage occurred with loosened but undamaged flanged bolts when the displacement applied by the actuator was 20 mm and the associated moment was 100 kN-m.

Comparing the test results and allowable bending moments, the capacity of flanged joints against leakage is much smaller than the allowable bending moment of 201.19 kN-m defined for Service Level B under the consideration of loads induced by an operating basis earthquake and normal operation or system operational transients. The capacity obtained from the test is also smaller than the allowable bending moment of 352 kN-m defined by Service Level D under the consideration of loads induced by normal operation, safe shutdown earthquake, a break loss-of-coolant accident, and/or Safety/relief valve actions. This implies that the code-defined capacity for Service Level B and D may be less conservative for the purpose to preventing excessive leakage at the flanged joint as a result of its loosened bolts.



(a) Force-displacement (b) Moment-rotation curve

Fig.4 Hysteretic loops of the flanged joint

Cyclic-Loading Tests for Components of a Flanged Joint

The interface layer of the flanged joint includes a flowmeter and a spiral-wound gasket, which consist of one inter and one outer metal ring, and a composite layer made of metal hoops and sealing material (graphite) between the metal rings. In order to clarify the relation between the leakage and characteristics of the interface layer, a series of quasi-static cyclic-loading tests of the interface layer and bolt, the interface layer, and the flowmeter only was carried out in this study.

In the cyclic-loading tests of the interface layers and bolt, the complete interface layer was divided into sixteen sets for use as the test specimens in the cyclic-loading test to simulate each bearing part of one bolt (Fig.5(b)). The fixtures between the bolt and the interface layer are 50 mm in thickness and made of medium carbon steel to simulate the metal flanges

(Fig.5(c)). The cyclic-loading tests were designed to be force-controlled in order to simulate external force on the bolt at the top position during the pure-bending test for the flanged joint. As shown in Fig.5(a), the external forces on the sixteen bolts during the pure-bending test were evaluated based on the assumption that the section of the flanged joint was kept in a flat surface.

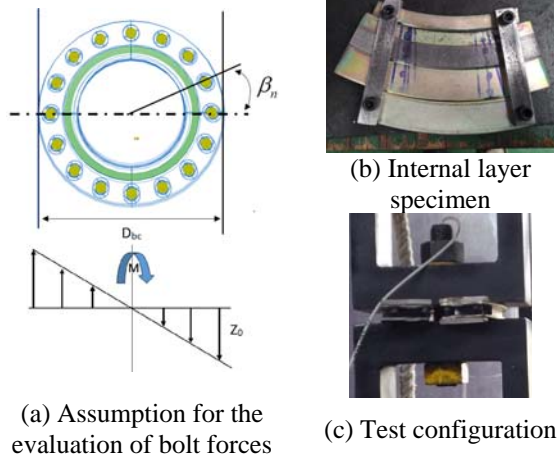


Fig. 5. Tests for the bolt and internal layer

The blue line in Fig.6 shows the simulated external force for the bolt and interface layer in the pure-bending test. It can be seen that the initially pre-stressed force of the bolt (approximately 55kN) gradually decayed to 12kN under the increasing cyclic axial loading. The decaying pre-stressed force of the bolt might be caused by the permanent deformation of the interface layer due to the broken graphite material. On the other hand, the pre-stressed tension force was decreased to zero while the compression loading reached to 75.8 kN, which explains the phenomenon that, during the pure-bending test of the flanged joint, leakage occurred by turns at the top or bottom bolts on the compression side.

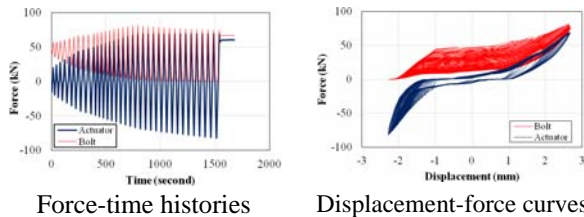


Fig. 6. Test results for the internal layer and bolt

As shown in Fig.7, cyclic-loading tests for the interface layer and for the flowmeter only were conducted to clarify the resistance behavior of the spiral-wound gasket and the flowmeter respectively during the cyclic-loading tests for the bolt and the interface layer. Comparing the force-displacement curves of the interface layer and the flowmeter (Fig. 8(a) and Fig.8(b)), it can be seen that the initial lower stiffness of the interface layer was mainly governed by the protruding composite layer of the spiral-wound gasket with the extremely high stiffness of the

flowmeter.

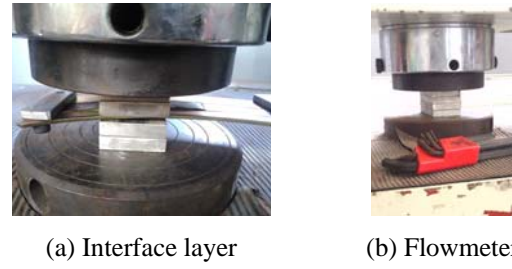


Fig. 7. Test configuration of cyclic-loading tests

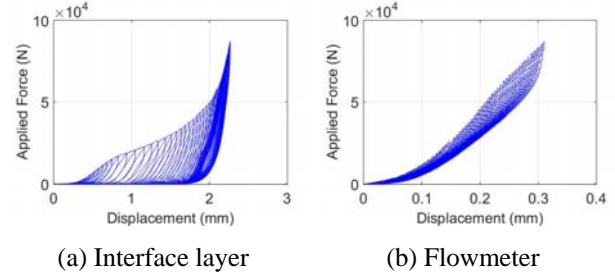


Fig. 8. Force-Displacement Curves

Numerical Analysis of the Flanged Joint

Spiral-Wound Gasket

According to the test results for the interface layer and for the flowmeter under cyclic loading, as shown in Fig.9, the simplified resistance behavior of the spiral-wound gasket was derived to establish a numerical model using ABAQUS. The inner and outer rings were ignored and only the shape of the composite layer was simulated to represent the gasket.

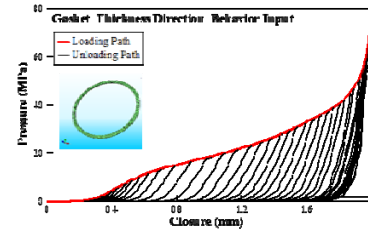


Fig. 9. Resistance behavior of the gasket and model

Verification of the Gasket Model

In order to use the results of cyclic-loading tests to verify the accuracy of the gasket model, simulation of the cyclic-loading tests for the bolt and the internal layer was established using the ABAQUS software. As shown in Fig.10(a), the green parts are the spiral-wound gaskets and the red part is the flowmeter. Fig.10(b) shows a comparison of the results of the cyclic-loading test and the numerical analysis. It shows that the numerical model simulated the phenomenon that the gradually increased residual deformation of the composite layer of the gasket caused the decrease of the axial tension force of the bolt.

Simulation of the Flanged Joint

According to the numerical model of the internal

layer and the bolt of the flanged joint, the simulation of the test specimen in the pure-bending test was established to observe the variation of the decrease of the bolt force during the increasing cyclic moment loading. As shown in Fig.11(a), the achieved displacement time-history of the actuator was applied at the two adapters on both sides of the flanged joint simultaneously. Fig.11(b) shows the analysis results of the axial forces on the top and bottom bolts. The axial force of the top and bottom bolts decreased to zero while the bending moment reached 152 kN-m. Comparing to the bending moment of 100 kN-m that caused the leakage happened, it means that before the bolts were loosened, leakage might happen due to the damage of the spiral-wound gasket.

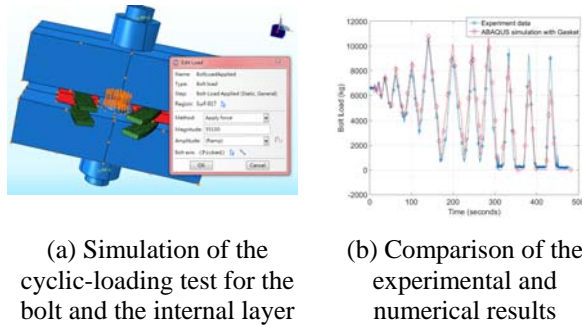


Fig. 10. Resistance behavior of the gasket and model

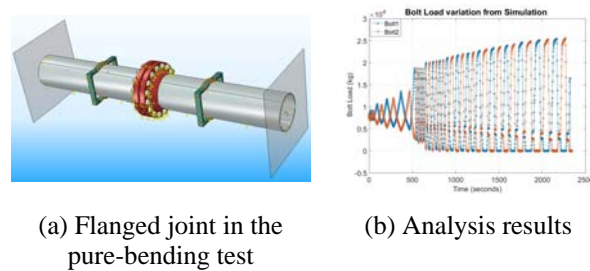


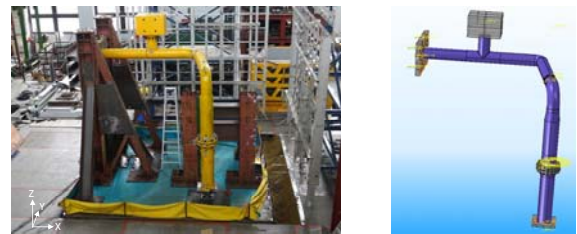
Fig. 11. Simulation of the flanged joint

Shaking Table Tests of the RHR Piping System

In addition to a series of tests for the flanged joint and its components, shaking table tests of the RHR piping system were carried out to clarify the seismic demand for the flanged joint under safe-shutdown earthquakes (SSEs). As introduced in Lai [1], the test specimen simulated a part of the RHR piping system (Fig.12a). According to the numerical model of the flanged joint in the pure-bending tests discussed above, the corresponding numerical model for the shaking table test was established with ABAQUS software (Fig.12b). The fundamental frequency of the test specimen and the numerical model were 7.4 Hz and 7.73 Hz respectively. Fig.13 depicts the comparison of the time histories of the experimental and numerical results of the piping system at the flanged position. It can be seen that the simulation of the test specimen including piping and the flanged joint was quite accurate in terms of the global response.

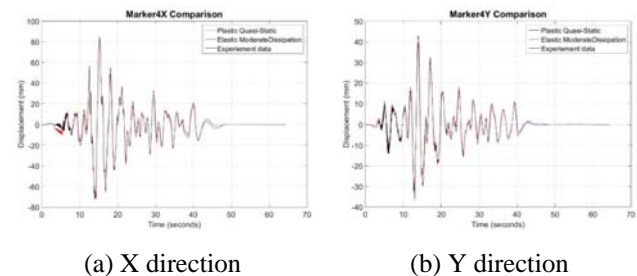
Conclusions

In the pure-bending test, the leakage condition occurred at the internal moment about 100 kN-m, which is much smaller than the allowable bending moment 352 kN-m for Service Level D in the ASME code. The top and bottom bolts of the flanged joint were also loosened during the pure-bending test. From the experimental results for the bolt and the interface layer of the flanged joint, damage to the composite layer of the gasket was confirmed to be the main reason for the leakage of the flanged joint and the loosened bolts. According to the simulation of the test specimen in the pure-bending test, leakage might be due to the damage to the spiral-wound gasket before the bolts were loosened. However, the shaking table tests for the RHR piping system in the NPP shows that the seismic demands for the flanged joint under the SSE level were much smaller than the capacity for leakage or loosened bolts of the flanged joint.



(a) Test configuration (b) Numerical model

Fig. 12. Shaking table test and simulation of the RHR piping system



(a) X direction (b) Y direction

Fig. 13. Dynamic response of the piping system at the position of the flanged joint

References

- Lai, Z.-Y., J.-F. Chai, F.-R. Lin, W.-F. Wu, and Y.-N. Huang (2017), an Experimental Study of a Residual Heat Removal Piping System in a NPP, in the Proceeding of SMiRT-24, Busan, Korea.
- ASME (2017), Rules for Construction of Nuclear Power Plant Components, ASME B&PV Code, Section III Div. 1, Subsection NB, Class 1 Component.
- G&E Engineering Systems Inc. (1997), Preliminary Safety Analysis Report for Lungmen Units 1 & 2, Taiwan Power Company, Taiwan.
- D. Terao et al. (1992), Functional Capability of Piping Systems, NUREG 1367, U.S. NRC, Washington, DC.
- International Organization for Standardization (2003), Joints made with mechanical fasteners – Quasi-static reversed cyclic test method, ISO-16670.

Experimental and Analytical Study on Multiaxial Hysteresis Behavior of Lead Rubber Bearings

Wang-Chuen Lin ¹, Shiang-Jung Wang ², Jenn-Shin Hwang ³, Cho-Yen Yang ⁴ and Chung-Han Yu ⁵

林旺春 ¹、汪向榮 ²、黃震興 ³、楊卓諺 ⁴、游忠翰 ⁵

Abstract

In this study, lead rubber bearings, which have been extensively applied in many seismic isolation designs for buildings, infrastructure, and facilities worldwide, were tested under unilateral reversal loading as well as non-proportional plane loading, including circular and figure-eight orbits. The test results indicate that unlike the unilateral hysteretic behavior, the bilateral behavior of lead rubber bearings is too complicated to be characterized adequately by a simplified bilinear hysteretic model using a bilateral coupling effect. The applicability and robustness of adopting Hwang et al.'s model for describing the coupled bilateral hysteretic behavior of lead rubber bearings are demonstrated by comparing their predictions with the unilateral reversal loading and non-proportional plane loading test results.

Keywords: lead rubber bearing; multiaxial hysteresis behavior; non-proportional plane loading; mathematical model; bilateral coupling effect

Introduction

The satisfactory performance of various kinds of laminated rubber bearings, including lead rubber (LR), natural rubber (NR), and high-damping rubber (HDR) bearings, under multidirectional seismic loading has been demonstrated through a large number of shaking table tests and practical applications in the past few decades. Among these different laminated rubber bearings, LR bearings undoubtedly were the most often used in the seismic isolation design for buildings, infrastructure, and facilities worldwide. Generally, a hysteretic model, which was either ideally deduced under unilateral loading or simply determined by unilateral reversal loading test results, was utilized to numerically characterize the mechanical properties of LR bearings under dynamic plane loading. However, the differences, if there are any and even if they are not very noticeable, between the unilateral and bilateral behavior of LR bearings, or any damage owing to bilateral loading, might cause inaccurate and even not conservative design results (Huang et al., 2000; Huang,

2002). In this study, the LR bearings are tested with different loading patterns, including unilateral reversal loading and non-proportional plane loading (Abe et al., 2004; Nakamura et al., 2012; Wang et al., 2017; Grant et al., 2004). Accordingly, a model respectively accounting for the hysteresis behavior of LR bearings under unilateral and bilateral loading has been developed based on modifications to the mathematical models from Hwang et al.. The accuracy and applicability of the model is demonstrated through comparisons with a series of test results. In addition, the bilateral coupling effect on the hysteresis behavior of LR bearings is experimentally discussed.

Unilateral and plane loading testing

The LR bearings are configured to be tested under unilateral reversal loading and non-proportional plane loading. The LR bearings are designed with a single, central lead plug whose diameter is 30 mm. It is comprised of 16 layers of rubber each with a thickness of 2 mm and 15 layers of steel shim with a thickness of

¹ Assistant Researcher, National Center for Research on Earthquake Engineering, wclin@ncree.narl.org.tw

² Courtesy Researcher, National Center for Research on Earthquake Engineering, sjwang@ncree.narl.org.tw

³ Division Director, National Center for Research on Earthquake Engineering, jshwang@ncree.narl.org.tw

⁴ Assistant Researcher, National Center for Research on Earthquake Engineering, cyyang@ncree.narl.org.tw

⁵ Assistant Researcher, National Center for Research on Earthquake Engineering, chyu@ncree.narl.org.tw

2 mm each. The diameter and height of the LR bearings are 128 mm and 62 mm, respectively. The test setup is illustrated in Figure 1.

As shown in Figure 1, the vertical load on the bearing is exerted by the servo-hydraulic actuator, while the lateral displacement is controlled by two mutually orthogonal servo-hydraulic actuators connected with the bilateral sliding platform. A linear guide system is installed underneath the platform to reduce the friction force induced by the dynamic tri-axial testing facility. An external load cell is installed to measure the actual force responses of the bearing during testing.

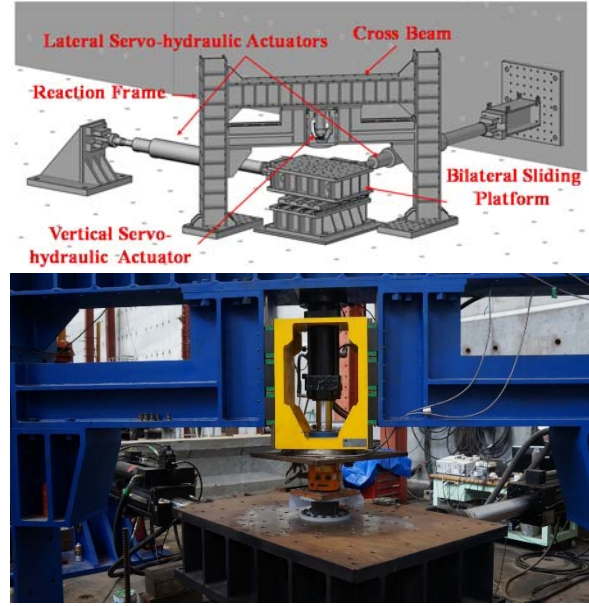
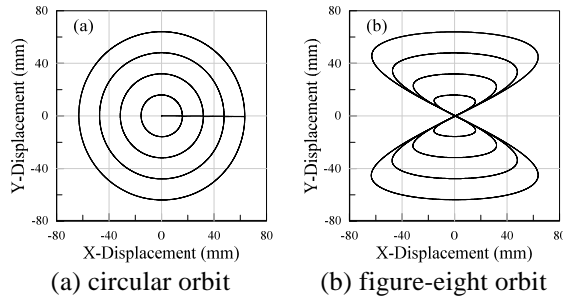


Figure 1. Test setup: dynamic tri-axial testing facility



(a) circular orbit (b) figure-eight orbit

Figure 2. Plane loading paths

The unilateral test protocols under triangular and sinusoidal reversal loading are respectively detailed in Tables 1 and 2, and the bilateral ones under non-proportional plane loading, including circular and figure-eight orbits, are described in Table 3. The equations of the plane loading paths shown in Figure 2 are given by

Circular orbit:

$$U_x = U_0 \sin \omega t \quad (1)$$

$$U_y = U_0 \cos \omega t \quad (2)$$

Figure-eight orbit:

$$U_x = U_0 \sin \omega t \quad (3)$$

$$U_y = U_0 \sin 2\omega t \quad (4)$$

where U_x and U_y are the displacement components in two principal horizontal directions, i.e. X and Y directions, respectively; U_0 is the displacement amplitude; ω is the angular frequency.

Table 1. Unilateral test protocols under triangular reversal loading

Vertical Stress (kg/cm ²)	Horizontal Shear Strain (%)	Horizontal Disp. Amplitude (mm)	Horizontal Vel. (mm/sec)	Cycles
50	50	16	16 32 48	3
75	100	32		
100	150	48		
120	200	64		

Table 2. Unilateral test protocols under sinusoidal reversal loading

Vertical Stress (kg/cm ²)	Horizontal Shear Strain (%)	Horizontal Disp. Amplitude (mm)	Freq. (Hz)	Cycles
50	50	16	0.0125 0.05 0.1	3
75	100	32		
100	150	48		
120	200	64		

Table 3. Bilateral test protocols under non-proportional plane loading

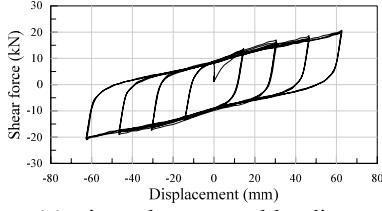
Orbit	Vertical Stress (kg/cm ²)	Horizontal Shear Strain (%)	Horizontal Disp. Amplitude (mm)	Freq. (Hz)	Cycles
Circular	50 100	50	16	0.0125	3
		100	32		
		150	48		
		200	64		
Figure-eight	50 100	50	16	0.0125	3
		100	32		
		150	48		
		200	64		

Test Results and Discussions

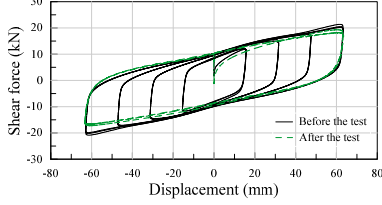
The hysteresis loops of the LR bearings under a compression stress of 50 kg/cm², triangular reversal loading with a constant rate of 16 mm/sec, and sinusoidal reversal loading with a frequency of 0.0125 Hz are depicted in Figure 3. The test observations show that the tested bearings have an excellent and stable energy dissipation capability without strain hardening and cyclic softening phenomena under both unilateral loadings. The only discrepancy observed is that under triangular reversal loading, the hysteresis loops become slightly sharper at the transition from loading to unloading compared to those under sinusoidal reversal loading. In addition, the hysteresis loops of the tested bearings under unilateral reversal loading can be adequately described by a simplified bilinear hysteretic model.

Exerting a compression stress of 100 kg/cm², the X and Y directional hysteresis loops of the LR bearings under circular and figure-eight plane loading with a frequency of 0.0125 Hz are depicted in Figures 4 and 5, respectively. As can be seen in Figure 4, the X and Y directional hysteresis loops under circular plane loading are similar to the mechanical behavior of a viscoelastic model. As can be seen in Figure 5, the X directional hysteresis loops under figure-eight

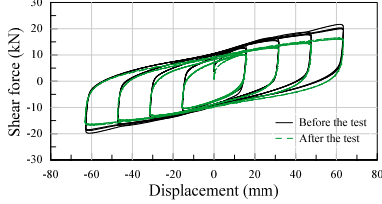
plane loading are very similar to, but have a smoother shape in comparison to, the typical mechanical behavior of LR bearings under unilateral reversal loading, while the Y directional hysteresis loops are like a special boomerang.



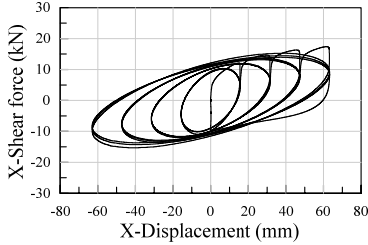
(a) triangular reversal loading



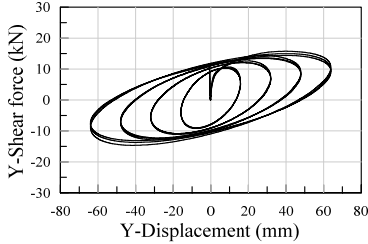
(b) sinusoidal reversal loading: circular plane



(c) sinusoidal reversal loading: figure-eight plane
Figure 3. Hysteresis loops under unilateral reversal loading before and after non-proportional plane loading tests

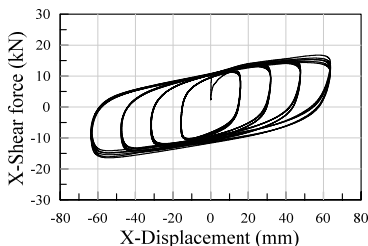


(a) X dir. hysteresis loop

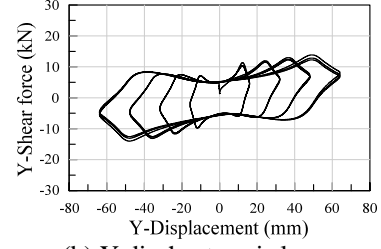


(b) Y dir. hysteresis loop

Figure 4. Hysteresis loops under circular plane loading



(a) X dir. hysteresis loop



(b) Y dir. hysteresis loop

Figure 5. Hysteresis loops under circular plane loading

Analytical Model by Hwang et al.

Taking the shear force experienced by elastomeric bearings as a combination of restoring force and damping force (Pan and Tang, 1996; Hwang et al., 2002), and assuming that the cyclic softening effect is insignificant, a mathematical model in the form of vectors for characterizing their hysteretic behavior under non-proportional plane loading was proposed by Hwang et al. (2017) and is given by:

$$\mathbf{F} = \mathbf{F}_H^1 + \mathbf{F}_H^2 = \begin{Bmatrix} F_x(t) & F_y(t) \end{Bmatrix}^T \quad (5)$$

$$\mathbf{F}_H^1 = a_1 \mathbf{U} + a_2 \mathbf{U}^3 + a_3 \mathbf{U}^5 \quad (6)$$

$$\mathbf{F}_H^2 = \int \left(a_4 + a_5 \mathbf{U}^2 \right) \left\{ \frac{\mathbf{F}_H^2 \otimes \mathbf{F}_H^2}{a_7 + \left[1 + \left(\|\mathbf{U}\|/a_8 \right)^{a_9} \right]^{a_6}} \right\} dt \quad (7)$$

where \mathbf{F}_H^1 and \mathbf{F}_H^2 correspond to the restoring and damping force vectors composed of X and Y directional components at time t , and $a_1 \sim a_9$ are the coefficients that are required to be determined from test results.

Experimental Verification for Analytical Model

The analytical model by Hwang et al. is examined by comparing its predictions to the unilateral reversal loading and non-proportional plane loading test results of the tested LR bearings, as shown in Figure 5. The coefficients of the model are mathematically determined by using the Levenberg-Marquardt algorithm (Moré, 1978) in the optimization routine to achieve the following objective function.

$$\min \sum_{i=1}^m \left(F_{test} - F_{prediction} \right)^2 \quad (8)$$

where m is the total number of data points, and F_{test} and $F_{prediction}$ are the experimental and predicted shear forces, respectively. An expedient representation to quantitatively evaluate the correlation between test results and predictions, the coefficient of determination (R^2), is also provided in Figure 6 and can be calculated by:

$$R^2 = 1 - \frac{SSE}{SST} \quad (9)$$

$$SSE = \sum_{i=1}^m \left[(F_{test})_i - (F_{prediction})_i \right]^2 \quad (10)$$

$$SST = \sum_{i=1}^m \left[(F_{test})_i - (F_{prediction})_{mean} \right]^2 \quad (11)$$

where $(F_{prediction})_{mean}$ is the mean of m values of $F_{prediction}$.

It is evident that when the model coefficients are determined from a given test, the model can provide a good match to the experimentally measured unilateral reversal loading and non-proportional plane loading results for the tested bearings, which demonstrates the accuracy and practicability of the model. Table 4 lists the coefficients of the model determined from the triangular reversal, circular, and figure-eight plane loading tests.

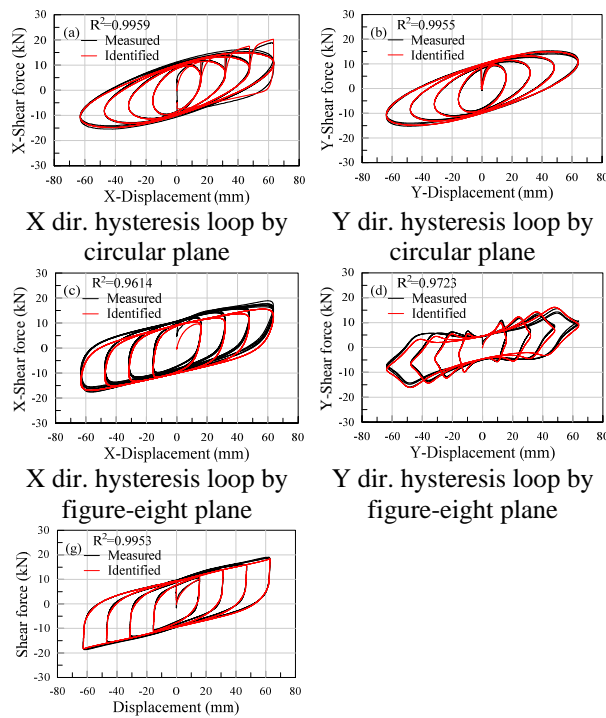


Figure 6. Comparison between the unilateral reversal loading and non-proportional plane loading test results and predictions

Table 4. Identified coefficients for predicting hysteretic behavior

Coefficient	Tests used for identification of coefficients		
	Circular plane loading	Figure-eight plane loading	Triangular reversal loading
	Compression stress: 50kg/cm² Frequency: 0.0125Hz		Compression stress: 50kg/cm² Rate: 16mm/sec
a_1	0.1844	0.1374	0.2436
a_2	-1.17E-05	1.26E-06	-4.63E-05
a_3	1.68E-09	-4.08E-10	7.71E-09
a_4	3.2179	3.3372	5.2329
a_5	0.0007	-0.0004	-6.44E-05
a_6	1.1729	0.4370	0.6979
a_7	2.3215	8.0256	2.4541
a_8	0.0028	0.0000	3.65E-10
a_9	0.1192	-0.0447	0.0484

Conclusions

In this study, the hysteretic behavior of LR bearings under unilateral reversal loading, as well as non-proportional plane loading including circular and figure-eight orbits, are experimentally investigated. In addition, the model by Hwang et al. is adopted to describe the coupled bilateral hysteretic behavior of LR bearings. The comparison of the unilateral reversal and plane loading test results indicates that the hysteretic behavior of the tested bearings is strongly dependent on loading paths and loading rates. The coefficients of the analytical model are determined from the unilateral reversal loading and identical plane loading tests. This study shows that the model can provide a good match of non-proportional plane loading test results for the tested bearings.

References

- Huang WH, Fenves GL, Whittaker AS, Mahin SA. Characterization of seismic isolation bearings for bridges from bi-directional testing. Proceedings of the 12th World Conference on Earthquake Engineering, Auckland, New Zealand, 2000.
- Huang WH. Bi-directional testing, modeling, and system response of seismically isolated bridges. Ph.D. Dissertation, University of California, Berkeley 2002.
- Abe M, Yoshida J, Fujino Y. Multiaxial behaviors of laminated rubber bearings and their Modeling. I: experimental study. Journal of Structural Engineering, ASCE 2004; 130(8): 1119-1132.
- Nakamura T, Kouchiyama O, Kikuchi M. Behaviors of lead rubber bearing under horizontal bi-directional loading test. Proceedings of the 15th World Conference on Earthquake Engineering, Lisbon, Portugal, 2012.
- Wang SJ, Lin WC, Hwang JS, Huang BW. Hysteretic behavior of high-damping rubber bearings under non-proportional plane loading. Proceedings of the 16th World Conference on Earthquake Engineering, Santiago, Chile, 2017.
- Grant DN, Fenves GL, Whittaker AS. Bidirectional modelling of high-damping rubber bearings. Journal of Earthquake Engineering 2004; 8(1): 161-185.
- Pan TC, Yang G. Nonlinear analysis of base-isolated MDOF structures. Proceedings of the 11th World Conference on Earthquake Engineering 1996, Acapulco, Mexico, 1996.
- Hwang JS, Wu JD, Pan TC, Yang G. A mathematical hysteresis model for elastomeric isolation bearings. Earthquake Engineering and Structural Dynamics 2002; 31(4): 771-789.
- Moré JJ. The Levenberg-Marquardt algorithm: implementation and theory. Lecture Notes in Mathematics 1978; 630: 105-116.

The Bi-Axial Testing System in the Tainan Laboratory of Taiwan's National Center for Research on Earthquake Engineering

Te-Hung Lin¹, Ker-Chun Lin² and Keh-Chyuan Tsai³

林德宏¹、林克強²、蔡克銓³

Abstract

The bi-axial testing system (BATS) is a major facility constructed in the Tainan laboratory of Taiwan's National Center for Research on Earthquake Engineering (NCREE) in 2017. The multi-axial testing system (MATS) constructed in 2008 in NCREE's Taipei laboratory allowed a large variety of structural tests to be successfully conducted with fruitful results. However, the longitudinal actuators adopted in the MATS are of a static type with small servo valves. In view of this, the NCREE team constructed the Tainan laboratory in National Cheng Kung University, which includes the high-performance BATS. In order to meet the requirements of high-speed and long-stroke tests, the BATS is designed to allow simultaneous application of horizontal forces, with high horizontal velocities, large displacements, and large vertical forces on the test specimen. The specimen can be anchored between the top cross beam and the bottom rigid platen within a 2-m-tall and 3.1-m-wide clear space. In addition to the four horizontal dynamic actuators in the longitudinal direction, a total of fifteen servo-hydraulic actuators are connected to the rigid platen. The design, construction, and key features of the BATS are described in this paper.

Keywords: BATS, testing system, SAP

Introduction

In recent years, the application of energy-dissipating devices and base-isolation technologies for earthquake protection of important buildings has significantly increased in Taiwan. Base-isolation bearings with large vertical load-carrying and lateral deformational capacities, and brace members with large axial-load capacities have been commonly incorporated into building designs and constructions. These earthquake protection devices are expected to undergo uni-axial or multi-axial force or displacement responses during an earthquake. For these reasons, Taiwan's National Center for Research on Earthquake Engineering (NCREE) built a multi-axial testing system (MATS) in 2008 [1], which has been in frequent use ever since. Over its many years of use, the MATS has allowed many researchers to conduct more than three hundred sets of experiments with very fruitful results. However, due to the limits of the existing hydraulic power supply and a limited budget,

the longitudinal actuators of the MATS were configured as a static type. The peak velocity capacity of these actuators is somewhat inadequate, imposing restrictions on the usage of the MATS.

In view of this, the NCREE team constructed the Tainan laboratory in National Cheng Kung University, which includes a similar but higher performance system. Figure 1 shows a schematic of the Tainan laboratory. The new laboratory includes a high-speed and long-stroke seismic simulation shaking table capable of reproducing near-fault ground motions, a strong floor and reaction wall system convenient for conducting large-scale structural experiments, and the high-performance bi-axial testing system (BATS) shown in Fig. 2. Similar to the MATS, the BATS was designed to allow the application of large horizontal forces, high-speed horizontal displacements, and large vertical forces on the test specimen simultaneously, in order to meet the requirements of high-speed and long-stroke tests. The primary function of BATS is to allow

¹ Assistant Researcher, National Center for Research on Earthquake Engineering

² Research Fellow, National Center for Research on Earthquake Engineering

³ Professor, Dept. of Civil Engineering, National Taiwan University

effective testing of large-size lead rubber bearings, high damping rubber bearings, and friction pendulum bearings. The key design requirements of BATS are (1) a maximum vertical force of 40 MN, (2) a maximum horizontal force of 4 MN, (3) a peak horizontal displacement of 1.2 m, and (4) a peak horizontal velocity of 1000 mm/s. This paper first describes the mechanical configuration and structural analysis of the BATS' platen and steel reaction frame. Then, the actuators and capacity of the BATS are introduced. Finally, the construction of the BATS and the bearing tests that have been conducted using the BATS are reported.

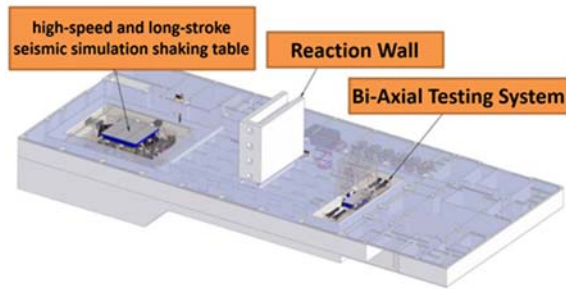


Fig. 1. Key features of NCREE's Tainan lab.



Fig. 2. The bi-axial testing system.

Mechanical Configuration and Structural Analysis

Figure 3 shows a schematic of the BATS. The overall dimensions are a length of 22.5 m, a width of 6.1 m, and a height of 3.8 m above the strong floor. As shown in Fig. 4, the BATS consists of a reinforced concrete base, a reinforced concrete side wall, a steel reaction frame, a steel platen, and various types of servo-hydraulic actuators. The reinforced concrete bases under the steel reaction frame and the remaining part are 1.9 m and 1.4 m thick, respectively. The width of the reinforced concrete side wall is 1.5 m. The reaction wall behind the actuator with an opening for maintenance purposes and for the piping to go through is 1.55 m thick. The specimen can be anchored between the top cross beam of the steel reaction frame and the rigid platen within a 2-m-high and 3.1-m-wide clear space. In addition to the longitudinal horizontal high-performance actuators, a total of fifteen servo-

hydraulic actuators are connected to the rigid platen.

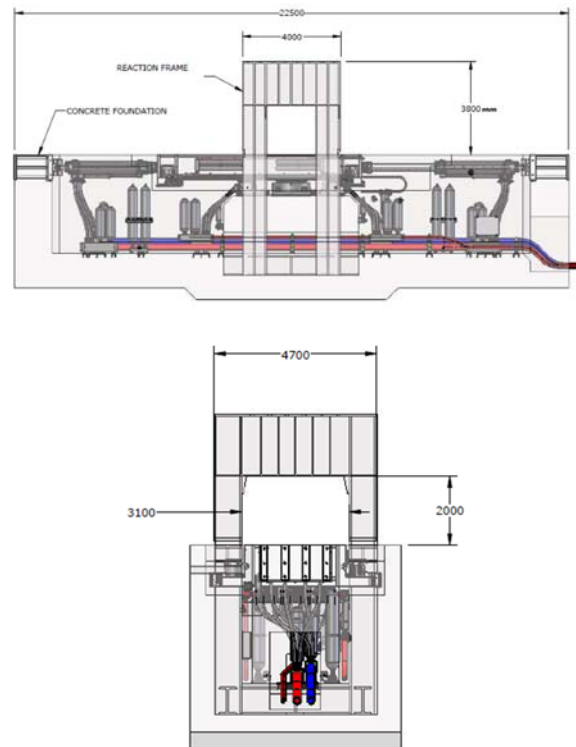


Fig. 3. Elevation views of the BATS.

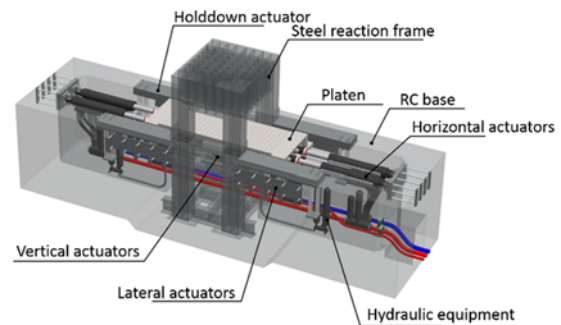


Fig. 4. Components of the BATS.

Platen

The platen is attached to all actuators. This allows their forces or displacements to be transferred to the specimen. The steel platen is box-shaped with interior longitudinal and transverse stiffeners. The dimensions of the platen are designed to be a length of 8.3 m, a width of 2.54 m, and a depth of 1.0 m. Figure 5 shows a structural plan of the platen. Figure 6 shows the interior stiffeners inside the platen. The top and bottom flanges are 90 mm thick, while the two end plates and two side webs are 80 mm thick. The stiffeners in the longitudinal and transverse directions are 50 mm and 40 mm thick, respectively. For mounting the specimen, 42-mm-diameter and 85-mm-deep threaded holes are made on the platen's top flange with a 250 mm spacing in both directions.

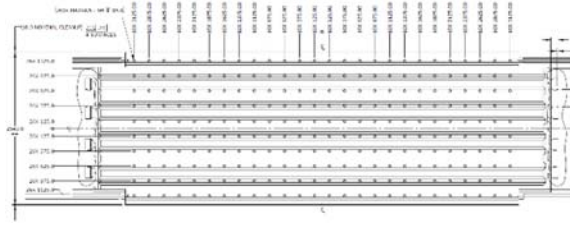


Fig. 5. Structural plan of the platen.

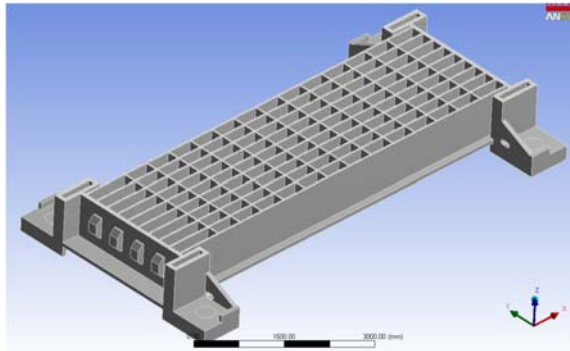
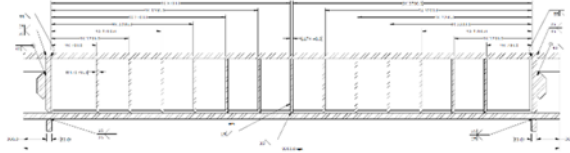


Fig. 6. Stiffeners in the platen.

Steel Reaction Frame

The steel reaction frame is self-reacting. As shown in Fig. 7, the dimensions of the steel frame are a height of 8.7 m, a width of 4.0 m, and a length of 4.7 m. The depths of the top, center, and bottom beams are 1.8 m, 1.0 m, and 0.8 m, respectively. Figure 8 shows the structural framing plans of the steel reaction frame members. The dimensions of the box column are a width of 0.8 m and a depth of 1.0 m. The flanges and outer webs of the column are 70 mm thick. The center web of the column is 50 mm thick. A total of 48 holes with an inner diameter of 93.6 mm were made through the cross beam depth in order to allow the mounting of the specimen and any reinforced concrete or steel shim blocks. The spacing of these mounting holes is 500 mm in both directions.

The maximum deformations and stresses of the steel frame were investigated through finite-element analysis using SAP2000. Figure 9 shows the finite-element model of the steel frame and some parts of the reinforced concrete base. An elastic shell and solid elements were used to represent all steel plates and the concrete base, respectively. The analytical results show that the maximum vertical deformation and rotation of the cross beam are 1.6 mm and 0.0004 radian, respectively. The frequency of the first mode is 23.36 Hz.

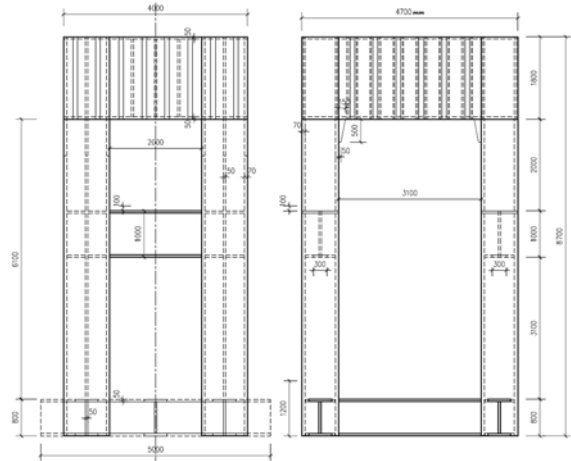


Fig. 7. Elevations of the steel reaction frame.

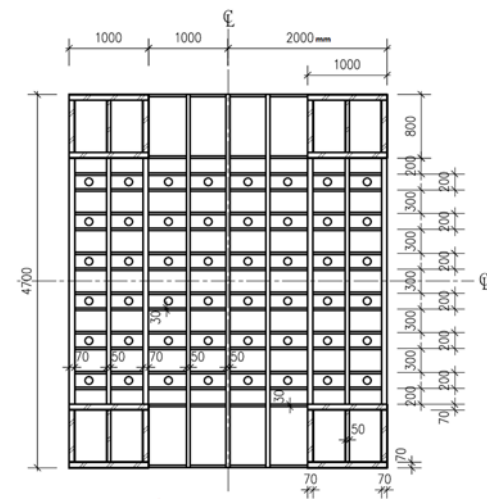


Fig. 8. Structural framing plans of the steel reaction frame (top beam).

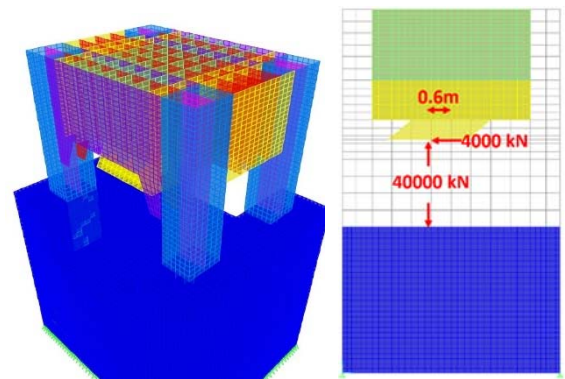


Fig. 9. Analysis model of the steel reaction frame, the maximum forces, and displacement considered.

Capacity of the BATS

The BATS is designed as a bi-axial testing facility, capable of applying large vertical loads and longitudinal displacements on a specimen through the platen. The BATS cannot impose forces and moments

in the transverse direction. The maximum allowable specimen height is 2 m. Figure 10 illustrates the arrangement of the actuators in the BATS. There are fifteen pressure-bearing (PB) or hydro-static (HS) servo-hydraulic actuators in the vertical and transverse directions. These include one 30,000-kN vertical static actuator, six 5,000-kN vertical dynamic actuators, four 2,000-kN vertical hold-down actuators, and four horizontal transverse actuators. All these PB and HS actuators are almost frictionless when the platen is moving in the longitudinal direction. There are four dynamic actuators in the longitudinal direction. As shown in Table 1, the platen can reach a peak displacement of ± 1.2 m, a peak velocity of ± 1.0 m/s, and a peak push or pull force of 4 MN. The vertical forces or overturning moment are mainly generated from one static actuator in the center and six dynamic actuators on the two sides. These seven vertical actuators are able to move with a maximum displacement of 0.125 m and a maximum velocity of ± 0.15 m/s. The maximum vertical force is 60 MN, including the 30 MN static load and the 30 MN dynamic load. In addition, the BATS can impose a maximum tensile force of 8 MN onto the specimen through the hold-down actuators.

Table 1. Capacity of the BATS

Dir.	Force (MN)		Disp. (mm)	Velocity (mm/s)
Ver.	Static	60.0 (comp.)	+125	± 150
	Dynamic	30.0 (comp.)		
		8.0 (tension)		
Hori.	± 4.0		± 1200	± 1000

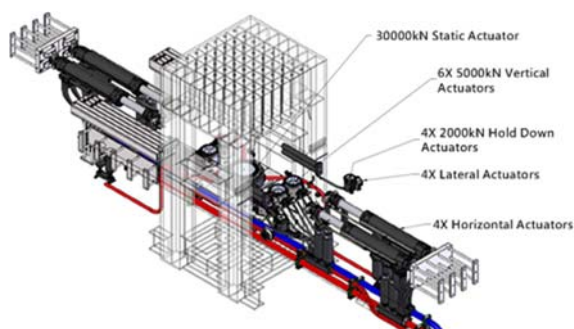


Fig. 10. Configuration of actuators in the BATS.

Constructions and Tests

The progress of construction of the BATS is shown in Fig. 11. The steel frame was first divided into four parts in the fabrication shop. After shop welding, they were transported to the Tainan laboratory and anchored in the reserved pit. Then, the reinforced concrete base and the side walls with the welded steel frame were constructed simultaneously. Finally, the

hydraulic equipment and platen were installed.



Fig. 11. Progress of construction of the BATS.

Several experiments have been conducted using the BATS as acceptance tests. One of the specimens is a high-damping rubber bearing (HDRB) and the other one is a friction pendulum bearing (FPB), which have been widely applied to buildings and bridges worldwide. Figure 12 shows the experimental setup for the HDRB. It is anticipated that testing of full-scale HDRBs and FPBs using the BATS will advance base-isolation technology.



Fig. 12. Test setup for an HDRB.

Conclusions

The bi-axial testing system (BATS) in the NCREC is a high-performance experimental system. The BATS was designed to allow the simultaneous application of large vertical forces, lateral forces with large displacements, and velocity capacities. The completion of the BATS has enhanced the experimental research capacity of the NCREC laboratory and met the requirements of advancing the research and development of base-isolation technology. Advanced experimental control techniques such as real-time hybrid simulation with sub-structuring and model updating procedures can be incorporated into future R&D in the NCREC.

References

- Lin TH, Chen PC, Lin KC. The multi-axial testing system for earthquake engineering researches. *Earthquakes and Structures* 2017; 13 (2): 165-176.

Online Model Updating with the Gradient-based Parameter Identification Method for Advanced Hybrid Simulations

Ming-Chieh Chuang¹

莊明介¹

Abstract

Hybrid simulation allows numerical and physical substructures to be integrated such that the interaction between the substructures can be taken into account in seismic performance assessment. As a result, hybrid simulation can offer a cost-effective alternative to the shaking table test. However, conventional hybrid simulation is always restricted due to the limited number of facilities and specimens. Some or many structural elements, that are similar to or the same as the physical substructures, must be modeled in hybrid simulations. Thus, the advantages and applicability of hybrid simulations diminish due to the inaccurate modeling of the numerical substructures. To address the aforementioned problem, this study develops a gradient-based parameter identification (PI) method for online model updating to advance hybrid simulation. A novelty of the proposed PI method is to fix parts of parameters along identification stages of different stress states, thereby resulting in a reduction in the number of design variables to be determined. The time consumed in computing the gradients can be reduced accordingly to improve the identification efficiency. To validate the proposed PI method, numerical verification using simulated hybrid tests were conducted with a five-story steel frame equipped with buckling-restrained braces on a shaking table at E-Defense in Japan in 2009. The numerical verification has confirmed the effectiveness of the proposed parameter identification method for advanced hybrid simulation with on-line model updating.

Keywords: Parameter identification, model updating, hybrid simulation, optimization, gradient-based method

Introduction

Well-designed structures that sustain seismic loadings should exhibit inelastic behavior in the form of significant hysteretic loops. In general, the relation of the restoring force to the structural deformation is hereditary in nature. Hence, it is difficult to represent the inelastic relations with a function of the instantaneous displacement and velocity. In the past few decades, various constitutive models have been proposed to represent the hysteretic behavior observed from structural experiments. For example, the two-surface model (Dafalias and Popov, 1975) is widely used to represent steel structure behavior under cyclic or random loadings. Figure 1 compares the experimental results of a buckling-restrained brace

(BRB) (Tsai et al., 2014) component test with the results of simulations with the two-surface model. In comparison to the famous bilinear model, the two-surface model can offer not only a smooth response but also a representation of the significant isotropic hardening effects. There are a total of 10 control parameters in the two-surface model. They can describe the desired simulation of the observed kinematic and isotropic hardening phenomena.

¹ Assistant Researcher, National Center for Research on Earthquake Engineering

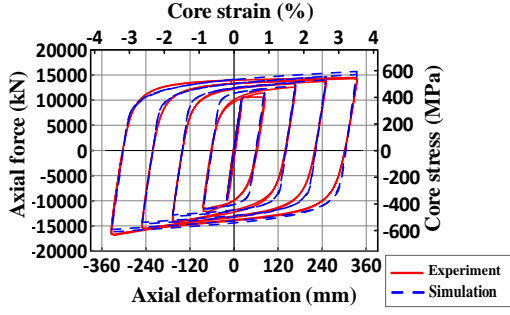


Fig. 1. Simulation with the two-surface plasticity model

When the two-surface model is adopted in nonlinear structural response simulations (Tsai et al., 2014), the lack of relations between the control parameters and the mechanical properties may result in difficulties in finding the proper parameter values. Therefore, the control parameters associated with the isotropic hardening effect (*Hiso1+*, *Hiso2+*, *Hiso1-*, *Hiso2-*) and the control parameters associated with the kinematic hardening effect (*Hkin1*, *Hkin2*) are often obtained through calibration with the trial and error method. This can be very tedious and time consuming. In order to improve the calibration efficiency, various parameter identification techniques have been studied and developed (Chuang et al., 2015).

Recently, the applications of parameter identification have migrated from offline model fitting to online model updating (Chuang et al., 2018). In hybrid simulation, also called hybrid testing, the target structure can be partitioned into multiple substructures. These substructures can be divided into two categories: numerical and physical substructures. The predicted displacements calculated from the time-stepping integration are imposed onto each substructure to determine the restoring forces associated with the degrees of freedom of the structural system. Based on the retrieved restoring forces, the command displacements of the next step can be predicted with a time-stepping integration scheme. Thus, hybrid simulation allows the numerical and physical substructures to be integrated such that the interaction between the substructures can be taken into account in seismic performance assessment. As a result, hybrid simulation can offer a cost-effective alternative to the shaking table test. However, conventional hybrid simulation is often restricted due to the limited numbers of facilities and specimens. To address this problem, the development of online model updating has gained increasing attention in recent years (Chuang et al., 2018). Figure 2 gives an example of the advanced hybrid simulation with online model updating on a five-story steel frame equipped with BRBs. In this example, one of the installed BRBs is selected for the physical substructure (PS). The selected PS is physically represented with a BRB specimen. The rest of the buckling-restrained braced frame (BRBF) is the numerical substructure (NS) in the hybrid simulations.

The auxiliary numerical model (ANM) is subjected to the same displacement history as the physical substructure. It should be noted that the boundary conditions of the auxiliary numerical model must be compatible with those of the corresponding PS. Through examination of the simulation results of the ANM, the proper parameter values can be identified using optimization methods. With the identified parameter values, the material models of relevant BRB elements in the NS can be rectified online during the hybrid simulations. In short, the errors in the nonlinear modeling of the numerical substructure can be reduced by updating the model with the parameter values that are identified online from the measured PS responses. The accuracy of hybrid simulations can be improved accordingly.

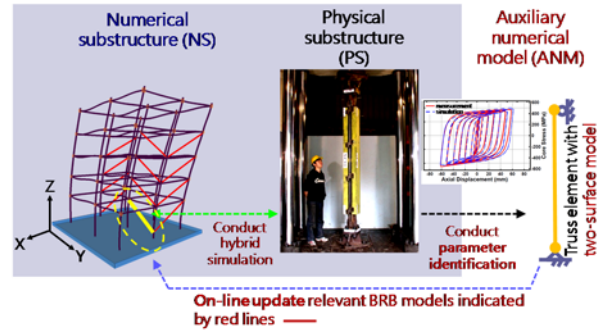


Fig. 2. Advanced hybrid simulation with online model updating

Proposed Gradient-based Parameter Identification Method

When the analytical results are compared with the experimental responses, the simulation errors can be evaluated by the root mean square error (RMSE) as follows:

$$RMSE = \sqrt{\frac{\sum_{i=1}^n (r_{sim}^{(i)} - r_{exp}^{(i)})^2}{n}}, \quad (1)$$

where r_{sim} and r_{exp} are the analytical and experimental results of the BRB axial force, respectively. Furthermore, i indicates the i th experimental data point and n indicates the total number of data points used for evaluation. In the study, for online model updating, Equation (1) was used as the objective function $F(X)$ to identify the approximate best-fit parameter values. Thus, the optimization problem of model fitting can be expressed as:

$$\begin{aligned} & \min F(X) \\ & \text{subject to } X \in R^6, \end{aligned} \quad (2)$$

where X = [Parameter Ratio (PR) of *Hiso1+*, PR of *Hiso2+*, PR of *Hiso1-*, PR of *Hiso2-*, PR of *Hkin1*, PR

of $Hkin2]^T$ as the design vector while the parameter identification with the optimization method is conducted. It should be noted that the 6 hardening parameters (i.e., $Hiso1+$, $Hiso2+$, $Hiso1-$, $Hiso2-$, $Hkin1$, $Hkin2$) are normalized for the design variables. Thus, the 6 design variables are dimensionless parameters in the proposed parameter identification method presented later. Finding a set of parameter values that can reduce simulation errors compared to the observed experimental response can be achieved by solving the constrained optimization problem with a single objective function, as in Equation (1).

In the proposed gradient-based parameter identification method for model updating (GBM_MU) (Chuang et al., 2018), the gradient of the parameters as the design variables must be computed using the finite difference method (FDM) with the perturbed parameter values. Specifically, the gradient is computed with a set of $(m + 1)$ points in \mathbf{R}^m , where m indicates the total number of design variables. In the GBM_MU method, the gradient descent method is adopted as the basis for parameter identification in model updating. The successive design variables from the k th step to the $(k+1)$ th step can be obtained with:

$$X_{k+1} = X_k - \lambda_k \nabla F(X_k). \quad (3)$$

λ_k is a positive scalar parameter used as the reduction factor to set the perturbed values in the iteration procedures. Whenever the gradient is nonzero, $-\nabla F(X_k)$ represents the descent direction at X_k for the k th step. While the model updating is conducted, the parameter identification for model updating can be resolved with the ANM. By monitoring the stress state of the ANM including the elastic, isotropic hardening, and the kinematic hardening, a novel modification of the classical gradient descent method is proposed to fix parts of parameters along the identification stages of different stress states, thereby resulting in a reduction of the number of design variables to be determined. The time spent on computing the gradients can be reduced accordingly to improve the identification efficiency.

Numerical Verification

To investigate the online model updating with the proposed GBM_MU method, this study describes three illustrative cases of a five-story steel frame equipped with BRBs tested using the shaking table at E-Defense in Japan in 2009 (Kasai et al., 2010). As shown in Figure 3, these cases can be categorized into three types including (i) the reference case (Case R), (ii) the erroneous case (Case E), and (iii) the corrected case (Case C).

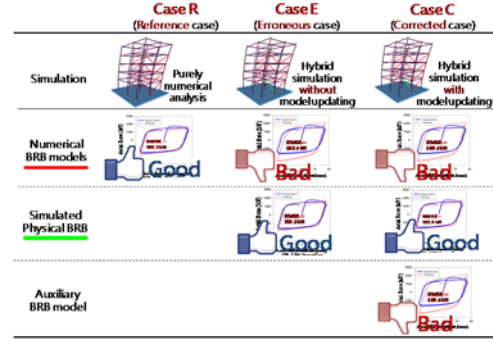


Fig. 3. Configurations of three illustrative cases

In Case R, the purely dynamic analysis is conducted with the reference model that is developed in PISA3D (Lin et al., 2009) and calibrated using the measured experimental data. The numerical model used in Case R is constructed to simulate the entire structure without any partitioned substructure. Thus, the analytical results of Case R can serve as the benchmark for investigations on the benefits resulting from model updating and the effectiveness of the proposed method (GBM_MU). By taking advantage of the object-oriented framework of PISA3D, it is convenient to extend PISA3D with the C++ programming language to accommodate the simulated hybrid tests of Case E and Case C, as in Figure 2. In Case E and Case C (Figure 3), the intentionally erroneous parameter values identical to those of the initial case are specified to model the 11 numerical BRB substructures. The rest of the numerical substructures, such as the BeamColumn elements for representing beams, columns, and foundations and the Joint elements for representing beam-to-column connections in the two cases, are identical to those of the Case R benchmark model. The selected PS is numerically simulated with the high-fidelity analytical model, which is identical to that of the reference model, with the parameter values calibrated from the results of the BRB component tests (Chuang et al., 2018).

Clearly, in Case E and Case C, using the intentionally erroneous parameter values to model the 11 numerical BRB substructures make the simulation results (e.g., base shear or roof displacement) different from those of Case R. The discrepancy between Case E and Case C is that online model updating is conducted only in Case C to correct the intentionally erroneous models of the 11 numerical BRB substructures. Hence, it is expected that the simulation results of Case C would be closer to those obtained from Case R than those of Case E. As shown in Figure 4, in Case C the parameter identification with the proposed method worked well without any divergence. The online model updating was terminated at the 900th step corresponding to the time of 4.5 seconds of excitation (after the peak ground accelerations). At this moment, the hardening parameter values are expected to be already identified from the physical substructure,

which has suffered significant plastic deformation. Clearly, for the actual hybrid simulation with online model updating, the proper time to terminate the online model updating should be carefully selected according to the online monitoring of the PS responses or the results of time history analyses prior to the hybrid simulation.

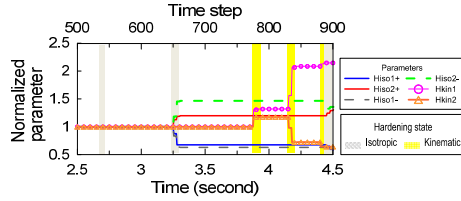


Fig. 4. Results of the parameter identification of Case C

As shown in Figures 5 and 6, by calculating the errors (or differences) of the roof displacements of Case E and Case C with Case R in both horizontal directions (i.e., the X and Y directions) as presented in Fig. 2, significant errors are revealed. Compared with the results of Case E, the improved results with reduced errors can be found in Case C in both directions.

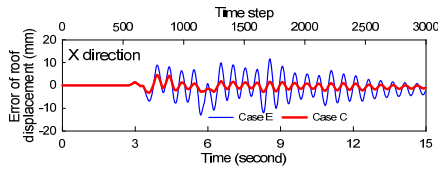


Fig. 5. Errors of the roof displacement responses in the X direction

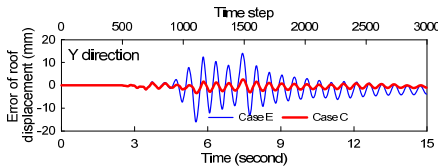


Fig. 6. Errors of the roof displacement responses in the Y direction

Similar results in the reduced errors can also be found in terms of the base shear in both directions. In addition, Figure 7 gives the distributions of the error ratios of Case C and Case E. The error ratio is computed by dividing the absolute maximum error by the absolute maximum value of Case R. The significant improvement of the accuracy of hybrid simulation is clearly shown in Case C.

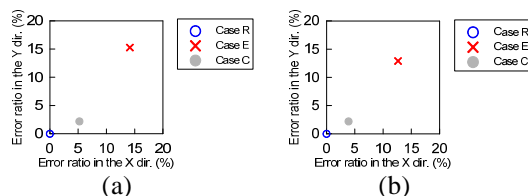


Fig. 7. Distributions of the error ratios of (a) relative roof displacement and (b) base shear

Conclusions

This paper presents and demonstrates the gradient-based parameter identification method (GBM_MU) for advanced hybrid simulation with online model updating. The proposed method is verified by using the simulated hybrid tests of a five-story BRBF. Case C shows that there is no significantly increasing error after the on-line model updating was terminated at the 900th step (4.5 seconds). Hence, this suggests that online model updating could be terminated in the hybrid simulation once the proper parameter values can be identified from the significant inelastic behavior of the physical substructure. Thus, the proposed GBM_MU can offer reasonably good effectiveness in online model updating for the advanced hybrid simulations. The details of the study related to online model updating and the gradient-based parameter identification method (GBM_MU) have been documented by Chuang et al. (2018).

References

- Chuang MC, Hsieh SH, Wu AC. (2015). Model fitting of the experiment of buckling-restrained brace by using gradient descent method. *Structural Engineering*, **30**(4): 79-106 (in Chinese).
- Chuang MC, Hsieh SH, Tsai KC, Li CH, Wang KJ, Wu AC. (2018). Parameter identification for on-line model updating in hybrid simulations using a gradient-based method. *Earthquake Engineering and Structural Dynamics*, **47**(2): 269-293.
- Dafalias YF, Popov, EP. (1975). A model of nonlinearly hardening materials for complex loading. *Acta Mechanica*, **21**(3): 173-192.
- Kasai K, Ito H, Ooki Y, Hikino T, Kajiwara K, Motoyui S, Ozaki H, Ishii M. (2010). Full-scale shake table tests of 5-story steel building with various dampers. Proceedings of the 7th CUEE and 5th ICEE Joint Conference, Tokyo, Japan.
- Lin BZ, Chuang MC, Tsai KC. (2009). Object-oriented development and application of a nonlinear structural analysis framework. *Advances in Engineering Software*, **40**(1): 66-82.
- Tsai KC, Wu AC, Wei CY, Lin PC, Chuang MC, Yu YJ. (2014). Welded end-slot connection and debonding layers for buckling-restrained braces. *Earthquake Engineering and Structural Dynamics*, **43**(12): 1785-1807.

Cloudization of An In-house Discrete Element Simulation Platform

Wei-Tze Chang¹

張慰慈¹

Abstract

VEDO (Versatile Discrete Objects simulation system) is a parallel computing platform developed by the Department of Civil Engineering at National Taiwan University (NTU) in 2005 to address the need for Discrete Element Simulation (DES) in the field of civil engineering. It was released as open-source software under the 3-clause BSD license in 2009, and it is currently co-maintained by the National Center for Research on Earthquake Engineering (NCREE) under the National Applied Research Laboratories (NARLabs) in Taiwan. This paper explores a procedure for transforming VEDO to cloud computing with information technologies such as unified data type, XML-based processing unit, and graphic/web-based user interface. The integration of the Python programming language, Qt application framework, and Flask web framework are also illustrated. The resulting new VEDO system has been applied to teaching college students at NTU, and the experience is useful for researchers interested in developing their own cloud computing platform.

Keywords: Cloudization, VEDO simulation system, discrete element simulation.

Background

VEDO (Versatile Discrete Objects simulation system) is an in-house discrete element simulation system developed in 2005 (Chang and Hsieh, 2009; VEDO, 2002; Yang and Hsieh, 2002). VEDO is a C++ Object-Oriented Program (OOP), which is made up of an XML-based data exchange standard (dosXML) (Yang and Hsieh, 2004), two analysis engines (ANNE & IRIS) (Chang and Hsieh, 2009), a command mode pre-/post-processing unit (KNIGHT) (Chang, 2009), and a visualization unit (Venus Painter) (Chen, 2004). Taking advantage of supercomputing power on a PC cluster platform, VEDO has been applied to study various engineering topics, including the dynamic behavior of soil and rock systems, Self-Compacting Concrete (SCC) flow, concrete cracking, sand arching, packing and self-assembly of colloids, particle flow, solid-liquid flow, and sieve analysis, which show its stability and practicality (Chang, 2009). Although VEDO has been applied to various research topics, the typical command-mode environment of PC clusters also results in difficulty in learning and operating VEDO. To resolve the issue, there is a need to promote

VEDO with suitable information technologies to meet cloud computing requirements.

Method

Unify Data Type

Before cloudizing, it is necessary to unify the data types for designing a cross-platform binary file in VEDO so that binary data can be exchanged correctly to different platforms. Standard C++ does not rigorously define the length of integers in different platforms (Table 1). That is, a C++ code using a default integer type (such as *int*, *long int*, or *unsigned*) leads to different binary types depending on its working environments. Thus, this study uses the unified type, *_int32_t*, *_int64_t*, *_uint32_t*, and *_uint64_t*, instead of 32-/64-bit integers and unsigned integer in C++. Pre-processing instructions, as shown in Fig. 1, were used to quickly specify the exact length of data type in VEDO. Programmers can use unified defined data types, *_uint_t* and *_int_t*, in whole codes of VEDO for LP32, ILP32, LLP64, and LP64-based platforms.

¹ Assistant Researcher, National Center for Research on Earthquake Engineering

Table. 1. Length of integers in C++ in different platforms.

Data type	Length				
	Standard C++	LP32 (Win16)	ILP32 (Win32 / Linux32)	LLP64 (Win64)	LP64 (Linux64)
short / short int / signed short / signed short int / unsigned short / unsigned short int	≥ 16	16	16	16	16
int / signed / signed int / unsigned / unsigned int	≥ 16	16	32	32	32
long / long int / signed long / signed long int / unsigned long / unsigned long int	≥ 32	32	32	32	64
long long / long long int / signed long long / unsigned long long / signed long long int & unsigned long long int (C++11)	≥ 64	64	64	64	64

```

typedef signed short int    _int16_t ;
typedef unsigned short int  _uint16_t ;
typedef signed int          _int32_t ;
typedef unsigned int        _uint32_t ;
typedef signed long long int _int64_t ;
typedef unsigned long long int _uint64_t ;

#ifdef _INT32
    typedef _int32_t    _int_t ;
    typedef _uint32_t    _uint_t ;
#else
    #ifdef _INT64
        typedef _int64_t    _int_t ;
        typedef _uint64_t    _uint_t ;
    #else
        typedef _int64_t    _int_t ;
        typedef _uint64_t    _uint_t ;
    #endif
#endif
#endif

```

Fig. 1. Pre-processing instructions in VEDO for quickly specifying the exact length of data types.

Application Development Framework

After setting the unified data types, the next step is to choose an appropriate application development framework as the user interface of VEDO. Considering the cross-platform needs and the learning curve of several frameworks (shown in Table 2), the Python programming language is a good choice for implementation of cloud VEDO. However, the built-in Graphic User Interface (GUI) libraries of Python (Tkinter) are not easy to use, so another well-known cross-platform application development framework, Qt (1991), was chosen in this study. This study promotes VEDO with two types of cloudization: (a) SaaS-type (Software as a Service) cloud using the Flask web framework, a Python web library that supports HTML5 and JAVA script. In this design, users can operate VEDO with a browser on a PC, laptop computer, tablet, or even a smartphone without installing any packages. The major loading of hardware is on the server end; (b) IaaS-type

(Infrastructure as a Service) cloud using Qt library with the Python programming language to design a GUI. Although this is not a client-server model, users can run VEDO on their own private cloud in several different platforms, such as Microsoft Windows, GNU/Linux, UNIX, and MacOS (Fig. 2). The final design of cloud VEDO and the relationship between components is shown in Fig. 3.

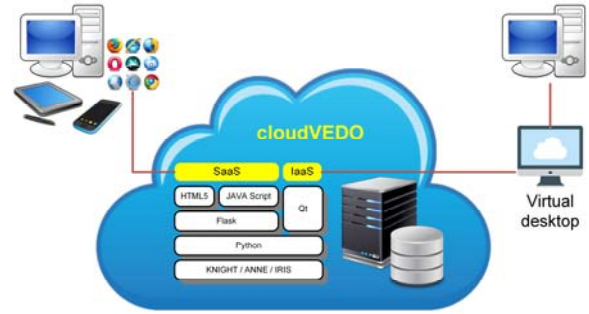


Fig. 2. VEDO supports two types of clouds, SaaS and IaaS.

External XML Parser Libraries

Since VEDO has its own XML format, the dosXML, as the data exchange standard, the choice of an appropriate XML parser library becomes an important issue in cloudization. Four well-known XML parser libraries, the Xerces-C XML Parser (2004), Boost C++ (2006), Python (ElementTree), and lxml (2006) libraries, were tested in this study. The former two libraries support C++ programming language and can be directly implemented in the VEDO kernel. Since the API of Xerces-C is more complex, we chose the property tree in the Boost C++ library for implementation of the XML parser API in the pre-processing unit (KNIGHT) of VEDO. In order to compensate for the lack of Boost C++ in the validation of XML documents, we also introduce the lxml library into the above mentioned Python-based application development framework for validating the format of dosXML before entering the pre-processing unit (KNIGHT) of VEDO.

Results and Conclusions

After integrating the Python programming language, Boost C++, and lxml XML parser libraries, Flask web library, and the Qt application development framework, this study successfully implemented an in-house discrete element simulation system, VEDO, to SaaS-/IaaS-type clouds. Users can easily operate VEDO through a web browser or directly execute it on a private cloud. The results are shown in Figs. 4 and 5. The experience illustrated in this paper should be suitable for not only VEDO, but also for other in-house engineering software.

Acknowledgments

The authors hereby extend sincere thanks to the Ministry of Science and Technology (MOST) in Taiwan for their financial support (Project No. MOST-104-2221-E-492-023 and NSC-103-2218-E-492-004).

References

- Boost C++. (2006). Retrieved from Bopost C++ website: <http://www.boost.org/>
- Chang, W. T. (2009). Parallel Discrete Element Simulation and Its Application to the Study of Solid-liquid Flow Behavior, Ph.D. Dissertation, National Taiwan University, Taipei, 124 pages.
- Chang, W. T. and Hsieh, S. H. (2009). "Parallelization of Discrete Element Simulation," *Journal of the Chinese Institute of Engineers*, 32(6), 825-841.
- Chen, S. H. (2004). A Visual Programming System for Postprocessing of Discrete Element Analysis, Master Thesis, National Taiwan University, Taipei, 93 pages.
- Flask (2010). Retrieved from Flask website: <http://flask.pocoo.org/>
- lxml. (2006). Retrieved from lxml website: <http://lxml.de/>
- Qt (1991), Retrieved from Qt website: <http://www.qt.io/>
- VEDO. (2002). Retrieved from VEDO website: <http://vedo.caece.net/>
- Xerces-C. (2004). Retrieved from Apache Software Foundation website: <http://xerces.apache.org/xerces-c/>
- Yang, C. T. and Hsieh, S. H. (2002). "Software Development for Particle Simulation of Self-Compacting Concrete," Proceeding of the 15th KKCNN Symposium on Civil Engineering, Singapore, Singapore, S280-S284.
- Yang, C. T., Hsieh, S. H., and Lin, L. S. (2004). "Design of an XML-based Markup Language for Discrete Object Simulations," *Bulletin of the College of Engineering*, National Taiwan University, 92, 89-103.

Table 2. Application development frameworks evaluated in this study.

Framework type	Framework	Cross-platform	Client-server model	Hardware requirement of client	Learning curve
Active-page language	ASP	No	Yes	Lower	Middle
	JSP	Yes	Yes	Lower	Middle
	PHP	Yes	Yes	Lower	Middle
Programming language	JAVA	Yes	Yes	Higher	Higher
Library	Flask (Python web library)	Yes	Yes	Lower	Lower
	Tkinter (Python built-in GUI library)	Yes	No	Higher	Middle
	Qt	Yes	No	Higher	Lower

Table 3. XML parser libraries tested in this study.

Libraries	Maintenance	Programming language	Preparation	Interface (API)	XML validation
Xerces-C XML Parser	Apache Software Foundation (ASF)	C/C++	Need to be compiled first	Powerful but more complex	Yes
Boost C++ Libraries (property tree)	Boost community	C/C++	Can be called directly	Easily	No
Python (ElementTree)	Python Software Foundation (PSF)	Python	Python built-in module	Easily	No
lxml	Matthias Klose	Python	Should be installed first (easily)	Easily	Yes

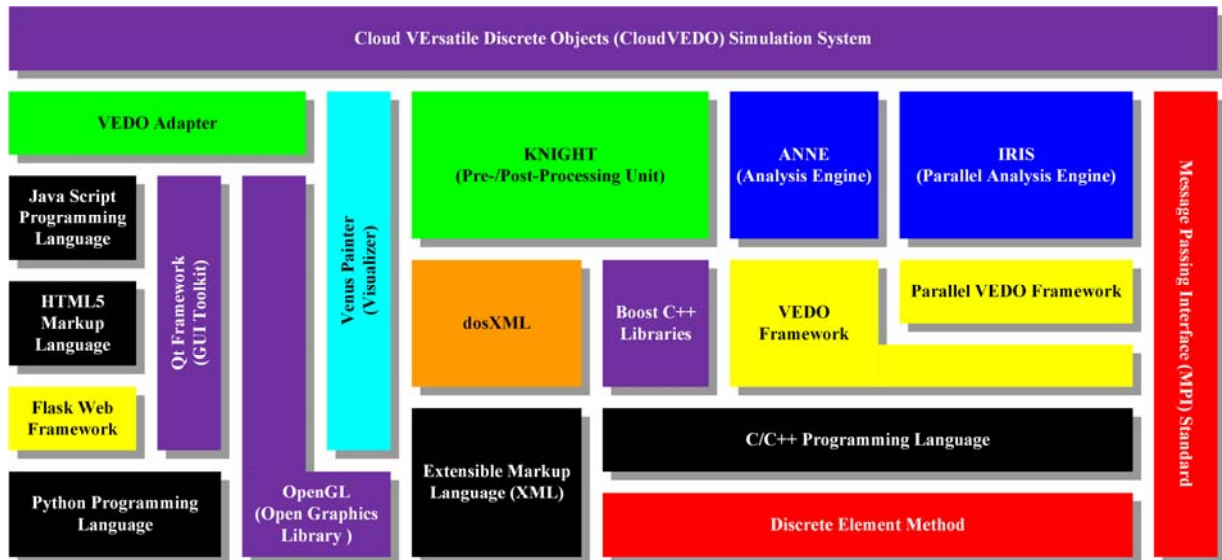


Fig. 3. Components of Cloud VEDO.

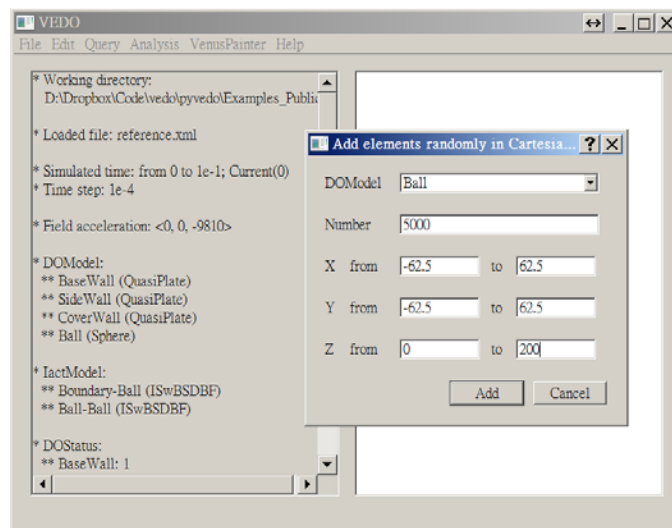


Fig. 4. VEDO interface in an IaaS-type cloud.

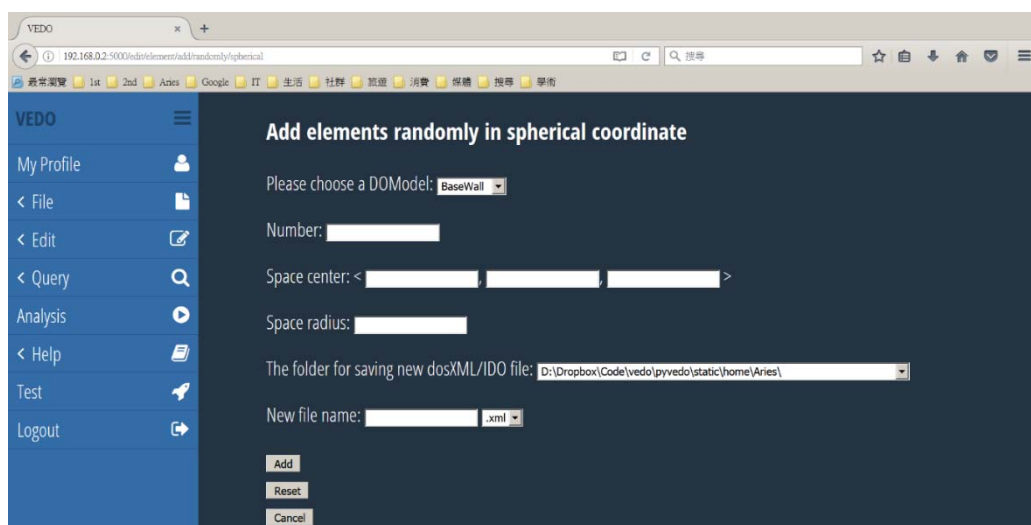


Fig. 5. VEDO interface of in a SaaS-type cloud.

Development of Adaptively Smoothed-Distributed Seismicity Model

Hsun-Jen Liu¹, Norman A. Abrahamson², and Chin-Hsun Yeh³

劉勛仁¹、Norman A. Abrahamson²、葉錦勳³

Abstract

To evaluate the earthquake activity rate of areal sources, conventional methods delineate a study region into subzones and analyze the recorded spatial and temporal earthquake distribution statistics within each subzone. Typically, each subzone is hypothesized to exhibit a uniformly seismic rate. Current studies adopt zoneless method to resolve the subjectivity and uncertainties of delineating a study region into subzones. The zoneless method employ Gaussian Kernel Density Estimation to conduct spatial analysis based on the distribution of seismic locations within a study region. Finally, the established smoothed-distributed seismicity model reflects the characteristics of seismic events and spatial distribution authentically. However, evaluation of the uncertainty of future seismic occurrence locations related to historical earthquake catalog and the spatial analysis parameter settings of smoothed-distributed seismicity model are the discussed issues. In consideration of future earthquake occurrence location uncertainties, this study adopted the magnitude versus rupture length scaling law to evaluate seismogenic areas based on historical earthquakes. In terms of the distance parameter setting, this study applied the K-nearest neighbor algorithm to spatial span earthquake activity rates adaptively based on the density of earthquake distribution. The two-dimensional correlation coefficient was employed to establish the optimal k-order and obtain a representative seismic density result. Finally, this study proposed a process to development an adaptively smoothed-distributed seismicity model to improve the areal source evaluation result.

Keywords: smoothed-distributed seismicity model, kernel density estimation, adaptive distance, K-nearest neighbor algorithm, two-dimensional correlation coefficient

Introduction

Taiwan is located on the plate convergence zone between the Philippine Sea Plate and the Eurasian Plate. Therefore, Taiwan's geological structures include fault systems, subduction zone systems, and oceanic and continental plates. Based on the different types of geological activities, the types of earthquake may be classified as fault earthquakes, subduction interface and intraslab earthquakes, and background seismicity. In hazard assessment, the subduction intraslab earthquakes and background seismicity usually be modeled as areal sources to consider the seismic source with unpredicted rupture directions and locations. For the temporal and spatial evaluation of earthquake activity rate (i.e., a -values calculated using the Gutenberg–Richter relationship) in previous areal

source analyses, a typical study region was delineated into numerous subzones according to the tectonic structures and seismicity, and the assumption of spatial uniformity for the earthquake rate over the areal zone is considered.

As zoning approach is subjective and uncertain, current studies have adopted zoneless method for superior objectivity and reliability. The proposed method adopts the earthquake distribution of the region and employs the Kernel Density Estimation (KDE) of the Gaussian Kernel Function to conduct spatial analysis, the results of which is the smoothed-distributed seismicity model. Its core concepts are as follows: (1) future disastrous earthquakes exhibit potential to recur at or near the locations of past medium- or large-scale earthquakes; (2) The level of

¹ Assistant Researcher, National Center for Research on Earthquake Engineering, hjliu@ncree.narl.org.tw

² Professor, University of California at Berkeley, abrahamson@berkeley.edu

³ Research Fellow, National Center for Research on Earthquake Engineering, chyeh@ncree.narl.org.tw

seismic activity potential is related to the density of the seismic distribution.

To address the first concept, this study adopted the magnitude versus rupture length ($L(M)$) scaling law to reasonably estimate future potential earthquake area based on historical earthquakes. Regarding the second concept, the K-nearest neighbor algorithm was adopted to make adaptive spanning of the earthquake occurrence probability according to the density of seismic distribution. Additionally, a two-dimensional (2-D) correlation coefficient was adopted to establish the optimal k-order, thus providing the stability and reliability of the KDE result.

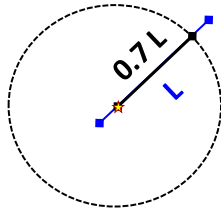
Finally, this study integrated the aforementioned processing concept logics and algorithms of zoneless method to propose a process for development of adaptively smoothed-distributed seismicity model. This model would be comprehensive seismic hazard assessment for the spatial distribution of the a -values of areal sources.

Potential Area Evaluation of Disastrous Earthquakes

In terms of the potential locations of future disastrous earthquakes, this study supposed that they would randomly occur within an area relevant to rupture length corresponding to historical earthquakes, and this range is positively correlated with the scale of earthquake magnitude. Therefore, the $L(M)$ scaling law in the empirical equation developed by Wells and Coppersmith in 1994 (W&C94) for all types of faulting style is chosen to specify the radius distance for the potential earthquake area. The equation is as follows:

$$\log_{10}(L) = -2.44 + 0.59M_w + \sigma \quad (1)$$

where, L is the ground surface rupture length, M_w is the seismic moment magnitude, and σ represents the standard deviation (i.e., 0.16) to consider the uncertainties of the estimated rupture length.



- L : surface rupture length by $L(M)$ scaling from W&C94
- $0.7L$: the range a earthquake will occurred mainly based on one sigma region of normal distribution

Fig. 1. Schematic diagram of the corresponding effective seismogenic radius based on the rupture length of $0.7L$.

For the effective seismogenic area, according to the seismic source dislocation mechanism, epicenters

may be not at the mid- or end-point but mostly occur at the middle section of a rupture length. Therefore, this study takes 0.7 times of the rupture length (L) as a future effective seismogenic radius, where the 0.7 refers to a normal distribution for most of the major distribution area for 68% of a standard deviation. Figure 1 illustrates the effective radius ($0.7L$) for a future seismogenic potential area of a historical earthquake.

Seismicity Potential Density Distribution Evaluation

For the future earthquake activity potential in a gridded study region, this study consider that the recurrence of seismic activity is related to the spatial density of historic earthquakes. Therefore, based on the degree of discrete distributions of possible epicenter locations, the KDE spatial analysis method was used to develop a gridded-smoothed seismicity model in a 2-D space. The KDE method is used to assign each grid in a study area with a density value instead of just the event point. The 2-D equation of KDE is as follows:

$$f(x, y) = \frac{1}{n h_x h_y} \sum_{i=1}^n K\left(\frac{x - X_i}{h_x}, \frac{y - Y_i}{h_y}\right) \quad (2)$$

where, $f(x, y)$ is the 2-D spatial probability density function of the earthquake distribution; x and y are the center point coordinates of the grid cell; n is the total number of main shocks; K is the kernel function; X_i and Y_i are the epicenter coordinates of each earthquake; and h_x and h_y are the two-way horizontal smoothing parameters for the kernel function, also known as the smoothing distance or bandwidth. The kernel function is determined using the Gaussian distribution model for representativeness; the equation is as follows:

$$K_i = \frac{1}{2\pi} \exp\left(-\frac{1}{2} \frac{d_i^2}{c^2}\right) \quad (3)$$

where, d_i is the distance between the grid centroid and the epicenter; c is the standard deviation same as smoothing distance h_x and h_y in equation (2). Here is assumed that the kernel density distribution is in a symmetrical circle, so c is identical to bandwidth as that in equation (2) (i.e., h_x and h_y are equal).

The smoothing distance is the critical parameter in the development of smoothed-distributed seismicity model. Liu et al. (2016) adopted a fixed bandwidth of 30 km to conduct the hazard assessment of shallow crust seismic sources in Taiwan. This study adopted adaptive bandwidth and employed the K-nearest neighbor algorithm to estimate the spatial distribution density of earthquakes. For areas with dense seismic distribution are set to exhibit smaller smoothing distances, thus indicating increased earthquake

activity rates in the area; on the contrary, for areas with sparse seismic distributions are set with greater smoothing distances to represent the decrease of earthquake activity in the area. Figure 2 displays the first- and fifth-order of the KDE results.

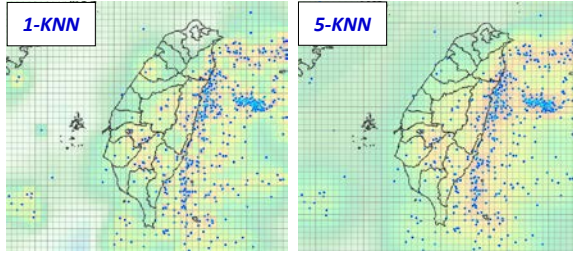


Fig. 2. Examples for first- and fifth-order of the KDE results.

This study adopted 2-D correlation coefficients to determine the neighbor order (k -order) of the KNN algorithm. The equation to calculate 2-D correlation coefficient is as follows:

$$r = \frac{\sum_m \sum_n A_{m,n} B_{m,n}}{\sqrt{\left(\sum_m \sum_n A_{m,n}^2\right)} \sqrt{\left(\sum_m \sum_n B_{m,n}^2\right)}} \quad (4)$$

where, r is a 2-D correlation coefficient and ranges from zero to one; A and B are the matrices of the gridded-smoothed seismicity model of orders k and $k+1$, respectively; and m and n represent the 2-D dimensionality of the aforementioned model matrices. Correlation coefficients are mainly adopted to measure

the correlation between two samples. If the correlation coefficient is closer to one, the two samples exhibit greater degrees of correlation. By reviewing the correlation coefficient of neighboring orders shows that taking the level at which the trend change started to exhibit stability will provide the optimal order. This indicates that the gridded-smoothed seismicity model of that order can be reliably represented.

Development Procedure of the Adaptively Smoothed-Distributed Seismicity Models

This study proposed a procedure to develop an adaptively smoothed-distributed seismicity model based on the aforementioned conceptual reasoning and estimation methods used to process the spatial distribution of earthquake rates for areal sources. The procedure is shown in Figure 3. The steps are as follows:

1. Illustrate the epicenter distribution of historical earthquakes: select moderate- and large-scale earthquake events from the earthquake catalog. Figure 3 displays the earthquake catalog that was integrated and relocated by Wu et al. (2016) according to the data from Geophysical Database Management System (GDMS) developed by Central Weather Bureau in Taiwan. The epicenter distribution is limited to main shocks with M_w of greater than or equal to 5.5 that occurred between 1900 and June 2015; however, consideration of data completeness, the main shocks occurred between 1900 and 1935 are limited to M_w of greater than or equal to 6.5.

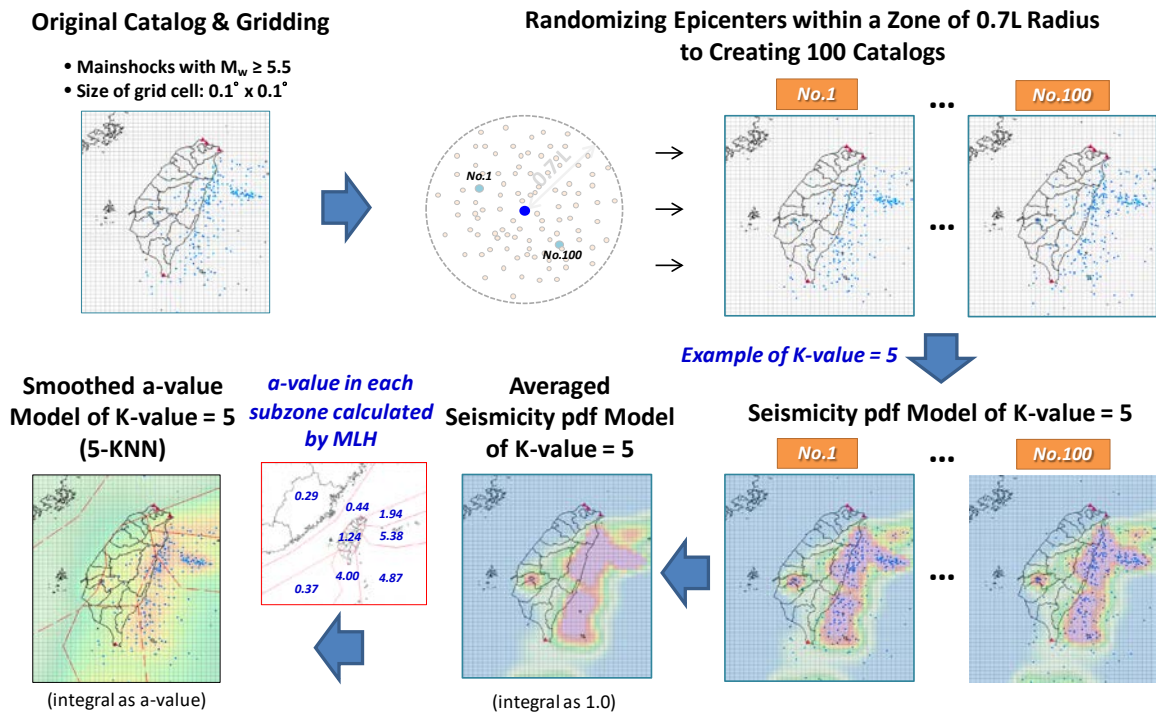


Fig. 3. Flow chart for the development of the adaptively gridded-smoothed seismicity model. Taking the shallow seismic source zones as an example.

2. Establish a gridded region: construct grid cells in study region for follow-up detailed processing of the discretized smoothed-distributed seismicity results. The size of a grid cell in Figure 3 is taken as $0.1^\circ \times 0.1^\circ$.
3. Establish multiple potential earthquake catalogs: adopt the L(M) scaling law to evaluate the effective seismogenic radius of each earthquake event. Randomly generate epicenter locations within the seismogenic areas to develop multiple earthquake catalogs, thereby simulating the possible disastrous earthquake scenarios in the future. Figure 3 displays 100 sets of developed earthquake catalogs and serves as the potential representatives.
4. Develop earthquake probability density model: employ the KNN algorithm to calculate the probability density model of earthquake distribution for each earthquake catalog. The final probability density result is taken as the average of 100 earthquake catalogs.

To select the proper order of KNN, this study evaluated gridded-smoothed seismicity models of different k -orders on the shallow crust areal sources (focal depth ≤ 35 km) of Taiwan (119° – 123° N, 21° – 26° E). Equation (4) was adopted to calculate the 2-D coefficient correlation changes. The results are displayed in Figure 4, which indicated that the 2-D correlation coefficient gradually stabilized after the 5th order. Therefore, the 5th order is the optimal k -order of this study.

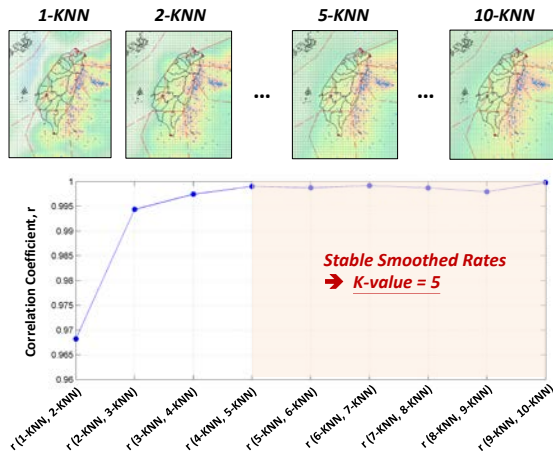


Fig. 4. Changing trend of 2-D correlation coefficient results of different k -orders calculated by the KNN algorithm of shallow crust areal sources in Taiwan. The changing trend of 2-D correlation coefficient results gradually stabilized after the 5th order.

5. Establish the a -value spatial distribution model: finally, normalize the aforementioned earthquake probability density model in each subzone then evaluate the a -value spatial distribution model.

The equation is as follows:

$$\lambda_z(x, y) = f'_z(x, y) \cdot \Delta_x \cdot \Delta_y \cdot a_z \quad (5)$$

where, z is the subzone code; $\lambda_z(x, y)$ represents the smoothed-distributed a -value of the unit grid cell in each subzone; $f'_z(x, y)$ represents the normalized earthquake probability density distribution of each subzone; Δ_x and Δ_y represent the length and width of the unit grid cells, respectively (both equal 0.1°); and a_z is the a -value of each subzone, which is calculated using maximum likelihood method (Weichert, 1980). The delineation of shallow crust areal sources shown in Figure 3 is referred to the research of Liu and Chang (2019).

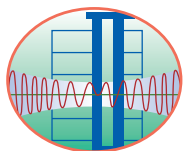
Conclusions

This study proposed a procedure to evaluate the a -value spatial distribution of areal sources. By referencing the L(M) scaling law (W&C94), this study set the effective seismogenic radius as $0.7L$ and estimated future disastrous earthquake potential areas. Additionally, this study integrated the KNN algorithm and the 2-D correlation coefficient to determine the optimal adaptively smoothed-distributed seismicity result, namely the 5th order of KNN.

Further discussion topics of this study are as follows: (1) employ small scale earthquakes ($M_w < 4.0$) to evaluate future disastrous earthquake probabilities and compare them with the results of moderate- and large-scale earthquakes; (2) adopt the Meinong earthquake in 2016 and the Hualien earthquake in 2018 as samples to verify the applicability of the potential earthquake evaluation method proposed in this study.

References

- Liu, H. J. and Chang, C. W. (2019). "Development of Regional Seismic Source Characterization Zones in and around Taiwan," 2018 NCREC Research Programs and Accomplishments Report.
- Weichert, D. H. (1980). "Estimation of the Earthquake Recurrence Parameters for Unequal Observation Periods for Different Magnitudes," *Bull. Seismol. Soc. Am.*, 70, 1337-1346.
- Wells, D. L. and Coppersmith, K. J. (1994). "New Empirical Relationships among Magnitude, Rupture Length, Rupture Width, Rupture Area, and Surface Displacement," *Bull. Seism. Soc. Am.*, 84(4), 974-1002.
- Wu, Y. M., Cheng, S. N., and Liu, T. Y., (2016). "A Foundation and Basic Analysis of Earthquake Catalog and Historical Earthquakes Database," Final report, prepared for Taiwan SSHAC Level 3 PSHA Project, 90 p.



National Center for Research on Earthquake Engineering

200, Sec. 3, HsinHai Rd., Taipei 106, Taiwan

Tel: +886-2-6630-0888 Fax: +886-2-6630-0858

<https://www.ncree.org>

